The Dissertation Committee for Doh Chang Lee Certifies that this is the approved version of the following dissertation:

Silicon Nanowires, Carbon Nanotubes, and Magnetic Nanocrystals: Synthesis, Properties, and Applications

Committee:

Brian A. Korgel, Supervisor

Allen J. Bard

James R. Chelikowsky

John G. Ekerdt

Gyeong S. Hwang

Yueh-Lin Loo

Silicon Nanowires, Carbon Nanotubes, and Magnetic Nanocrystals:

Synthesis, Properties, and Applications

by

Doh Chang Lee, B.S., M.S.

Dissertation

Presented to the Faculty of the Graduate School of

The University of Texas at Austin

in Partial Fulfillment

of the Requirements

for the Degree of

Doctor of Philosophy

The University of Texas at Austin

August 2007

Dedicated to my family

Acknowledgements

As I am finishing the chapters in this dissertation, I am about to burst with gratitude to the nanocrystals and nanowires for behaving honestly in all the successful or failed experiments. These babies awarded me a paddle to travel around the sea of materials science. However, I would never have been able to sail through this journey without the support and help from people around me. As I am moving on to a next chapter in my life, I would like to thank the people whose helps and prayers were priceless.

First, I am deeply indebted to my advisor, Dr. Brian Korgel, who made it possible for me to enjoy this chapter here at the University of Texas at Austin. He imbued me with fresh ideas, prompted me into the direction on target with cheerful clangs, and showed me a big picture of the science.

My profound gratitude also goes to all the past and present members of the Korgel group, who have shown wholehearted friendship and support, and I would like to name a few. Fred Mikulec, Chris Doty, Parag Shah, Cindy Stowell, Lindsay Pell, Tobias Hanrath, Michael Sigman, Aaron Saunders, Ali Ghezelbash, April Schricker and Felice Shieh offered perspective and advice, and helped me stay entertained all the time in the otherwise dry laboratory. Tripp Davidson, Dayne Fanfair, Hsing-Yu Tuan, Danielle Smith, Andy Heitsch, Bonil Koo, Damon Smith, Vince Holmberg, Matt Panthani, Mike Rasch, and Vahid Akhavan all deserve a thank-you for sharing their time to discuss in-depth science and for the joyful moments that kept me smiling.

I deeply thank my committee members, who have been the role models and guiding lights. Their sage advices nourished me with the elements quintessential to grow up as a mature scientist. I would also like to thank my former advisor, Dr. Sang Heup Moon, whose passion and education philosophy certainly provided a cornerstone upon which I was able to establish my stance as a researcher. In addition, the Harrington Fellowship granted the opportunities to freely explore the world of science without having to worry about the financial needs. I am very grateful for the generosity.

It would be difficult for me to adequately thank the El Camponians whose presence was invaluable through the years. They have been a resource to which I have resorted at all times. I am also indebted to all the loved ones whose warmth kept me from being a cold scientist and whose feeling I happened to hurt. Finally, my sincerest thanks go to my parents and my brother, Doh Young Lee, for their love and prayers.

Silicon Nanowires, Carbon Nanotubes, and Magnetic Nanocrystals:

Synthesis, Properties, and Applications

Publication No._____

Doh Chang Lee, Ph.D.

The University of Texas at Austin, 2007

Supervisor: Brian A. Korgel

Central to the practical use of nanoscale materials is the controlled growth in technologically meaningful quantities. Many of the proposed applications of the nanomaterials potentially require inexpensive production of the building blocks. Solution–based synthetic approach offers controllability, high throughput, and scalability, which make the process attractive for the potential scale–up. Growth kinetics could be readily influenced by chemical interactions between the precursor and the solvent. In order to fully utilize its benefits, it is therefore pivotal to understand the decomposition chemistry of the precursors used in the reactions.

Supercritical fluids were used as solvent in which high temperature reactions could take place. Silicon nanowires with diameters of 20~30 nm was synthesized in supercritical fluids with metal nanocrystals as seeds for the nanowire growth. To unravel the effect of silicon precursors, several silicon precursors were reacted and the resulting products were investigated. The scalability of the system is discussed based on the experimental data. The nanowires were characterized with various characterization

tools, including high–resolution transmission electron microscopy and electron energy loss spectroscopy. The crystallographic signatures were analyzed through the transmission electron microscopic study, and fundamental electrical and optical properties were probed by electron energy loss spectroscopy. Carbon nanotubes were prepared by reacting carbon–containing chemicals in supercritical fluids with organometallic compounds that form metal seed particles *in-situ*. A batch reaction, in which the temperature control was relatively poor, yielded a mixture of multiwall nanotubes and amorphous carbon nanofilaments with a low selectivity of nanotubes in the product. When reaction parameters were translated into a continuous flow-through reaction, nanotube selectivity as well as the throughput of the total product significantly improved.

Magnetic properties of various metal nanocrystals were also studied. Colloidal synthesis enables the growth of FePt and $MnPt_3$ nanocrystals with size uniformity. The as-synthesized nanocrystals, however, had compositionally disordered soft-magnetic phases. To obtain hard magnetic layered phase, the nanocrystals must be annealed at high temperatures, which led to sintering of the inorganic cores. To prevent sintering, the nanocrystals were encapsulated with silica layer prior to annealing. Interparticle magnetic interactions were also explored using particles with varying silica thickness.

Table of Contents

List of Tables

List of Figures

xxx

Chapter 1: Introduction

In the past few decades, many different approaches to nanomaterials synthesis and processing have been developed. These strategies can be loosely categorized as either "top-down" or "bottom-up". "Top-down" generally refers to processes that rely on lithography or patterning to define the dimensions of the nanostructure. "Bottom-up" processes do not require lithography and patterning. Solution-based (*e.g.*, colloidal) nanomaterial synthesis is "bottom-up". Bottom-up and top-down approaches each have their advantages and disadvantages. Top-down approaches can be extremely effective at reproducibly defining nanostructure dimensions—lithography is the foundation of the microelectronics industry and sub-100 nm transistor gate lengths are defined by lithography in commercially available transistors. However, lithography faces fundamental limitations in defining features smaller than ~20 nm in diameter. Top-down processing costs are also becoming prohibitively expensive, with ever-shrinking feature size. Bottom-up routes to nanostructures on the other hand, such as colloidal syntheses, are inexpensive and scalable. These methods have the potential to produce nanocrystals, nanotubes and nanowires with characteristic dimensions less than 20 nm in large quantities with low cost. One significant challenge facing bottom-up processes, however, is that the nanostructures are "free-standing" and must then be assembled at specific positions on a substrate for device applications. This can be a significant technological hurdle. Nonetheless, there are applications, as in the medical sciences, in which dispersed particles are in fact desired. The dispersibility of nanocrystals and nanowires in various solvents and the ability to deposit them by spin-coating, inkjet printing, stamping, roll-to-roll processing, *etc.*, can also be a processing advantage compared to top-down processes by enabling low temperature deposition on alternative

substrates like polymers. This capability could lead to new low-cost electronic and photonic technologies.

1.1 NANOWIRES AND NANOTUBES

Semiconductor nanowires and carbon nanotubes have been synthesized in gas-phase reactions (laser pyrolysis, CVD, *etc.*). Despite similarities in final morphology (high aspect ratio, seeded growth, <50 nm diameter), these two different materials pose stark contrast in the detailed growth mechanism. In the past few decades, atomic precision in the growth of the 1D nanomaterials has been acquired through painstaking parameter studies. The drive to improve the versatility of the synthesis systems has also witnessed the growth of unique structures of materials of rich variety. However, the fundamental difficulty in integrating the free-standing materials into desired device structures poses a huge challenge.

In order to capitalize on the synthetic capability, an increasing amount of research effort has focused more on using these 1D nanomaterials in a bulk quantity. Carbon nanotubes, for example, increase the elastic modulus of polymer when blended at a certain concentration. Nanowire- or nanotube-based electronic devices could benefit from decreased failure rate, compared to when a single entity is used as an active component. Apparently, the applications eventually will require cheap production cost. Solution-based approaches are promising in high production rate; however, silicon nanowires and carbon nanotubes have rarely been synthesized in the desirable quantity in solution because the reaction temperature significantly exceeds the boiling point of conventional solvents. In supercritical fluid media, the reaction can reach the temperatures while high precursor concentration is retained.

1.1.1 VLS Growth Mechanism

The vapor-liquid-solid (VLS) process has been the most successful for growing semiconductor nanowires with single-crystalline structures. The growth mechanism was first proposed by Wagner and Ellis, who studied the growth of micrometer-sized whiskers in 1960s. The discovery has provided insight into the crystal growth mechanism that is operative for many types of nanowires. In fact, their discovery was quite serendipitous: they originally intended to deposit Si films on thin Au film, but Si atoms instead dissolved into Au and formed liquid alloy droplets. Continued Si atom supply led to the precipitation upon saturation, giving rise to one-dimensional growth.

The VLS process was later adopted to grow semiconductor nanowires by Lieber, Yang, and other research groups. Morales and Lieber used laser pyrolysis of Si molecules to grow Si nanowires in the presence of Fe target to form Fe particles in-situ. Chemical vapor deposition (CVD) process later replaced the laser-based approach, enabling the tuning of nanowire diameter and size distribution. The CVD route has been extended to the synthesis of rich variety of semiconductor nanowires. However, the gas-phase approach poses a key limitation in the throughput. Solution-based growth presents a remedy for the issue since it utilizes free seed particles for the synthesis of orders-of-magnitude larger quantities of nanowires. Buhro and coworkers developed a solution-liquid-solid (SLS) method to synthesize III-V semiconductors at relatively low temperatures in solution. They used low melting point metal nanoparticles (In, Sn, or Bi) as seeds, and organometallic precursors as nanowire materials. For Si or Ge nanowires, conventional solvents cannot accommodate the growth because the precursor decomposition occurs at temperatures higher than the boiling point.
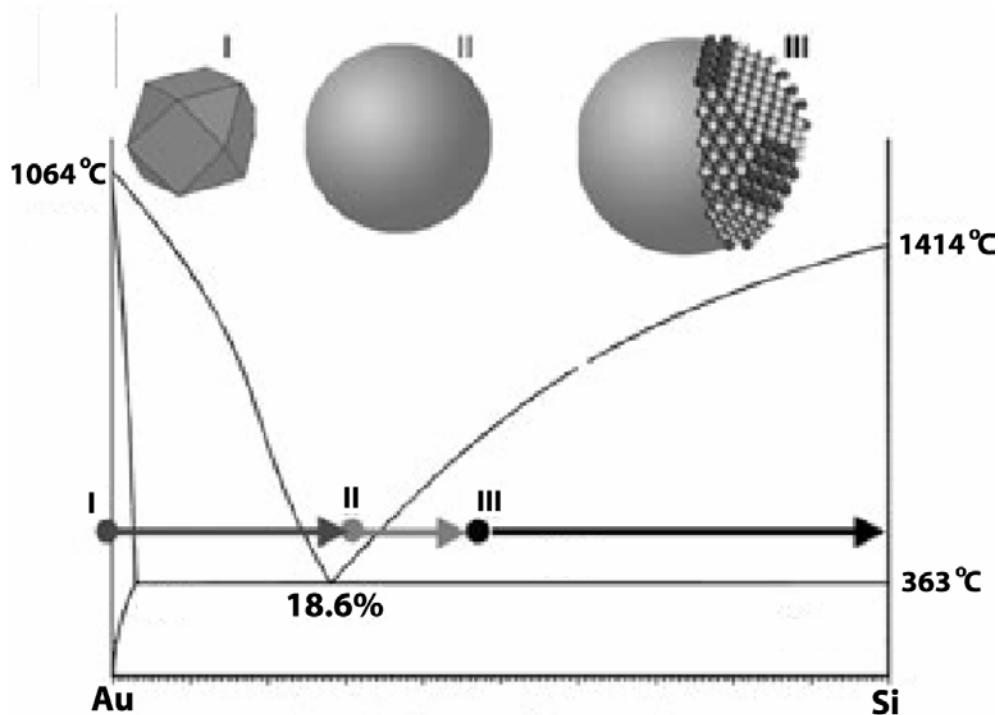
Figure 1.1. Schematic diagram of vapor-liquid-solid growth mechanism of silicon nanowires with Au nanoparticles as seeds.   The nanowire seeding illustration courtesy of Hanrath.

The supercritical fluid media therefore offer high-temperature capability and potentially high-throughput settings.   In addition, the scalability of the system provides an advantage of growing technologically meaningful quantities of nanowires.   Surface modification is also possible, which furnishes the system with additional tenability.

1.1.2 Carbon Nanotube Growth

Although carbon nanotubes are perceived to be very new materials, they have been found to exist for geologically long time in nature, such as on the moon.   However, only since 1990's have metal seed particles been used to catalyze the growth of high-quality single-wall and multiwall carbon nanotubes (SWNTs and MWNTs, respectively) at relatively low temperature (500~800 °C) through CVD.[1]   Although CVD growth can

4

be very effective, nanotube formation occurs on a substrate surface in batch synthetic processes, which limits the product yield and throughput. For microelectronics applications and other high value-added applications, such as high-resolution displays, CVD might be a suitable route. However, for other applications such as fabrics or structural composites that require very large amount of nanotubes at low cost, an alternative high throughput synthetic process is needed.

Solution-based approaches for carbon nanotube synthesis are limited by the high growth temperatures typically required. Using supercritical fluids as solvents, high growth temperatures can be reached. Unlike the CVD process, a continuous high throughput of nanowires is possible.
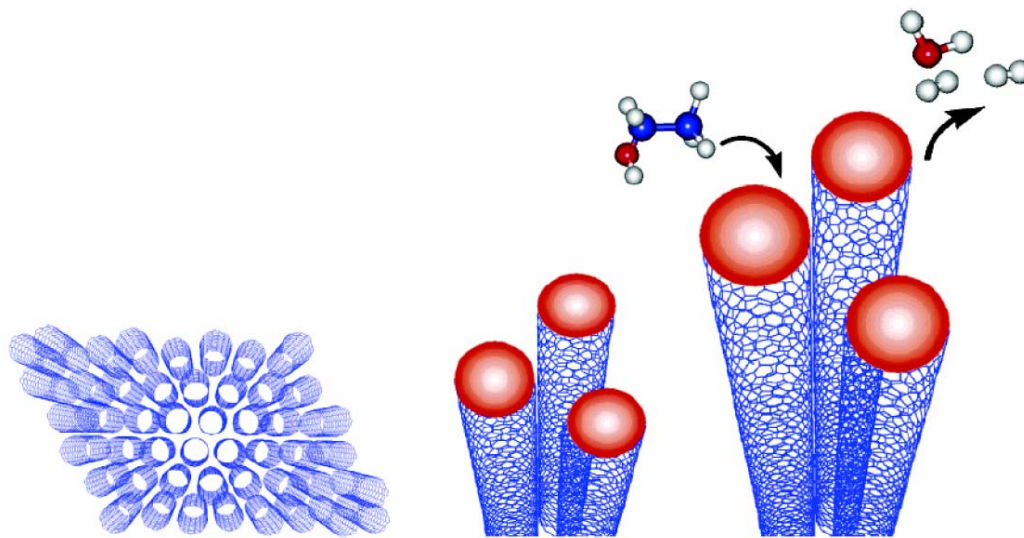
Figure 1.2. Schematic illustration of carbon nanotube growth. Courtesy of Y. Wang *et al.*, *Nano Lett.*, 5, 997, 2005.

1.1.3 Supercritical Fluid

A supercritical fluid is any substance at a temperature and a pressure above its thermodynamic critical point. It has the unique ability to diffuse like a gas, and dissolve materials like a liquid. Additionally it can readily change in density upon minor

changes in temperature or pressure. Supercritical fluids offer the great flexibility as a reaction medium because of these features. They have been used in a variety of processes, including extraction, chromatography, reactions, and materials processing. The benefits of supercritical fluids have been exploited in the synthesis and processing of various nanomaterials. Seminal efforts by Korgel and coworkers have revealed the interesting synthesis and self-assembly properties of inorganic nanomaterials in supercritical fluid media. High-temperature availability, high precursor concentration, and scalability all add up to make the supercritical fluid system very suitable and attractive choice for the nanomaterial growth.
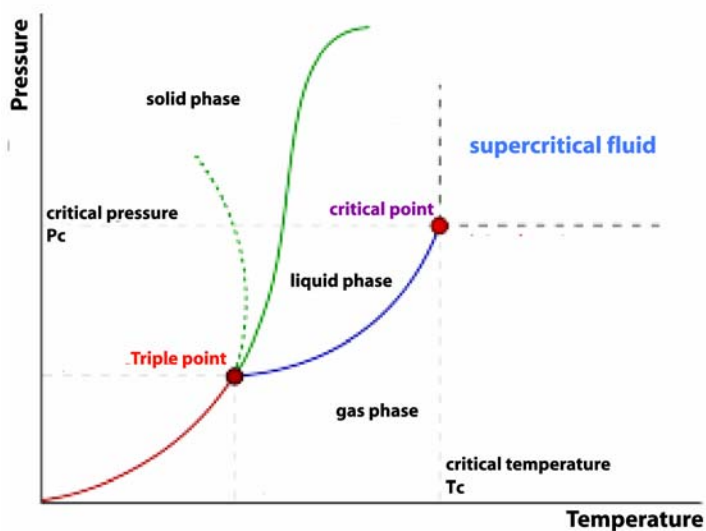
Figure 1.3. Phase diagram in T-P plot. Supercritical fluid is a phase of a material heated and pressured above its critical temperature and pressure, respectively.

1.2 COLLOIDAL MAGNETIC NANOCRYSTALS

Interest in nanoscale phenomena in magnetic materials dates back nearly 80 years when researchers recognized that the magnetic behavior of ferromagnets, such as magnetization hysteresis, derived not only from spin coupling between neighboring atoms but from the formation of sub-micrometer magnetic domains. Frenkel and Dorfman claimed in 1930 that magnetic particles smaller than this domain size would have different magnetic properties than the bulk material. Kittel, Néel, and Bean and Livingston made important contributions through the 1930's to 1950's in understanding the magnetic properties of nanoscale materials. This early work had direct bearing on the geological sciences—many minerals occur naturally as small particulates in non-magnetic hosts and their magnetic properties reflect their nanometer size. "Nanomagnetism" later emerged in industrial materials, such as particulates of steels, catalysts and new computer elements like the ferrite coil. Contemporary nanomagnetics research is motivated primarily by the development of new information technology and medical applications, in which many of the same aspects of "nanomagnetism" still apply, such as nanoscale size effects and the influence of the interfaces in the system.

A flurry of new nanoscale magnetic materials research has occurred during the last several years, encouraged by dramatic improvements in materials synthesis and processing, characterization tools and theoretical understanding. Rapid technological progress in the microelectronics industry—driven by continued emphasis on reduced device dimensions and integrated circuit device densities—has also pushed research in magnetic nanostructures, particularly in the continued development of higher-density memory storage materials and devices and the search for a solution to a non-volatile low-power random access memory. Fundamental discoveries of giant magnetoresistance (GMR), spin-dependent electrical transport, spin torque transfer and dilute magnetic

7

semiconductors that exhibit ferromagnetism have all served as both products and motivators of continued active research in the area.
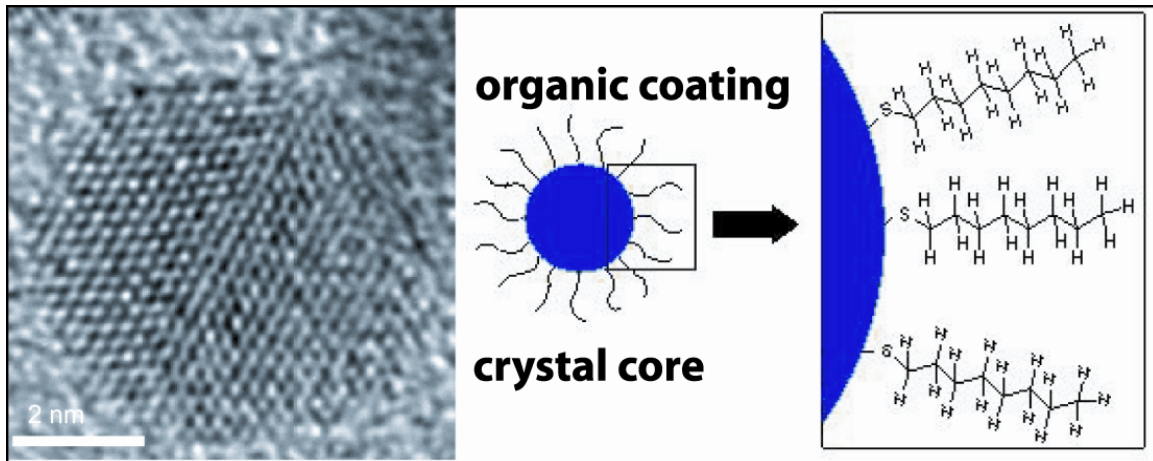
Figure 1.4. TEM image (left) and schematic illustration of crystalline nanocrystal synthesized via the 'arrested precipitation' method. The organic coating is dodecanethiol (C_{12}-SH). This Figure is taken from ChE 384 class taught by B. A. Korgel at the University of Texas at Austin.

1.2.1 Colloidal Magnetic Nanocrystal Synthesis

1.2.1.1 Transition metal nanocrystals

Nanocrystals of the magnetic transition metals, Fe, Co and Ni, have been synthesized by high temperature arrested precipitation.   TOP and TOPO are generally not used as the solvent for the synthesis of transition metal nanocrystals because they are reactive and produce the transition metal phosphides, FeP or Fe_2P , Co_2P or Ni_2P, as the product.   The phosphorous-carbon bond in the TOP-Fe, TOP-Co, and TOP-Ni complexes cleaves, as opposed to the phosphine ligand dissociating to leave the metal. This is an important lesson for nanocrystal synthesis: capping ligands that work well for one material may not work at all for another material, even participating in the reaction and becoming part of the nanocrystal reaction product in some cases.   There is currently little predictive understanding of how to choose the appropriate capping ligands to synthesize different nanocrystal materials.

For transition metal nanocrystal, high boiling *non-coordinating* solvents like diphenylether or dioctylether are employed and long chain carboxylic acids and amines, such as octenoic acid and tetradecylamine, are added as capping ligands. $Fe(CO)_5$ has been used extensively as a source for Fe in nanocrystal growth.   CO is a relatively good leaving group and $Fe(CO)_5$ decomposes to Fe at relatively mild temperatures ($>100^oC$) in dioctyl ether.   Co nanocrystals have been synthesized by a number of different routes. Pileni and co-workers used reverse micelles of Na(AOT) (sodium bis(2-ethylhexyl)sulfosuccinate) and $Co(AOT)_2$ (cobalt bis(2-ethylhexyl)sulfosuccinate), with $NaBH_4$ (sodium borohydride) as a reducing agent.   The Co nanoparticles synthesized using this method were monodisperse and could be organized into superlattices.   Sun and Murray synthesized Co nanocrystals by combining $CoCl_2$ with oleic acid and

trialkylphosphine in dioctylether at 200 °C with added superhydride (LiBEt$_3$H) as a reducing agent.

$$CoCl_2 + oleic\,acid + TOP \xrightarrow[200\,°C,\,dioctyl\,ether]{superhydride} (Co)_{nc}$$

The Co nanocrystal size could be adjusted using different alkylphosphines as capping ligands in combination with oleic acid: trioctylphosphine gave smaller nanocrystals (2-6 nm), and tributylphosphine gave larger nanocrystals (7-11 nm). Interestingly, the Co nanocrystals had an unusual ε-Co phase. Dinega and Bawendi also found that Co nanocrystals had an ε-Co structure when synthesized by thermal decomposition of Co$_2$(CO)$_8$ at relatively low temperatures in TOPO (50-110 °C). Puntes *et al.*, however, produced hcp Co nanocrystals, as well as ε-Co nanocrystals, under slightly different reaction conditions, by Co$_2$(CO)$_8$ decomposition in oleic acid/TOPO at ~182 °C. In some cases, the Co nanocrystals had a disk shape. Ni nanocrystals with narrow size distributions have been synthesized by high temperature arrested precipitation, using nickel acetate in diphenyl ether as a solvent with TOP, oleic acid and trioctylamine as a mixture of capping ligands. The use of multiple capping ligands in a single reaction is common practice for transition metal nanocrystals and appears to be important for obtaining nanocrystals with good size control. However, the role of each different capping ligand remains poorly understood.

1.2.1.2 Hard magnetic intermetallic compounds

L1$_0$ FePt has high magnetocrystalline anisotropy (K_u), saturation magnetization and maximum energy product (($BH)_{max}$) (6.6×10^7 erg/cm^3 (~60 meV/nm^3), 1140 emu/cm^3 and 13 MGOe, respectively). L1$_0$ FePt domains as small as 3 nm in diameter could be used as memory bits—their magnetic anisotropy energy ($K_u V$) would exceed kT (at room temperature) by about a factor of 25. 1 Tb/in^2 storage density could be achieved using 3

nm diameter FePt domains as individual bits in a monolayer with an edge-to-edge separation of about 25 nm. The detection sensitivity required to read the magnetic information stored on each bit is well beyond the current detection sensitivity of magnetic read heads; but nevertheless, such a magnetic storage media should be possible to construct with nanocrystals of this material. The so-called superparamagnetic limit can be pushed to smaller particle size by using materials with very high magnetocrystalline anisotropy with K_u of the order $\sim 10^6$ J/m^3.

FePt nanocrystal synthesis is complicated by the inherent difficulty in achieving atomic order in the material. When FePt is synthesized or deposited as a thin film, it is compositionally disordered. It has an fcc crystal structure, but Fe and Pt atoms are distributed randomly in lattice and the magnetic anisotropy of the material is low. The hard magnetic phase of FePt is the $L1_0$ phase, in which Fe and Pt atoms are ordered as layers in a tetragonally distorted unit cell. The preferred magnetization direction is correspondingly in the direction of the *c*-axis of the crystal. The ordered phase is thermodynamically favored, but the disordered phase is kinetically trapped and the material must be heated to enable the atoms to rearrange. This situation is complicated in most metal platinides by the presence of more than one thermodynamically stable phase. For example FePt, Fe_3Pt and $FePt_3$ are all thermodynamically stable and have very different magnetic properties. The phase boundary between $FePt_3$ and FePt is around 58% Fe and subtle variations in composition can lead to dramatic changes in magnetic properties. Additionally, many syntheses produce a mixture of two different phases.

Sun and Murray first showed how to obtain $L1_0$ FePt nanocrystals by colloidal synthesis. FePt nanocrystals are first synthesized by arrested precipitation with random atomic order of FePt. The nanocrystals are then annealed at ~ 550 °C to enable the

transformation of the FePt to the atomically ordered $L1_0$ phase. Nanocrystal growth in solution occurs by essentially two steps. $Pt(acac)_2$ is first reduced with polyol, e.g., 1,2-hexadecanediol, to form Pt nanocrystals. Then either $Fe(CO)_5$ is thermally decomposed or $Fe(acac)_2$ is reduced, to supply Fe atoms that coat the Pt-rich nuclei. The Fe/Pt core/shell nanocrystals are then alloyed as the dispersion is held at ~290 °C.

Carboxylic acids and amines are employed in the reaction as capping ligands because each of the chemicals bonds stronger to Fe and Pt, respectively, and the use of both $RCOOH/RNH_2$ ligands helps provide robust passivation of the nanocrystal surface. The materials transformation from core/shell to random alloy nanocrystals that occurs during particle growth is rather complex and the nanocrystal size can be controlled only to a limited extent. Slightly different recipes are needed to obtain FePt nanocrystals of different sizes and compositions, as the final particle size depends sensitively on the entire particle growth process and the ligand-surface interactions — size tuning is not just a matter of taking a synthetic prescription and heating for longer times or increasing the reaction temperature slightly.

1.2.2 Magnetism in Nanoscale Materials

Magnetic nanoparticles exhibit size-dependent properties that differ from the bulk materials. The magnetic properties of the materials are governed by the competition between two energy components: exchange energy and thermal energy. Magnetic exchange energy is proportional to the volume of the magnetic domains, so with decreasing particle size, magnetic energy decreases until the thermal energy can disrupt the interaction between the magnetic units. An applied field induces spin alignment, which is opposed by thermal randomization. But at zero applied magnetic field, the moment will go back to zero just as in a paramagnet. This phenomenon is called superparamagnetism.

1.2.3 Magnetic Measurements on Magnetic Nanostructures

Quantitative studies of *individual* magnetic nanocrystals are rare because of limited resolution of magnetic measurement capabilities, *e.g.* magnetic force microscopy (MFM). However, *single particle* analytical tools are very important because they yield information about heterogeneity in the sample and what really happens at the level of the individual nanocrystal. Optical measurements of the photoluminescence from individual semiconductor quantum dots for example have revealed unexpected properties such as blinking, or intermittency.

For magnetic nanostructures, Wernsdorfer *et al.* have developed a micro-superconducting quantum interference device (SQUID) that is approaching single particle measurement capability. They recently detected the magnetization of individual Ni nanowires. The technique has been further improved and they measured the magnetization switching fields of a single 3 nm Co particle in a niobium matrix. The essential part of the micro-SQUID magnetometer is a 20 nm-thick Nb microbridge,

which allows detection of $\sim 10^4$ μ_B.   Although the spatial resolution of this tool is not practical for measuring the magnetic properties of an individual nanocrystal in an ensemble, the tool can provide measurements of magnetic properties at the single nanocrystal level.   Another promising technique for studying the magnetic properties of individual nanocrystals is electron holography in specially-equipped transmission electron microscopes (TEM).   Using this technique, Che and co-workers studied the magnetic properties of ~ 150 nm-thick FePt nanorods fabricated by electron beam-induced metal deposition.   By converting holography images into a residual magnetic flux density, they were able to measure 1.53 T of residual magnetic flux in the FePt nanorods.   Combined with techniques for measuring the collective magnetic properties of ensembles of nanocrystals, such as magnetic force microscopy (MFM), holography can provide insight into magnetic interactions between nanocrystals in close-packed assemblies.

1.2.4 Magnetic Interparticle Interactions

In magnetic storage media, the close proximity of the nanostructures can influence their magnetic properties.   Magnetic dipole coupling between nanocrystals can occur, which favors antiparallel alignment of neighboring magnetic moments.   In superlattices of organic ligand-coated nanocrystals, the interparticle separation is only 1 to 3 nm and magnetic dipole coupling is important as Murray and co-workers found for Co nanocrystal superlattices.   Since magnetic dipole coupling can induce spin flipping and demagnetization, it is unwanted in magnetic memory storage applications.   When the interparticle spacing is less than a nanometer, magnetic nanocrystals can also interact through magnetic exchange interactions.   Zeng *et al.* investigated annealed mixtures of FePt and Fe_3O_4 nanocrystals, and observed exchange coupling between large anisotropy

14

FePt grains and small anisotropy Fe_3O_4 grains, which enhanced the energy product $(BH)_{max}$ (20.1 MG Oe) by ~37%, compared to pure FePt.

The magnetic properties of a nanocrystal ensemble also depend on the relative orientations of the magnetic easy axis of the particles. Controlling the direction of the magnetic easy axis of colloidal nanocrystals in an evaporated film is a challenge. Simple deposition yields nanocrystals with randomly oriented crystallographic directions. Attempts have been made to deposit or anneal under applied magnetic fields, but these studies have had only a marginal degree of success. There is currently no effective approach to depositing colloidal nanocrystal films with preferred crystallographic orientation and new methods are needed.

1.3 DISSERTATION OVERVIEW

Silicon nanowire synthesis in supercritical fluids is discussed in Chapter 2. Several silicon precursors were tested in the system where sufficient silicon atom supply was required to grow nanowires with Au nanoparticles present as seeds. Kinetically and thermodynamically labile silicon precursors for the growth are discussed. Chapter 3 covers HRTEM and EELS studies of the silicon nanowires. The growth direction of silicon nanowires, defect formation, and plasmon response are discussed. Chapter 4 describes the synthesis of carbon nanotubes in supercritical fluid reactions.

Chapters 5 and 6 explore colloidal magnetic nanocrystals and silica-coated magnetic nanoparticles, respectively. Control of the growth and magnetic properties of the ensembles are examined. Chapter 7 summarizes the main conclusions of this dissertation and offers suggestions for future research works.

1.4 REFERENCES

(1) Dai, H.; Rinzler, A. G.; Nikolaev, P.; Thess, A.; Colbert, D. T.; Smalley, R. E., *Chem. Phys. Lett* **1996,** 260, 471.

(2) Dresselhaus, M. S.; Dresselhaus, G.; Avouris, P., *Carbon Nanotubes : Synthesis, Structure, Properties, and Applications*. Springer: New York, 2002.

(3) Hu, J. T.; Odom, T. W.; Lieber, C. M., *Acc. Chem. Res.* **1999,** 32, 435.

(4) Wu, Y.; Cui, Y.; Huynh, L.; Barrelet, C. J.; Bell, D. C.; Lieber, C. M., *Nano Lett.* **2004,** 4, 433.

(5) Qian, F.; Li, Y.; Gradecak, S.; Wang, D. L.; Barrelet, C. J.; Lieber, C. M., *Nano Lett.* **2004,** 4, 1975.

(6) Duan, X. F.; Lieber, C. M., *Adv. Mater.* **2000,** 12, 298.

(7) Duan, X. F.; Huang, Y.; Lieber, C. M., *Nano Lett.* **2002,** 2, 487.

(8) Stach, E. A.; Pauzauskie, P. J.; Kuykendall, T.; Goldberger, J.; He, R. R.; Yang, P. D., *Nano Lett.* **2003,** 3, 867.

(9) Huang, M. H.; Wu, Y. Y.; Feick, H.; Tran, N.; Weber, E.; Yang, P. D., *Adv. Mater.* **2001,** 13, 113.

(10) Lieber, C. M., *Sci. Am.* **2001,** 285, 58.

(11) Huang, Y.; Duan, X. F.; Cui, Y.; Lauhon, L. J.; Kim, K. H.; Lieber, C. M., *Science* **2001,** 294, 1313.

(12) Hahm, J.; Lieber, C. M., *Nano Lett.* **2004,** 4, 51.

(13) Dai, H. J.; Kong, J.; Zhou, C. W.; Franklin, N.; Tombler, T.; Cassell, A.; Fan, S. S.; Chapline, M., *J. Phys. Chem. B* **1999,** 103, 11246.

(14) Davidson, F. M.; Schricker, A. D.; Wiacek, R.; Korgel, B. A., *Adv. Mater.* **2004,** 16, 646.

(15) Hanrath, T.; Korgel, B. A., *J. Am. Chem. Soc.* **2002,** 124, 1424.

(16) Hanrath, T.; Korgel, B. A., *Adv. Mater.* **2003,** 15, 437.

(17) Holmes, J. D.; Johnston, K. P.; Doty, R. C.; Korgel, B. A., *Science* **2000,** 287, 1471.

(18) Xia, Y.; Yang, P.; Sun, Y.; Wu, Y.; Mayers, B.; Gates, B.; Yin, Y.; Kim, F.; Yan, H., *Adv. Mater.* **2003,** 15, 353.

(19) Wagner, R. S.; Ellis, W. C., *Appl. Phys. Lett.* **1964,** 4, 89.

(20) Wu, Y. Y.; Yang, P., *J. Am. Chem. Soc.* **2001,** 123, 3165.

(21) Westwater, J.; Gosain, D. P.; Tomiya, S.; Usui, S.; Ruda, H., *J. Vac. Sci. Technol. B* **1997,** 15, 554.

(22)   Morales, A. M.; Lieber, C. M., *Science* **1998,** 279, 208.

(23)   Dingman, S. D.; Rath, N. P.; Markowitz, P. D.; Gibbons, P. C.; Buhro, W. E.,
         Angew. Chem. Int. Ed. **2000,** 39, 1470.

(24)   Holmes, J. D.; Ziegler, K. J.; Doty, R. C.; Pell, L. E.; Johnston, K. P.; Korgel, B.
         A., *J. Am. Chem. Soc.* **2001,** 123, 3743.

(25)   Shah, P. S.; Holmes, J. D.; Doty, R. C.; Johnston, K. P.; Korgel, B. A., *J. Am.
         Chem. Soc.* **2000,** 122, 4245.

(26)   Shah, P. S.; Holmes, J. D.; Johnston, K. P.; Korgel, B. A., *J. Phys. Chem. B* **2002,**
         106, 2545.

(27)   Shah, P. S.; Husain, S.; Johnston, K. P.; Korgel, B. A., *J. Phys. Chem. B* **2001,**
         105, 9433.

(28)   Bloch, F., *Z. Phys.* **1932,** 74, 295.

(29)   Brown, W. F., *Rev. Mod. Phys.* **1945,** 17, 15.

(30)   Frenkel, J.; Dorfman, J., *Nature* **1930,** 126, 274.

(31)   Kittel, C., *Phys. Rev.* **1946,** 70, 965.

(32)   Neel, L., *Rev. Mod. Phys.* **1953,** 25, 293.

(33)   Bean, C. P.; Livingston, J. D., *J. Appl.   Phys.* **1959,** 30, S120.

(34)   Park, J.; Koo, B.; Yoon, K. Y.; Hwang, Y.; Kang, M.; Park, J.-G.; Hyeon, T., *J.
         Am. Chem. Soc.* **2005,** 127, 8433.

(35)   Peng, S.; Wang, C.; Xie, J.; Sun, S., *J. Am. Chem. Soc.* **2006,** 128, 10676.

(36)   Petit, C.; Taleb, A.; Pileni, M.-P., *Adv. Mater.* **1998,** 10, 259.

(37)   Pileni, M.-P., *Appl. Surf. Sci.* **2001,** 171, 1.

(38)   Sun, S. H.; Murray, C. B., *J. Appl. Phys.* **1999,** 85, 4325.

(39)   Dinega, D. P.; Bawendi, M. G., *Angew. Chem. Int. Ed.* **1999,** 38, 1788.

(40)   Puntes, V. F.; Krishnan, K. M.; Alivisatos, A. P., *Science* **2001,** 291, 2115.

(41)   Puntes, V. F.; Zanchet, D.; Erdonmez, C. K.; Alivisatos, A. P., *J. Am. Chem. Soc.*
         2002, 124, 12874.

(42)   Sun, S. H.; Murray, C. B.; Weller, D.; Folks, L.; Moser, A., *Science* **2000,** 287,
         1989.

(43)   Murray, C. B.; Norris, D. J.; Bawendi, M. G., *J. Am. Chem. Soc.* **1993,** 115, 8706.

(44)   Park, J.; Lee, E.; Hwang, N. M.; Kang, M. S.; Kim, S. C.; Hwang, Y.; Park, J. G.;
         Noh, H. J.; Kini, J. Y.; Park, J. H.; Hyeon, T., *Angew. Chem. Int. Ed.* **2005,** 44,
         2872.

(45)   Peng, X.; Manna, L.; Yang, W. D.; Wickham, J.; Scher, E.; Kadavanich, A.; Alivisatos, A. P., *Nature* **2000,** 404, 59.

(46)   Chen, J. P.; Sorensen, C. M.; Klaubunde, K. J.; Hadjipanayis, G. C., *Phys. Rev. B* **1995,** 51, 11527.

(47)   Wernsdorfer, W.; Doudin, B.; Mailly, D.; Hasselbach, K.; Benoit, A.; Meier, J.; Ansermet, J.-P.; Barbara, B., *Phys. Rev. Lett.* **1996,** 77, 1873.

(48)   Murray, C. B.; Sun, S. H.; Doyle, H.; Betley, T., *MRS Bull.* **2001,** 26, 985.

(49)   Zeng, H.; Li, J.; Wang, Z. L.; Liu, J. P.; Sun, S., *Nano Lett.* **2004,** 4, 187.

Chapter 2: Synthesis of Silicon Nanowires in Supercritical Fluid†

2.1 INTRODUCTION

The "bottom-up" chemical synthesis of semiconductor nanowires has been developed in recent years as an alternative strategy to conventional lithographic patterning approaches for obtaining functional nanostructures suitable for applications like logic gates, memory devices, light emitting devices, sensors, and photonic circuits. Nanowire growth by the vapor-liquid-solid (VLS) mechanism has been very successful for a variety of different materials, including Group IV, III-V, and II-VI semiconductors, and metal oxides. These nanowires can be suspended in solvents and then deposited on substrates or mixed with polymers as composites, making them in many ways like macromolecules. Ideally, one would like to employ solution-phase chemistry to synthesize these nanomaterials and move away from slow and expensive gas-phase chemical vapor deposition (CVD).

The colloidal solution-phase synthesis of Si nanomaterials has been extremely challenging and represents to some extent a "holy grail" in colloidal nanomaterials chemistry. In 2000, Holmes *et al.* showed that crystalline Si nanowires could be synthesized in solution using Au nanocrystals as seeds to lower the crystallization barrier and promote crystalline nanowire growth. By pressurizing the organic solvent, reaction temperatures exceeding the Au:Si eutectic could be reached (363 °C), and "VLS"-like nanowire growth could be promoted. This nanowire growth mechanism has been called *supercritical fluid-liquid-solid* (SFLS) synthesis. Central to this solution-based approach is to understand the kinetics of precursor decomposition. In contrast to well-studied gas-phase silane decomposition, very little is known about the relevant

silane chemistry (*i.e.*, aryl- and alkyl-substituted silanes and trisilane) in high temperature pressurized solvents, and many of the other "obvious" precursor choices do not work at all. In fact, the SFLS process is very sensitive to precursor decomposition kinetics, requiring careful tuning to optimize the nanowire quality to prevent unwanted homogeneous Si particle nucleation.

Despite common use as seeds due to reachable eutectic temperature and ease of synthesis, Au nanocrystals pose a problem in their potential use in microelectronics industry. Au forms deep carrier traps in Si and must be avoided for the ultimate device integration. Metals routinely used in Si electronics, such as Ti, Fe, Co, and Ni, exhibit eutectic temperatures far exceeding the degradation temperatures of organic solvents. Some of these metals, however, undergo eutectoid transformation in which solid-phase diffusion allows for alloying of the metals and silicon. Kamins *et al.* reported the Ti-seeded Si nanowire growth at 640 °C, which is ~600 °C below the Ti-Si eutectic temperature. Assisted by their possible catalytic properties, transition metal (Fe, Co, and Ni) nanocrystals could promote Si nanowire growth in supercritical fluids.

2.2 EXPERIMENTAL SECTION

2.2.1 Seed Metal Nanocrystal Synthesis

2.2.1.1 Gold nanocrystal synthesis

Gold nanocrystals, passivated with thiol or phosphine molecules, were prepared according to methods published elsewhere. For a typical synthesis, 95 mg of hydrogen tetrachloroaurate trihydrate (HAuCl$_4$·3H$_2$O, Aldrich) dissolved in 9 mL deionized water (DI-H$_2$O) was combined with 675 mg of tetraoctylammonium bromide (TOAB, Aldrich) in 6.125 mL toluene. The mixture turned to darker brown upon stirring. After 30

minutes of vigorous stirring, the mixture was separated using a separation funnel and then 60 μL dodecanethiol ($C_{12}H_{25}SH$, Aldrich), or 100 μL trioctylphosphine (($C_8H_{17})_3P$, Fluka) was introduced to the dark-purple organic phase under stirring. 3 mmol of $NaBH_4$ in 7.5 mL DI-H_2O was added dropwise to the organic phase and the reaction was allowed to proceed for 4 hours. The aqueous phase was removed and discarded, leaving the nanocrystal-rich toluene solution. Excess ethanol was added to the toluene solution as an antisolvent, and the nanocrystals were precipitated by centrifugation. The supernatant was discarded and the nanocrystals were redispersed in hexane or toluene. The nanocrystals were washed with ethanol once more and stored in hexane solution inside a nitrogen-filled glove box. The TEM images of Au nanocrystals passivated with trioctylphosphine and dodecanethiol are shown in Figure 2.1.
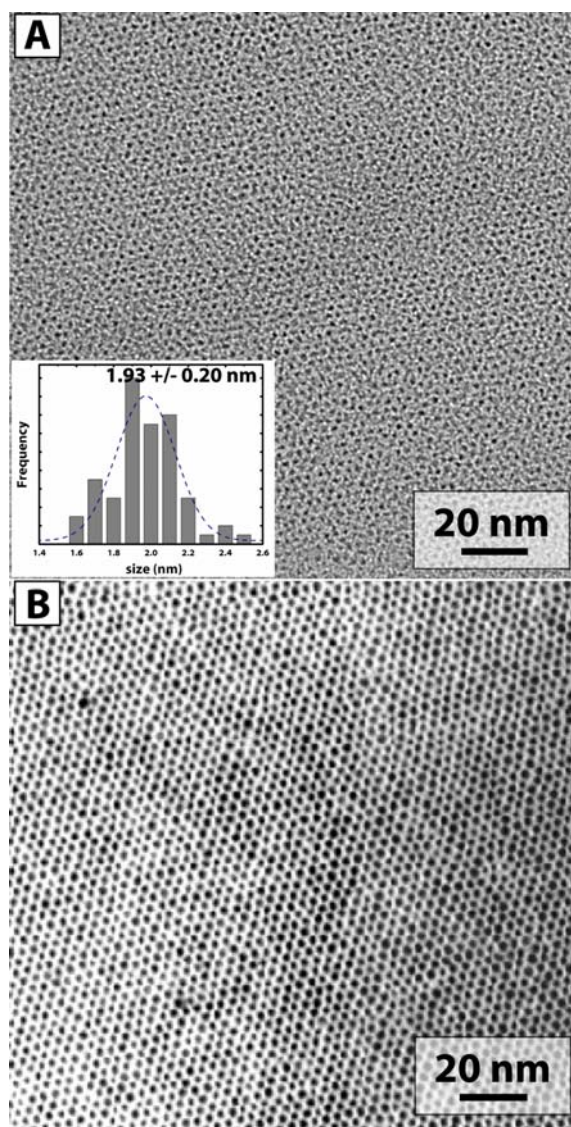
Figure 2.1. TEM images of Au nanocrystals synthesized with (A) trioctylphosphine or (B) dodecanethiol as a capping ligand.   TEM image in (B) is reproduced from the work by Saunders *et al.*

2.2.1.2 Nickel nanocrystal synthesis

Ni nanocrystals were prepared by nickel carbonyl reduction following procedures developed by Murray and coworkers.   At room temperature, 1 mmol of

Ni(CH$_3$COO)·4H$_2$O (Aldrich) was mixed with 0.5 mmol of oleic acid (Aldrich), 2 mmol of trioctylamine (Aldrich) and 0.25 mmol of trioctylphosphine (Fluka) in 10mL of diphenylether (Aldrich) in a three-neck flask.   The mixture was agitated at room temperature while flushing with nitrogen for ~20 min.   After heating the solution to 200 °C, 0.5 mmol of trioctylphosphine was injected.   At this point, the green solution becomes a dark-green color.   The mixture was then heated to 250 °C.   Separately, 0.5 g 1,2-hexadecanediol (Aldrich) was dissolved in 2.5 mL of diphenylether and heated to 80°C under nitrogen atmosphere.   The ether solution was injected into the nickel carbonyl/phosphine solution once it reached 250 °C.   The solution temperature immediately dropped to ~220 °C after injection, and was raised back to 250 °C.   The mixture was held at 250 °C for 20 min with stirring.   The nanocrystals were removed from heat and allowed to cool to room temperature.   The solution was collected and centrifuged at 8000 rpm for 10 min.   A small amount of poorly capped particles precipitated and was discarded.   The well-dispersed nanocrystals were then mixed with 20 mL of ethanol.   The hydrophobic Ni nanocrystals flocculated and were collected by centrifugation at 8000 rpm for 10 min.   The supernatant was discarded.   After an additional rinse with ethanol, the purified Ni nanocrystals were collected and dried on a rotary evaporator.   The nanocrystals could be redispersed readily in hexane.   The nanocrystals were stored in a nitrogen-filled glove box until needed.

2.2.1.3 Iron nanocrystal synthesis

Fe nanocrystals were prepared following a reported recipe.   Dioctyl ether ((C$_8$H$_{17}$)$_2$O) (10 mL) and oleic acid (C$_{17}$H$_{33}$COOH) (1.55 mL, 4.9 mmol) were heated under nitrogen to 100°C.   Iron pentacarbonyl (Fe(CO)$_5$) (0.2 mL, 1.5 mmol) was injected and the solution was slowly heated to reflux.   After refluxing for one hour, the solution was removed from heat and cooled to room temperature.   The oleic acid-

passivated iron nanocrystals were separated from the reaction mixture by precipitation with methanol and centrifugation. After redispersing the nanocrystals in chloroform, they were again precipitated using methanol in order to remove excess oleic acid and dioctyl ether. The iron nanocrystals were finally dispersed into chloroform for characterization and further processing.

2.2.1.4 MnPt₃ nanocrystal synthesis

$MnPt_3$ nanocrystals were synthesized using a method published elsewhere. 0.5 mmol of $Pt(acac)_2$ and 2.5 mmol of 1,2-hexadecanediol (Aldrich) were added to 20 mL of dioctylether (Fluka). The mixture was stirred and purged with nitrogen at room temperature for 30 min. The solution is cloudy at this point. The solution was then heated to 100 °C. Upon heating, the Pt precursor becomes reduced and the solution becomes optically clear. At 100 °C, a solution of 0.5 mmol $Mn_2(CO)_{10}$ in 12 mL dioctylether was injected into the reaction flask, followed by the injection of 4 mmol oleic acid (Aldirch) and 4 mmol oleylamine (Aldrich). The reaction mixture was heated to reflux at about 297 °C. During heating, the solution turns black at ~170 °C, indicating the onset of nanoparticle growth. At the heating rate of 5 °C/min, the initially Pt-rich nuclei absorb Mn atoms to form Mn-Pt alloy nanocrystals that ultimately acquire an equilibrium composition after aging for 30 min at the reflux temperature. After 30 min at the reflux temperature, the heating element was removed from the flask and the solution was allowed to cool to room temperature.

2.2.1.5 Other nanocrystal synthesis

For the preparation of Mn nanocrystals, 295 mg $Mn_2(CO)_{10}$ (Aldrich) was mixed in 10 mL octylether and the mixture was degassed for 10 minutes followed by agitation for 30 min. Under the blanket of N_2, the dispersion was heated to 100 °C, at which

25

capping ligands, oleic acid (90 μL) and oleylamine (92.5 μL) were injected. Mn precursor became soluble at temperatures above ~85 °C, and the color of the solution was pale yellow. After the injection, the heating continued until the temperature reached the reflux temperature (~297 °C) at a heating rate of ~5 °C/min.   The solution turned orange at about 150 °C, indicating onset of thermal decomposition of Mn precursor, and became dark red at ~250 °C, at which the Mn nuclei started to form. The reflux was maintained for 3 hours. The nanocrystals were collected using conventional arrested precipitation method, and cleaned prior to TEM characterization and the use for nanowire seeding.

Other metal nanocrystals, including Co and Ir, were prepared by and supplied from our group members using published methods.

2.2.2 Supercritical Fluid Synthesis Apparatus

2.2.2.1 Batch reaction

A 10 mL Ti grade-2 (TI2) reaction cell (High Pressure Equipment, Inc.) was used as a reaction cell.   A Si substrate with a 100 nm thermally-grown oxide layer was cut into 6.3 X 1.0 cm sections and ultrasonically cleaned in acetone, ethanol, and acetone for 10 min each.   The cut substrate was placed inside the reaction cell and the product was deposited on the substrate.   The precursor solution containing silicon precursor and Au nanocrystals was loaded into the cell in a nitrogen glove box with oxygen levels typically less than 1 ppm.   The volume of the solution was adjusted so that the pressure determined from the phase diagram of the solvent should go above its critical value. The cell was then inserted into heating blocks preheated to ~50 °C higher than the reaction temperature.   The reactor reached the reaction temperature within 5 min. Upon insertion of the cell, the set temperature was lowered to the reaction temperature to

allow the reaction cell and the heating blocks to equilibrate at the reaction temperature. The temperature was monitored by a K-type thermocouple (Omega, Inc.) and controlled by a digital temperature controller (Omega). The thermocouple was placed at the interface between the reaction cell and the heating blocks. Once the specified reaction time had elapsed, the sealed reactor was removed from the blocks and immediately immersed in an ice-water bath for cooling. The reaction cell reached room temperature after 5 min in the water bath. The reaction product was collected from the reactor in air. The deposition substrate was recovered and then hexane was used to extract the remaining product that had adhered to the reactor walls. The product deposited on the substrate was stored under nitrogen prior to characterization.
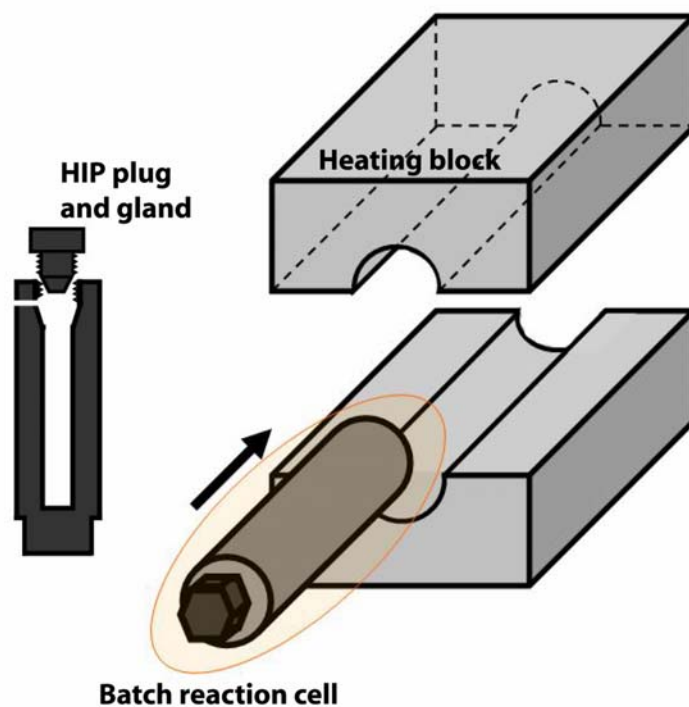
Figure 2.2. Schematic diagram of high-temperature, high-pressure batch reaction system.

2.2.2.2 Semi-batch (injection) reaction

An injection-based reactor was devised to minimize the ramping time and therefore to allow more precise control over temperature change in the system. A TI2-grade reactor of the same dimensions as the batch reaction was used but the plug had a female fitting for LM-6 HiP reducers (High Pressure Equipment). The 10 mL reactor was connected through high-pressure tubing (0.76 mm i.d.) to a 2-way valve. The deposition substrate, ultrasonically degreased in acetone-ethanol-acetone for 10 min each, was loaded in the reactor and the reaction cell was sealed in a nitrogen glove box. The nitrogen-filled reactor was then taken out of the box and inserted into preheated heating blocks, where the temperature was monitored and controlled by a K-type thermocouple and a temperature controller. The heating blocks were insulated with heating tapes and insulation, allowing the system temperature to be maintained within ±1 °C throughout the reaction. A reaction solution containing silicon precursor and metal nanocrystals was prepared inside a nitrogen-purged glove box and then loaded in a 500 μL injection loop connected to a 6-way valve (Valco). A high-pressure liquid chromatography (HPLC) pump (Alcott) was used to pressurized a piston with DI-H_2O, which pressurized the injection system with anhydrous reaction solvent (hexane or toluene). The injection reaction system is shown in Figure 2.3.

Prior to injection, the tubing was slowly flushed with the solvent while being connected to a 2-way valve (High Pressure Equipment) attached to the reactor to ensure an oxygen-free synthesis environment. The reaction solution was injected when the reactor reached the pressure of ~3.4 MPa and the reactor was further pressurized with the solvent to ~8 MPa. The reaction was allowed to proceed for 5 min from the injection before immersion of the cell into an ice-water bath to quench the reaction. Care must be exercised when opening the reactor as it could still be under high pressure! The product

was collected on the deposition substrate and from the side wall, and stored under nitrogen prior to characterization.
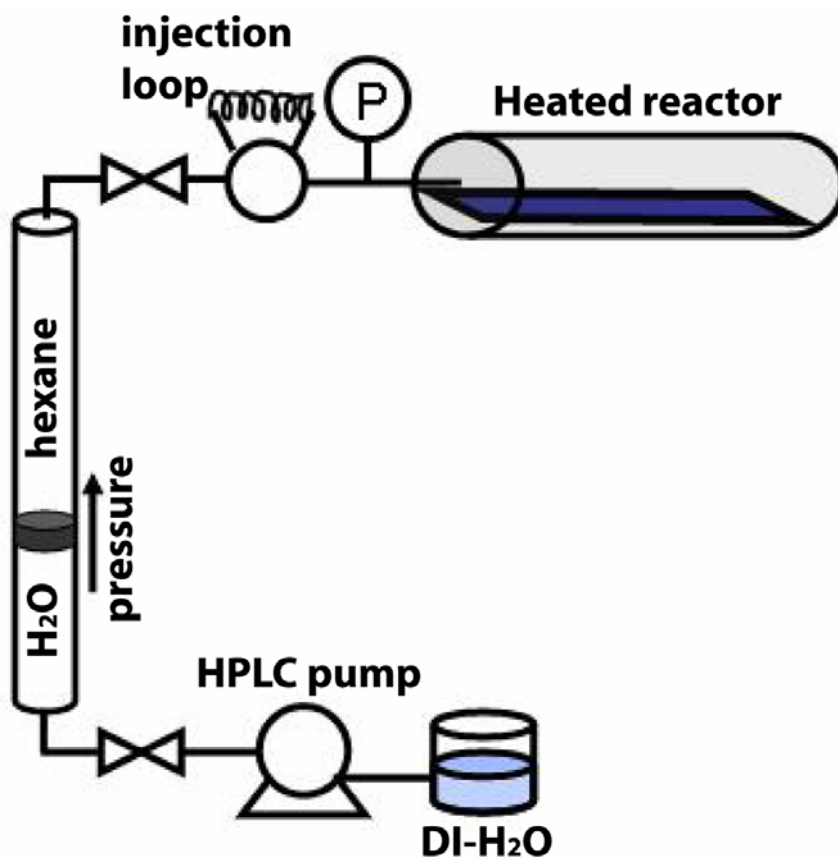
Figure 2.3. Schematic of injection (semi-batch) reaction system.

2.2.2.3 Continuous flow-through reaction (Plug flow reaction)

For flow-through reactions, the aforementioned 500 μL injection loop was replaced with a 27 mL high-pressure cylinder or a 10 mL injection loop. The reactor with openings on both sides was used. A micrometering valve (High Pressure Equipment) at the effluent stream allowed the precise control over the pressure inside the eaction cell. The reactor, assembled to a HPLC pump, was leak-tested prior to heating. The reaction cell tucked in heating blocks was heated to the reaction temperature while

being continuously flushed at a flow rate of ~0.3 mL/min.   The reaction proceeded for ample time to ensure that all the reaction solution was introduced to the reactor and was quenched by removing an upper heating block and cooling with air flow.   The product was recovered from the deposition substrate or the inside wall of the reactor, and stored under nitrogen prior to characterization.
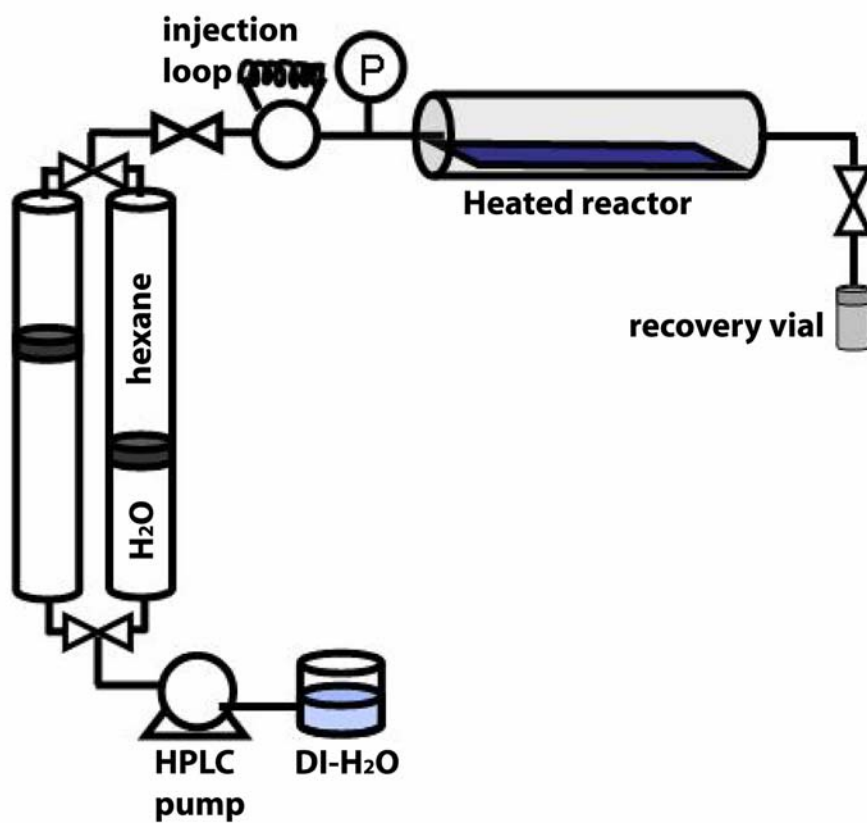
Figure 2.4. Schematic diagram of continuous flow-through reaction system.   Most of product was collected on the deposition substrate inside the reactor.

2.2.3 Reaction Solutions

All silicon precursors, phenylsilane ($C_6H_5SiH_3$, Aldrich), diphenylsilane ((C_6H_5)$_2SiH_2$, Aldrich), octylsilane ($C_8H_{17}SiH_3$, Gelest), diethylsilane ((C_2H_5)$_2SiH_2$, Aldrich), tetraethylsilane ((C_2H_5)$_4Si$, Aldrich), and trisilane (Si_3H_8, Gelest), were stored in a nitrogen-purged glove box. The Au nanocrystals prepared according to the method described in Section 2.2.1 were dissolved in hexane or toluene inside the glove box. For a typical stock solution, silicon precursor was added to anhydrous hexane or toluene and then metal solution was mixed to attain the desired Au:Si ratio. Precursor solutions with alternative metal particles were prepared similarly.

2.2.4 Characterization Methods

The reaction products were characterized using high-resolution scanning electron microscopy (HRSEM), high-resolution transmission electron microscopy (HRTEM), and X-ray energy dispersive spectroscopy (EDS). HRSEM images were obtained on a field emission LEO 1530 SEM operated at 2 to 3 kV accelerating voltage. HRTEM was performed using a JEOL 2010F operating at 200kV accelerating voltage. For TEM, samples were prepared by dispersing in chloroform with brief sonication and then drop-casting on a lacey carbon grid (Electron Microscopy Sciences, LC200-Cu, Mesh 200). The nanowires were sufficiently long to stretch across the lacey carbon to provide a vacuum background for high resolution TEM images. Fast Fourier transforms (FFT) of TEM images were obtained using Digital Micrograph (Gatan) software. EDS (Oxford INCA) was equipped with a JEOL 2010F TEM and the spectra were obtained in the data range of 0~20 keV.

2.3 RESULTS AND DISCUSSION

2.3.1 Batch reaction

In a typical batch reaction, a solution containing Au nanocrystals and Si precursor is loaded in a reaction cell and sealed under inert nitrogen conditions. The reactor is heated to the reaction temperature within 5 minutes. As the reactor approaches the set temperature, the Si precursor decomposes to yield Si atoms, which then dissolve into Au nanocrystals to form Au:Si liquid alloys. When these liquid droplets nucleate, it is likely that they are prone to agglomeration since the Si supply to the droplets are limited by the decomposition rate of the Si precursor. Slow ramping rate could thus pose a challenge, particularly because there is no stirring in the reaction system. The reaction solvent (hexane) could disperse the reactants inside the system as the temperature approaches the reaction temperature because of the expansion of the solvent from liquid to gas-phase. However, above the critical temperature, the pressure gradient would not be large enough to create a continuous stirring.

Agglomeration of the liquid droplets would likely give rise to the growth of Si wires of a larger diameter. The product shown in Figure 2.5 was collected from the reaction, in which diphenylsilane (500 mM) and Au nanocrystals ([Si]/[Au]=1000) were reacted at 500 °C and ~13.8 MPa. The product generally entails 10 μm-thick rods with aspect ratio of <1:10. The rods exhibit a diameter orders-of-magnitude larger than the size of Au nanocrystals used as a reactant, indicating that agglomeration of the liquid droplets is the nascent stage of the whisker growth. Wu and Yang reported that the nanowire growth rate is proportional to the nanowire diameter, which is consistent with the Gibbs-Thompson effect — smaller liquid alloy droplets are consequently more likely to agglomerate into larger droplets during the initial stages of nanowire nucleation. Suppressed Si supply in the batch reaction limits the nucleation of nanowires, instead the

Au nanocrystals or the Au:Si liquid alloy agglomerated until the temperature reached the point where enough Si atoms were supplied from the Si precursor decomposition to allow Si nucleates on the seed particles.
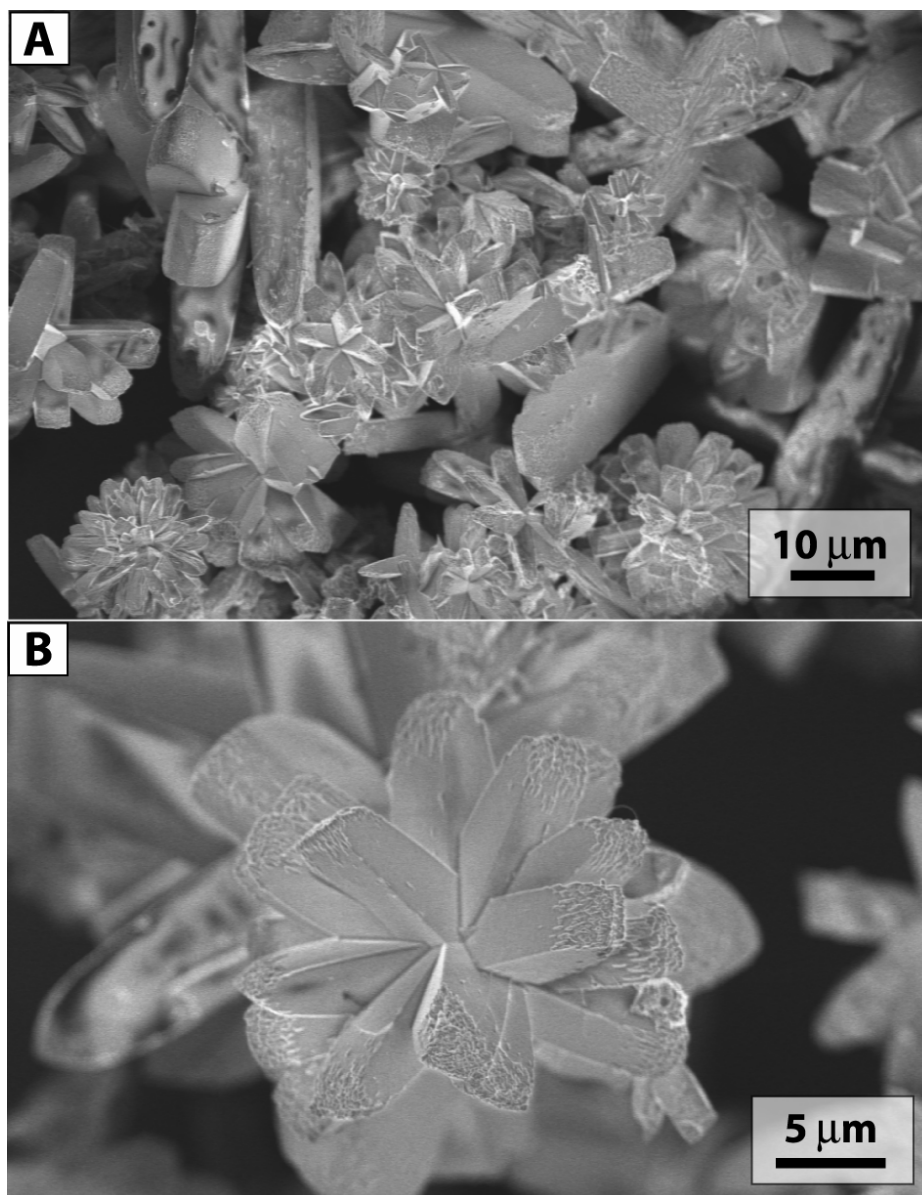
Figure 2.5. HRSEM images of reaction product obtained from a batch reaction of 500 mM diphenylsilane and Au nanocrystals at 500 °C and ~13.8 MPa, with Au:Si ratio 1:1000.

2.3.2 Effect of Silicon Precursor

Figure 2.6 shows scanning electron microscopy (SEM) images of solid product obtained from six different Si precursors injected into anhydrous hexane at 450 °C and 7.2 MPa with dodecanethiol-coated Au nanocrystals with average diameter of ~4 nm. The silane concentration in each case was 350 mM with a Au:Si mole ratio of 1:1000, and the reactions were carried out for 5 min. The images in left column in Figure 2.7 shows the products obtained using the alkylsilanes, octylsilane (Figure 2.6A), diethylsilane (Figure 2.6B), and tetraethylsilane (Figure 2.6C). In all cases, the yield of nanowires was extremely low, or even nonexistent. Only the monosubstituted alkylsilane, *e.g.*, octylsilane, produced a measurable amount of crystalline Si nanowires, but with miniscule yield and large amounts of oligomeric silicon and carbon-containing impurities. The multi-substituted alkylsilanes, diethylsilane and tetraethylsilane, did not produce any crystalline nanowires, only curly *amorphous* wires in the case of diethylsilane and only amorphous particulates in the case of tetraethylsilane. It appears that the Si-H bond is sufficiently labile and reactive for nanowire growth, but homolytic cleavage of the alkyl Si-C bond is very slow, preventing adequate Si addition to the Au seed particles to sustain crystalline nanowire growth.
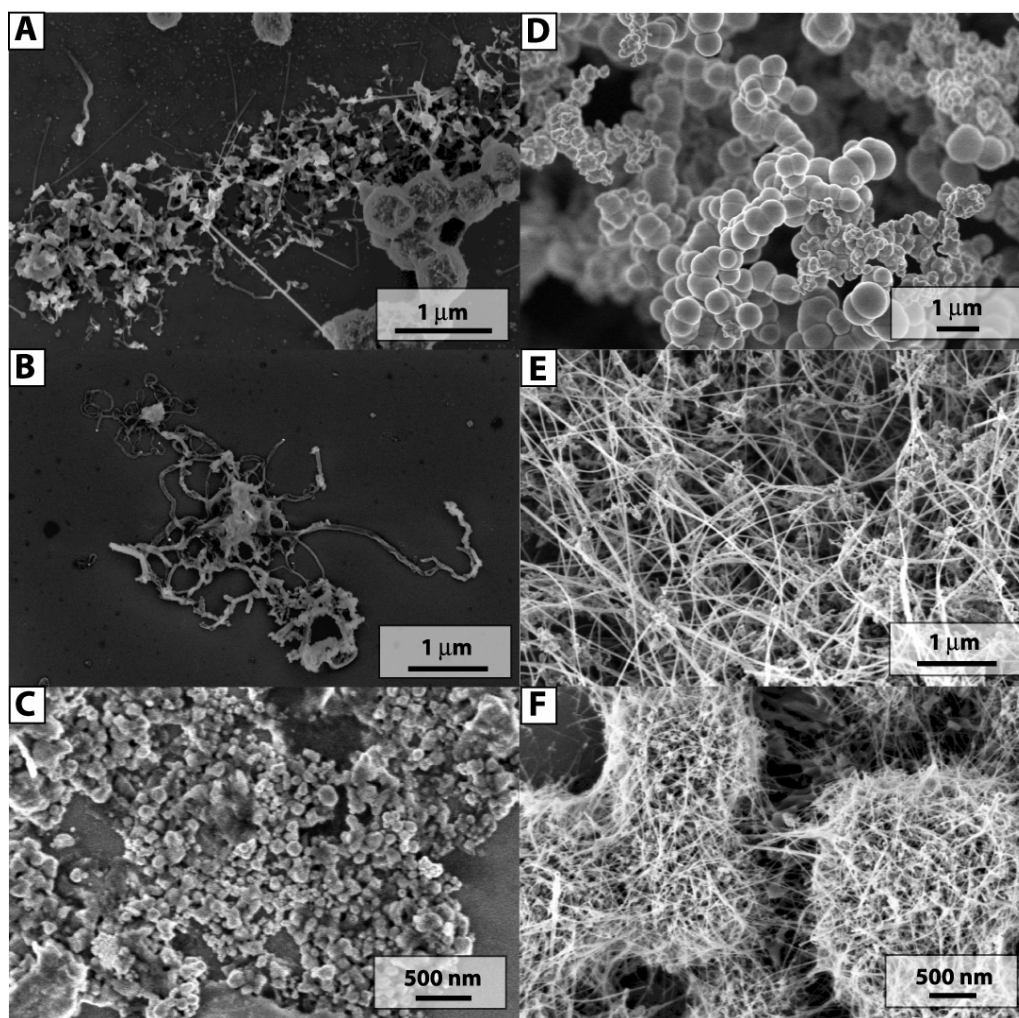
Figure 2.6. HRSEM images of reaction product obtained from (A) octylsilane, (B) diethylsilane, (C) tetraethylsilane, (D) trisilane, (E) phenylsilane, and (F) diphenylsilane injected into hexane at 450 °C and ~7.2 MPa.   The reactions were carried out for 5 minutes with 350 mM concentrations of silicon precursor with a Au:Si mole ratio of 1:1000.

On the other hand, trisilane is very reactive and decomposes above 350 °C. However, as shown in Figure 2.7D, trisilane does not form Si nanowires in the presence of Au nanocrystals.   Instead, micrometer-size amorphous Si colloids are produced, which is surprisingly the same product that is obtained in the absence of the Au

nanocrystals.   Unlike the alkylsilane or arylsilane precursors, trisilane can undergo thermolysis through heterogeneous insertion at a hydrogen-terminated Si surface site, which can lead to rapid particle formation once an amorphous Si colloid is nucleated. Furthermore, the Si-Si bonds in trisilane are very stable, and do not dissociate at the typical SFLS reaction temperatures of 450~500 °C.   Therefore, even if trisilane undergoes dehydrogenation, a "bare" Si trimer is left which may not dissolve in the gold nanocrystal seeds for crystallization into a nanowire.   The other problem is that even if some trisilane forms a nanowire, trisilane left in solution can then rapidly decompose on the nanowire surface through unwanted sidewall growth.   Due to its high reactivity, trisilane decomposes to Si with close to 100% yield, however, the product is colloidal amorphous Si, not nanowires.   Higher reaction temperatures simply speed up the homogeneous trisilane decomposition and increase the particle formation rate making it impossible to obtain crystalline Si nanowires using trisilane as a reactant with gold nanocrystals as seeds.

Figures 2.6E and 2.6F show the Si product obtained using phenylsilane and diphenylsilane: both precursors yield large quantities of Si nanowires as the primary reaction product.   In contrast to the alkyl-substituted organosilanes, phenyl-substituted organosilanes readily decompose to produce crystalline nanowires at ~450 °C, since the aryl group can disproportionate, while the alkyl group cannot, making them kinetically labile.   The disproportionation reaction yields SiH_4, which decomposes to Si above ~350 °C, and ultimately tetraphenylsilane, which is chemically stable above 500 °C. Few studies have devoted to the comprehensive comparison of Si-C bond energies of Si-aryl and Si-alkyl.   Nonetheless, it is expected that the Si-C bond dissociation enthalpy (the reported value of the enthalpy is about 435 kJ/mol) has a slightly lower value in the

case of Si-alkyl bond than the case of Si-aryl bond, and therefore thermodynamically Si-aryl bond cleavage is even less favorable than the Si-alkyl dissociation.

2.3.3 Effect of Temperature

Figure 2.7 shows HRSEM images of the reaction products synthesized using phenylsilane (Figures 2.7A-C) and diphenylsilane (Figures 2.7D-E) at different reaction temperatures, ranging from 400 to 500 °C. Performing the synthesis at 350 °C (not shown)—just below the bulk Si-Au eutectic temperature (363 °C)—with either phenyl- or diphenylsilane did not yield significant quantities of solid product. In reactions carried out just above the eutectic temperature, at 400 °C, nanowires did not form, and only visually poor particulate materials were obtained. This is in stark contrast to the Au nanocrystal-promoted SFLS synthesis of Ge nanowires, which are routinely grown at 385 °C with very high quality. Since Au:Ge exhibits a similar eutectic temperature to Au:Si (361 °C), one would expect similar results for Si nanowires. The significantly lower growth temperature for Ge nanowires appears to be directly related to the higher arylgermane reactivity compared to the arylsilanes—the slow precursor degradation kinetics appear to be limiting Si nanowire growth at temperatures just above the Au:Si eutectic. The reaction temperature must reach approximately 450 °C to produce high quality crystalline Si nanowires. However, further increases in reaction temperature do not improve nanowire growth: at 500 °C, phenylsilane produces nanowires, but with a relatively high proportion of carbon-containing amorphous Si byproduct. Reactions at temperatures higher than 500 °C result in significant hexane pyrolysis.
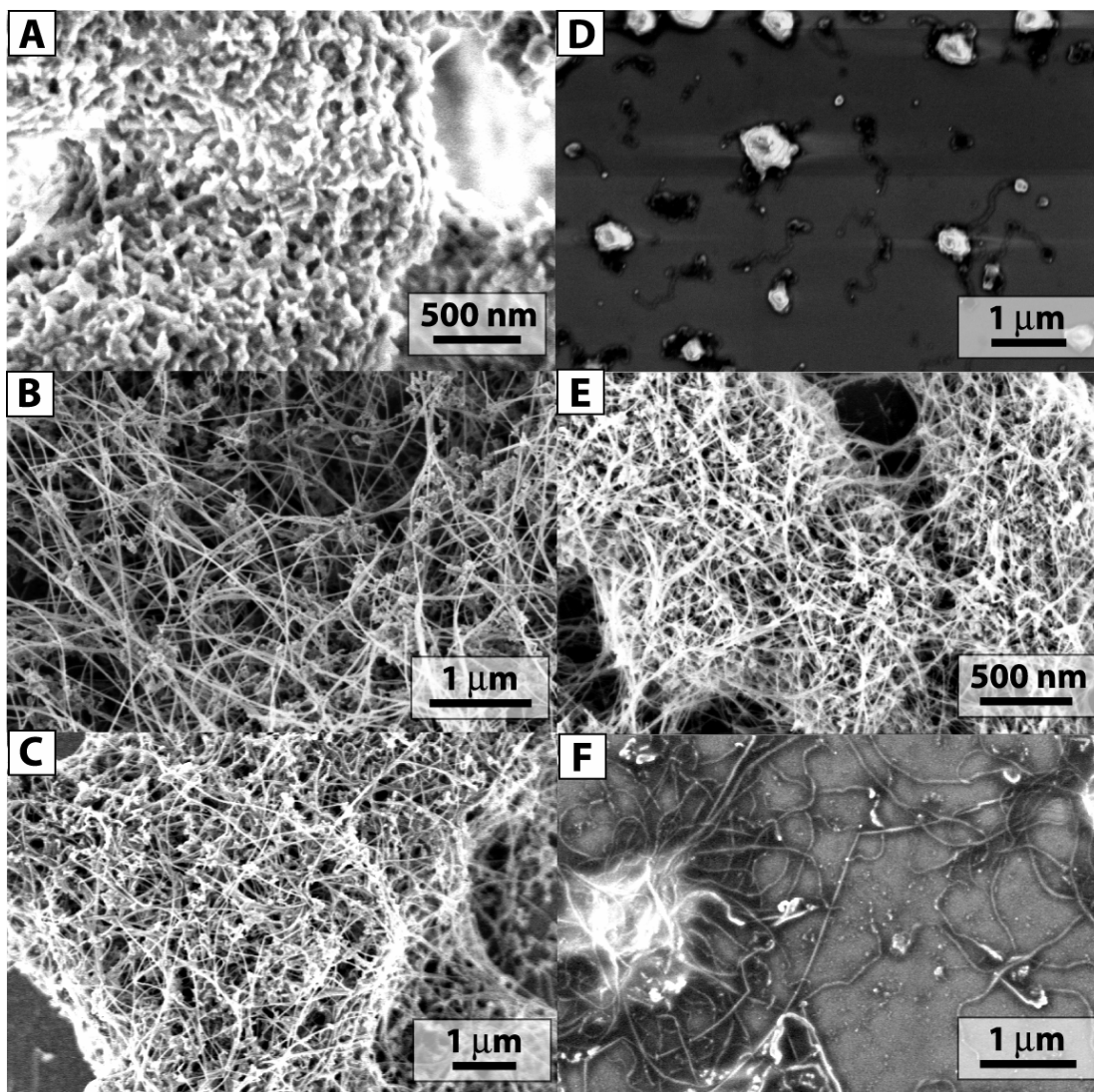
Figure 2.7. HRSEM images of Si product formed when phenylsilane (A-C) or diphenylsilane (D-F) were reacted in hexane at 400 °C (A, D), 450 °C (B, E), and 500 °C (C, F).   For both precursors, reaction temperatures of at least 450 °C are required to form nanowires.

2.3.4 Decomposition of Arylsilanes

As expected based on a disproportionation reaction mechanism for phenylsilane decomposition to Si, phenylsilane provides a higher crude product yield than diphenylsilane.   As shown in Figure 2.8, phenylsilane requires only one

disproportionation step to form silane, compared to diphenylsilane, which requires *two* consecutive reactions to yield silane.   HRSEM of Si nanowires produced using diphenylsilane at 500 °C also showed a significantly higher amount of carbonaceous byproducts compared to phenylsilane.   Perhaps due to its additional phenyl moiety, diphenylsilane exhibits a higher likelihood to form carbonaceous byproducts in addition to nanowires.   In the case of both diphenylsilane and phenysilane, there also appears to be a "threshold" concentration (~120 mM for phenylsilane), below which little or no nanowire product is formed.
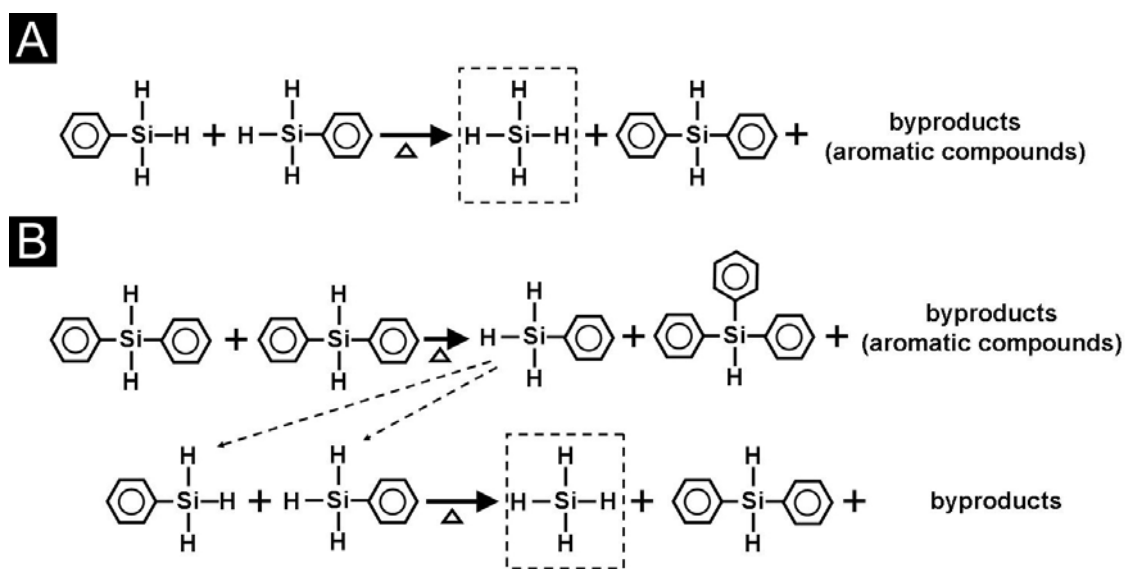
Figure 2.8. Illustrative schematics of bimolecular disproportionation reactions of (A) phenylsilane and (B) diphenylsilane at high temperatures.   Silane decomposes at temperatures above ~350 °C to produce Si atoms.

2.3.5 Trisilane Decomposition

The reactions using phenylsilane or diphenylsilane yielded crystalline Si nanowires.   The decomposition of the arylsilanes usually produces phenyl-substituted

silanes as by-products, limiting the yield of Si nanowires. To alleviate organosilane byproduct formation, trisilane was explored as an alternative Si precursor. As described in Section 2.3.2, trisilane is very reactive at temperatures above ~400 °C. Si-Si bond is very strong and hard to break, so Si trimer reacts uncleaved producing spherical amorphous particles. Pell *et al.* demonstrated the synthesis of amorphous silicon colloids of ~100 nm size using trislane. The trisilane molecules, albeit very reactive, are too big to be dissolved in Au nanocrystals, and consecutively preformed Au nanocrystals are not effective seed particles. In an attempt to produce crystalline Si nanowires or nanocrystals, aluminum-containing reducing agents (*e.g.*, diisobutylalumininum hydride) were reacted with trisilane in batch reactions.
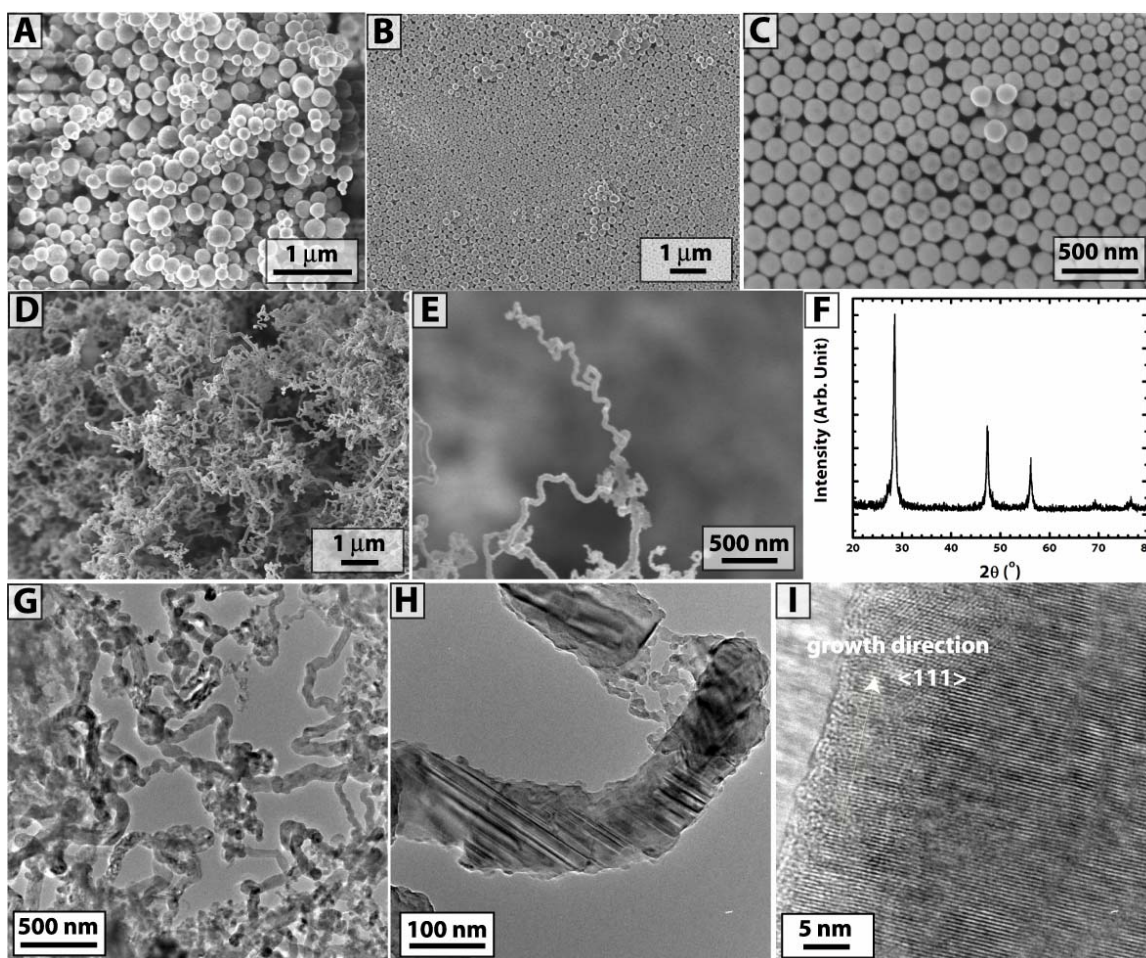
Figure 2.9. (A-C) SEM images of amorphous Si particles synthesized by the pyrolysis of trisilane in supercritical hexane at (A) 400 °C and (B-C) 500 °C.   Size of the particles grown at 400 and 500 °C is 213 ± 59 and 243 ± 50 nm, respectively. SEM image in (C) shows an area in which monodisperse particles (139 ± 18 nm) form a monolayer.   (D-F) SEM images and XRD pattern of crystalline Si wires produced from the reaction of 10 mM trisilane in hexane at 500 °C and ~13.8 MPa with equimolar diisobutylaluminum hydride.   The wires are curly but single-crystalline.   (G)~(I) show TEM images of the product. There is no particularly preferred growth orientation.

41

2.3.6 Crystallographic Characterization of Silicon Nanowires

As shown in Figures 2.10, <111> is the predominant growth direction for Si nanowires synthesized at 450 °C using Au nanocrystals and either phenylsilane and diphenylsilane. A few nanowires could be found with <110> or <112> growth directions. The preference for <111> Si nanowire growth is consistent with Si whiskers grown in the gas phase by Au-seeded VLS under similar reaction temperatures. TEM imaging of the Au/Si tip of the SFLS-grown nanowires reveals a flat, atomically abrupt, interface with the Si (111) surface. Nanowires with <112> or <110> growth directions do not exhibit this flat cross-sectional interface, as shown in Figure 2.10B, but rather a "curved" interface that appears to *reconstruct* to achieve flat Si (111):Au interfaces at the tip, as observed by Wu *et al.* for <110> oriented Si nanowires grown by Au-seeded VLS. The influence of the liquid–crystal interface, and the fact that the Si (111)/Au interface exhibits the lowest free energy relative to other possible interfaces has in fact been well-established from early work on Si whiskers. The stability of the Si (111)/Au interface is further confirmed in our observations of a migrating gold/Si interface under the electron beam in the TEM. As shown in Figure 2.11, long exposure time results in sufficient thermal energy for the Au interface to migrate ~14 nm into the nanowire. The interface remains sharp and atomically smooth, despite this progression. Compare this interfacial structure to the curved Au/SiO_2 interface that forms at the tip of a Si nanowire after 2 months of exposure to air as shown in Figure 2.10D. The difference in Au/SiO_2 interfacial energy is reflected in the qualitatively different structure relative to Au/Si.
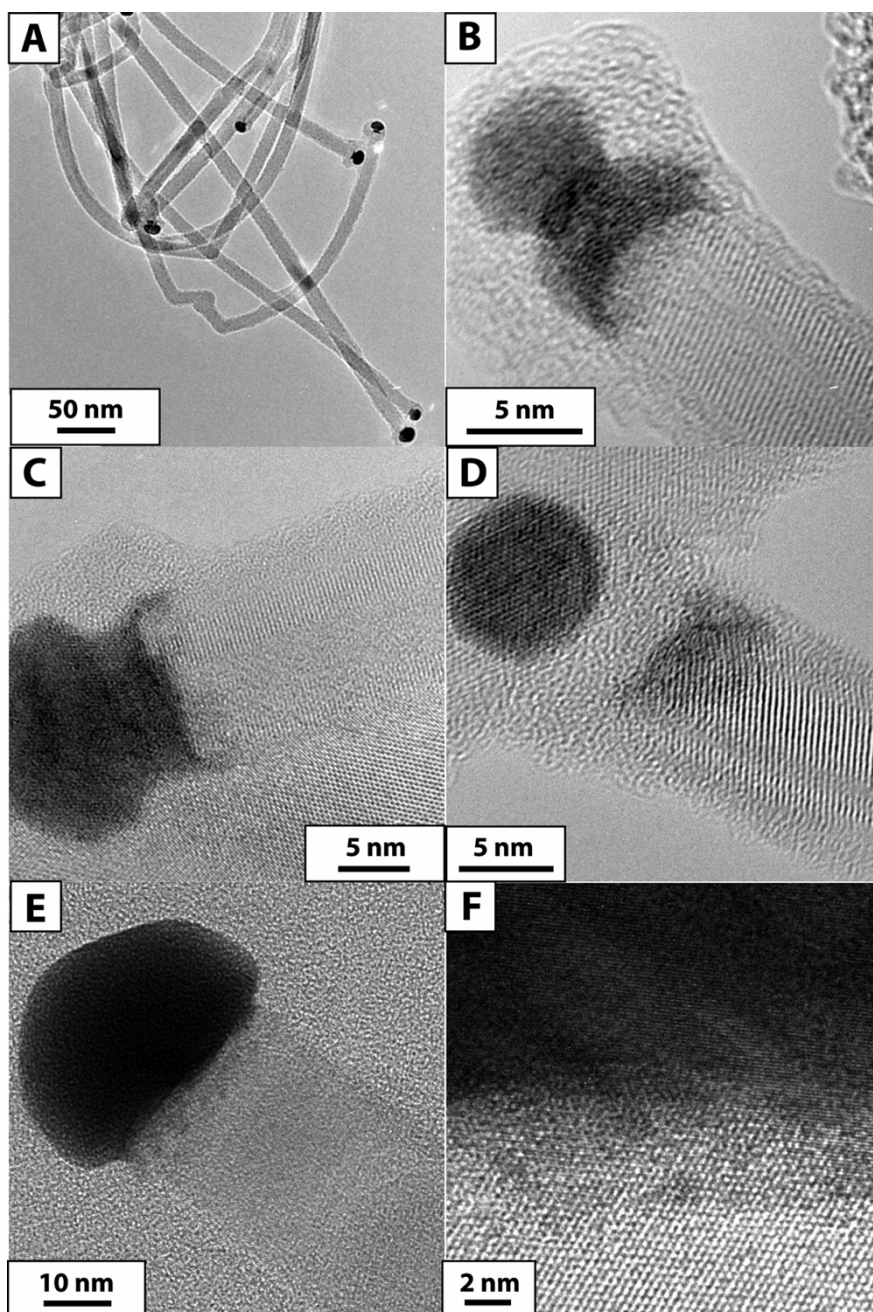
Figure 2.10. HRTEM images of Au seed particles at the Si nanowire tip.   (A) HRTEM image of several nanowires with Au tips.   (B) The "curved" Au-Si interface of a <211> oriented nanowire.   (C) Au tip at the end of a <111> oriented Si nanowire.   (D) Nanowire exposed for 2 months in air oxidized at the Au/Si interface as well as the nanowire surface.   (E-F) Au tip at the end of a <111> oriented Si nanowire.

43
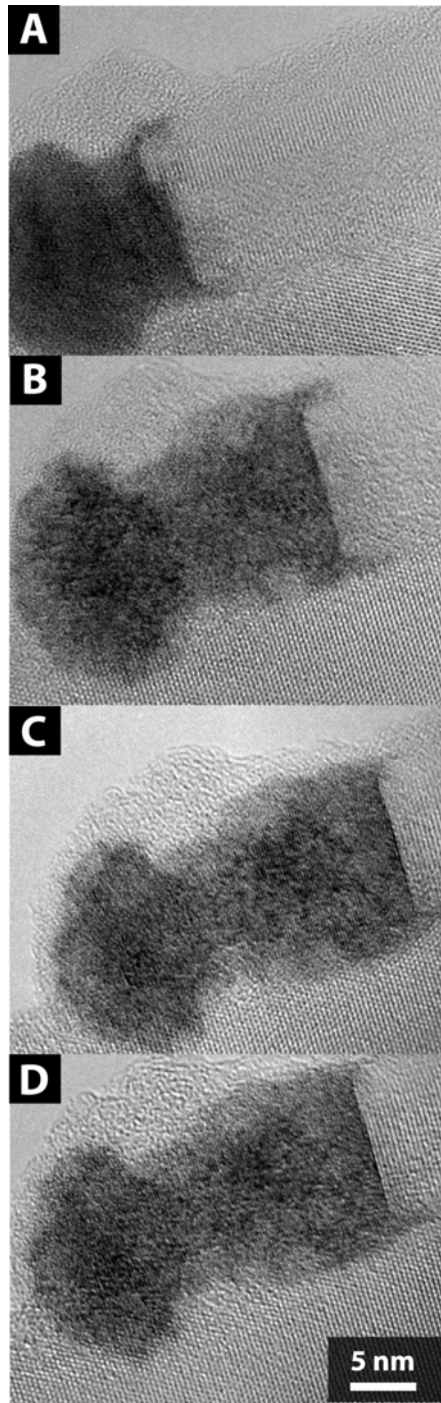
Figure 2.11. Au metal tip at the end of a Si nanowire exposed to a converged electron beam at 200 kV after (A) 0 min, (B) 1.5 min, (C) 3 min, and (D) 4.5 min.   The Au tip migrates into Si nanowire until penetrating ~14 nm.   The nanowire maintains the sharp {111} interface at the Au-Si tip.
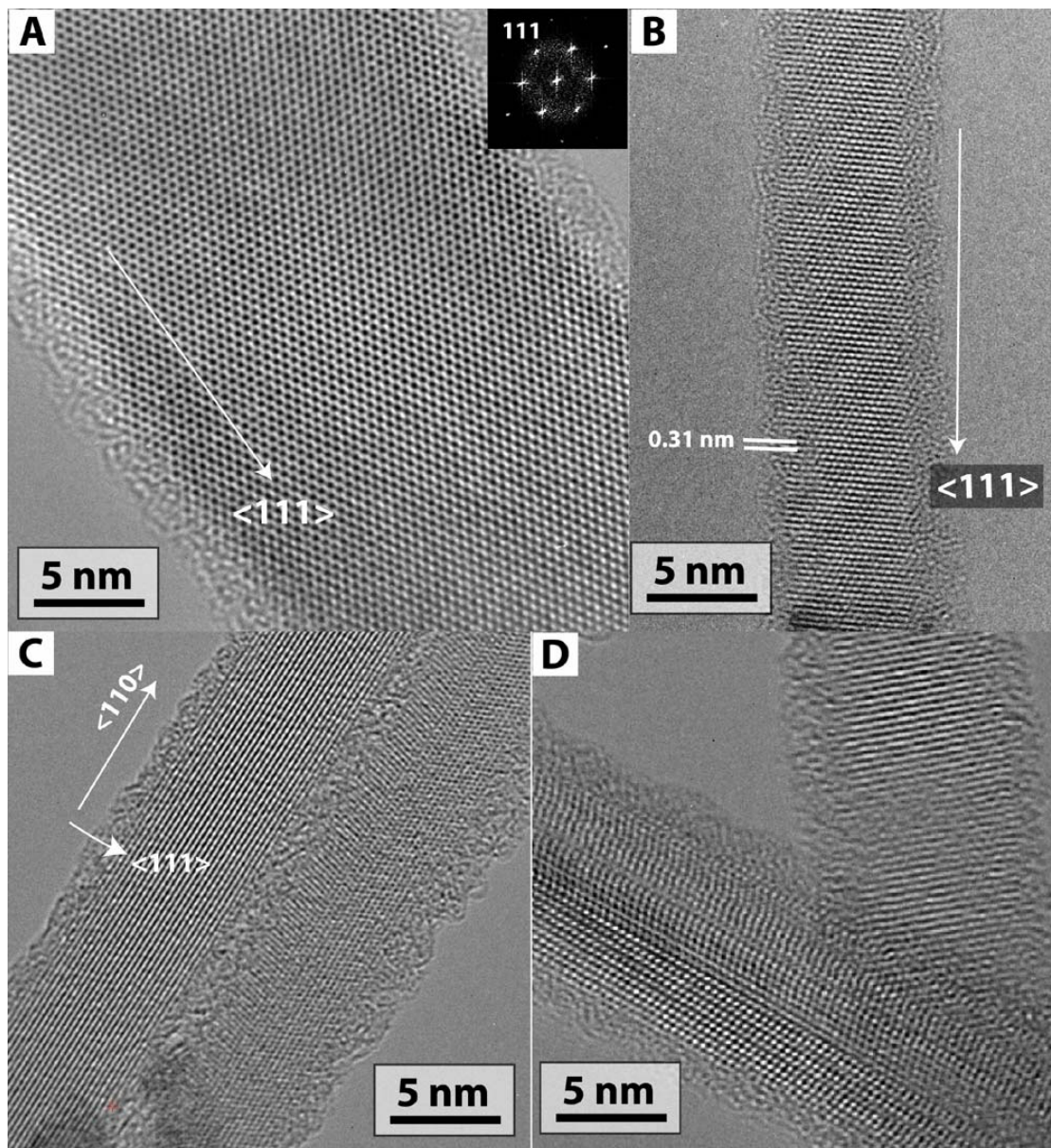
Figure 2.12. HRTEM images of Si nanowires produced by SFLS with gold nanocrystals and diphenylsilane at 450 °C.   Under these conditions, SFLS yields predominantly <111> oriented nanowires, as shown in (A) and (B), however, limited examples of <110> or <211> oriented nanowires were found with diameter smaller than 10 nm (C, D).   The FFT of the image (A) is shown in the inset.

2.3.7 Effect of Gold Nanocrystal Passivation

In order to control the nanowire diameter, the agglomeration of seed nanocrystals must be limited.   The capping ligand offers particle-particle separation, which keeps the collision-induced agglomeration minimal.   A hydrophilic functional group in a capping ligand molecue bonds to the surface of the nanocrystals in dynamic equilibrium.   Strong bonding between the capping ligand molecules and nanocrystals also allows the nanocrystals to disperse uniformly in the reactor.   To investigate the effect of capping ligands to the nanowire growth, Au nanocrystals passivated with trioctylphosphine (TOP) and dodecanethiol (DDT) were prepared via the two-phase arrested precipitation methods as described in Section 2.2.1.1 (Figure 2.1) and tested in injection semi-batch reactions at 450 °C.   The TOP-passivated nanocrystals were 1.93 ± 0.20 nm in diameter, and the DDT-capped nanocrystals were ~4 nm.

Figure 2.13 shows the SEM images of the product.   When TOP-capped Au nanocrystals were reacted, few or no nanowires were produced (Figure 2.13A) in the reaction conditions where the DDT-capped Au nanocrystals were reacted to yield Si nanowires (Figure 2.13C).   The Au-P bonding is weaker than Au-S (ref), and at the reaction temperature (450 °C), the nanocrystals with TOP passivation are more prone to the agglomeration.   Furthermore, the TOP molecules in free space could serve as nucleation sites for the phenylsilane decomposition, resulting in the formation of amorphous particulates.   The TOP-capped Au nanocrystals were ligand-exchanged with DDT by adding DDT (100 μL) into 10 mL toluene solution of the nanocrystals.   The nanocrystals after ligand exchange were used in the reaction and Si nanowires were produced! (Figure 2.13B)   The yield and selectivity of nanowires in the reaction product were still lower than when the DDT-passivated Au nanocrystals were used, but significantly improved compared to the TOP-capped nanocrystals.   This suggests that

the ligand exchange was incomplete, leading to the product morphology in between the two extremes.
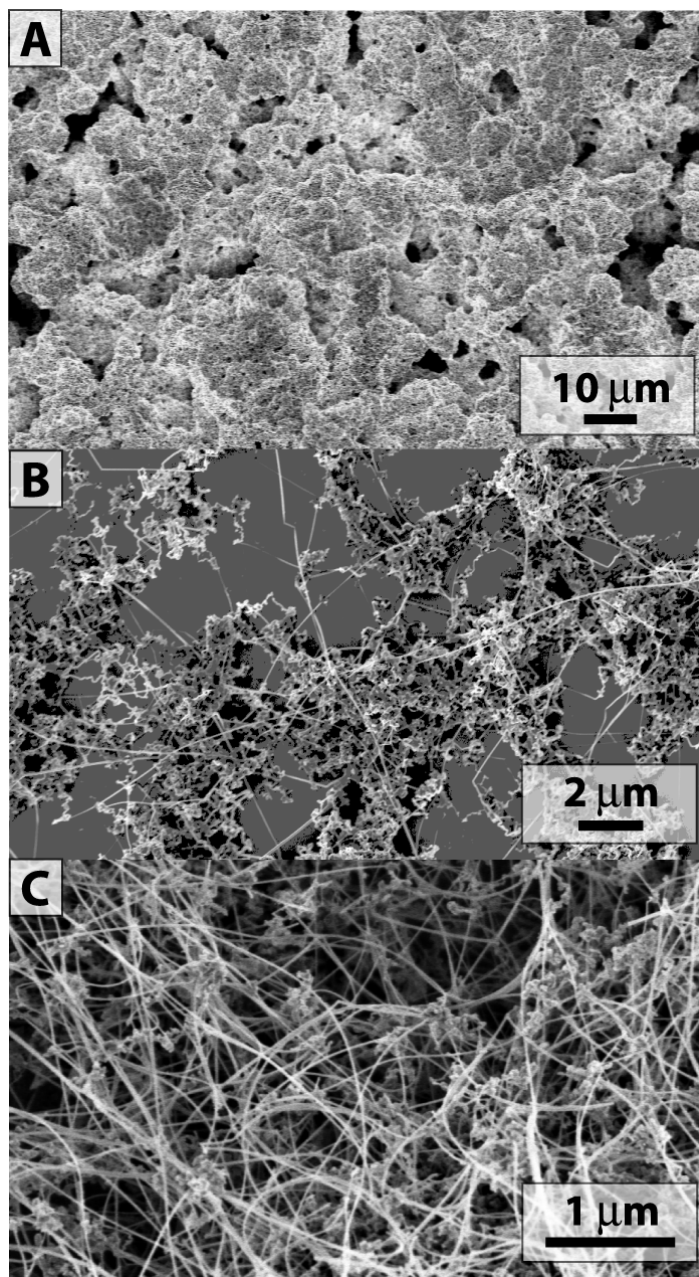
Figure 2.13. SEM images of Si nanowire reaction results, using (A) TOP-capped Au nanocrystals, (B) Au nanocrystals that are initially TOP-capped and ligand-exchanged to DDT, and (C) DDT-capped Au nanocrystals.

2.3.8 Alternative Metal Seeds for the Silicon Nanowire Growth

2.3.8.1 Nickel nanocrystals

Figure 2.14 shows SEM and TEM images of Si nanowires synthesized using phenylsilane as a precursor in toluene at 460 °C and 23.4 MPa in the presence of Ni nanocrystals.   At 460 °C, nanowires longer than 10 μm with a Si diamond cubic crystal structure and few dislocation defects were produced (Figure 2.14C).   The nanowires exhibit predominantly <110> growth direction.   Although TEM images of the nanowire surface show a significant amount of roughness, the diameter fluctuates by only ~1 nm along the entire length of the nanowire with negligible sidewall growth.
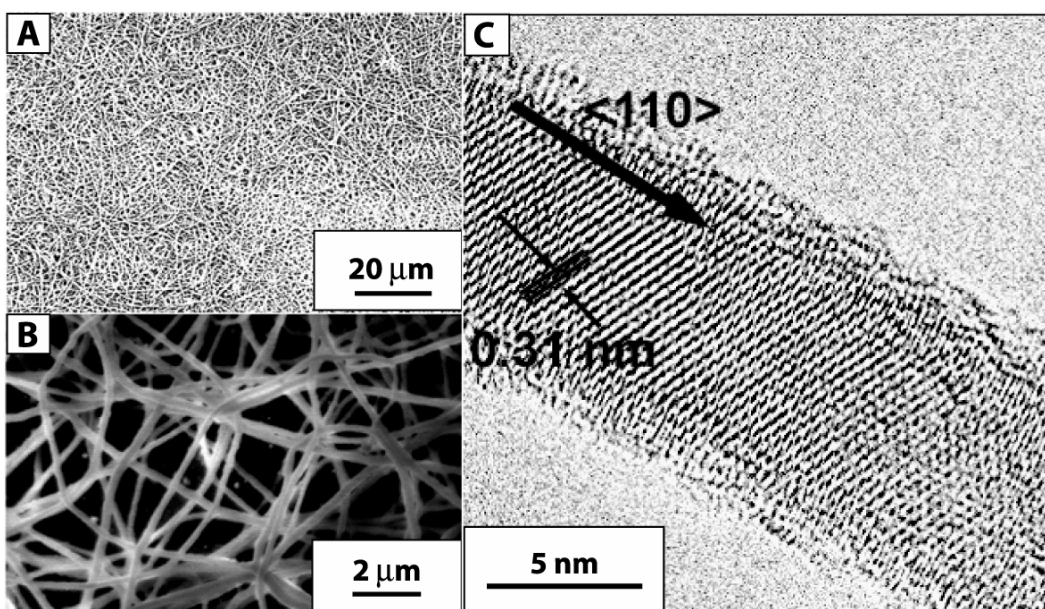
Figure 2.14. (A, B) SEM images of Si nanowires synthesized from MPS in toluene at 23.4 MPa (10 min, 27.4 mM MPS, [Si]/[Ni]=100) at 460 °C. EDS of the product shows an abundance of Si.   (C) HRTEM image of Si nanowires seeded by Ni nanocrystals in toluene at 460 °C, 23.4 MPa (10 min, 27.4 mM MPS, [Si]/[Ni]=100).   Typically, the Si nanowires exhibit the <110> growth direction.   Courtesy of Tuan.

The Ni nanocrystals were found to catalyze the decomposition of silane precursors, such as alkylsilanes and trisilane, which do not yield crystalline nanowires in the Au nanocrystal-seeded SFLS process due to their poor reactivity. Figure 2.15 shows Si nanowires synthesized from trisilane and octylsilane using Ni nanocrystals. It was nearly impossible to thermally decompose these precursors to *crystalline* Si in organic solvents, even in the presence of Au nanocrystals (for example, see Figure 2.6), due to the thermal stability of the Si-C and Si-Si bonds in alkylsilanes and trisilane. The Si-C bond in octylsilane is very stable and does not undergo thermolysis at temperatures lower than ~500 °C. Furthermore, the alkyl moiety in octylsilane is not kinetically labile like the phenyl group in arylsilanes and cannot disproportionate to yield silane. In trisilane, hydrogen atoms dissociate easily from the molecule but the Si-Si bonds do not cleave at temperatures accessible in organic solvents. Thermal decomposition of trisilane in toluene at 460 °C yields very reactive Si trimers that homogeneously nucleate into amorphous Si colloids and do not produce nanowires by Au-seeded SFLS. Apparently, the Si-Si bonds must be "cracked" in order to form nanowires. Ni nanocrystals promote Si nanowire growth with relatively high yield from both trisilane and octylsilane.
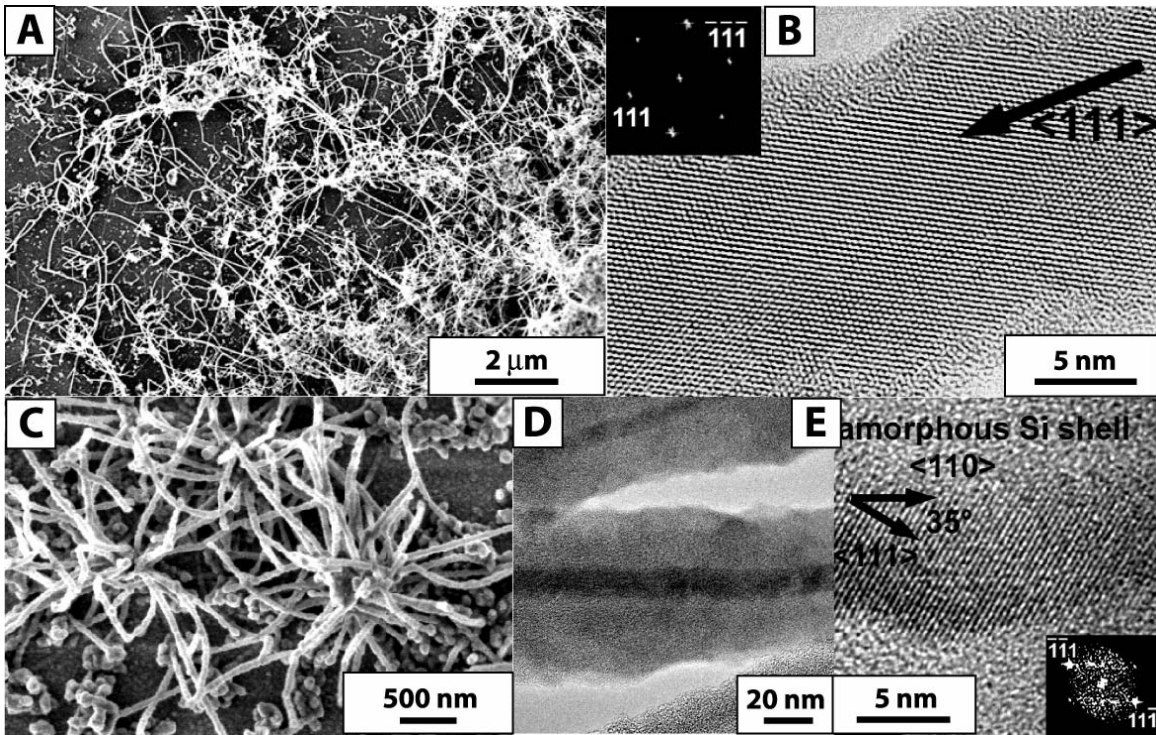
Figure 2.15. SEM (A) and HRTEM (B) images of Si nanowires synthesized from trisilane in toluene at 14.3 MPa (10 min, 27.4 mM trisilane, [Si]/[Ni]=5) at 450 °C.   SEM (C) and TEM (D, E) images of Si nanowires synthesized from octylsilane in toluene at 460°C, 17.9 MPa ([Si]/[Ni]=100).   Courtesy of Tuan.

Although the Si nanowires formed using octylsilane and trisilane are crystalline and relatively long, the quality of the wires is still not as high as those obtained with phenylsilane.   In contrast to phenylsilane, both octylsilane and trisilane gave significant amounts of amorphous sidewall deposition.   The more significant sidewall deposition from trisilane is certainly expected, as it undergoes rapid dehydrogenation to a very reactive "bare" Si trimer that will "stick" to anything it sees in solution.   Sidewall growth could be eliminated to some extent by using higher [Ni]/[Si], with the best Si nanowires obtained from trisilane by using nearly two orders of magnitude larger [Ni]/[Si] than in the case of phenylsilane (5 vs 100).   One drawback with using very

high [Ni]/[Si] is that the Si supply to the metal seeds can become starved, which leads to crystallographic defects. Sidewall-deposited Si from octylsilane is amorphous, but in contrast to trisilane, most likely contains significant carbon contamination. Octylsilane dehydrogenation may happen quite rapidly at 460 °C, however, the Si-C bond is thermally very stable and at these temperatures in supercritical toluene, and octylsilane tends to dimerize and form thermally stable oligomers.

Figure 2.16A-F shows TEM images of colloidal Co, Ni, Fe_2O_3, Ir, Mn, and $MnPt_3$ nanocrystals used to seed Si nanowires; their size distributions had standard deviations less than 20% about mean diameters ranging between 4.2 and 10.2 nm. Figure 2.16a-f shows the reaction products: all nanocrystals seeded Si nanowires in reactions with monophenylsilane (MPS), but with varying success. In general, straight nanowires are crystalline with few extended defects; whereas, very curly wires are usually amorphous or riddled with defects. Co nanocrystals gave the highest yield of straight, long (>10 µm) crystalline Si nanowires. Ni nanocrystals produced crystalline Si nanowires with good yield—on par with what is obtained using Au nanocrystals. Fe_2O_3 nanocrystals produced Si nanowires with relatively low yield.

All of the nanocrystals studied produced nanowires at temperatures significantly below the bulk semiconductor:metal eutectic temperature. Although the eutectic temperature might be reduced by the small size of the seed nanocrystals, a temperature drop of nearly $350^{o}C$ is unlikely and crystallization probably occurs from a solid-phase seed as opposed to a liquid eutectic. Provided that the seed particles are small enough for rapid saturation by solid-state diffusion and there is a high solid solubility of semiconductor in the metal, solid-phase nanowire seeding appears to be a general occurrence. Indeed, Co, Ni, and Fe all form alloys with Si at the nanowire growth

temperatures and EDS analysis of the seed particles found at the tips of many nanowires revealed silicide.

In VLS growth, the metal seed simply dissolves the semiconductor and recrystallizes it as a nanowire, only playing a passive role in the chemistry. In contrast, transition metals such as Ni and Co are well-known catalysts for many chemical reactions. In CVD-growth of carbon nanotubes, catalytic seed metals like Co and Ni enhance hydrocarbon decomposition particle surface, followed by graphitization and tube growth. In CVD nanowire growth, widely-used reactants, such as silane, are very reactive and there is generally no need to use catalytic seed metals to promote reactant decomposition. However, sidewall deposition plagues many gas-phase reactions and leads to substantial diameter variation over the length of the wire—enhanced precursor decomposition at the seed metal could help eliminate this problem by enabling lower growth temperature. In solution nanowire growth, sidewall deposition has not been a problem because organosilane precursors are relatively unreactive. In fact, many organosilane reactants, like octylsilane for example, are unreactive at typical nanowire growth temperatures in solution to promote nanowire growth, unless the seed metal could catalyze the reaction. Co and Ni nanocrystals were tested with reactants like octylsilane and trisilane to see if nanowires would form, which do not in the presence of chemically inert Au nanocrystals.
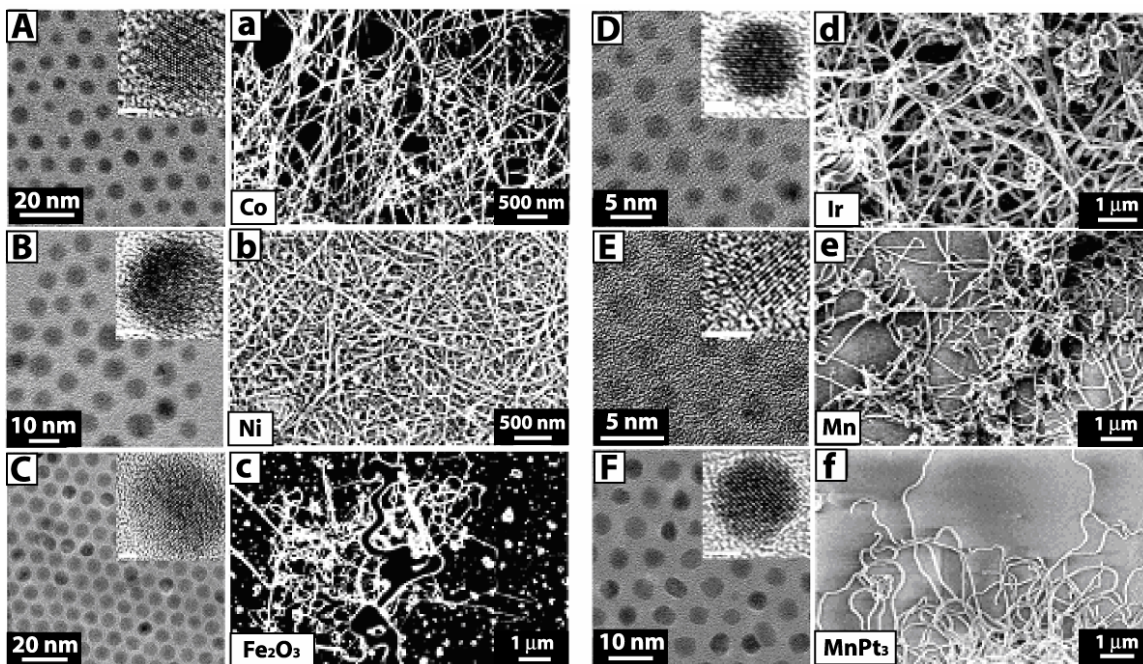
Figure 2.16. SEM images (a~f) of Si nanowires synthesized in supercritical toluene from MPS (150 mM, 500°C, 10.3 MPa) using various metal nanocrystals.   TEM images (A~F) of the nanocrystals used in each synthesis are shown on the left side of the corresponding SEM images.   Courtesy of Tuan.

2.4 CONCLUSIONS

Arylsilanes are effective precursors for crystalline Si nanowire growth by Au nanocrystal-seeded SFLS, whereas alkylsilanes and trislane are not.   The quantity of the Si product relates directly to the precursor decomposition chemistry – the precursors must be sufficiently reactive to produce enough Si to saturate the Au nanocrystal seeds and promote nanowire growth, but not so reactive that homogeneous particle nucleation and sidewall deposition overwhelms the metal particle-directed crystallization.   The kinetics of Si supply serves as a keystone for a controlled synthesis, and also plays an important role in determining the growth orientation of crystalline Si nanowires as will be discussed in more details in Chapter 3.   Transition metal particles other than Au could also seed Si

nanowire growth, and it is believed that Si atoms diffuse into the metal particles in solid phase far below their eutectic temperatures.

2.5 REFERENCES

(1)   Huang, Y.; Duan, X. F.; Cui, Y.; Lauhon, L. J.; Kim, K. H.; Lieber, C. M., *Science* **2001,** 294, 1313.

(2)   Duan, X. F.; Huang, Y.; Lieber, C. M., *Nano Lett.* **2002,** 2, 487.

(3)   Gudiksen, M. S.; Lauhon, L. J.; Wang, J.; Smith, D. C.; Lieber, C. M., *Nature* **2002,** 415, 617.

(4)   Hahm, J.; Lieber, C. M., *Nano Lett.* **2004,** 4, 51.

(5)   Qian, F.; Li, Y.; Gradecak, S.; Wang, D. L.; Barrelet, C. J.; Lieber, C. M., *Nano Lett.* **2004,** 4, 1975.

(6)   Barrelet, C. J.; Greytak, A. B.; Lieber, C. M., *Nano Lett.* **2004,** 4, 1981.

(7)   Westwater, J.; Gosain, D. P.; Tomiya, S.; Usui, S.; Ruda, H., *J. Vac. Sci. Technol. B* **1997,** 15, 554.

(8)   Wang, D.; Dai, H., *Angew. Chem. Int. Ed.* **2002,** 41, 4783.

(9)   Kamins, T. I.; Li, X.; Williams, R. S., *Nano Lett.* **2004,** 4, 503.

(10)   Chen, C. C.; Yeh, C. C.; Chen, C. H.; Yu, M. Y.; Liu, H. L.; Wu, J. J.; Chen, K. H.; Chen, L. C.; Peng, J. Y.; Chen, Y. F., *J. Am. Chem. Soc.* **2001,** 123, 2791.

(11)   Duan, X. F.; Lieber, C. M., *Adv. Mater.* **2000,** 12, 298.

(12)   Stach, E. A.; Pauzauskie, P. J.; Kuykendall, T.; Goldberger, J.; He, R. R.; Yang, P. D., *Nano Lett.* **2003,** 3, 867.

(13)   Huang, M. H.; Wu, Y. Y.; Feick, H.; Tran, N.; Weber, E.; Yang, P. D., *Adv. Mater.* **2001,** 13, 113.

(14)   Holmes, J. D.; Johnston, K. P.; Doty, R. C.; Korgel, B. A., *Science* **2000,** 287, 1471.

(15)   Yaws, C. L., *Handbook of Thermodynamic Diagrams*. Gulf Publishing Company: Houston, Texas, 1996; p 294.

(16)   Hanrath, T.; Korgel, B. A., *Adv. Mater.* **2003,** 15, 437.

(17)   Kamins, T. I.; Williams, R. S.; Basile, D. P.; Hesjedal, T.; Harris, J. S., *J. Appl. Phys.* **2001,** 89, 1008.

(18)   Saunders, A. E.; Sigman, M. B.; Korgel, B. A., *J. Phys. Chem. B* **2004,** 108, 193.

(19)   Grebinski, J. W.; Richter, K. L.; Zhang, J.; Kosel, T. H.; Kuno, M., *J. Phys. Chem. B* **2004,** 108, 9745.

(20)   Murray, C. B.; Sun, S. H.; Doyle, H.; Betley, T., *MRS Bull.* **2001,** 26, 985.

(21)   Hyeon, T.; Lee, S. S.; Park, J.; Chung, Y.; Bin Na, H., *J. Am. Chem. Soc.* **2001,** 123, 12798.

(22)   Lee, D. C.; Ghezelbash, A.; Stowell, C. A.; Korgel, B. A., *J. Phys. Chem. B* **2006,** 110, 20906.

(23)   Stowell, C. A.; Korgel, B. A., *Nano Lett.* **2005,** 5, 1203.

(24)   Wu, Y. Y.; Yang, P., *J. Am. Chem. Soc.* **2001,** 123, 3165.

(25)   Wu, Y.; Fan, R.; Yang, P., *Nano Lett.* **2002,** 2, 83.

(26)   Vanderwielen, A. J.; Ring, M. A.; Oneal, H. E., *J. Am. Chem. Soc.* **1975,** 97, 993.

(27)   Pell, L. E.; Schricker, A. D.; Mikulec, F. V.; Korgel, B. A., *Langmuir* **2004,** 20, 6546.

(28)   Swihart, M. T.; Girshick, S. L., *J. Phys. Chem. B* **1999,** 103, 64.

(29)   Gilman, H.; Tomasi, R. A.; Wittenberg, D., *J. Org. Chem.* **1959,** 24, 821.

(30)   Nelson, L. E.; Angelotti, N. C.; Weyenberg, D. R., *J. Am. Chem. Soc.* **1963,** 85, 2662.

(31)   Coutant, R. W.; Levy, A., *U.S. Clearinghouse Fed. Sci. Tech. Inform.* **1969**.

(32)   *Lange's Handbook of Chemistry*. 15 ed.; Mc-Graw Hill, Inc.: New York, 1999.

(33)   Hanrath, T.; Korgel, B. A., *J. Am. Chem. Soc.* **2002,** 124, 1424.

(34)   Wu, Y.; Cui, Y.; Huynh, L.; Barrelet, C. J.; Bell, D. C.; Lieber, C. M., *Nano Lett.* **2004,** 4, 433.

(35)   Levitt, A. P., *Whisker Technology*. John Wiley & Sons, Inc.: New York, 1970.

(36)   Tuan, H.-Y.; Lee, D. C.; Hanrath, T.; Korgel, B. A., *Nano Lett.* **2004,** 5, 681.

(37)   Lu, X. M.; Hanrath, T.; Johnston, K. P.; Korgel, B. A., *Nano Letters* **2003,** 3, 93.

(38)   Hu, J. T.; Odom, T. W.; Lieber, C. M., *Acc. Chem. Res.* **1999,** 32, 435.

(39)   Dai, H. J.; Kong, J.; Zhou, C. W.; Franklin, N.; Tombler, T.; Cassell, A.; Fan, S. S.; Chapline, M., *J. Phys. Chem. B* **1999,** 103, 11246.

(40)   Lee, D. C.; Mikulec, F. V.; Korgel, B. A., *Journal of the American Chemical Society* **2004,** 126, 4951.

(41)   Lee, D. C.; Korgel, B. A., *Mol. Simul.* **2005,** 31, 637.

(42)   Lee, D. C.; Hanrath, T.; Korgel, B. A., *Angew. Chem. Int. Ed.* **2005,** 44, 3573.

(43)   Tuan, H.-Y.; Lee, D. C.; Korgel, B. A., *Angew. Chem. Int. Ed.* **2006,** 45, 5184.

Chapter 3: Transmission Electron Microscopy Analysis of Si Nanowires

3.1 INTRODUCTION

Research, development, and manufacturing of nanotechnology, especially nanoelectronic technology requires the ability to image at near atomic dimensions. In many circumstances, transmission electron microscopy (TEM) can now provide the necessary imaging. The recent introduction of aberration corrected lens technology has extended spatial resolution to less than 0.1 nm. High Resolution TEM images and electron diffraction patterns of nanowires show phenomena not present in images of bulk materials. Particularly in nanomaterials research, high-resolution transmission electron microscopy (HRTEM) is arguably the most powerful characterization tool. It is, therefore, of significant importance to understand the physics involved in HRTEM. Caution must be exercised in the interpretation of the images since the acquired images *do not* necessarily correspond to the actual atomic arrangement in the crystal.

Defects present in nanostructures can hamper the accurate analysis of their crystal configuration. These effects are more pronounced in nanostructures due to the presence of high surface-to-volume ratio. The defects may not be easily visualized and may require careful tilting experiments to precisely characterize. By simulating the images, a fine conclusion can be drawn on which factors contribute more to the TEM images. Atomic modeling in fact would require understanding of detailed structures of the atoms in the nanostructures, but structures simplified through assumptions could also help determine how the electrons interact with the nanostructures in actual microscopes.

EELS has found its use in a wide variety of applications including identification of composition, bonding, and electronic structure in microelectronic devices. Today, thanks to advances in microscopy and sample fabrication technology, electronic

properties of nanostructures can be recorded even on an atomic scale. By combining EELS with a scanning transmission electron microscope (STEM), it is possible to scan the EELS spectrum across nanometer-sized samples in a sub-1nm resolution, thus allowing the study of position-dependent properties. In particular, for one-dimensional nanostructures, line-scan EELS spectrum provides rich information on radial distribution of electronic structures. However, the few studies that have been dedicated to this technique have generated controversy and uncertainty over fundamental matters including the size effect and volume plasmon shift.

This chapter discusses the structural analysis of silicon nanowires in HRTEM and EELS. The defects present in silicon nanowires are analyzed experimentally and in simulated structures with twinning in silicon nanowires also being discussed. EELS analysis of silicon nanowires will also be covered. The central focus in this chapter is to correlate the probe position and energy losses of electrons, thereby justifying the underlying fundamental physics. The line-scan EELS spectrum shows the volume plasmon shift; the quantitative analysis tells us that the shift is due to the size confinement near the surface of nanowires. The size-dependence of plasmon energy indicates that oscillation of valence electrons is confined in radial directions in the Si nanowire.

3.2 EXPERIMENTAL SECTION

3.2.1 Sample Preparation

Si and Ge nanowires were prepared via the supercritical fluid-liquid-solid (SFLS) method as reported elsewhere. For detailed synthetic procedures, see Chapter 2. A Ti-2 grade high pressure reactor (HiP Inc., PA) that contained anhydrous hexane was heated

and pressurized to 450 °C and ~3.4 MPa for Si nanowire synthesis.   A precursor solution containing 1 M phenylsilane and dodecanethiol monolayer passivated Au nanocrystals (Si:Au molar ratio of 1000:1) was prepared inside a nitrogen glove box. The precursor solution was then injected into the supercritical fluid reactor by using a HPLC pump and pressure as adjusted at ~8.2 MPa.   After the elapsed reaction time, the reactor vessel was allowed to cool in air for 5 min followed by quenching in an ice bath. The Si nanowire reaction product deposited on the reactor wall and on a 10×63 mm Si substrate was recovered with chloroform.   The Si nanowire suspension in chloroform was briefly sonicated, then dropcast onto a holey carbon-coated copper TEM grid (Electron Microscopy Science Inc.).   Ge nanowires were prepared by a similar procedure described in detail elsewhere.

3.2.2 TEM Characterization

The nanowires are long enough to span to holey regions of the lacey carbon film, allowing TEM imaging without a carbon substrate background.   A JEOL 2010F and operating at 200 kV accelerating voltage was used for TEM imaging.   Aberration-corrected images were collected using Carl Zeiss Sub-Angstrom TEM (SATEM).

3.2.3 Atomic Modeling and TEM Simulation

Accelrys Materials Studio Modeling v3.0 was used to form nanowire crystal models based on crystallographic orientation and nanowire surface faceting, which were experimentally determined in previous HRTEM studies.   Surface relaxation and thermal crystal vibration effects were neglected.   The assumption of neglecting surface relaxation is supported by the fact that the change in the lattice contstant for the crystal closer to the surface is lower than the resolution of the HRTEM microscope.   Thermal vibration effects were not accounted for in this model.   The imaging artifacts caused by

the non-empirical conditions could be removed by slightly tilting the nanowire model crystal by ~ 0.5 deg of the microscope axis. The crystal models were then analysed in SimulaTEM^{TM} to obtain simulated TEM images based on phase contrast images. The three dimensional nanowire model consisting of at least 1,500 atoms were then used to simulate phase contrast HRTEM images under the following conditions: incident electron energy (E) = 200 kV, defocus spread = 3.8 nm, the spherical aberration (Cs) = 1 mm (unless stated otherwise) and the defocus = –50.0793 nm (the Scherzer condition at Cs = 1 mm, E = 200 kV). The simulation was carried out with 10 theoretical slices, where the impact of the atomic structure on the transmission of an electron beam is simulated in terms of transmission from one slice of a sample to the next.

3.2.4 Electron Energy Loss Spectroscopy (EELS) Analysis

EELS data were obtained using a Gatan DigiPEELS equipped with a JEOL 2010F high-resolution transmission electron microscopy (HRTEM). Incident electrons with accelerating voltage of 200 kV were used to probe the nanowire samples. The positions of the electron beam and the nanowire sample were recorded by using a scanning transmission electron microscopy (STEM) mode with a probe size of 0.5 nm. Combination of EELS and STEM allowed us to direct the electron beam probe onto the desirable sample position at a resolution of <1 nm. The aperture size and the camera length were 3 and 10 cm respectively, leading to a 3 mrad convergence angle and an 11 mrad collection angle. The electron beam was focused so that the full-width at half-maxima (FWHM) of a zero-loss peak becomes as small as 1.0 eV. After having recorded the spectroscopy data, we subtracted the background from zero-loss peak using the method suggested by Reed *et al.* Schematic illustration of EELS measurement is shown in Figure 3.1.
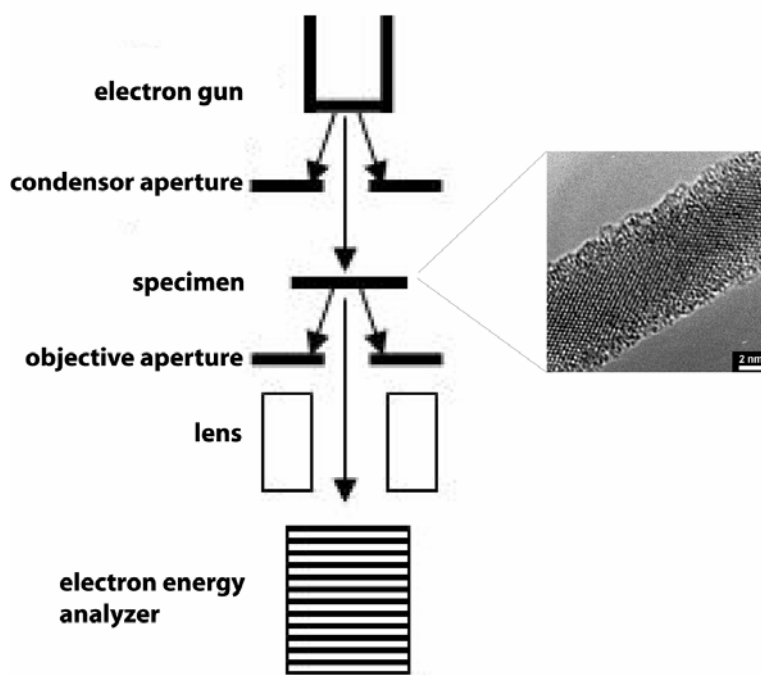
Figure 3.1. Schematic illustration of STEM-ELS measurement. Fast probing incident electron interacts with the nanowire sample (an example shown in the inset), resulting in the energy losses, which will be analyzed in the energy analyzer.

3.3 RESULTS AND DISCUSSION

3.3.1 TEM Analysis of Si Nanowires

3.3.1.1 Single crystallinity of Si nanowires

Figure 3.2 shows TEM images of Si nanowires acquired using a JEOL 2010F microscope (E_{HT} = 200 kV). Most of the nanowires have native oxide layers thinner than ~10 nm, as revealed in HRTEM analysis. Nanowires bent when they were deposited on TEM grids exhibited bending contrast fringes. Nanowires are single crystalline with only a marginal number of exceptions. The single crystallinity relates to

the growth direction of the nanowires. The general trend appears to be that the Si nanowires grown in the supercritical fluid reaction system favor <111> growth orientation. It is interesting to note that Ge nanowires grown similarly in the high pressure cell exhibited a predominant growth direction of <110>. As addressed in Chapter 2, the decomposition of Si precursors takes place via disproportionation reactions, while Ge precursors are thermolyzed to supply Ge atoms in the reactions. Consequently, the Si precursor concentration is much higher than that of Ge precursors in the nanowire synthesis. This could lead to high supersaturation conditions with fast nanowire growth. It has been known that at high supersaturation, Si and Ge nanowires favor <111> growth directions, and the high population of <111> oriented nanowires in Si than in Ge is consistent with this general trend.

The structure of the initial Si nucleus is governed by energy minimization. For bulk Si, the surface energies of the {111} faces are the lowest, and in addition, the Au-Si {111} interface plane is likely the determining parameter for the growth direction. Namely, energetically favored Au-Si {111} face forms and the nanowire grows normal to this plane.
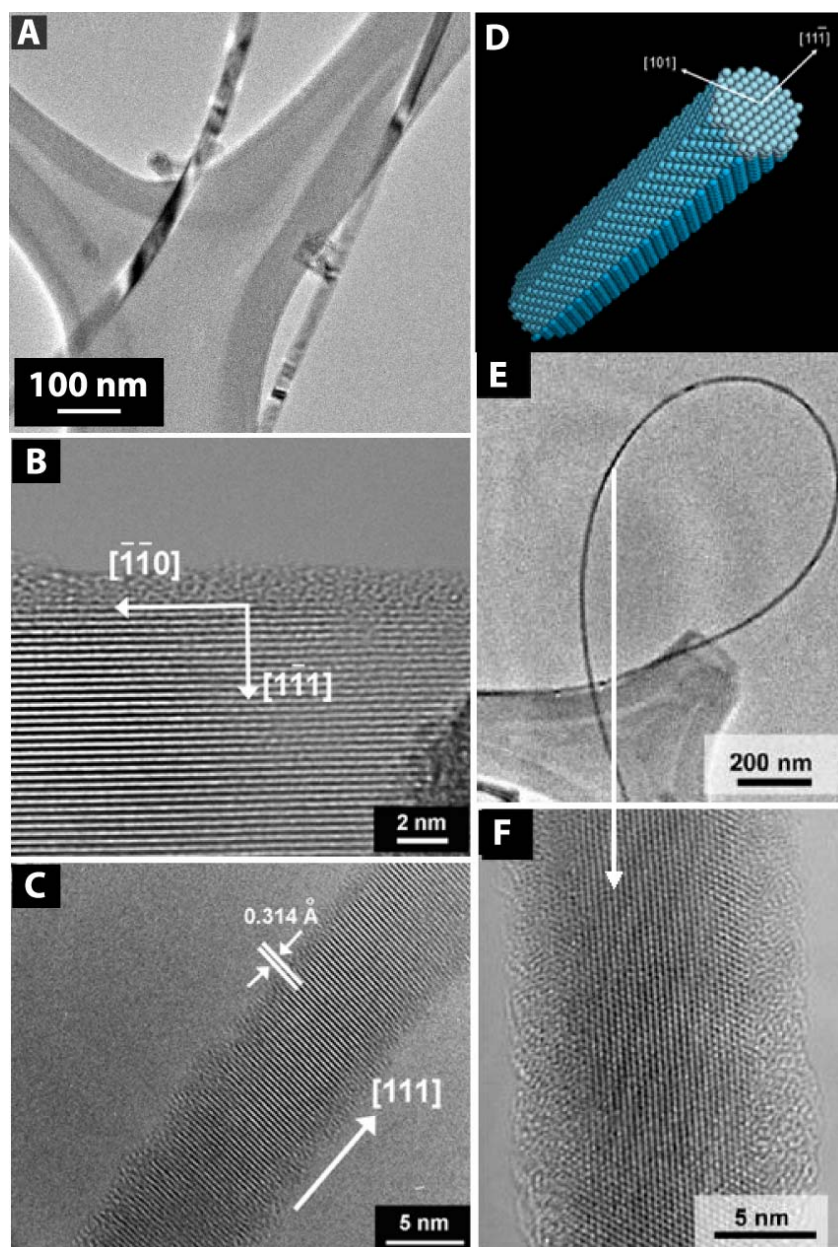
Figure 3.2. Overview of the materials studied in this chapter.   (A) TEM image of Si nanowires.   (B and C) HRTEM images of nanowires, whose growth directions are <110> and <111>, respectively.   (D) Structural models constructed using Materals Studio v. 3.0.   (E) A low-resolution image of a single crystal Ge nanowire undergoing a 270° bend and forming a complete loop.   (F) HRTEM image of the same wire showing the same wire showing the defect-free [110]-oriented crystal structure.   TEM images of Ge nanowires courtesy of T. Hanrath.

3.3.1.2 Growth direction assessment

Since the {111} plane is very stable, most of the nanowires exhibit single crystallinity according to the TEM data. The growth direction was interpreted by taking a Fourier transform of the HRTEM images as shown in Figure 3.3. The nanowires are normally very thin (<30 nm), so it is very difficult to accurately align them to an exact zone axis using a double-tilt TEM sample holder. Fast Fourier transform(FFT)-ed images provided enough crystallographic information to assess the growth directions. Single crystalline nanowires reveal an amazing flexibility (Figures 3.2E and F), and the bending of the single crystals appears in the form of contrast bending fringes in TEM as shown in Figure 3.2A. Certain atomic planes are bent to satisfy the Bragg diffraction and hence diffract stronger than neighboring crystal sections. Yet, the crystal exhibits a perfect single crystallinity throughout the bent region, as shown in Figure 3.4D.
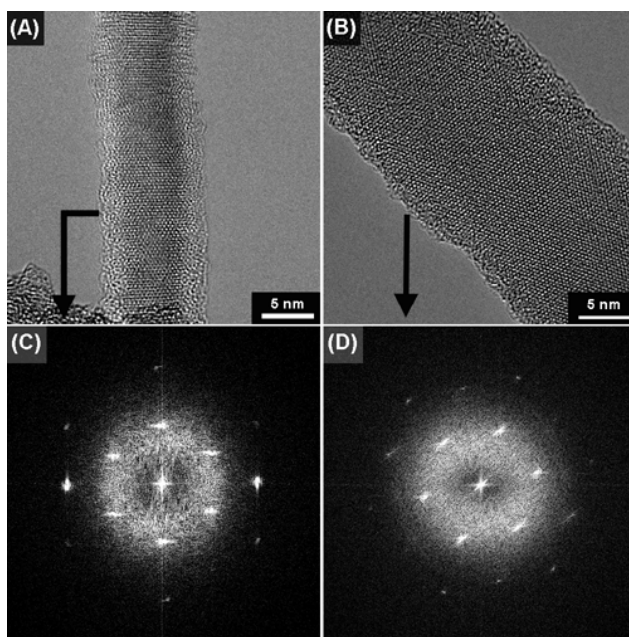
Figure 3.3. (A, B) TEM images of Si nanowires. Due to slightly different zone axis of the incident electron beam, the d-spacings calculated from FFTs (C, D) are different for the two images.
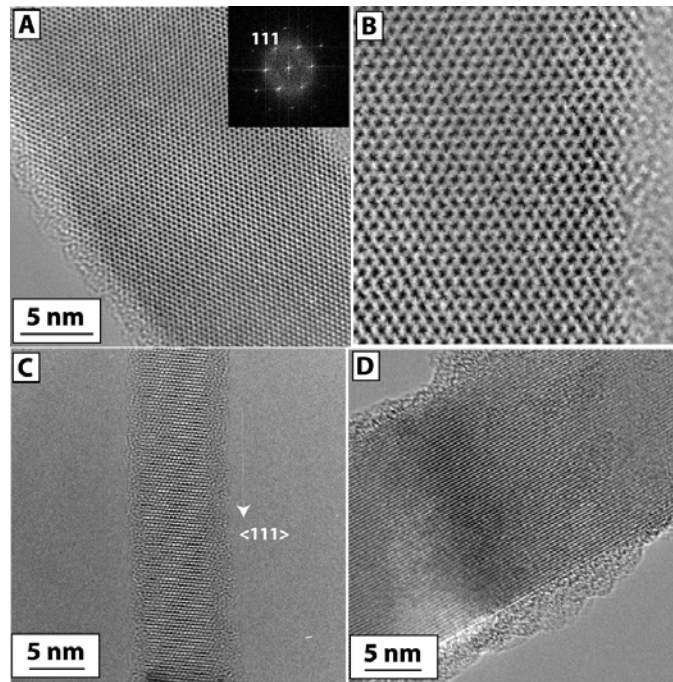
Figure 3.4. (A-B) HRTEM images of <111>-grown Si nanowire. (C) Si nanowire exhibiting {111} lattice fringes, indicating the <111> growth orientation. (D) Si nanowire with bending contrast fringes with perfect crystallinity.

3.3.1.3 Change of the crystallographic direction of nanowires

Figures 3.5A and B show TEM images of a Si nanowire with the less common <110> growth axis.   The Au-Si nanowire interface does not appear to be as sharp as in the case of <111>-oriented nanowires.   The crystallographic direction could also be altered during the growth (Figures 3.5C and D).   Likely due to a disturbance at the Au-Si interface during the growth, the growth reverts to the new direction without apparent defects.   Figure 3.6 shows TEM images taken at different tilting angles.   At a certain nanowire orientation with respect to the beam axis, the nanowire shows a twinning plane running down the length of the nanowire.

64
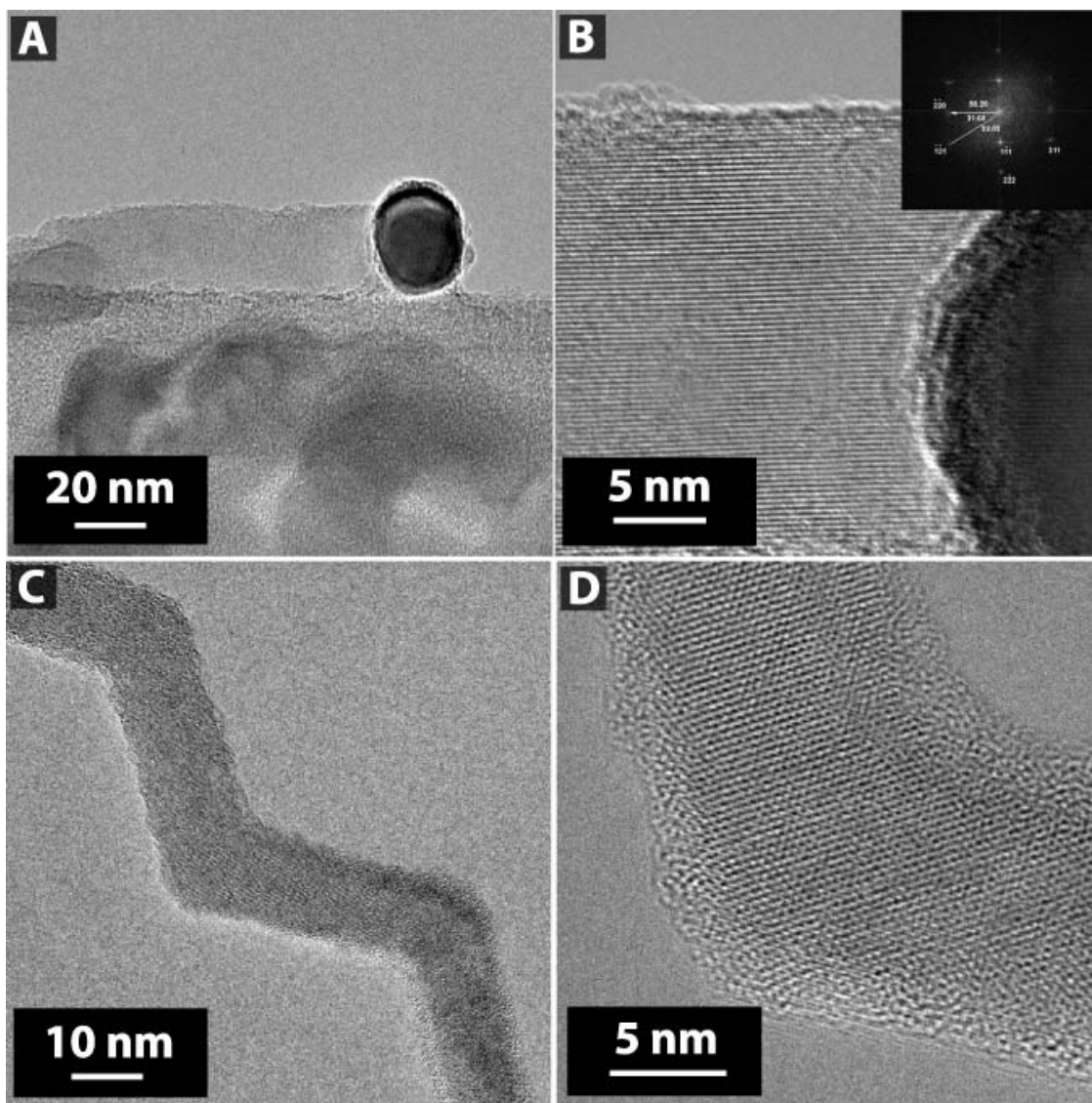
Figure 3.5. (A-B) HRTEM images of a <110>-oriented Si nanowire. (C-D) HRTEM images of a Si nanowire that shows a zigzag growth pattern.
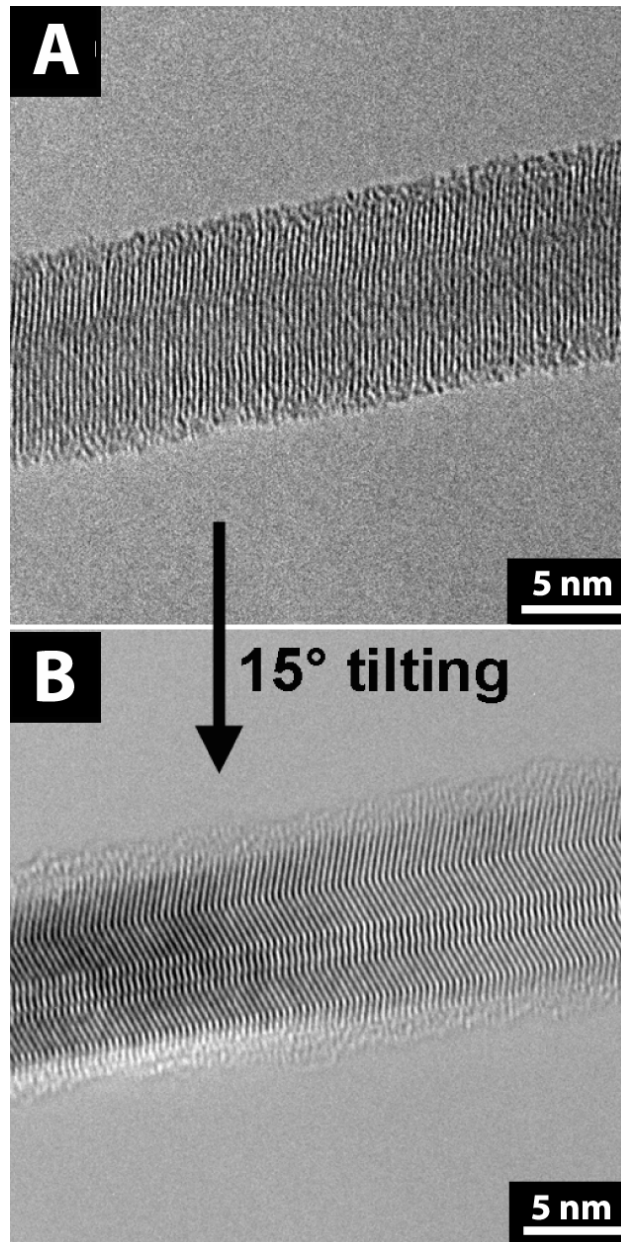
Figure 3.6. HRTEM image of a Si nanowire with different electron beam zone axes.   15 degree tilting makes the twinning faults running along the growth direction of the nanowire disappear.

3.3.1.4 Understanding TEM images through simulation

A complete interpretation of TEM images involves understanding of the interaction of electrons with the atoms in the crystal lattice. The finite size of the nanowire requires a simulation tool that does not rely on a typical periodic boundary conditions that can be employed in extended solids and thin films. SimulaTEM^{TM} is a TEM simulation tool with such capability. An atomic model of the Si nanowire was built using Materials Studio and then input into SimulaTEM^{TM}. SimulaTEM^{TM} utilizes a multi-size simulation method in which the impact of the atomic structure on an electron beam transmission is simulated in terms of transmission from one slice of a sample to the next. This program also accomodates nonperiodic structures and can calculate focal series and diffraction patterns. The capability to solve the wave equation with no restrictions in periodicity is ideal for calculating nanoparticles and nanowires. The simulations shown in Figures 3.7 and 3.8 reveal that at one angle, a <112>-oriented Si nanowire with a single {111} twin plane appears to have multiple twins.
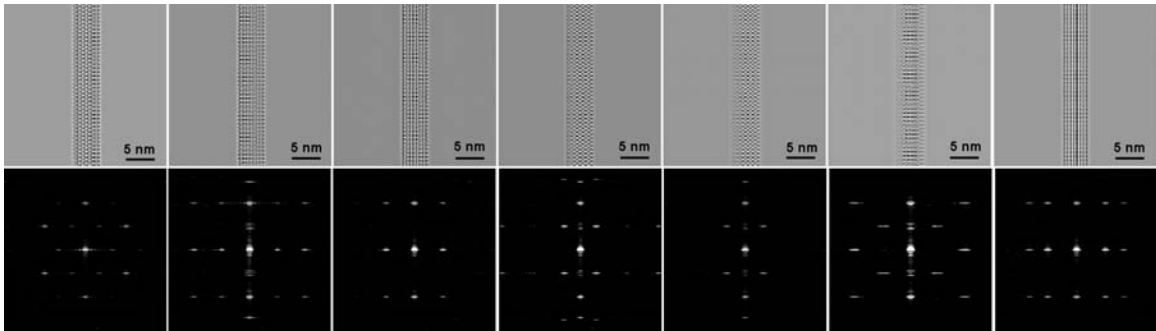
Figure 3.7. Simulated TEM images and diffraction patterns of a <110>-oriented Si nanowire with a single {111} twin plane running the length of the wire.
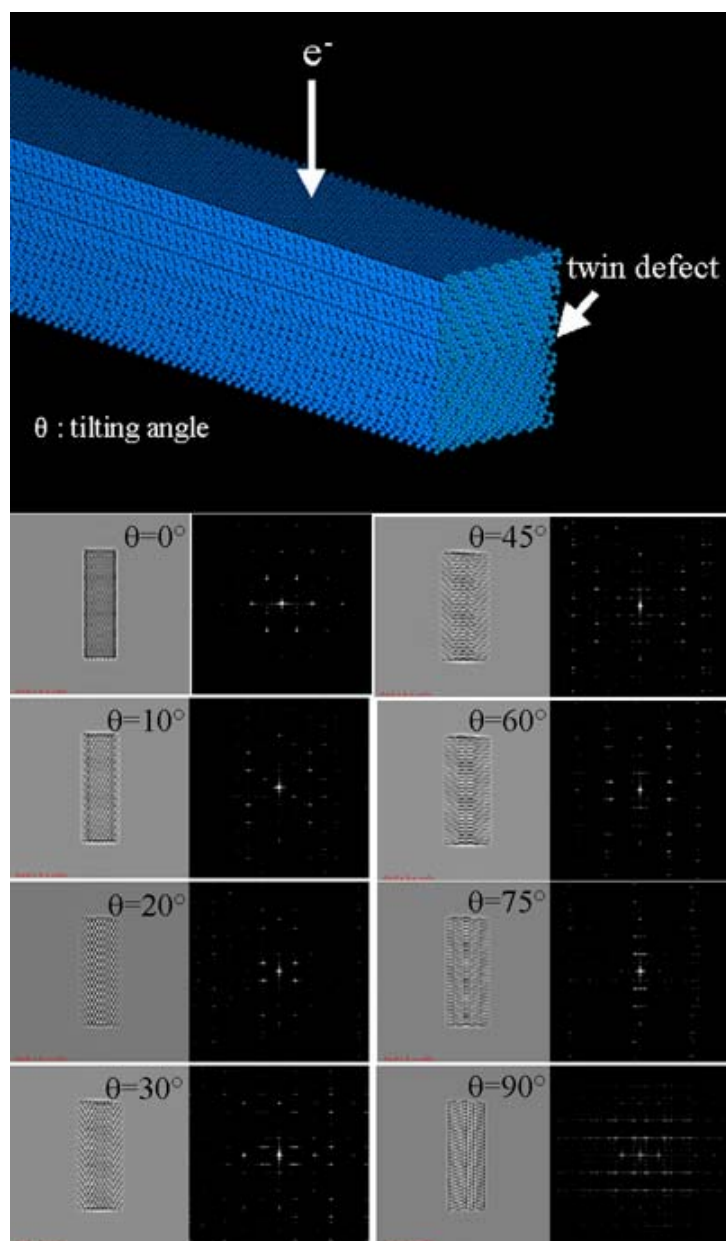
Figure 3.8. (Top) A Si nanowire constructed in the Materials Studio program.   The growth direction of the nanowire is <211> with {111} and {110} side surfaces and with a twin defect propagating through the middle of the nanowire.   The zone axis of the incident electron beam is initially set at [111], but as the nanowire is tilted around the growth axis the resulting image becomes off the zone axis.   (Bottom) HRTEM images simulated using SimulaTEM are obtained at different nanowire tilting angles.   Their corresponding diffraction patterns (also simulated) are shown right by the TEM images.

68

3.3.1.5 Crystallographic defects in experimental TEM data

Figure 3.9 shows a TEM image of a Si nanowire with the <112> growth direction. The nanowire appears to have multiple twins running the length of the wire. The Au-Si interface appears to show an epitaxial interfacing between the two materials (Figure 3.9A inset). The many twins observed in this image indicate that the nanowire does not have perfect crystalline structure. Unlike III-V nanowires that show relatively large population of {111} twins perpendicular to their growth orientation, Si nanowires exhibit {111} twinning only along the axis. Therefore, no {111} twins were observed in Si nanowires with the {111} growth conditions. Davidson *et al.* calculated the twin formation based on three-phase boundary equilibrium at the tip interface, and concluded that the Si and Ge nanowires cannot exhibit the {111} planes normal to the growth direction, because the sidewall faceting cannot be accommodated by the three-phase boundary between the seed particle and the nanowire. Thus, the contact angle fluctuations cannot support twinning in Au-seeded Si and Ge nanowires, explaining why they do not occur experimentally.
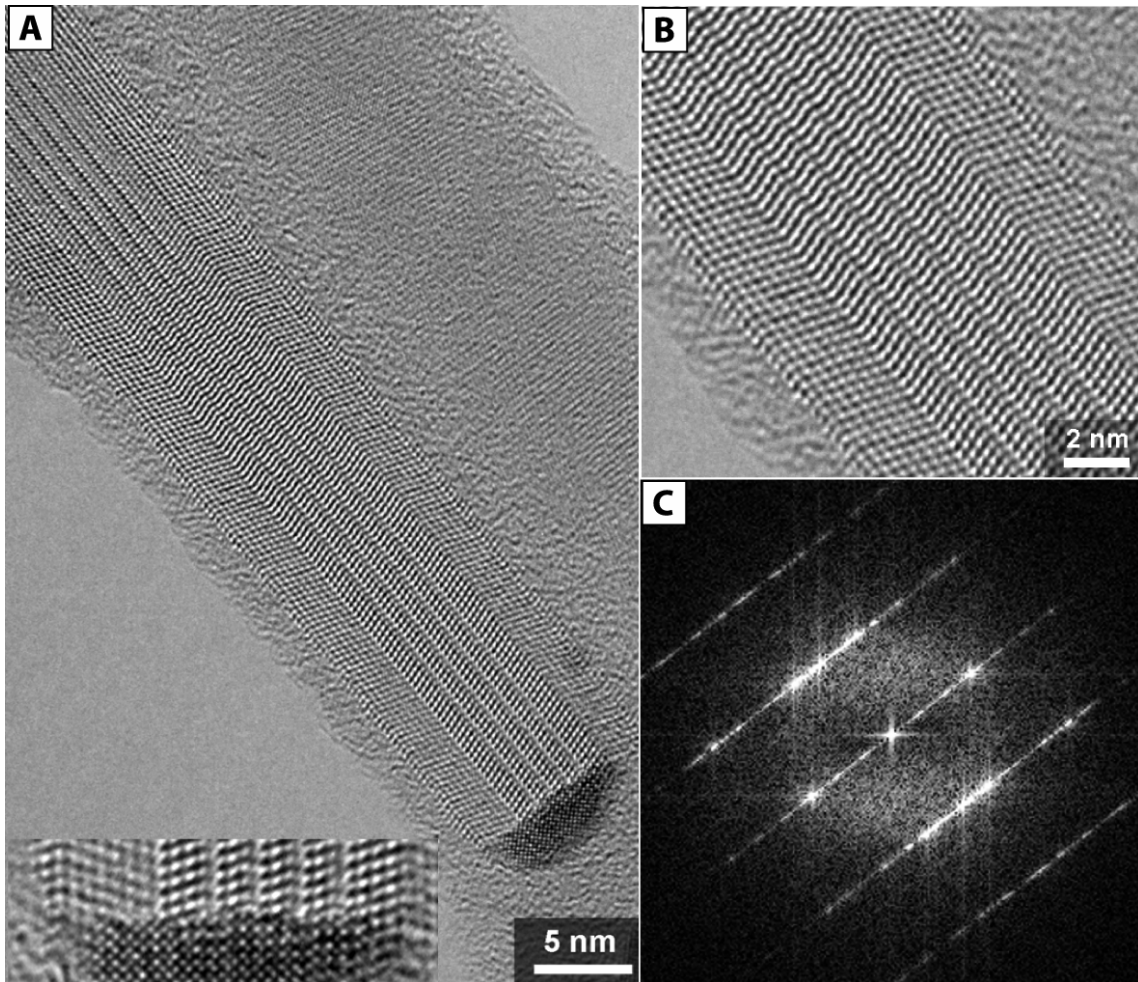
Figure 3.9. HRTEM image of a Si nanowire with twinning faults running along the growth axis, taken with a spherical aberration (C_s)-corrected microscope.

3.3.1.6 Growth analysis using TEM

A low-magnification TEM image in Figure 3.10 shows an interesting growth signature: the nanowire is wavy at its tail. The Si nanowire was grown in a semi-batch reaction; therefore, the Si supply decreased as the reaction proceeded, consuming the precursors. Toward the end of the growth, the lack of Si atoms supply likely resulted in

70

the tortuous growth.   This is an interesting observation, although quantitative analysis of the growth remains yet to be carried out.
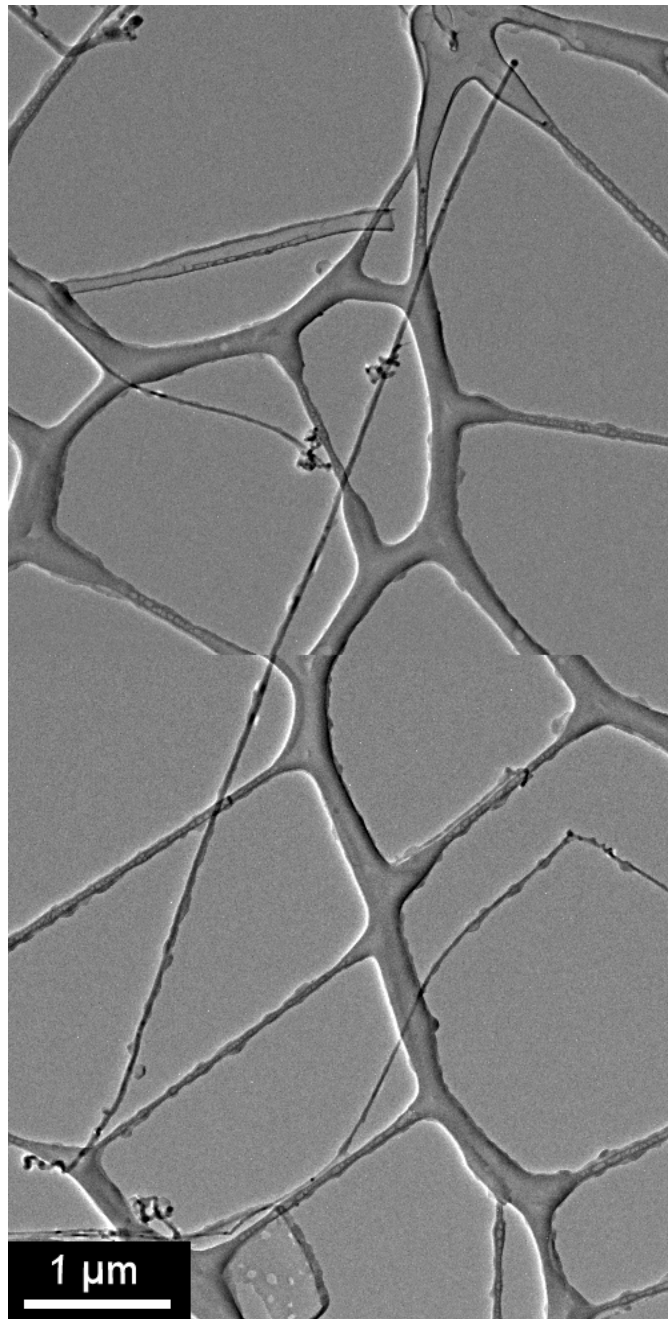
Figure 3.10. A low-magnification TEM image of Si nanowire grown in a semi-batch reaction.

3.3.2 EELS analysis of Si nanowires

3.3.2.1 Low loss and core loss peak assignments and calibration

Obtaining accurate low-loss and high-loss profiles of plasmon and core-loss spectra requires precise determination of the individual positions and painstaking calibrations. Plasmon and core-loss peaks were probed with line-scan spectra acquired from averaging 4 spectra per pixel with an acquisition time of 0.5~2 seconds per spectrum. High-resolution scanning transmission electron microscopy (STEM) images were taken before and after the scan to ensure that there were no significant drift during the scan. All spectra were aligned with respect to the zero-loss peak (ZLP). Removal of the ZLP from low loss spectra was performed by a technique similar to the one described by Reed *et al.* as illustrated in Figure 3.11.
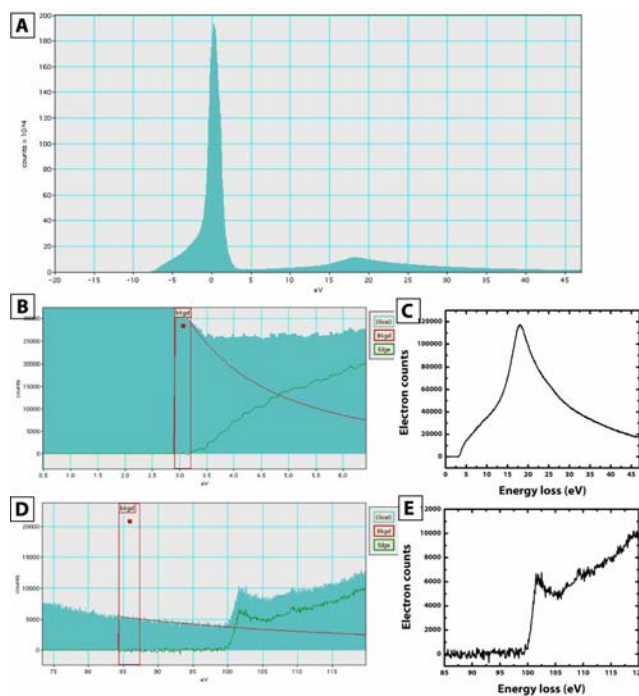
Figure 3.11. Calibration and subtraction of ZLP. Raw data (A) can be processed by substracting the ZLP (B and D) to give the low-loss spectrum (C) or core-loss spectrum (D).

3.3.2.2 Probe Position Dependent Plasmon Losses

EELS can be measured as a function of the probe position by scanning the probe radially across the nanowire sample.   Figure 3.12 shows an EELS line scan for a ~16 nm diameter Si nanowire.   The peak intensities in the spectra vary with probe position, because of the relative contributions of each mode on electronic excitation.   The maximum scattering intensity occurs when the electron probe is positioned at the center of the nanowire.   Peak position also changed as the probe scanned away from the center. The change qualitatively indicates that the oscillations of the valence electrons are dependent on their radial position in the nanowire.

As the probe is positioned at the surface of the nanowire, the peak at ~11 eV evolves, and the volume plasmon peak at ~17 eV exhibits blue-shift.
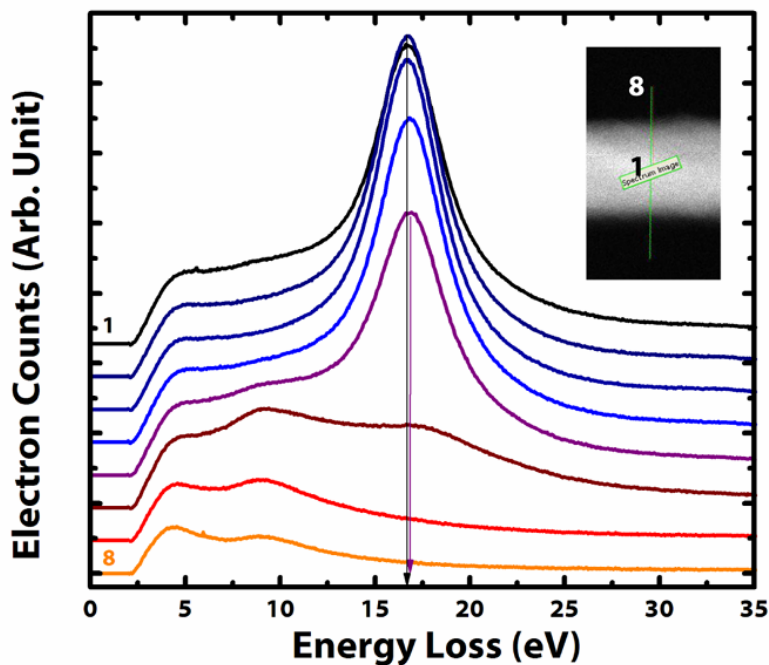
Figure 3.12. Energy loss spectra with varying probe positions.

3.4 CONCLUSIONS

Si nanowires synthesized in supercritical fluid predominantly exhibited the <111> growth direction with minor contributions from <211> and <110> oriented nanowires. The growth direction of Si nanowires is governed by the structure and faceting at the interface of Au-Si. Small population of Si nanowires that exhibit the <211> growth direction have lamellar twinning running the length of the nanowires. <111> grown nanowires do not show any twinning planes due to the stability of the Au-Si interface. Simulated TEM images reveal that a single twin present in a nanowire could appear as multiple twins in TEM. EELS analysis of Si nanowires reveals that the volume plasmon energy is size-dependent, due most likely to the surface effect on the oscillation wave of the valence electrons.

3.5 REFERENCES

(1) Batson, P. E., *IBM J. Res. & Dev.* **2000,** 44, 477.

(2) Lee, D. C.; Hanrath, T.; Korgel, B. A., *Angew. Chem. Int. Ed.* **2005,** 44, 3573.

(3) Hanrath, T.; Korgel, B. A., *J. Am. Chem. Soc.* **2002,** 124, 1424.

(4) Hanrath, T.; Korgel, B. A., *Small* **2005,** 1, 717.

(5) Reed, B. W.; Chen, J. M.; MacDonald, N. C.; Silcox, J.; Bertsch, G. F., *Phys. Rev. B* **1999,** 60, 5641.

(6) Kamins, T. I.; Li, X.; Williams, R. S., *Nano Lett.* **2004,** 4, 503.

(7) Wu, Y.; Cui, Y.; Huynh, L.; Barrelet, C. J.; Bell, D. C.; Lieber, C. M., *Nano Lett.* **2004,** 4, 433.

(8) Davidson, F. M.; Lee, D. C.; Fanfair, D. D.; Korgel, B. A., *J. Phys. Chem. C* **2007,** 111, 2929.

Chapter 4: Synthesis of Carbon Nanotubes in Supercritical Fluids

4.1 INTRODUCTION

Carbon nanotubes exhibit a variety of unique properties, which make them suitable for many potential uses, including structural, electronic and optical applications. The commercial use of carbon nanotubes in real-world applications requires a cost-effective method to fabricate large amounts of nanotubes with the desired material properties. With only a couple of exceptions, carbon nanotube formation has been explored exclusively in the gas phase using synthetic methods such as arc-discharge, laser vaporization, and chemical vapor deposition (CVD), because they provide access to the high synthetic temperatures required for nanotube formation. Under the extremely high temperature conditions of arc-discharge and laser vaporization (2000 to 4000 °C), carbon atoms can be vaporized from a solid carbon target and condensed into high quality single-wall nanotubes. Although CVD growth can be quite effective, nanotube formation occurs on a substrate surface in a batch synthetic processes, which limits the product yield and throughput. For microelectronics applications, and other high value-added applications, such as high-resolution displays, this may not be an issue. However, for other applications such as fabrics and structural composites that require large amounts of nanotubes at low cost, an alternative high throughput synthetic process is needed.

Metal catalysts have enabled high quality carbon nanotube synthesis at much lower temperatures (500~1200 °C) by using hydrocarbon species as reactants in conventional CVD reactors. Metal-catalyzed decomposition of CO to carbon nanotubes had been observed as early as 1955; however, not until recently have researchers embarked on a concerted effort to produce high quality nanotubes by metal catalyzed

CVD.   Andrews *et al.*, for example, have produced high quality MWNTs by CVD at 625~775 °C and atmospheric pressure using ferrocene to catalyze the decomposition of aromatic compounds to nanotubes.   In comparison to vapor-phase synthetic methods, supercritical fluid phase approaches have the potential for much higher throughput due to orders-of-magnitude higher precursor concentration and catalyst particle dispersibility, which would enable a continuous homogeneous synthetic process. Since carbon nanotube synthesis requires high temperatures (>600 °C), the solvents must be pressurized to achieve this temperature range.   Solvents at high pressures and temperatures—above their critical points—have been used to synthesize a variety of materials, and more recently have played an important role in the synthesis of a variety of nanostructures.

A supercritical fluid-liquid-solid (SFLS) approach to synthesize various semiconductor nanowires, including Si, Ge, and GaAs, has demonstrated potential for solution-based growth of seeded nanostructures at high temperatures.   Sterically-stabilized metal nanocrystals are input as seed particles that direct wire growth at temperatures, which exceed the metal/semiconductor eutectic temperature (approximately 360 °C for Au:Ge and Au:Si).   The temperature must be sufficiently high to degrade the molecular precursor and induce nanowire formation.   The synthesis of multiwall carbon nanotubes in supercritical toluene involves catalytic decomposition of toluene by ferrocene, or nanocrystals of Fe or FePt.   In this process, toluene serves as both the carbon source for nanotube growth and the reaction solvent.   Under the synthetic conditions producing the highest quality nanotubes, toluene degrades catalytically at the metal particle surfaces, with only minimum homogeneous toluene degradation. MWNTs ranging from 10 nm to 50 nm in outer diameter with wall thicknesses ranging from 5 nm to 40 nm were produced along with carbon nanofilaments.   High-resolution transmission electron microscopy (HRTEM) reveals that although the MWNT growth

mechanism exhibits similarities to SFLS growth, the processes are distinct. The morphology of the nanotubes appears to depend on the growth catalyst, with larger particles producing solid nanofilaments and smaller particles yielding MWNTs. Furthermore, nanotube growth appears to occur on the catalyst particle surface. The nanotubes were characterized by HRTEM, HRSEM and electron energy loss spectroscopy (EELS). EELS of individual MWNTs and filaments provided a particularly powerful tool for distinguishing MWNTs from carbon nanofilaments.

4.2 EXPERIMENTAL SECTION

4.2.1 Synthesis

4.2.1.1 Batch reaction

Anhydrous toluene, ferrocene, and hexane were purchased from Aldrich, and stored under nitrogen and used as received. Fe nanocrystals were synthesized by thermal decomposition of iron pentacarbonyl ($Fe(CO)_5$) (Aldrich) in octyl ether (Fluka) in the presence of oleic acid (Fluka) as a cappling ligand at 100 °C, following published procedures. FePt nanocrystals were prepared by thermal decomposition of platinum acetylacetonate ($Pt(CH_3COCCHCH_3)_2$) (Aldrich) and iron pentacarbonyl ($Fe(CO)_5$) in the presence of oleic acid and oleylamine (Aldrich).

Carbon nanotubes were synthesized in a high-pressure 10 mL stainless-steel reactor. Solutions of toluene and catalyst were loaded into the reactor in a nitrogen-filled glovebox. In the case of ferrocene, 0.1, 2.5 and 5 mM toluene solutions were prepared and tested, and the nanocrystal concentration was set to 2.5 mM. The volume of the solutions was adjusted so that the pressure determined from the toluene phase diagram should be ~12.4 MPa. Note that extreme care must be taken not to exceed the

pressure rating on the reactor, as the pressure-density isotherm rises sharply just above the critical point and small deviations in volume can lead to large increases in pressure. For example, for a reaction carried out at 600 °C, 2mL of toluene solution was loaded in the 10 mL cell to give ~12.4 MPa at the reaction temperature. The sealed reactor was removed from the glovebox and placed into a heating block pre-heated to 670 °C. The reactor temperature was determined using a thermocouple placed inside the heating block next to the reactor. The reaction cell reached the reaction temperature within 5 minutes. 15 minutes after placing the reactor in the heating block, it was removed from the heating block and cooled rapidly in a water bath. The reactor reached room temperature after five minutes in the water bath.

The reaction product consisted of a black solution of nanotubes in toluene. It was collected from the reactor in air. Hexane was used to extract the remaining product that had adhered to the reactor walls. The dispersed product removed from the reactor was centrifuged at 8000 rpm for 10 minutes to isolate a black precipitate containing the nanotubes. The supernatant was discarded, and the precipitate was redispersed in hexane and centrifuged again. This washing step was repeated once more to ensure that all of the organic molecular byproducts had been separated from the nanotube product.

4.2.1.2 Continuous flow-through reaction

A high-pressure 10 mL stainless steel vessel (High-Pressure Equipment Company, Erie, PA) was connected to 1/8" O.D. and 0.060" size I.D. stainless steel high pressure tubing (High Pressure Company, HiP) via stainless steel reducers (HiP) and stainless steel high-pressure valves as shown in Figure 4.1. The inlet was connected to a 6-way valve (Valco) with a 10 ml injection loop. The outlet was connected to a micrometering valve (HiP). The reactor was pressurized using a high-pressure liquid chromatography (HPLC) pump (Alcott) connected to a piston filled with anhydrous

toluene.   The piston was pressurized using water to avoid having to run solvent through the HPLC pump.   The reactor pressure was measured with a digital pressure gauge (Sensotech), and the temperature of the brass heating block is monitored with a type K thermocouple and temperature controller (Omega).   A silicon wafer cut to 1 cm × 5 cm was placed inside the reactor to facilitate nanotube collection.
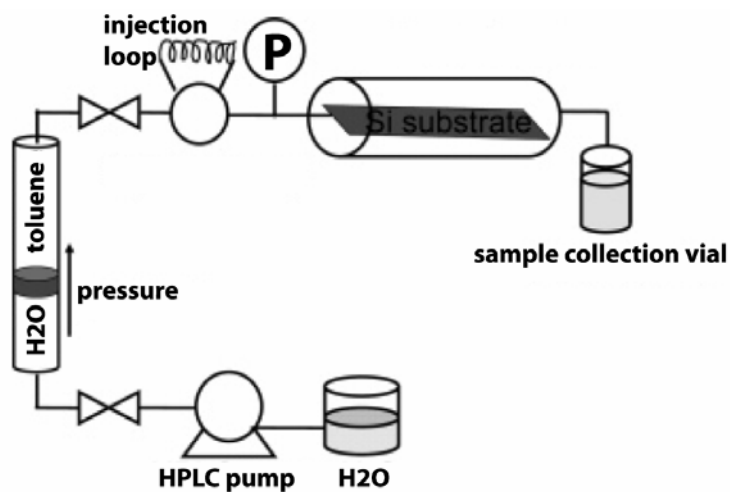
Figure 4.1. Schematic diagram of continuous flow-through supercritical fluid reaction system.

The reactor was loaded with toluene and preheated to the reaction temperature (between 600 and 645 °C) and pressurized to 1200 psig (8.3 MPa) with anhydrous toluene.   (Extreme caution must be exercised in all reactions close to 650 °C, as these conditions are close to the equipment limitations of the reactor connections.)   Catalyst was dissolved in anhydrous toluene, and the supplemental carbon source and DI-H_2O (if present) were added and vigorously mixed.   This reactant solution was then immediately injected from a 10 mL injection loop at a rate of 1 mL/min.   As the reaction proceeded, product was collected in a vial at the outlet of the reactor.   Reactions were always performed in a fume hood and the collection vial was sealed, yet vented to prevent

pressure buildup upon cooling. The reaction was carried out for 10 minutes before removing the reactor from the heating block and cooling to room temperature. The reactor was then opened under ambient conditions, the deposition substrate was removed and the remaining loose product of black soot was collected by rinsing with chloroform.

4.2.1.3 Purification

Only the sample from continuous flow-through reactions were purified via the following method: the nanotubes were treated with nitric acid and hydrogen peroxide to remove residual soot—purification that enabled high resolution imaging of the nanotubes. Approximately 3 mg of product was refluxed at 120 °C in 10 mL of 7 M nitric acid (Aldrich) for 3 hours. The solution was cooled to room temperature and centrifuged at 8000 rpm for 10 minutes. The supernatant was discarded, and the precipitate was redispersed in DI-H_2O and centrifuged again after brief sonication. This precipitation/centrifugation step was repeated again to ensure that residual acid, amorphous carbon, and catalyst particles were removed. The nanotubes were then dispersed in a 9% hydrogen peroxide (H_2O_2) solution and refluxed at 80 °C for 6 hours. The solution was cooled to room temperature and centrifuged at 8000 rpm for 10 minutes. The supernatant was discarded and the precipitate was redispersed in ethanol and centrifuged again. This precipitation/centrifugation step was repeated again. The nanotubes were then ultrasonicated for 2 hours using a Cole Parmer 8891(Vernon Hills, IL) sonication bath and 10 minutes using a Branson Sonifer 250 (Danbury, CT) sonication horn. The horn was set to a duty cycle of 10% with an output control of 2.

4.2.2 Characterization

The product was characterized by high-resolution transmission electron microscopy (HRTEM), scanning electron microscopy (HRSEM), and electorn energy

80

loss spectroscopy (EELS). For TEM and EELS, the final dry product was redispersed in hexane and dropped onto a lacey carbon-coated TEM grid (Electron Microscopy Sciences). The nanotubes are sufficiently long to span to holey regions of the lacey carbon film, allowing TEM imaging and collection of EELS without a carbon substrate background. This was of primary importance for the EELS measurements, where the background carbon signal obscures the spectroscopic data. A JEOL 2010F operating at 200 kV accelerating voltage was used for TEM imaging and for EELS. The JEOL 2010 F was equipped with a Gatan parallel-EELS spectrometer. Electron energy loss spectra were acquired in STEM mode with the field emission gun operating at 200 keV, and the EELS aperture size set at 2mm and a 10 cm camera length, which translates into 5 mrad of collection semi-angle. The electron beam size was set at 1 nm for performing the EELS measurements. HRSEM images were obtained on a field emission LEO 1530 SEM operated at 4kV. For SEM observation, the product was dispersed by brief sonication in hexane and then drop-cast on a piece of silicon wafer (2cm×2cm), which had been washed ultrasonically in ethanol (5 min) – acetone (5 min) – ethanol (5 min) beforehand.

4.3 RESULTS

4.3.1 Ferrocene-Catalyzed Nanotube Synthesis

Figures 4.2A and B show HRSEM images of the crude carbonaceous product obtained by degrading toluene at 600 °C and ~12.4 MPa in the presence of 2.5mM ferrocene. The product appears as an entangled mesh of fibrous material. TEM images reveal that the wires are a mixture of MWNTs and solid carbon nanofilaments. In the absence of ferrocene, there is no appreciable degradation of toluene at 600 °C at

~12.4 MPa.   HRTEM images of MWNTs and nanofilaments—such as those in Figures 4.2C-F —show the filament core to consist of randomly stacked graphene sheets (Figure 4.2E); whereas, the nanotubes exhibit coaxially stacked graphene sheets (Figure 4.2C) with a layer spacing of 0.344 nm, which agree well with previously reported intertubule spacing.   The yield of carbon nanotubes relative to the total carbonaceous material produced in the reaction is approximately 2% based on TEM observations.   Catalyst particles were always observed at the tips of the MWNTs and nanofilaments.   The fiber morphology—whether the carbon structures end up as tubes or solid filaments—appears to depend on the size and shape of the catalyst particle, with nanotubes generation resulting from smaller catalytic particles.
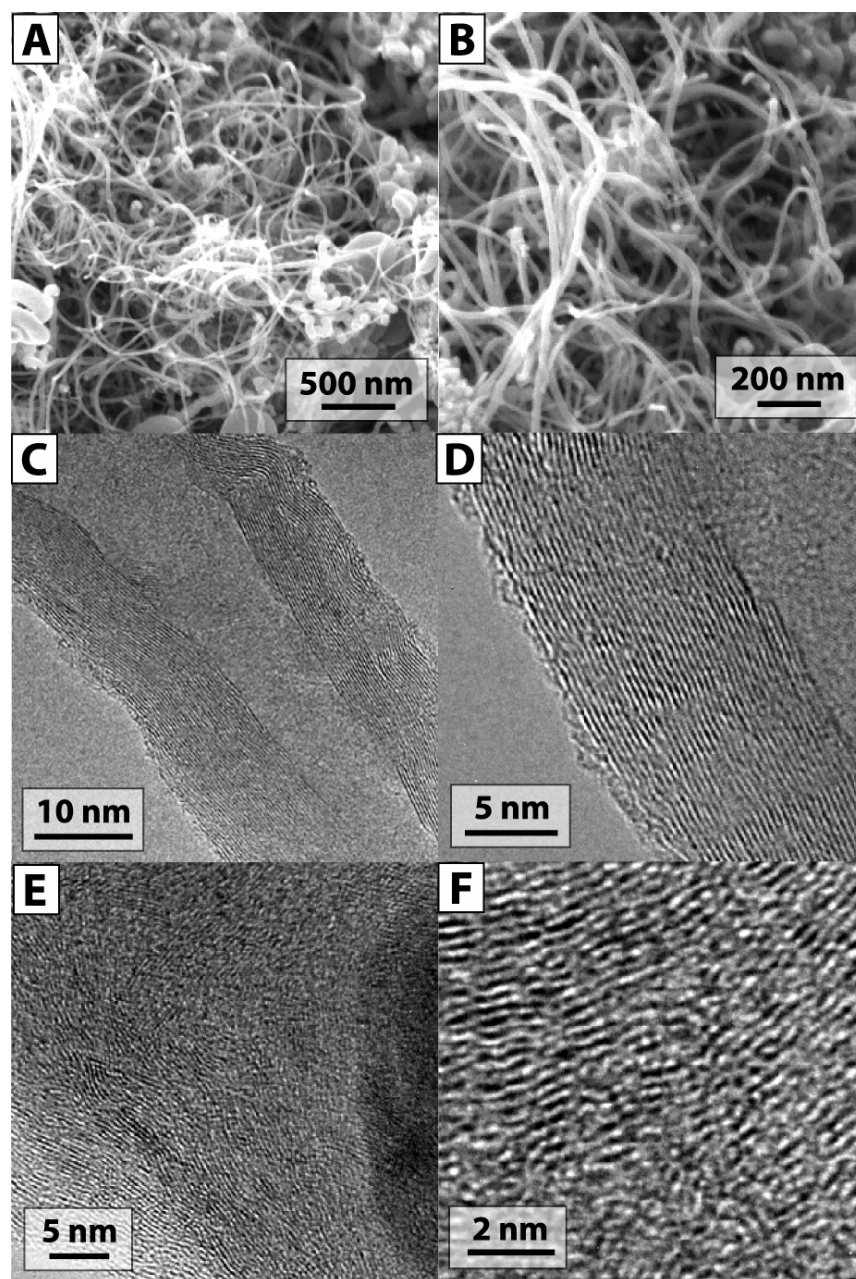
Figure 4.2. High resolution scanning electron microscopy (HRSEM) images (A, B) of the crude reaction product consisting of carbon nanofilaments and MWNTs obtained by heating 2.5 mM ferrocene in toluene solutions for 15 min at 600 °C and ~12.4 MPa. HRTEM images of a MWNT (C, D), and a carbon filament (E, F), isolated from the reaction at 600 °C, ~12.4 MPa, using ferrocene as the growth catalyst. The MWNTs exhibit concentrically stacked graphite sheets (D), whereas the nanofilaments exhibit disordered stacking along the length of the filament (F).

After examining the effects of catalyst concentration, hydrocarbon species, reaction pressure, and temperature on the reaction product, the temperature appears to be the most significant parameter in determining the quality of the nanotube product (Table 4.1). Figure 4.3 shows TEM images of product obtained after heating solutions of toluene and ferrocene (2.5 mM) to temperatures ranging from 400°C to 650°C for 15 min, with a reaction pressure of ~12.4 MPa. At 400°C, the product isolated from the reactor consists only of Fe particles. Toluene does not degrade at this temperature. At 500°C, larger Fe particles were produced that were coated with a thin layer of amorphous carbonaceous material. The amorphous coating indicates that 500°C is below the temperature required for graphitization. Fibrous structures, which form at 550°C, are filamentous but not graphitic. All of these fibers embed Fe particles ranging from 30 to 50 nm in diameter at their tips, indicating that the particles promote fiber formation in the reactor. Interestingly, smaller particles isolated from the reaction mixture did not appear to be associated with the carbonaceous material. Reactions at 600°C produced MWNTs and graphitic carbon nanofilaments. 600°C was found to be the optimum reaction temperature for MWNTs. The Fe particles that form as ferrocene thermally decompose and *catalyze* toluene degradation, while also promoting nanotube and nanofilament formation. Pure toluene is stable at 550°C and ~12.4 MPa, and begins to partially degrade at 600 °C. At 650 °C, toluene degrades rapidly and reactions carried out at 650 °C did not produce filaments or nanotubes. At 650°C, primarily amorphous carbonaceous material is obtained. The homogeneous solvent pyrolysis rate overwhelms nanotube and nanofilament growth, which leads to amorphous particulate formation and catalyst poisoning.

Table 4.1. Description of the reaction products from different reaction conditions

	T (°C)	P (MPa)	Fe source	C source	Conc. (mM)	Results
1	400	~12.4	ferrocene	toluene	2.5	Only Fe particles were produced.
2	500	~12.4	ferrocene	toluene	2.5	Fe particles were wrapped with carbonaceous stuff.
3	550	~12.4	ferrocene	toluene	2.5	A number of nanofilaments formed, while trace amount of nanotubes were observed.
4	600	~12.4	ferrocene	toluene	2.5	Multiwall nanotubes formed.
5	650	~12.4	ferrocene	toluene	2.5	Carbonaceous by-product due to severe degradation.
6	675	~12.4	ferrocene	toluene	2.5	Carbonaceous by-product due to severe degradation.
7	600	~12.4	ferrocene	toluene	0.1	MWNTs, coated with amorphous layer, were formed. But the amount of the nanotubes were smaller than the case of 4.
8	600	~12.4	ferrocene	toluene	5	More nanofilaments were formed than in 4.
9	600	~12.4	ferrocene	xylene	2.5	No nanotubes were produced.
10	600	~12.4	ferrocene	benzene	2.5	No nanotubes were produced.
11	600	~12.4	ferrocene	hexane /benzene	2.5	Large carbonaceous sheets were obtained, but no nanotubes were observed.
12	600	~27.6	ferrocene	toluene	2.5	Nanotubes were observed. No big difference from 4.
13	600	~12.4	Fe NCs	toluene	2.5	Low yield of nanotubes with smaller diameter.
14	600	~12.4	FePt NCs	toluene	2.5	Low yield of nanotubes with smaller diameter.
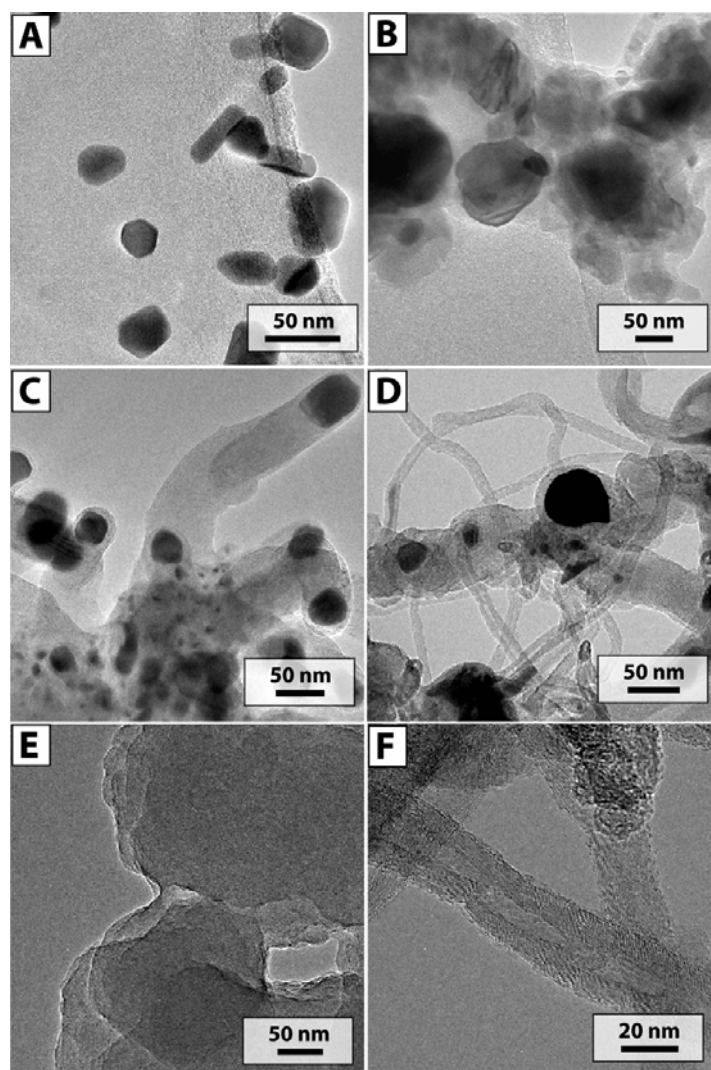
Figure 4.3. HRTEM images of reaction product obtained at (A) 400 °C, (B) 500 °C, (C) 550 °C, (D) 600 °C, and (E) 650 °C. All reactions were conducted at ~12.4 MPa for 15 min with 2.5 mM ferrocene in toluene loaded into the cell. At temperatures lower than 500°C, only Fe particles were produced. At 550 °C, amorphous carbon fibers with Fe particles embedded at their tips were produced. At 600 °C, multiwall carbon nanotubes were produced. At 650 °C, severe toluene degradation results in the production of mostly carbonaceous by-product without MWNTs. (F) shows enlarged images of the nanotubes in (d).

86

4.3.2 EELS Characterization of Nanotubes and Filaments

Figure 4.4 shows electron energy loss spectra of an individual multiwall nanotube compared to spectra obtained from a nanofilament.   In the experiments, a 1 nm diameter electron beam was scanned radially across the nanotube, while simultaneously collecting EELS data as a function of probe position.   These EELS line scans confirm that the structure in Figure 4.4A is a multiwall nanotube and the structure in Figure 4.4B is a nanofilament.   EELS spectra taken in the low loss region exhibit two plasmon peaks corresponding to inelastic electron scattering from collective oscillations (plasmons) of π (~6 eV) and $\pi+\sigma$ (~26 eV) valence electrons.   The key differences in the nanotube and filament spectra appear when the electron beam is positioned at the outer edge of the structures.   For the MWNT, the $\pi+\sigma$ plasmon shifts to significantly lower energy— approximately 18 eV—when the probe is positioned at the nanotube surface.   An additional lower lying sideband at approximately 14 eV also appears in the spectra.   In the nanofilament, the $\pi+\sigma$ plasmon energy does not depend on the probe position. Energy dispersive X-ray spectroscopy (EDS) did not reveal the presence of any impurities, such as iron debris from the catalyst; furthermore, the peak shift is not due to a change in carbon-carbon bonding.   The peak shifting that occurs in the nanotube EELS spectra is the result of the anisotropic symmetry of the π electrons delocalized parallel to the graphene sheets in the nanotube wall.   Due to the plasmon dispersion relation, when the beam is positioned orthogonally incident to a (002) graphite plane, as is the case in the center of the nanotube, the $\pi+\sigma$ plasmon energy is 26.5 eV.   When the beam is positioned at the nanotube edge, the beam is directed parallel to the graphitic sheets, resulting in a lower energy plasmon peak position.   Results from angle-dependent EELS measurements from graphite are well known and our measurements match the expected values for the plasmon energies at both the center (orthogonal to the

(002) plane) and the surface (parallel to the (002) plane) of the nanotubes. The plasmon energy does not shift as a function of probe position in the nanofilament since the graphitic carbon is randomly oriented. The EELS spectra clearly demonstrate that MWNTs were obtained from these reactions.
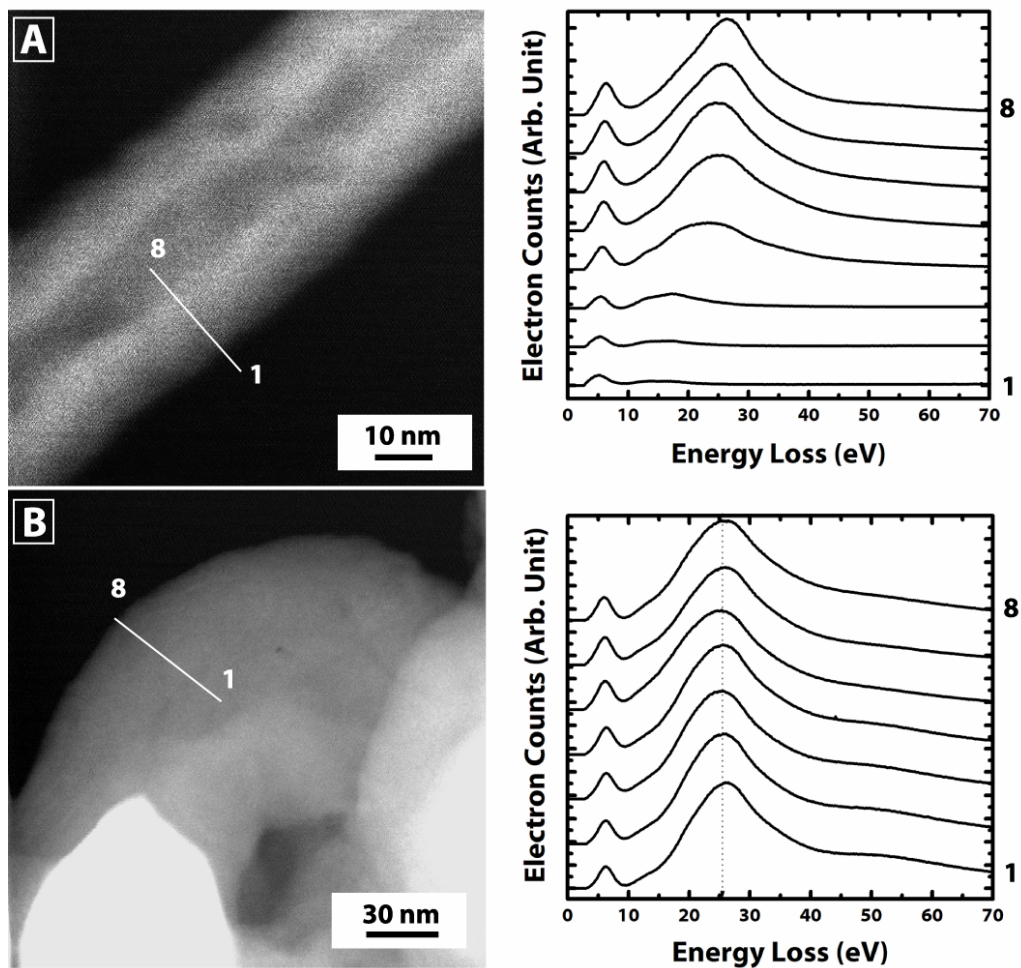
Figure 4.4. Dark-field TEM images and EELS line scans across a (A) multiwall nanotube and a (B) carbon nanofilament. The numbered labels on the spectra correspond to the labeled axial positions in the corresponding TEM image.
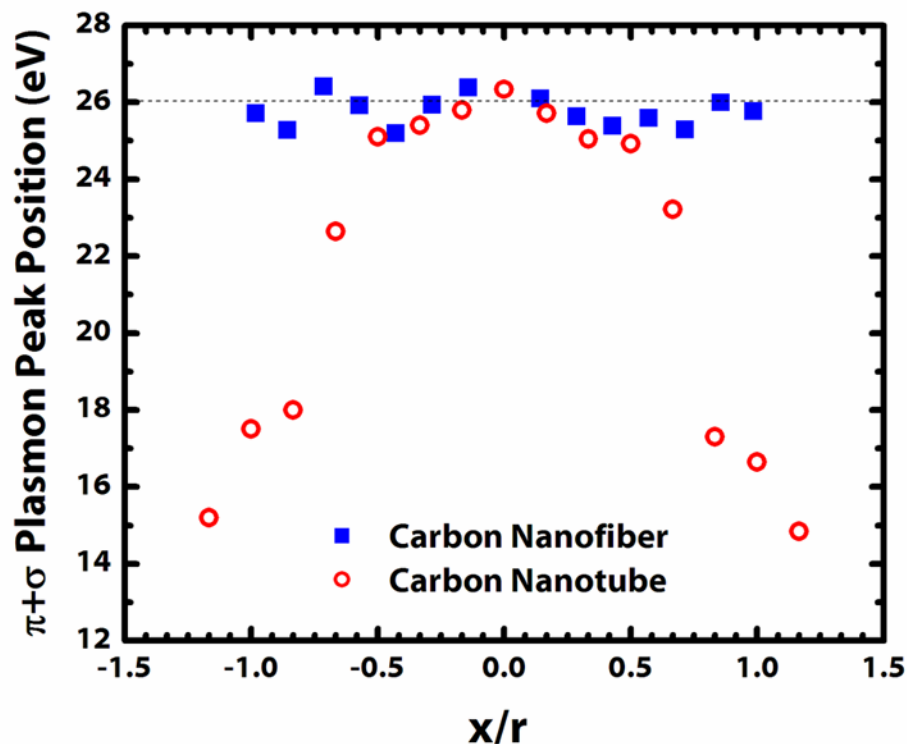
Figure 4.5. Plot of peak positions of the π+σ plasmon peak positions as a function of probe position. The peak position depends upon the way of graphene layer stacking.

4.3.3 Fe and FePt Nanocrystal- Seeded MWNT Formation

MWNTs were also synthesized by direct injection of sterically-stabilized Fe and FePt nanocrystals. The Fe and FePt particles were injected with diameters less than 10 nm, which is significantly less than the 20 to 50 nm diameter Fe particles formed by *in situ* ferrocene degradation. The MWNTs generated using the pre-formed catalyst particles were generally of smaller diameter, reflecting the more stable smaller diameter seed particles; however, the nanotube yield was lower. Figure 4.6 shows high-resolution TEM bright-field images of carbon nanotubes grown using the different catalysts. The smaller MWNTs were typically straighter than the larger tubes, most likely as a result of greater surface stress due to the increased curvature of the graphite

sheets in the nanotube shell. The lower yield could be due to the adsorbed organic passivation layer on the nanocrystals, which initially could potentially inhibit surface-directed nanotube growth. In addition, smaller diameter nanotube formation may simply be less efficient under these low temperature growth conditions. Although smaller nanotubes should form more efficiently at higher reaction temperatures, we could not explore this possibility since the homogeneous solvent degradation at 650 °C and above eliminated nanotube formation; thus, preventing the exploration of a wider range of synthetic temperatures in this system.
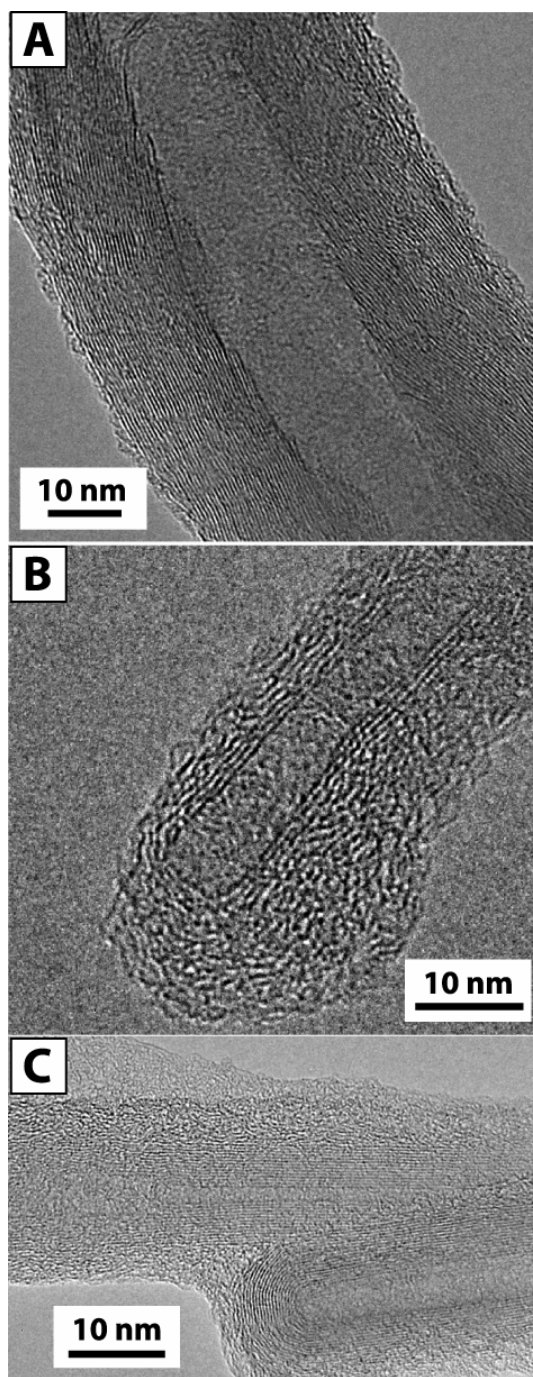
Figure 4.6. MWNTs formed from toluene catalyzed using (a) ferrocene, (b) Fe nanocrystals (9.2 nm diameter), (c) FePt nanocrystals (4 nm diameter). All reactions are carried out at 600°C, ~12.4 MPa, for 15 min. Scale bars are 10nm.

4.3.4 Continuous flow-through reaction

Figure 4.7 shows SEM images of MWNTs synthesized in continuous flow-through reaction at 640 °C using ferrocene, cobaltocene, and nickelocene as catalysts in reactions carried out with water and ethanol. These metallocenes catalyze MWNT formation, with varying degree of yield. In the cobaltocene-catalyzed reactions, ~4% of the toluene fed into the reactor was converted to carbonaceous product, and ~70% of this product was MWNTs. The nanotube production rate and selectivity increased significantly by switching the system from batch reaction to plug-flow reactor.
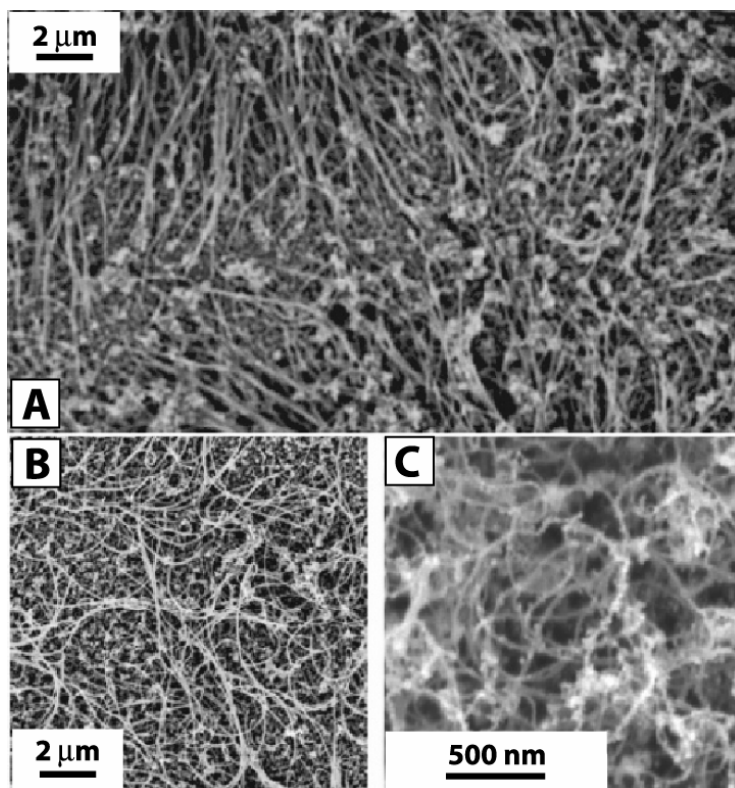
Figure 4.7. SEM images of MWNTs synthesized in supercritical toluene at 640 °C and 8.3 MPa with (a) 26 mM ferrocene, 1.6 mM hexane, and 0.2 mM DI-H_2O; (b) 8.2 mM cobaltocene, 3.7 mM ethanol, and 0.2 mM DI-H_2O; (c) 8.2 mM nickelocene, 3.7 mM ethanol, and 0.2 mM DI-H_2O. The reaction product was imaged on the collection substrate taken from the reactor without further purification. Images courtesy of D. K. Smith.

4.4 DISCUSSION

4.4.1 Growth mechanism of MWNT and carbon nanofilament

Fe catalyst particles were observed at the ends of the nanotubes and the filaments grown using ferrocene injection. Transition metal particle catalyzed carbon filament and nanotube growth has been extensively studied since the 1950's and a few critical steps in the carbon filament formation process are well known: (1) catalytic hydrocarbon decomposition occurs at the particle surface, which results in (2) carbidization of the catalyst, subsequently saturating the particle with carbon giving rise to (3) surface-directed graphitization and nanotube or nanofilament formation. Figure 5 shows a schematic representation of the growth process. Although the mechanistic steps have been identified, many important details about nanotube formation are still not well understood. For example, carbon will alloy with the Fe particle, but may be associated with either the Fe nanoparticle surface or the interior of the particle. And nanotube growth itself has been proposed to occur by either "root growth," in which the nanotube base interfaces directly with the nanoparticle, or a "folded growth mode," in which the carbon shell that forms the nanotube wraps around the nanparticle leading to the curved graphitic layers that extrude from the particle surface. In fact, it appears from extensive data in the literature that both of these mechanisms can occur depending on the synthetic conditions. Information about the growth mechanism in the supercritical solvent can be deduced by examining the particle tips of the nanotubes and filaments.
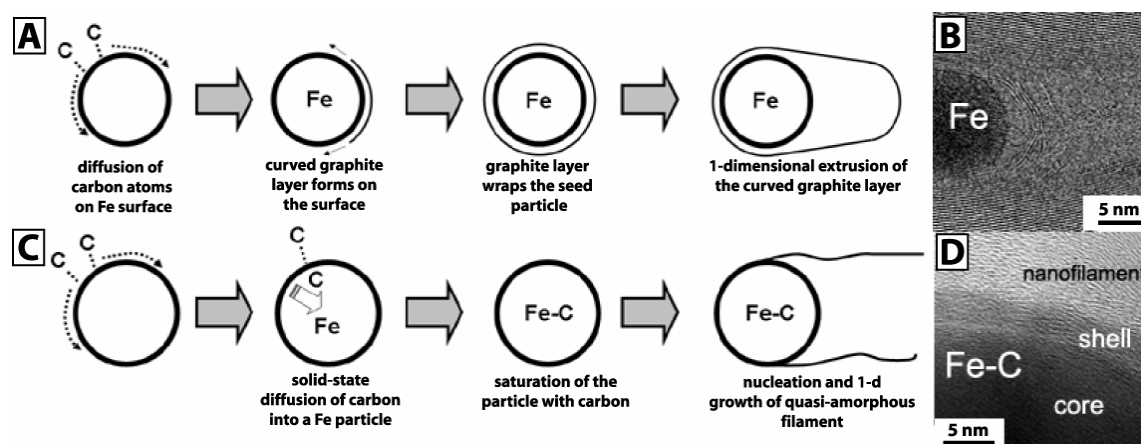
Figure 4.8. Schematic representation of the (A) nanotube and (B) nanofilament growth process.

4.4.2 TEM observation of tip particles of MWNT and carbon filament

Figure 4.9 shows two representative TEM images of the catalyst particles at the end of a MWNT and a carbon filament, along with the fast Fourier transform (FFT) of the image. We observed two primary differences between particles associated with nanotubes and those associated with filaments. First, the particles associated with the nanotubes were smaller (less than 30 nm in diameter); whereas, larger particles were attached to filaments. Second, the seed particle compositions of nanotubes and filaments were different. The particles at the tips of the nanotubes were composed of pure fcc Fe while the particles at the end of the nanofilaments were composed of an Fe-C alloy. Both seed particles are coated with a carbon shell. However, the filament seed particles exhibit a thin Fe-C shell that surrounds the particle core, which appears to be composed of a different Fe-C composition or structure. The Fe seed particle embedded at the tip of the MWNT interfaces directly with the graphitic carbon shell.
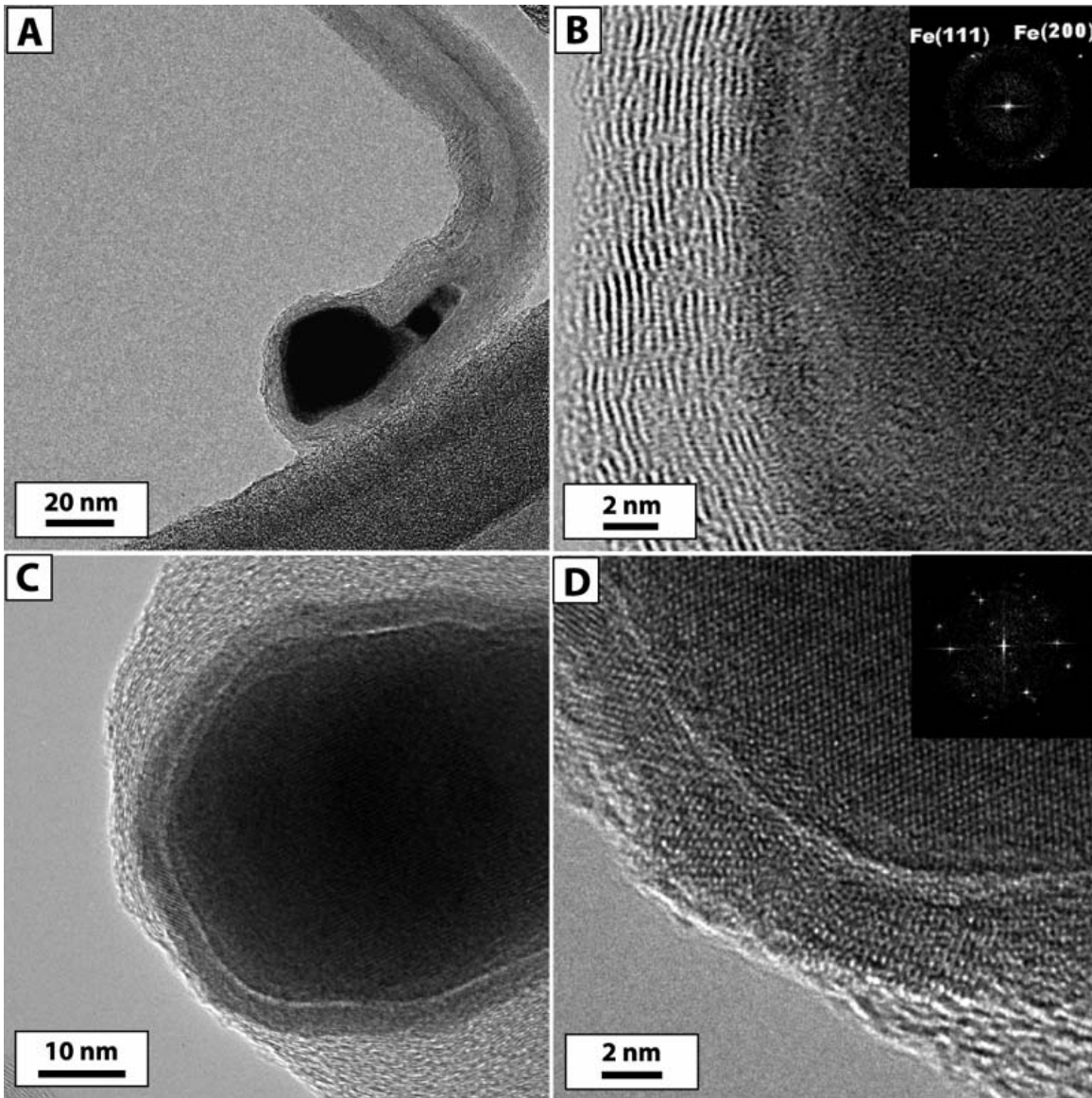
Figure 4.9. HRTEM images of catalyst particles at the tip of a MWNT (A, B), and a carbon filament (C, D), produced at 600 °C, ~12.4 MPa, using ferrocene as the catalyst. The particle at the the nanotube tip is Fe, while the particle in the nanofilament has a core-shell structure with a crystal structure different than pure Fe.   Insets in (b) and (d) show FFTs of the HRTEM images.   FFTs of the Fe-C alloy seeds, as in (d), do not match any Fe or Fe-C alloy crystal structure available from the literature, however the presence of both Fe and C are confirmed by EDS.

Based on TEM observations, it appears that the nanotubes produced in supercritical toluene form by the folded-growth mechanism; whereas, the nanofilaments grow by a VLS-type (vapor-liquid-solid) mechanism. The VLS mechanism has been adopted in the supercritical fluid reactions to produce Si, Ge, and GaAs nanowires using gold nanocrystals to seed growth, a process termed supercritical fluid-liquid-solid (SFLS) growth. The carbon filaments produced in supercritical toluene form by this mechanism, with the exception that the seed particles may be a solid Fe-C alloy instead of a liquid, since the growth temperatures are well below the Fe-C eutectic temperature. However, nanometer-size particles exhibit a melting point depression, which means that a liquid-phase seed particle cannot be entirely ruled out. Regardless, the only requirement from VLS-type growth from nanometer particles is limited solubility of the wire material in the seed. The fact that the graphitic layers in the carbon nanofilament cores form disordered stacks oriented orthogonal to the growth direction further supports the idea that the filaments form at the surface of a metal seed.

In order for *nanotubes* to form, the graphitic layers must be curved by the seed particle. The higher surface curvature of the smaller seed particles presumably adds the needed driving force to induce nanotube formation. Below some critical particle diameter, the relatively strong van der Waals attraction between the condensing graphite sheets and the nanoparticle surface stabilizes the formation of hollow nanotubes. Surface templated graphite sheet formation is clearly evident in the TEM image of the Fe particle at the MWNT tip in Figure 4.9. Figure 4.10 shows additional TEM images of MWNTs that reveal the tube morphology near the seed particle. In the folded-growth mechanism, a graphene cap forms at the particle surface, and the carbon layers extend as additional carbon diffuses through the graphitic shell to reach the Fe-nanotube interface. We did not find evidence of the root-growth mechanism for nanotube formation.
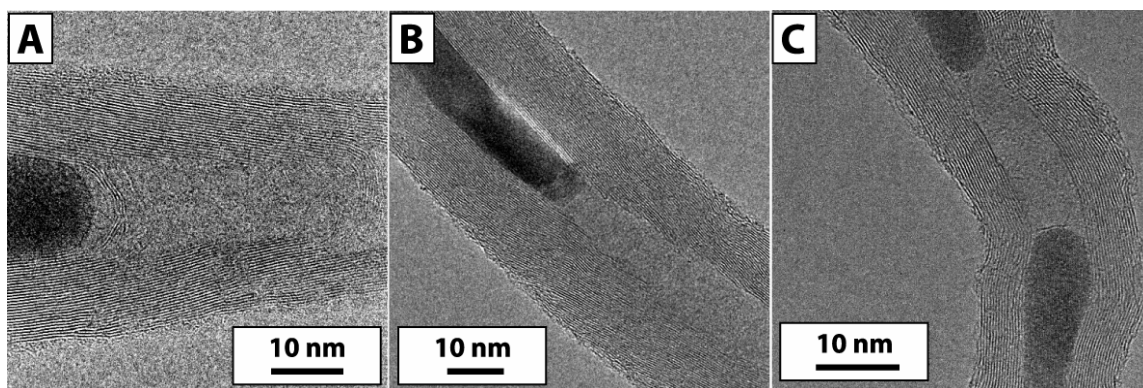
Figure 4.10. HRTEM images of (a) an embryonic MWNT, (b) a fully-grown MWNT, and (c) a MWNT with two Fe particles trapped inside the nanotube.

4.4.3 Effect of seed particle size

The carbon content in the seed particles of different size most likely plays a significant role in determining the nanotube and nanofilament morphology as well. The larger seed particles exhibit higher carbon content, which could favor filament formation due to enhanced wetting between the graphite layers and the seed particle that makes nanotube formation less energetically favorable over filament formation.

Although we certainly tried, we did not produce SWNT under any of the conditions we explored. This does not appear to be a problem related to the seed particle diameter in the reactor, but rather a limitation imposed by the relatively low temperatures available in supercritical toluene. Homogeneous solvent degradation at temperatures much higher than ~625 °C, completely quenches nanotube and nanofilament formation. In the available temperature window <~625 °C, the thermal energy cannot overcome the higher energetic barrier (relative to MWNTs) to surface curvature needed to produce SWNTs. This curvature energy relates the critical radius of the nanotube nucleus that forms on the particle surface. At low temperatures, the critical radius of the nucleus is simply too large to permit SWNT formation. In metal

97

particle-catalyzed CVD, higher reaction temperatures are reached by using methane and CO as precursors, which are relatively stable to homogeneous decomposition, yet degrade catalytically at the particle surface. Other potential supercritical solvents available for nanotube formation that could help limit homogeneous precursor degradation are water and CO_2. These two solvents provide different engineering and safety challenges that must be addressed; however, there is no fundamental reason to believe that the supercritical approach to nanotube formation could not be successful for SWNTs as well as MWNTs.
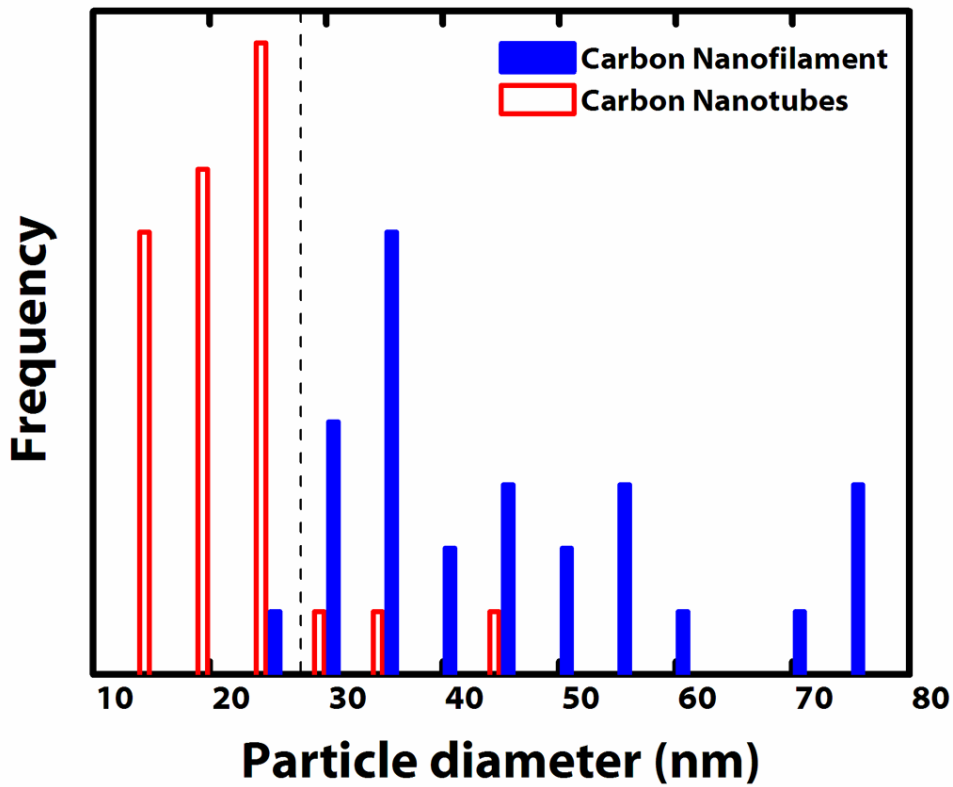
Figure 4.11. Size distribution of the particle size at the tip of carbon nanotubes (filled) and carbon nanofilaments (hollow). Very few MWNTs are observed with metal particles at their tips with diameters larger than 25 nm (dashed line), and no fibers were observed with metal particles at their tips smaller than 23 nm. Data were sampled from images of 60 nanotubes and nanofibers.

98

4.4.4 Scale-up of carbon nanotube synthesis in supercritical fluid

System development from batch to continuous flow-through reaction allows for a significant improvement in the materials production and selectivity. Figure 4.12 contrasts the TGA data of amorphous carbon products and nanotubes. The MWNT purity of the sample was enhanced by far. In batch reactions, the heating rate is relatively slow, and the supply of carbon atoms to catalyst seeds is limited by the rate of the decomposition. Therefore, it is relatively difficult to pin down the reaction conditions that yield good nanotube selectivity. In flow-through reactions, parameters, such as flow-rate, temperature, and injection solution concentration, could come into play, and the carbon decomposition becomes more controllable.
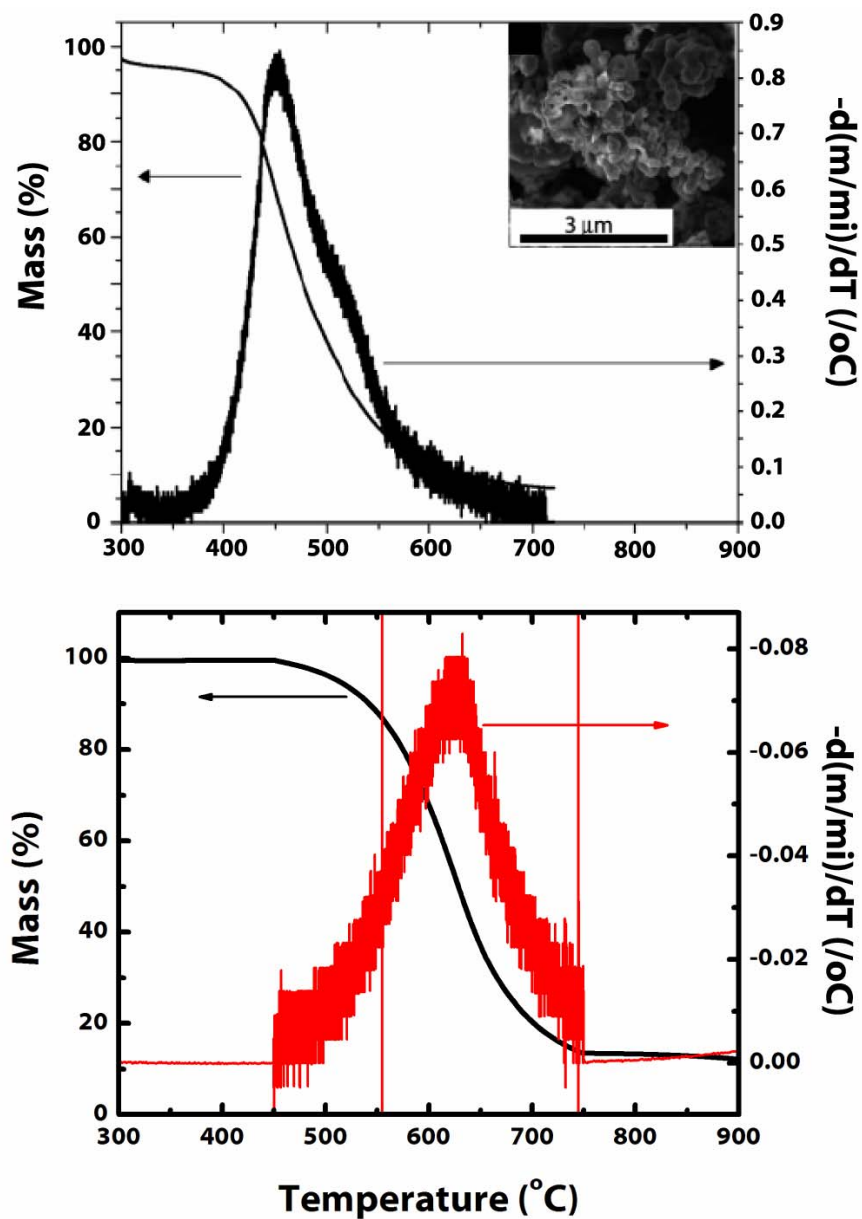
Figure 4.12. TGA of (top) amorphous carbon and (bottom) MWNTs produced from supercritical fluid toluene reactions. (top; inset) SEM images of the analyzed products.   The samples were scanned at 1 °C/min.   The quantity m/m_i is the mass fraction of the sample remaining.   The absence of significant thermal decomposition below ~500 °C in the bottom panel indicates that the sample is primarily MWNTs.

4.5 CONCLUSIONS

Carbon MWNTs and nanofilaments can be produced in supercritical toluene using either the molecular additive, ferrocene, or prefabricated sterically-stabilized nanocrystals of Fe or FePt, to catalyze their growth. The carbon nanostructure morphology depends on the reaction temperature and the seed particle size. The temperature must be sufficiently high for (1) significant hydrocarbon decomposition, which occurs *heterogeneously* at the particle surfaces at temperatures exceeding at least 500 °C for toluene, and (2) carbon graphitization at the metal seed particle surface, which requires temperatures greater than ~550 °C. At temperatures much exceeding ~625 °C, homogeneous solvent decomposition spoils nanotube growth. Smaller seed particles (<~30 nm diameter) promote MWNT formation, while larger particles produce nanofilaments with disorderd graphitic cores.

The supercritical fluid approach to carbon nanotube synthesis has the potential for much higher throughput relative to the heterogeneous gas-phase approaches. However, the quality of the nanotubes currently does not match that of nanotubes produced in the vapor-phase. There are many scientific and engineering considerations in process optimization, including reactor design, as well as optimization of catalyst and precursor reactivity. In comparison to the vapor-phase process, which has been studied and optimized by many researchers over the past 10 years, little effort has been spent developing wet nanotube synthesis. One currently open question in the supercritical fluid approach relates to single wall nanotube growth. Considering that SWNTs are known to require more energy to form than MWNTs, the use of thermally stable alternative supercritical solvents, *e.g.* supercritical CO_2, could improve the quality of nanotubes, eventually leading to SWNT formation. The use of these kinds of

supercritical solvents could also improve MWNT yield by limiting homogeneous solvent

decomposition and catalyst poisoning at higher temperature.

4.6 REFERENCES

(1)   Dresselhaus, M. S.; Dresselhaus, G.; Avouris, P., *Carbon Nanotubes : Synthesis, Structure, Properties, and Applications*. Springer: New York, 2002.

(2)   Gogotsi, Y.; Libera, J. A.; Yoshimura, M., *J. Mater. Res.* **2000,** 15, 2591.

(3)   Libera, J.; Gogotsi, Y., *Carbon* **2001,** 39, 1307.

(4)   Shao, M.; Li, Q.; Wu, J.; Xie, B.; Zhang, S.; Qian, Y., *Carbon* **2000,** 40, 2961.

(5)   Ebbesen, T. W.; Ajayan, P. M., *Nature* **1992,** 358, 220.

(6)   Thess, A.; Lee, R.; Nikolaev, P.; Dai, H.; Petit, P.; Robert, J.; Xu, C. H.; Lee, Y. H.; Kim, S. G.; Rinzler, A. G.; Colbert, D. T.; Scuseria, G. E.; Tomanek, D.; Fischer, J. E.; Smalley, R. E., *Science* **1996,** 273, 483.

(7)   Ren, Z. F.; Huang, Z. P.; Xu, J. W.; Wang, J. H.; Bush, P.; Siegal, M. P.; Provencio, P. N., *Science* **1998,** 282, 1105.

(8)   Dai, H. J.; Kong, J.; Zhou, C. W.; Franklin, N.; Tombler, T.; Cassell, A.; Fan, S. S.; Chapline, M., *J. Phys. Chem. B* **1999,** 103, 11246.

(9)   Delzeit, L.; Nguyen, C. V.; Chen, B.; Stevens, R.; Cassell, A.; Han, J.; Meyyappan, M., *J. Phys. Chem. B* **2002,** 106, 5629.

(10)   Hofmann, S.; Ducati, C.; Robertson, J.; Kleinsorge, B., *Appl. Phys. Lett.* **2003,** 83, 135.

(11)   Hofer, L. J. E.; Sterling, E.; McCarthy, J. T., *J. Phys. Chem.* **1955,** 59, 1153.

(12)   Nikolaev, P.; Bronikowski, M. J.; Bradley, R. K.; Rohmund, F.; Colbert, D. T.; Smith, K. A.; Smalley, R. E., *Chem. Phys. Lett* **1999,** 313, 91.

(13)   Bronikowski, M. J.; Willis, P. A.; Colbert, D. T.; Smith, K. A.; Smalley, R. E., *J. Vac. Sci. Technol. A* **2001,** 19, 1800.

(14)   Andrews, R.; Jacques, D.; Qian, D. L.; Rantell, T., *Acc. Chem. Res.* **2002,** 35, 1008.

(15)   Gogotsi, Y. G.; Yoshimura, M., *Nature* **1994,** 367, 628.

(16)   Hubert, H.; Garvie, L. A. J.; Devouard, B.; Buseck, P. R.; Petuskey, W. T.; McMillan, P. F., *Chem. Mater.* **1998,** 10, 1530.

(17)   Barns, R. L.; Freeland, P. E.; Kolb, E. D.; Laudise, R. A.; Patel, J. R., *J. Cryst. Growth* **1978,** 43, 676.

(18)   Watkins, J. J.; Blackburn, J. M.; McCarthy, T. J., *Chem. Mater.* **1999,** 11, 213.

(19)   Ziegler, K. J.; Doty, R. C.; Johnston, K. P.; Korgel, B. A., *J. Am. Chem. Soc.* **2001,** 123, 7797.

(20)   Holmes, J. D.; Johnston, K. P.; Doty, R. C.; Korgel, B. A., *Science* **2000,** 287, 1471.

(21)   Holmes, J. D.; Ziegler, K. J.; Doty, R. C.; Pell, L. E.; Johnston, K. P.; Korgel, B. A., *J. Am. Chem. Soc.* **2001,** 123, 3743.

(22)   Hanrath, T.; Korgel, B. A., *J. Am. Chem. Soc.* **2002,** 124, 1424.

(23)   Hanrath, T.; Korgel, B. A., *Adv. Mater.* **2003,** 15, 437.

(24)   Lu, X. M.; Hanrath, T.; Johnston, K. P.; Korgel, B. A., *Nano Letters* **2003,** 3, 93.

(25)   Lee, D. C.; Hanrath, T.; Korgel, B. A., *Angew. Chem. Int. Ed.* **2005,** 44, 3573.

(26)   Davidson, F. M.; Schricker, A. D.; Wiacek, R.; Korgel, B. A., *Adv. Mater.* **2004,** 16, 646.

(27)   Hyeon, T.; Lee, S. S.; Park, J.; Chung, Y.; Bin Na, H., *J. Am. Chem. Soc.* **2001,** 123, 12798.

(28)   Sun, S. H.; Murray, C. B.; Weller, D.; Folks, L.; Moser, A., *Science* **2000,** 287, 1989.

(29)   Yaws, C. L., *Handbook of Thermodynamic Diagrams*. Gulf Publishing Company: Houston, Texas, 1996; p 294.

(30)   Burian, A.; Dore, J. C.; Fischer, H. E.; Sloan, J., *Phys. Rev. B* **1999,** 59, 1665.

(31)   Zeppenfeld, K., *Z. Phys.* **1968,** 211, 391.

(32)   Kim, N. S.; Lee, Y. T.; Park, J.; Han, J. B.; Choi, Y. S.; Choi, S. Y.; Choo, J. B.; Lee, G. H., *J. Phys. Chem. B* **2003,** 107, 9249.

(33)   Dai, H.; Rinzler, A. G.; Nikolaev, P.; Thess, A.; Colbert, D. T.; Smalley, R. E., *Chem. Phys. Lett* **1996,** 260, 471.

(34)   Evans, E. L.; Thomas, J. M.; Thrower, P. A.; Walker, P. L., *Carbon* **1973,** 11, **441**.

(35)   Bower, C.; Zhou, O.; Zhu, W.; Werder, D. J.; Jin, S., *Appl. Phys. Lett.* **2000,** 77, 2767.

(36)   Louchev, O. A.; Hester, J. R., *J. Appl. Phys.* **2003,** 94, 2002.

(37)   Kuznetsov, V. L.; Usoltseva, A. N.; Chuvilin, A. L.; Obraztsova, E. D.; Bonard, J. M., *Phys. Rev. B* **2001,** 64, 235401.

Chapter 5: Controlled Synthesis of Colloidal Nanocrystals and Study of Morphology Change under High-Temperature Annealing

5.1 INTRODUCTION

A successful colloidal synthesis produces crystalline nanomaterials with controlled size and shape, composition and crystal phase with a narrow size distribution. The nanomaterials must be dispersible in solvents and stable during subsequent processing steps. Ideally, nanocrystal surfaces should be protected from unwanted surface reactions like oxidation that degrade the materials properties. Arrested precipitation is a powerful synthetic technique for making high quality nanomaterials. Molecular reactants are decomposed to a crystalline solid in a solvent in the presence of organic ligands that bond to the surface of the crystals to control their size. For example, CdS nanocrystals can be formed in water at room temperature by combining solutions of cadmium (Cd^{2+}) and sulfide (S^{2-}) salts in the presence of a capping ligand like mercaptoacetic acid (MAA). The thiol adsorbs strongly to the CdS surface and limits the nanocrystal size to a few nanometers by providing steric and electrostatic barriers to aggregation. Another example of arrested precipitation is the synthesis of gold (Au) nanocrystals at room temperature using dodecanethiol as a capping ligand. The thiol bonds to the Au surface to form a monolayer of C_{12} hydrocarbon that sterically stabilizes the particles and provides dispersibility in organic solvents.

Au, Ag, CdS, CdSe and a few other nanocrystal materials can be made at room temperature, but elevated temperatures are generally required for most reactions. One of the most significant aspects of "modern" colloid chemistry has been the use of relatively high synthesis temperatures, *e.g.*, between 250~350 °C, to grow nanocrystals with well-

controlled size and shape. The crystallinity and number of dangling bonds at the particle surface is typically improved with elevated synthesis temperature, which gives better materials properties, such as the photoluminescence efficiency of semiconductor nanocrystals. Higher reaction temperatures make available a wide range of materials chemistry, such as thermal decomposition and reduction reactions of organometallic reactants, which has been particularly useful in the case of magnetic nanocrystal synthesis.

A wide variety of magnetic nanocrystals, including γ-Fe_2O_3, Co, FePt, $CoPt_3$, $CoFe_2O_4$, and $MnFe_2O_4$, have been synthesized in the hot-temperature solution using organometallic reactants as starting materials and these syntheses can be scaled to ultra-large quantities ($\sim$g) in some cases while still maintaining tight size control. Nanocrystal size tuning requires a detailed understanding of the organometallic decomposition chemistry at the reaction temperature. The nanocrystal composition is also influenced by precursor decomposition and nanocrystal growth kinetics. The synthesis of Mn-doped InAs nanocrystals revealed that subtle changes to the Mn precursor chemistry led to rather dramatic changes in nanocrystal quality and doping concentration. Nanocrystal synthesis requires the appropriate choice of reaction parameters, such as precursors, reaction solvent, and stabilizing agents.

Nanocrystals of MPt (M = transition metal; Fe or Co) materials have been the focus of recent synthetic interest because of their high magnetocrystalline anisotropy and potential application as nanoscale magnetic memory storage elements. For example, $L1_0$ FePt has high magnetocrystalline anisotropy (K_u), saturation magnetization and maximum energy product (($BH)_{max}$) (6.6×10^7 erg/cm^3 ($\sim$60 meV/nm^3), 1140 emu/cm^3 and 13 MGOe, respectively). $L1_0$ FePt domains as small as 3 nm in diameter could be used as memory bits—their magnetic anisotropy energy (K_uV) would exceed kT (at room

temperature) by about a factor of 25.   1 Tb/in^2 storage density could be achieved using 3 nm diameter FePt domains as individual bits in a monolayer with an edge-to-edge separation of about 25 nm. The detection sensitivity required to read the magnetic information stored on each bit is well beyond the current detection sensitivity of magnetic read heads; but nevertheless, such a magnetic storage media should be possible to construct with nanocrystals of this material. The so-called superparamagnetic limit can be pushed to smaller particle size by using materials with very high magnetocrystalline anisotropy with K_u of the order $\sim 10^6$ J/m^3.

The MPt (M=Co, Ni, or Fe) nanomaterials have also been relatively easy to synthesize in high boiling solvents with good size control, which has stimulated more interest.   For magnetic nanocrystals to be of use for magnetic storage, their magnetocrystalline anisotropy must be sufficient to enable a high maximum energy product at room temperature.   The colloidal syntheses tend to produce nanocrystals with very good size control, but the crystalline cores of the MPt materials tend to be compositionally disordered, with weak magnetic properties.   The nanocrystals therefore generally require high temperature annealing to convert their crystal structure to the compositionally ordered phases that exhibit hard magnetic properties.   In this chapter, the colloidal synthesis of PbSe and Mn-Pt nanocrystals is demonstrated.   PbSe shows interesting nanocrystal growth, in a sense that the shape changes drastically as the surface capping ligands change.   The annealing of the nanocrystals and nanowires revealed interesting fusing properties.   In Mn-Pt alloy, the Mn-Mn separation essentially determines the magnetic properties of the material.   The as-made nanocrystals are chemically disordered, with Mn and Pt atoms in an fcc unit cell.   By annealing films of the nanocrystals at 580 °C, the nanocrystals undergo an internal phase change from A1 to L1$_2$; thus, improving the magnetic properties of the materials.   The sintering of the

106

nanocrystals during the annealing will be discussed, and in Chapter 8, silica-coating will be introduced to prevent the sintering of the particles.

5.2 EXPERIMENTAL SECTION

Figure 5.1 schematically shows the setup for colloidal synthesis. The reactants, solvent, capping ligands, reaction temperature, reaction time, and even how the reactants are combined, collectively influence the size and shape of the nanocrystals. It is important to understand that capping ligands that work well for one material may not work at all for another material, even participating in the reaction and becoming part of the nanocrystal reaction product. The reactants of course play a crucial role in determining the shape and size of the final product. Different combinations of the reaction parameters were introduced to grow nanostructures of different materials.
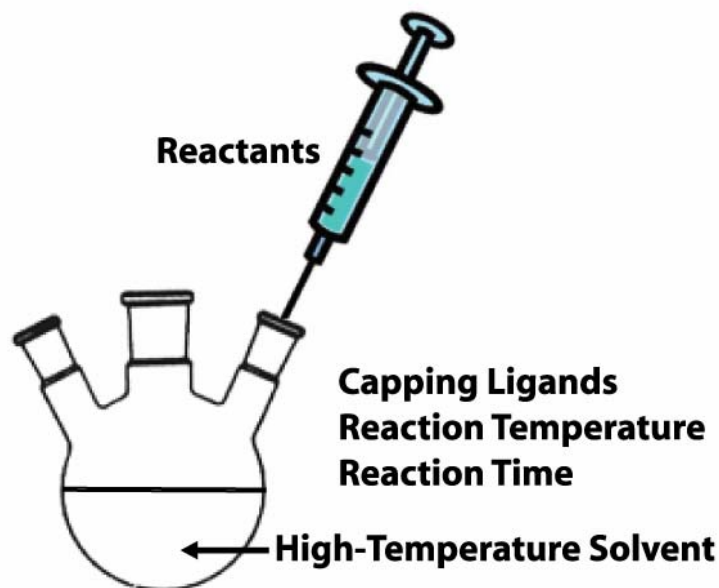
Figure 5.1. Schematic of colloidal nanomaterials synthesis. Normally, a 3-neck flask is under inert conditions during the synthesis.

5.2.1 Synthesis of PbSe Nanocrystals and Nanowires

PbSe nanocrystals and nanowires were synthesized via previously reported methods. For nanocrystal synthesis, 0.54 g of lead acetate trihydrate ($Pb(CH_3COO)_2 \cdot 3H_2O$, Fisher) and 1.83 mL of oleic acid ($CH_3(CH_2)_7CH=CH(CH_2)_7COOH$, Aldrich) were dissolved in 10 mL phenyl ether (Fluka), and heated to 100 °C under vacuum for 1 hr. Then the solution was heated to 180 °C under nitrogen. 0.35 g Se powder (Strem) in 4.5 mL trioctylphosphine (TOP, Aldrich) was injected to the solution under vigorous stirring. The reaction mixture was cooled to 155 °C upon injection, and was kept at 151-157 °C for 5 minutes. The reaction was then allowed to cool to room temperature. 10 mL of ethanol was added to the crude solution and the mixture was centrifuged at 8000 rpm for 10 min. Solid precipitate was collected in hexane and washed with ethanol. The final product was stored in chloroform. For nanowire synthesis, 0.76 g of lead acetate trihydrate and 2 mL of oleic acid were dissolved in 10 mL of phenyl ether. Heating the mixture to 150 °C for 30 min under a nitrogen flow led to the formation of Pb-oleate complex. After cooling to 60 °C, the lead oleate solution was mixed with 4 mL of 0.167 M TOP-Se solution in TOP and injected under vigorous stirring into a 250 °C solution containing 0.2 g of tetradecylphosphonic acid dissolved in 15 mL phenyl ether. The injection initiated the temperature drop and after ~50 s of heating at ~200 °C, the reaction mixture was cooled to room temperature using an ice-water bath. The solution was then mixed with hexane and centrifuged at 8500 rpm for 10 min. The precipitated nanowires were redispersed in chloroform and washed with ethanol again.

5.2.2 FePt Nanocrystal Synthesis

FePt nanocrystals were made by the high temperature reduction of a platinum (Pt) precursor and thermal decomposition of an iron (Fe) source in the presence of capping

ligands.   At room temperature, 197 mg of platinum acetylacetonate (Aldrich) was mixed with 390 mg of 1,2-hexadecanediol (Aldrich) in 20 mL dioctylether (Fluka) in a three-neck flask.   The mixture was agitated at room temperature while flushing with nitrogen for ~20 min.   The mixture was then heated to 100 ºC, at which point 1.0 mmol iron pentacarbonyl (Aldrich), 0.75 mL oleic acid (Fluka), and 0.75 mL oleylamine (Aldrich) were injected, and the resulting mixture continued to be heated to the refluxing temperature of dioctylether.   The reaction mixture was held at the refluxing temperature for 30 min, and was allowed to cool to room temperature by removing the heating element.   The solution was collected and centrifuged at 8000 rpm for 10 min.   Poorly capped particles and very large nanocrystals formed a precipitate that was discarded. The supernatant was then mixed with 20 mL of ethanol to precipitate the FePt nanocrystals and separate them from organic molecular byproducts.   The nanocrystals were collected as a precipitate after another centrifugation at 8000 rpm for 10 min.   For the MFM studies and magnetic measurements, the nanocrystals were precipitated one more time from chloroform using ethanol as the antisolvent to obtain a clean sample with minimal organic byproducts and free capping ligands.   The nanocrystals redisperse in a variety of organic solvents, including chloroform, toluene and hexane.

5.2.3 MnPt$_3$ Nanocrystal Synthesis

5.2.3.1 Synthesis using Mn$_2$(CO)$_{10}$ as the Mn source

0.5 mmol of Pt(acac)$_2$ and 2.5 mmol of 1,2-hexadecanediol (Aldrich) were added to 20mL of dioctylether (Fluka).   The mixture was stirred and purged with nitrogen at room temperature for 30 min.   The solution became cloudy at this point.   The solution was then heated to 100°C.   Upon heating, the Pt precursor becomes reduced and the solution becomes optically clear.   At 100°C, a solution of   0.5 mmol Mn$_2$(CO)$_{10}$ in 12

mL dioctylether was injected into the reaction flask, followed by the injection of 4 mmol oleic acid (Aldirch) and 4 mmol oleylamine (Aldrich). The reaction mixture was heated to reflux at about 297 °C. During heating, the solution turned black at ~170 °C, indicating the onset of nanoparticle growth. At the heating rate of 5 °C/min, the initially Pt-rich nuclei absorb Mn atoms to form Mn-Pt alloy nanocrystals that ultimately acquire an equilibrium composition after aging for 30 min at the reflux temperature. After 30 min at the reflux temperature, the heating element was removed from the flask and the solution was allowed to cool to room temperature.

5.2.3.2 Synthesis using Mn(acac)₂ as the Mn source

0.5 mmol of $Pt(acac)_2$ and 0.5 mmol of $Mn(acac)_2$ were added to a solution of 1 mmol 1,2-hexadecandiol in 10 mL dioctylether . The mixture was heated to reflux at 297 °C and then stirred for 30 min. The heating mantle was then removed from the flask and the solution was allowed to cool to room temperature.

The nanocrystals were isolated by precipitation with 10 mL of ethanol added to the reaction flask. The mixture was centrifuged and the supernatant was discarded. This precipitate is enriched with Mn-rich clusters. More Mn nanocrystals were produced when $Mn_2(CO)_{10}$ was used as the Mn source compared to $Mn(acac)_2$. Excess ethanol (~60 mL) was added and the mixture was centrifuged at 8000 rpm for 10 minutes to collect the nanocrystals. The precipitate was reprecipitated one more time prior to characterization.

5.2.4 Characterization

The nanocrystals and nanowires were characterized by TEM, XRD and magnetization measurements. Samples were prepared for TEM by drop casting from chloroform onto carbon-coated Cu TEM grids (200-mesh, LADD science). TEM

images were acquired at an accelerating voltage of 200 kV using a JEOL 2010F equipped with an energy dispersive x-ray spectrometer (EDS, Gatan).

Nanocrystals and nanowires were annealed in a furnace under nitrogen flow. The heating rate was as high as ~25°C/min.   The magnetic properties of the nanocrystals were measured using superconducting quantum interference device (SQUID, Quantum Design, Inc.) magnetometer.   XRD was performed using a Bruker-Nonius D8 Advance Theta-2Theta powder diffractometer with Cu K_{α} radiation (λ=1.54 Å).   Samples were prepared for XRD by drop casting a concentrated dispersion of nanocrystals onto a quartz substrate to give a film ~200 μm thick.   XRD scans were acquired at 12 deg/min with the sample rotated at 15 deg/min per angle increment (0.02 deg).   Diffraction patterns were collected for ~10 hrs.

5.3 RESULTS AND DISCUSSION

5.3.1 Synthesis of Nanocrystals and Nanowires of Different Materials

Figure 5.2 shows TEM images of PbSe nanocrystals with the diameter of ~6 nm. When the temperature of the reaction system is well maintained, the nanocrystal size is very uniform, and the passivation of the particles with organic capping ligands leads to high solubility in non-polar solvents and consequently good ordering in the film.   The nanocrystals exhibit high crystallinity as shown in Figure 5.2B, with few defects detectible.   In the synthesis of the nanocrystals, solvent and heating rate could play an important role in determining size distribution.   When the nanocrystals were synthesized in another non-coordinating solvent, such as squalane, the size distribution was relatively poor.   The poor size uniformity was attributed to the heating rate of the solution during

111

heating; nucleation and growth of the nanocrystals could be a sensitive function of the ramping rate.
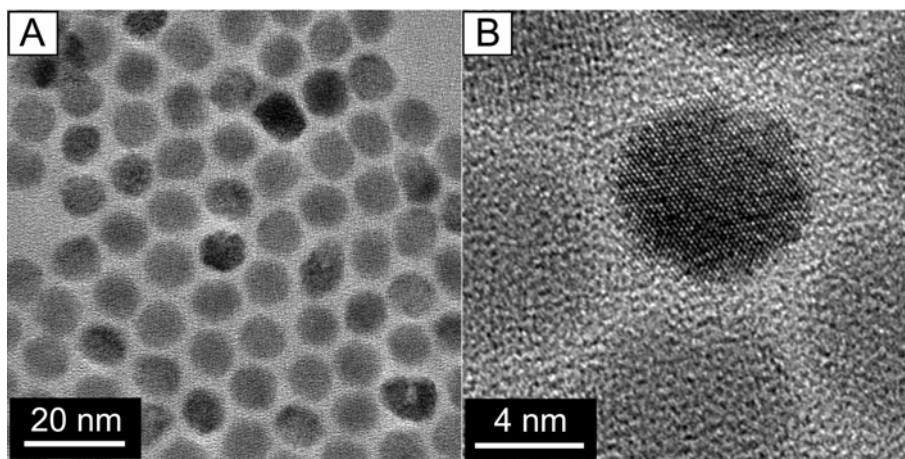
Figure 5.2. TEM images of PbSe nanocrystals.

Oriented attachment is another mechanism of nanorod and nanowire formation that has been demonstrated to work for a variety of different materials, including nanowires of Ag, CdTe, and ZnS. In the oriented attachment mechanism, particles aggregate with specific crystallographic orientation and fuse into single crystal nanorods and nanowires. This method has turned out to be surprisingly robust and applicable to a variety of different materials, such as PbSe. PbSe nanocrystals in different shapes are shown in Figure 5.3. Capping ligands play an important role in determining the degree of nanowire growth in the oriented attachment process. TEM results have revealed that the anisotropic growth originates from the fusion of the particles in an anisotropic fashion.
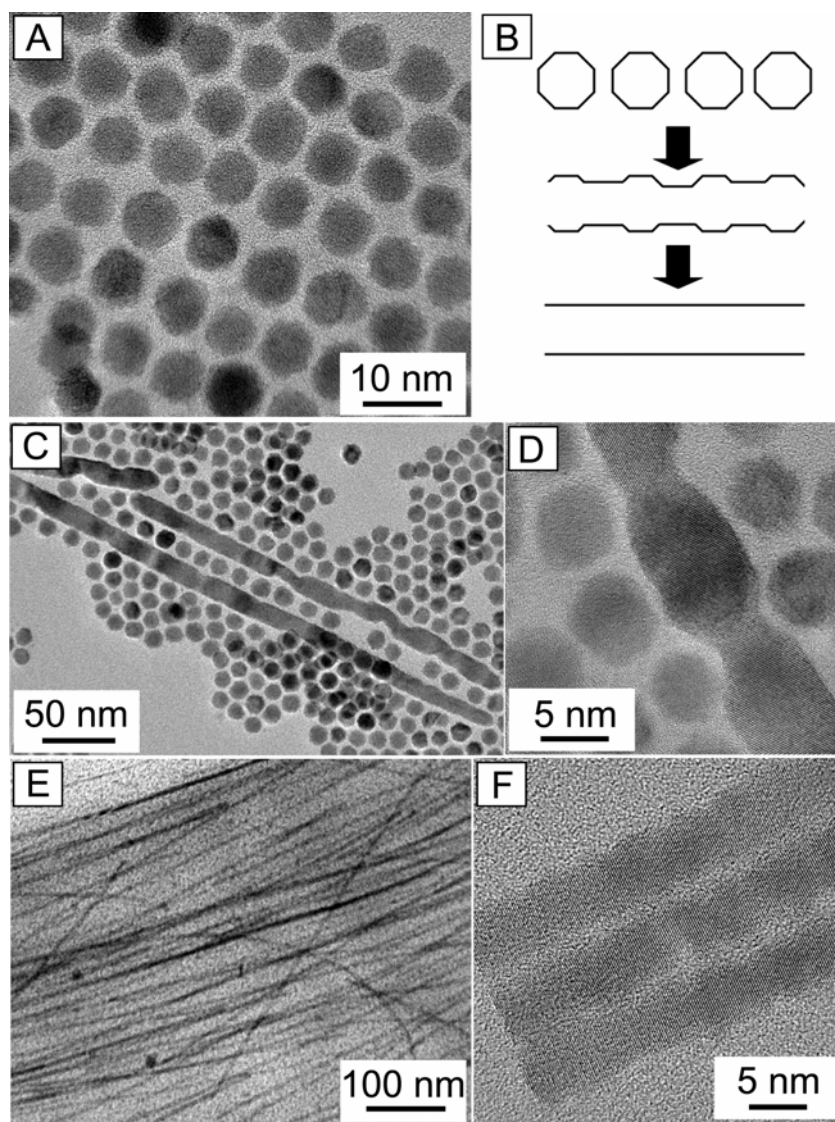
Figure 5.3. (A) TEM image of PbSe nanocrystals synthesized from Pb-oleate and TOP-Se at 180 °C and letting the mixture react at 160 °C for 5 min. (B) Illustration of PbSe nanowire evolution from nanocrystals. (C-D) TEM images of PbSe nanocrystals and nanowires. Pb-oleate complex and TOP-Se solution was mixed at 60 °C and injected to 250 °C hexadecylamine(HDA)-phenyl ether solution. The reaction was continued at 180 °C. The nanowires with rugged surface are seen, and it appears that the nanowires are formed through the oriented attachment as depicted in (B). (E-F) TEM images of PbSe nanowires. Pb-oleate complex and TOP-Se solution was mixed at 60 °C and injected to 250 °C TDPA-phenyl ether solution. The reaction was continued at 180 °C for 1 min. The surface appears to be smooth as shown in the bottom part of (B).

113

5.3.2 Effect of Mn Precursor on MnPt₃ Nanocrystal Size

Figure 5.4 shows TEM images of Fe_2O_3, FePt, and CoPt nanocrystals synthesized via previously reported colloidal techniques. Relatively high monodispersity was acquired after one or no size-selective precipitation process.
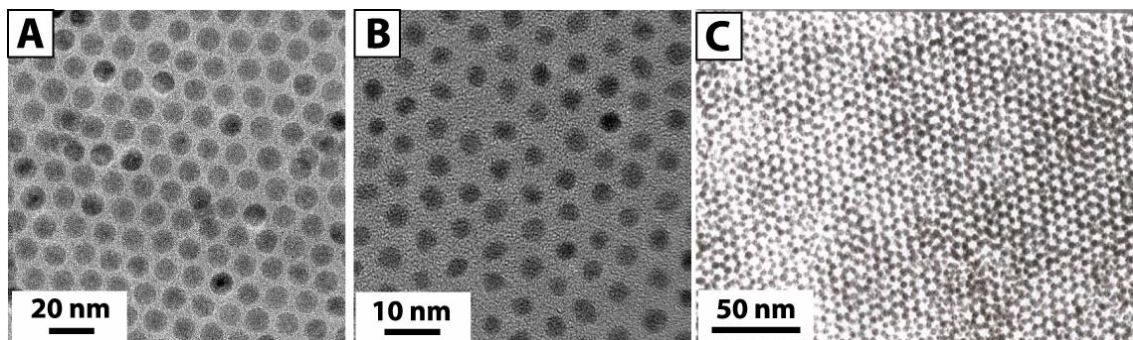
Figure 5.4. TEM images of (A) Fe_2O_3, (B) FePt, and (C) CoPt nanocrystals.

Figure 5.5 shows Mn-Pt nanocrystals obtained from reactions with $Pt(acac)_2$ and either $Mn_2(CO)_{10}$ or $Mn(acac)_2$ as the Mn source. EDS mapping of individual particles, as well as from fields of particles, revealed that the particles have an Mn:Pt ratio of 1:3, regardless of which Mn precursor was used. The average diameter of the $MnPt_3$ nanocrystals depended on the Mn reactant used. $Mn_2(CO)_{10}$ gave larger nanocrystals, approximately 5 nm in diameter, and $Mn(acac)_2$ gave smaller nanocrystals approximately 2 nm in diameter. The size difference appears to originate from the difference in decomposition rates of the two reactants. It was found that nanocrystal reactions proceeded faster with $Mn_2(CO)_{10}$ than $Mn(acac)_2$, presumably due to its higher decomposition rate.

Under all reaction conditions explored, the Mn-Pt composition of the nanocrystals was found to be $MnPt_3$. Other intermetallic phases such as MnPt were never obtained, regardless of how the Mn precursors were added to the reaction (*e.g.*, Mn first followed

by Pt). MnPt$_3$ nanocrystals were still obtained when the Mn reactant was added in excess, but with the addition of pure Mn nanocrystals larger than 10 nm in diameter. The more Mn reactant added, the more Mn particles that were formed, and it was impossible to incorporate additional Mn into the nanocrystals.
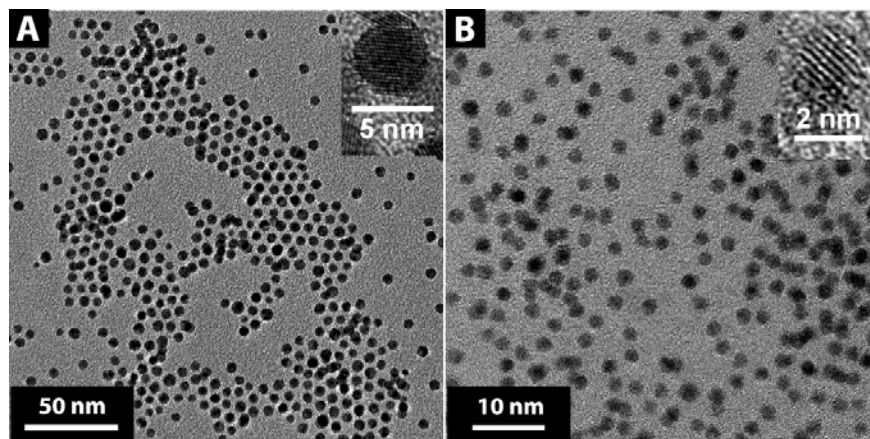
Figure 5.5. TEM images of MnPt$_3$ nanocrystals synthesized by Pt(acac)$_2$ reduction using 1,2-hexadecanediol and decomposition of (A) Mn$_2$(CO)$_{10}$ and (B) Mn(acac)$_2$ in octylether at 300 °C.

Figure 5.6 shows a TEM image of a sample obtained from the reaction with Mn$_2$(CO)$_{10}$ as a Mn source. Although most of the TEM grid was covered with nanocrystals separated by at least a few nanometers, some of the MnPt$_3$ particles form pairs with a shared crystallographic orientation with their <111> direction of the MnPt$_3$ unit cell perpendicular to their shared interface. It is unclear what the pairing mechanism is; however, perhaps the different Pt atom population on {111} facets leads to oriented attachment.
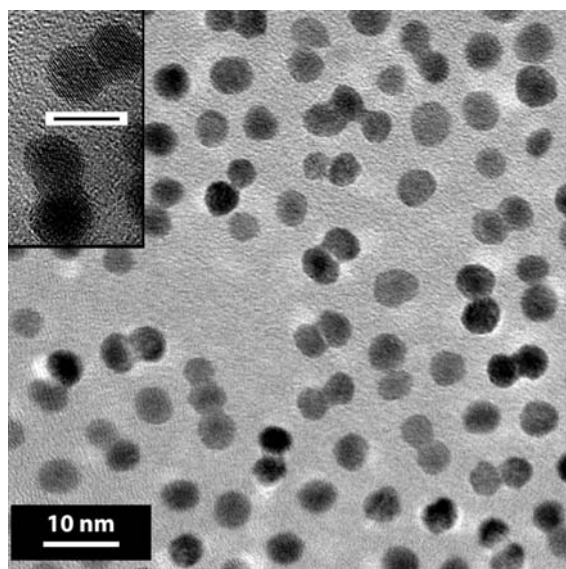
Figure 5.6. TEM image of MnPt$_3$ nanocrystals synthesized with Pt(acac)$_2$ and Mn$_2$(CO)$_{10}$. The TEM sample was prepared by drop-casting a hexane dispersion of MnPt$_3$ nanocrystals. Several nanocrystals are paired along the <111> direction of the MnPt$_3$ unit cell. The scale bar in the inset is 5 nm.

5.3.3 Composition Stability of MnPt$_3$ Nanocrystals

Figure 5.7 shows TEM images of nanocrystals synthesized with both Mn$_2$(CO)$_{10}$ and Mn(acac)$_2$ before and after size-selective precipitation. Both Mn reactants yielded large (>10 nm diameter) Mn particles when the reaction stoichiometry was greater than 1:3 Mn:Pt (i.e., excess Mn). Since the Mn particles are much larger than the MnPt$_3$ nanocrystals, size-selective precipitation easily removes these particles to give a pure MnPt$_3$ product. Figure 5.8 shows the EDS data showing that Mn:Pt ratio was kept at 1:3 (Figure 5.8A), while increasing the Mn$_2$(CO)$_{10}$ concentration increased the relative amount of Mn particles.
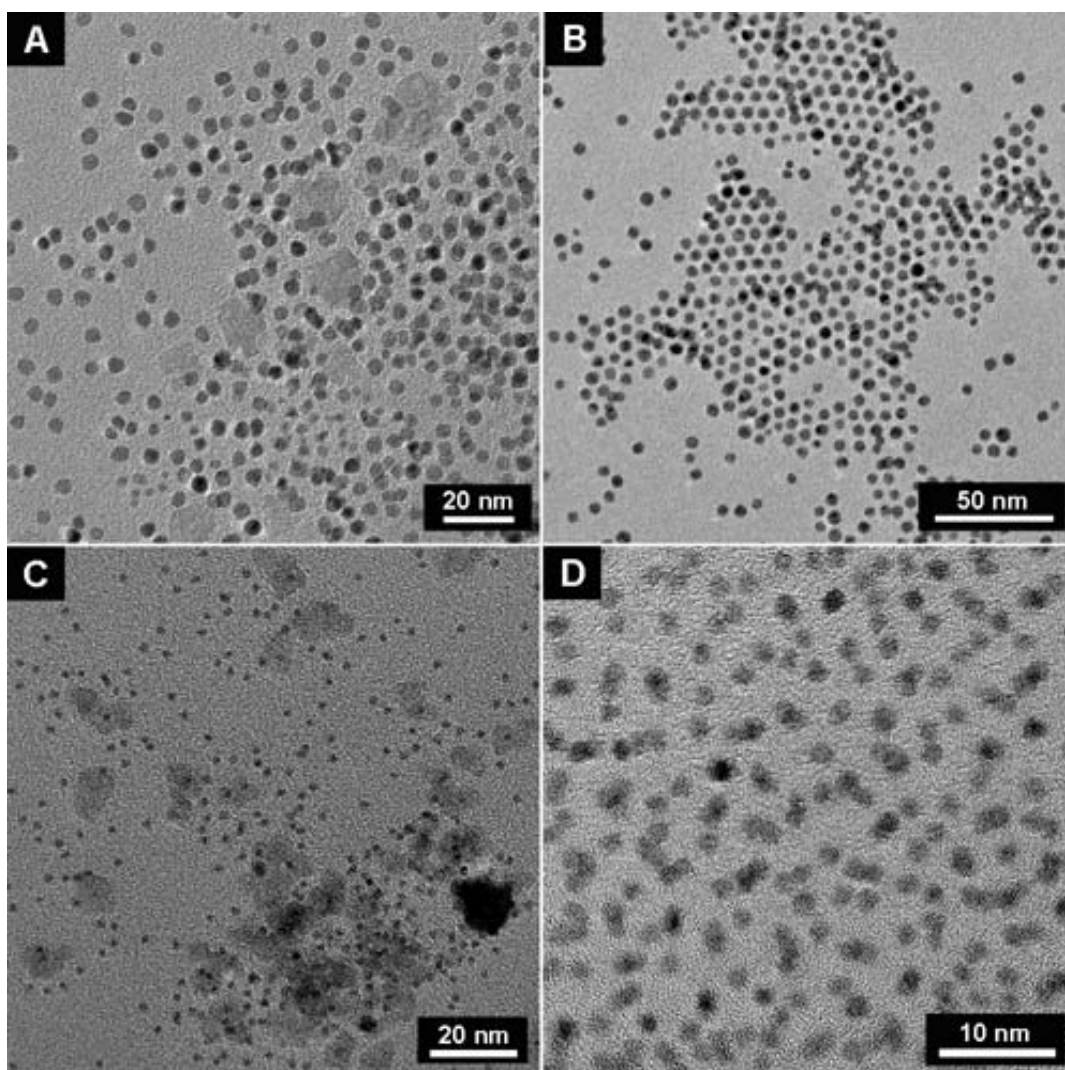
Figure 5.7. TEM images of the nanocrystal product before (A, C) and after (B, D) size-selective precipitation from reactions with (A, B) $Mn_2(CO)_{10}$ and (C, D) $Mn(acac)_2$ as the Mn source. In panels A and C, the large faint particles are pure Mn particles and the smaller darker particles are $MnPt_3$. The Mn particles are larger than 10 nm in diameter and are removed from the sample by size-selective precipitation, as confirmed by their absence in panels B and D.

117
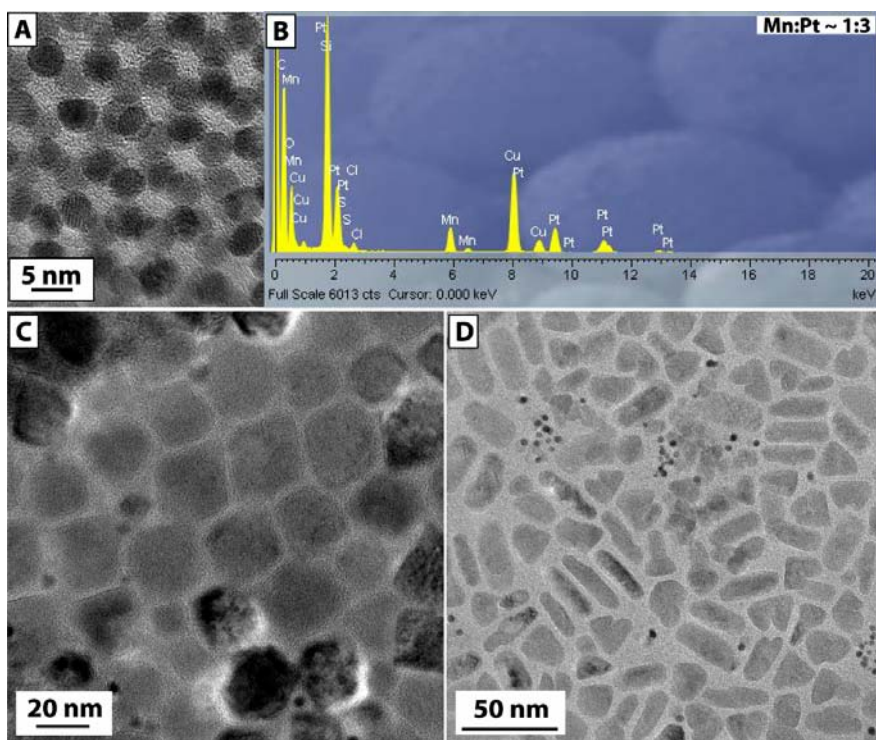
Figure 5.8. (A) TEM image of MnPt$_3$ nanocrystals synthesized with Pt(acac)$_2$ and Mn$_2$(CO)$_{10}$.   (B) X-ray energy dispersive spectroscopy (EDS) data of the TEM image in (A), showing 1:3 Mn:Pt ratio.   (C-D) Mn nanoparticles filtered during the size-selective precipitation steps.

5.3.4 Annealing of PbSe Nanocrystals and Nanowires

Stability of capping ligand passivation around colloidal nanocrystals and nanowires is crucial in the solution-based process of the nanomaterials into devices.   A process could involve high-temperature annealing for the device functionalization.   It is therefore very important to test their durability in severe conditions.   Figure 5.9B-D shows SEM images of PbSe nanocrystals after annealing under vacuum at different temperatures.   Note that the nanocrystals sintered into different shapes when they were annealed at different temperatures (90 °C versus 200 °C).   At a higher temperature, the

nanoparticles coalesced to form more isotropic structures, although the mechanism by which the anisotropic structures were formed at 90 °C is not clear.   Melting point of PbSe is 1078 °C, but the surface melting could occur at significantly lower temperatures.
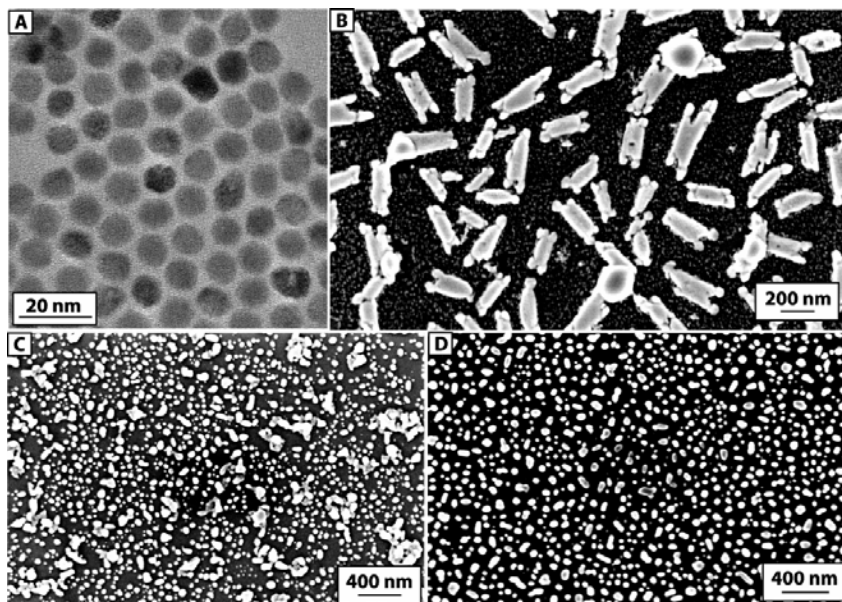
Figure 5.9. (A) TEM image of PbSe nanocrystals. The nanocrystals are passivated with trioctylphosphine and oleic acid.   (B-C) SEM images of PbSe nanocrystal sample after annealing (B) at 90 °C under vacuum for 1hr, (C) at 200 °C under vacuum for 30 min, and (D) at 200 °C under vacuum for 5 hrs.

Annealing of PbSe nanowires showed more pronounced sintering effects. Panels A and B in Figure 5.10 show SEM and TEM images of PbSe nanowires synthesized with tetradecylphosphonic acid as one of the capping ligands.   When the nanowires deposited on a silicon substrate were heated to 200 °C under vacuum, the nanowires were fused into shorter and thicker rods (Figure 5.10C-F).   As the time progressed, the shape of the nanorods became more uniform likely due to the Oswald ripening.   The crystal structure of the resulting nanorods was surprisingly orthorombic PbCl$_2$, evidenced from XRD and HRTEM.   The Cl contamination inside the vacuum

119

oven is attributed to the PbCl$_2$ crystal formation, because in nitrogen, the nanowires sustained their morphology as shown in Figure 5.10H.
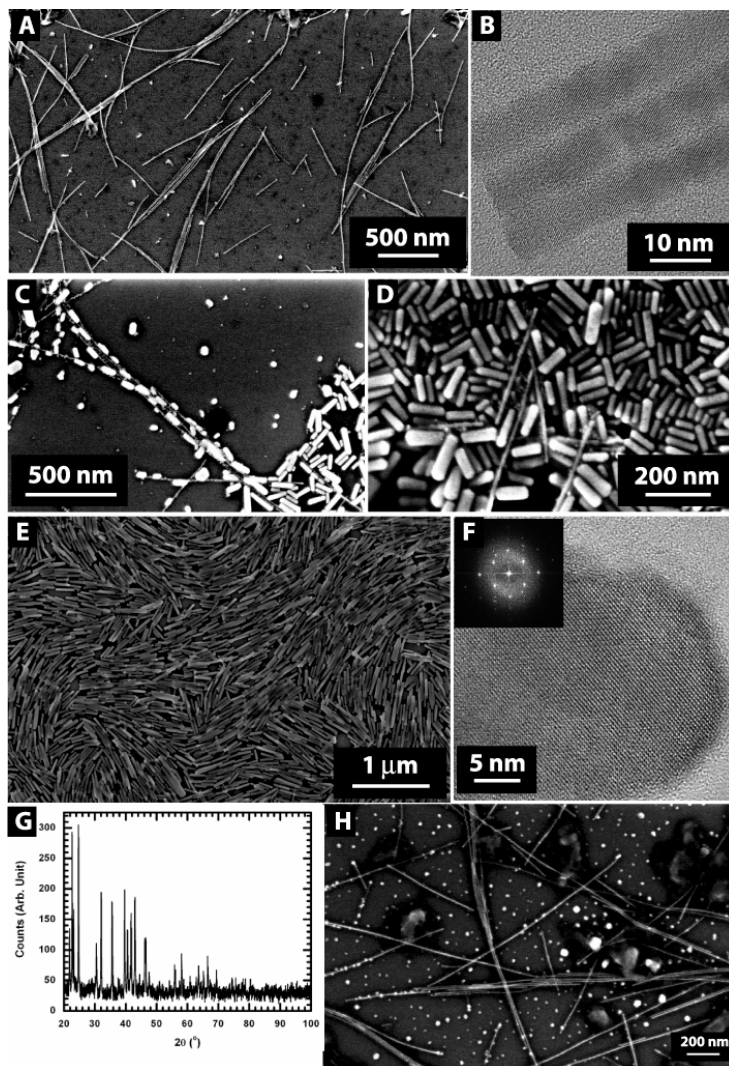
Figure 5.10. (A) TEM and (B) SEM images of PbSe nanowires.   The growth direction of the PbSe nanowires is <111>.   The nanowires are passivated with tetradecylphosphonic acid, trioctylphosphine and oleic acid.   (C-E) SEM images of PbSe nanowire sample after annealing at 200 °C under vacuum for (C) 10 min, (D) 30 min, and (E) 1 hr.   (F-G) HRTEM image and XRD pattern of nanorods shown in (E).   The crystal structure is orthorhombic PbCl$_2$.   (H) PbSe nanowires annealed under nitrogen at 200 °C for 1hr. The nanowires remained relatively intact after nitrogen annealing.

5.3.5 Magnetic Properties of FePt and MnPt₃ Nanocrystals

Magnetic properties of FePt nanocrystals annealed under nitrogen at 580 °C were investigated in their field-sweep scans at different measurement temperatures. As shown in Figure 5.11, the nanocrystal ensemble exhibited room-temperature ferromagnetism, and the coercivity of the sample at each temperature was in good agreement with previously reported results.
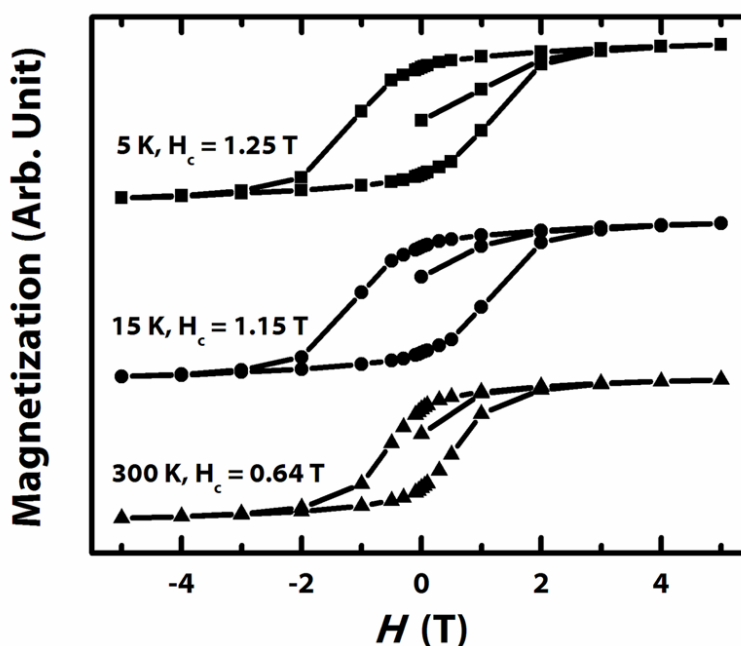
Figure 5.11. Field-sweep scans of FePt nanocrystals annealed at 580 °C. The nanocrystals exhibited ferromagnetism (H_c=0.64 T) at room temperature.

Figure 5.12 shows temperature-dependent zero-field-cooled (ZFC) and field-cooled (FC) magnetization scans under an applied field of 1000 Oe for 4.3 nm diameter MnPt₃ nanocrystals synthesized with $Mn_2(CO)_{10}$ before and after annealing at 580 °C. Before annealing, the nanocrystals are paramagnetic. After annealing at 580 °C, the nanocrystals become superparamagnetic with a blocking temperature at approximately 30

K.   The Curie temperature of bulk $L1_2$ $MnPt_3$ is 380 K.   The field sweep of the annealed particles at 5 K exhibits hysteresis with a coercivity of ~500 Oe (Figure 5.12D). The change in magnetic properties results from the phase change from paramagnetic A1 $MnPt_3$ to ferromagnetic $L1_2$ $MnPt_3$ upon annealing.
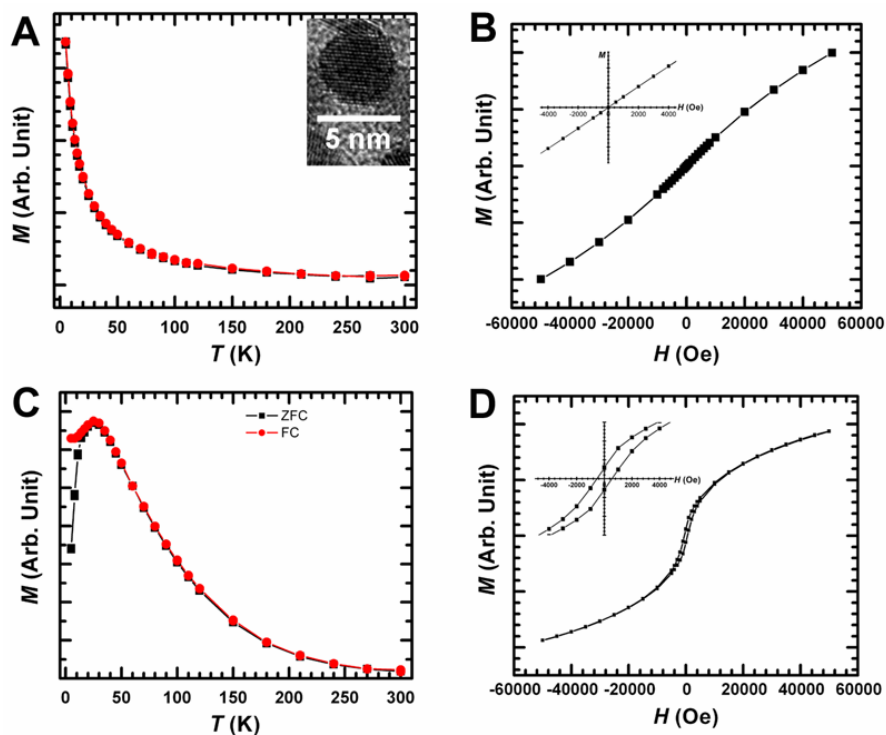
Figure 5.12. Magnetization measurements of 4.3 nm diameter $MnPt_3$ nanocrystals synthesized with $Mn_2(CO)_{10}$ (A,B) before and (C,D) after annealing at 580 °C: (A,C) field-cooled and zero-field-cooled scans and (B,D) field sweeps at 5 K.   No hysteresis is seen in panel B, while the plot in panel D shows the coercivity of ~500 Oe. (Insets in panels B and D are magnifications of the field sweeps near zero field to magnify the hysteresis). Note that sintering occurred during annealing and increased the average particle diameter to 7.0 nm, as determined by the Scherrer equation from XRD.

Figure 5.13 shows temperature-dependent ZFC magnetization scans under an applied field of 1000 Oe for 1.7 nm diameter $MnPt_3$ nanocrystals synthesized with

Mn(acac)$_2$ before and after annealing at 580 °C. The magnetic properties of these MnPt$_3$ nanocrystals were qualitatively similar to those of the nanocrystals synthesized with Mn$_2$(CO)$_{10}$ as the Mn source measured in Figure 5.12: the as-synthesized A1 MnPt$_3$ nanocrystals were paramagnetic and the annealed MnPt$_3$ nanocrystals were superparamagnetic. However, the blocking temperature of the annealed nanocrystals made with Mn(acac)$_2$ was significantly higher than the annealed particles made with Mn$_2$(CO)$_{10}$ at ~100 K (Figure 5.13B). The coercivity at 5 K was also significantly higher: 2.2 kOe versus only 500 Oe. Larger particle size should give higher blocking temperatures of superparamagnetic particles. However, this is not the case here, as the average particle diameter determined from the peak breadth in XRD was 5.8 nm, which is smaller than the nanocrystals with Mn$_2$(CO)$_{10}$ after annealing (7.0 nm). The XRD data and analysis will be covered in Section 5.3.6.
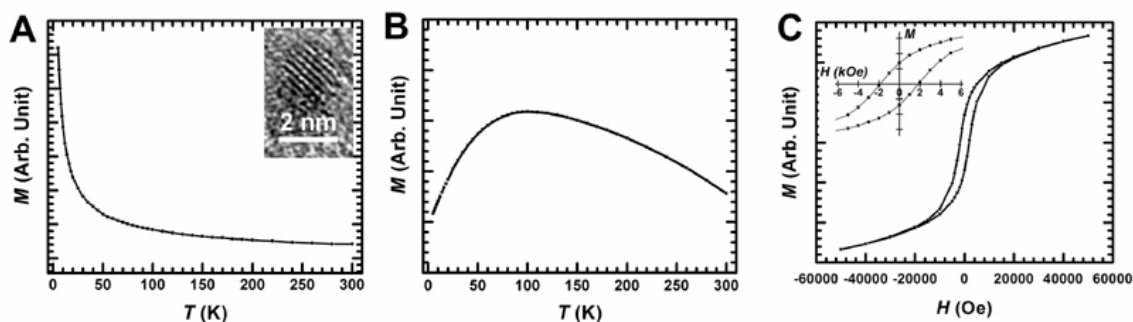
Figure 5.13. Magnetization measurements of 1.7 nm diameter MnPt$_3$ nanocrystals synthesized with Mn(acac)$_2$: zero-field-cooled temperature-dependent magnetization scans under an applied field of 1000 Oe (A) before and (B) after annealing at 580 °C. Annealing at 580 °C led to sintering and an increase in average particle diameter to 5.8 nm determined from the Scherrer equation and the peak breadth in the XRD patterns. (C) Field sweep scan of the magnetization of the annealed nanocrystals at 5K; the coercivity is 2.2 kOe.

123

The magnetic properties of MnPt$_3$ are also very sensitive to Mn-Pt composition and atomic order. Although the analysis of the particles by EDS and XRD did not reveal a noticeable difference in Mn:Pt ratio, if the MnPt$_3$ nanocrystals synthesized with Mn$_2$(CO)$_{10}$ were slightly Mn-poor there would be weaker ferromagnetic coupling between Mn spins, which leads to a decreased coercivity and Curie temperature in bulk MnPt$_3$ and would lead to a decreased blocking temperature in the nanocrystals.

5.3.6 Sintering of FePt and MnPt$_3$ Nanocrystals under Annealing

The nonuniform areal density of the FePt due to sintering makes it difficult to understand the magnetic properties of the film. Sintering of FePt was studied in TEM observation (Figure 5.14). The particle coalescence at 580 °C was not significant when monolayer FePt nanocrystals were annealed, but when a multi-layered FePt nanocrystal film was annealed the particle sintering was noticeably profound. The particle size increase was also supported by the XRD data, where the peak breadth decreased after the thick layer particles were annealed, indicating that the crystal domain size increased. After annealing at 630 °C, the FePt nanocrystals exhibit significant sintering even in a monolayer as shown in Figure 5.14.
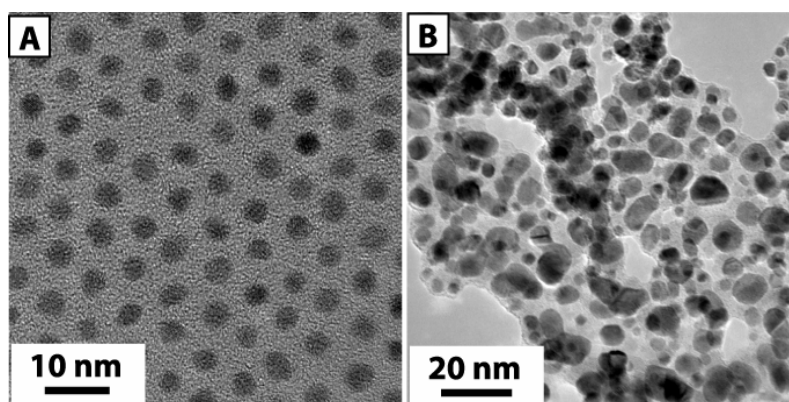
Figure 5.14. TEM images of FePt nanocrystals (A) before and (B) after annealing at 630 °C. Annealing led to sintering and the particle size increase.

124

Figure 5.15 shows XRD data obtained from MnPt$_3$ nanocrystals after all the Mn particulate byproducts were removed by size-selective precipitation. The MnPt$_3$ nanocrystals exhibit the A1 phase of MnPt$_3$ that has a compositionally disordered face-centered cubic (fcc) unit cell (JCPDS number 65-5033). When the nanocrystals are annealed at 580 °C and above, new diffraction peaks appeared as shown in Figure 6.15, which can be assigned to the (100), (110), (210), (211), (221), and (310) lattice planes of L1$_2$ MnPt$_3$ (JCPDS number 65-3260). L1$_2$ MnPt$_3$ has atomically ordered Mn and Pt atoms in the unit cell: Mn occupies the face centers. No significant structural change was detected when the nanocrystals were annealed at temperatures below 500 °C.
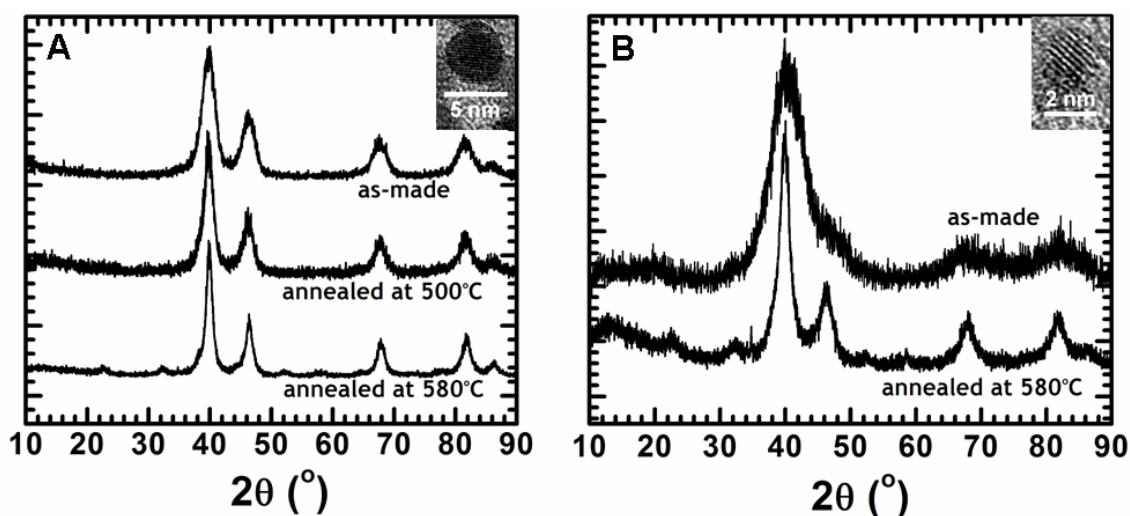
Figure 5.15. XRD of MnPt$_3$ nanocrystals synthesized with (A) Mn$_2$(CO)$_{10}$ and (B) Mn(acac)$_2$ as the Mn reactant. By use of the Scherrer equation to determine the average particle diameter, the nanocrystals have average diameter of (A) 4.3 and (B) 1.7 nm. The XRD patterns of as-made nanocrystals match with the fcc A1 structure (JCPDS 65-5033). The patterns of annealed sample index to the L1$_2$ phase of MnPt$_3$ (JCPDS 65-3260).

After annealing of the nanocrystals at 580 °C, the XRD peaks have also noticeably sharpened, indicating that the sintering and grain growth of the particles occurs in the nanocrystal film. The average MnPt$_3$ crystalline grain sizes determined by

use of the Scherrer equation were 4.3 and 7.0 nm before and after annealing (with $Mn_2(CO)_{10}$) and 1.7 and 5.8 nm before and after annealing (with $Mn(acac)_2$). The smaller 1.7 nm diameter nanocrystals made with $Mn(acac)_2$ undergo a proportionally larger size increase and more dramatic peak sharpening in the XRD pattern, although the final particle diameters are similar for both samples: 7.0 versus 5.8 nm. Sintering of organic ligand-coated nanocrystals annealed at temperatures above ~500 °C is well-known.

To probe more effectively the influence of particle size and composition on the magnetic properties of the $L1_2$ $MnPt_3$ nanocrystals, it would be desirable to encapsulate them in a ceramic coating that can withstand the annealing temperatures and prevent sintering. The encapsulation of FePt nanocrystals in SiO_2 has been carried out and covered in Chapter 6. The coating chemistry is, however, very oxidative, and the particles chemically degraded during the coating procedure. The Mn appears to be more sensitive to oxidation than Fe, and the strong base required for SiO_2 formation appears to attack Mn in the particles. New coating chemistry that is less aggressive is needed for the system.

It is also worth noting that the chemical approach to $MnPt_3$ nanocrystals developed here is very similar to the chemistry used by Ono *et al.* to make MnPt nanocrystals. We were unable to find conditions suitable to make MnPt, and excess Mn reactant only generated pure Mn particles in the presence of $MnPt_3$ nanocrystals. It is possible that the MnPt nanocrystals reported by Ono *et al.* were in fact $MnPt_3$ contaminated with Mn nanocrystals, which would explain their observation of ferromagnetic spin coupling in their system. Furthermore, they did not see a phase transition from cubic to tetragonal crystal structure in XRD of their materials after annealing, as would be expected from $L1_0$ MnPt, which has a tetragonal unit cell.

Magnetic force microscopy (MFM) images were taken using a FePt nanocrystal film made by dropcasting FePt nanocrystals onto a mica substrate (Figure 5.16). The contrast due to topographic signature exceeded the contrast by magnetic signal by far, so the sintering of the particles directly lead to the difficulty in reading and writing the data in the nanocrystal films.
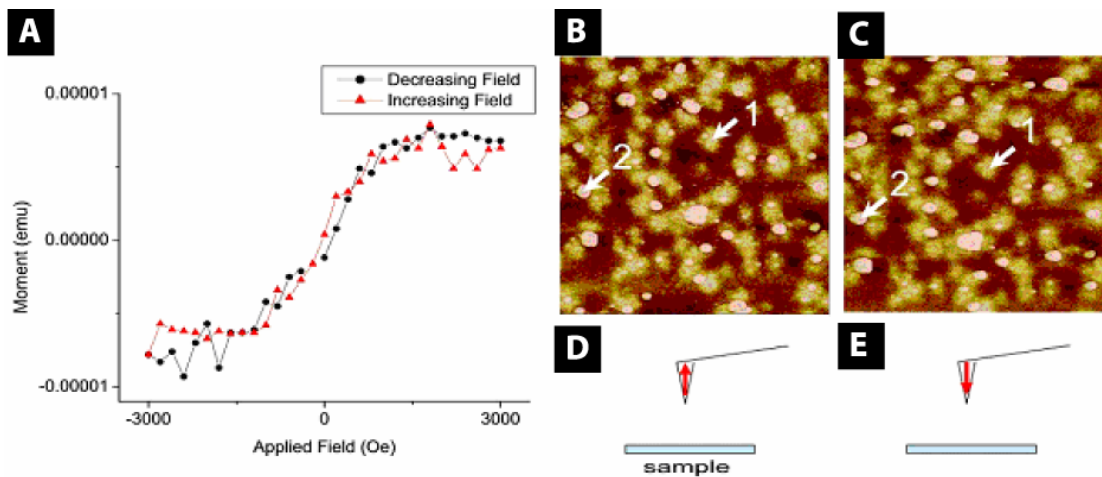
Figure 5.16. (A) Perpendicular M-H loop at 300 K of the 50-nm-thick sample. (B) MFM (5 μm × 5 μm) image is taken by an HM-MESP MFM tip magnetized upward as shown in (D). (C) MFM image using an HM-MESP MFM tip magnetized downward as shown in (E). MFM images courtesy of C. Hyun.

5.4 CONCLUSIONS

PbSe, FePt and $MnPt_3$ nanostructures were synthesized by a colloidal approach. The synthesis of the materials produced a uniform particle size and shape and yielded a high crystallinity. In $MnPt_3$, however, the stoichiometry of Mn:Pt was not controlled, and at high Mn concentrations, pure Mn particles were produced in addition to $MnPt_3$ nanocrystals. The $MnPt_3$ nanocrystals obtained from the reaction have the chemically

disordered fcc A1 phase. Annealing films of the nanocrystals at 580 °C converted the nanocrystals to the compositionally ordered $L1_2$ phase ($AuCu_3$ structure). These annealed films were superparamagnetic.

Annealing of different colloidal nanomaterials was investigated. In PbSe, both PbSe nanocrystals and nanowires coalesced at temperatures as low as 90 °C under vacuum, although the sintering could be a result of reaction of Cl and PbSe to yield $PbCl_2$ crystals. Size control of magnetic nanocrystals is very important in the context of using the particles in ultra-high areal density storage media. Annealing is required to make the particles ferromagnetic at room temperature, but after the necessary annealing process it was found that both FePt and MnPt nanocrystals sintered. High-temperature annealing gave rise to the phase transformations in these materials and magnetic properties depended on the degree of compositional ordering. Protection of the nanocrystals from sintering at the necessary annealing steps will be discussed in Chapter 6.

5.5 REFERENCES

(1) Nosaka, Y.; Yamaguchi, K.; Miyama, H.; Hayashi, H., *Chem. Lett.* **1988**, 605.

(2) Vossmeyer, T.; Katsikas, L.; Giersig, M.; Popovic, I. G.; Diesner, K.; Chemseddine, A.; Eychmuller, A.; Weller, H., *J. Phys. Chem.* **1994,** 98, 7665.

(3) Brust, M.; Walker, M.; Bethell, D.; Schiffrin, D. J.; Whyman, R., *J. Chem. Soc., Chem. Commun.* **1994**, 801.

(4) Korgel, B. A.; Fullam, S.; Connolly, S.; Fitzmaurice, D., *J. Phys. Chem. B* **1998,** 102, 8379.

(5) Steigerwald, M. L.; Alivisatos, A. P.; Gibson, J. M.; Harris, T. D.; Kortan, R.; Muller, A. J.; Thayer, A. M.; Duncan, T. M.; Douglass, D. C.; Brus, L. E., *J. Am. Chem. Soc.* **1988,** 110, 3046.

(6) Murray, C. B.; Norris, D. J.; Bawendi, M. G., *J. Am. Chem. Soc.* **1993,** 115, 8706.

(7) Park, S. J.; Kim, S.; Lee, S.; Khim, Z. G.; Char, K.; Hyeon, T., *J. Am. Chem. Soc.* **2000,** 122, 8581.

(8)   Hyeon, T.; Lee, S. S.; Park, J.; Chung, Y.; Bin Na, H., *J. Am. Chem. Soc.* **2001,** 123, 12798.

(9)   Sun, S. H.; Murray, C. B., *J. Appl. Phys.* **1999,** 85, 4325.

(10) Sun, S. H.; Murray, C. B.; Weller, D.; Folks, L.; Moser, A., *Science* **2000,** 287, 1989.

(11) Shevchenko, E. V.; Talapin, D. V.; Schnablegger, H.; Kornowski, A.; Festin, O.; Svedlindh, P.; Haase, M.; Weller, H., *J. Am. Chem. Soc.* **2003,** 125, 9090.

(12) Hyeon, T.; Chung, Y.; Park, J.; Lee, S. S.; Kim, Y. W.; Park, B. H., *J. Phys. Chem. B* **2002,** 106, 6831.

(13) Kang, E.; Park, J.; Hwang, Y.; Kang, M.; Park, J. G.; Hyeon, T., *J. Phys. Chem. B* **2004,** 108, 13932.

(14) Park, J.; An, K. J.; Hwang, Y. S.; Park, J. G.; Noh, H. J.; Kim, J. Y.; Park, J. H.; Hwang, N. M.; Hyeon, T., *Nat. Mater.* **2004,** 3, 891.

(15) Park, J.; Lee, E.; Hwang, N. M.; Kang, M. S.; Kim, S. C.; Hwang, Y.; Park, J. G.; Noh, H. J.; Kini, J. Y.; Park, J. H.; Hyeon, T., *Angew. Chem. Int. Ed.* **2005,** 44, 2872.

(16) Stowell, C. A.; Wiacek, R. J.; Saunders, A. E.; Korgel, B. A., *Nano Lett.* **2003,** 3, 1441.

(17) Woods, S. I.; Kirtley, J. R.; Sun, S. H.; Koch, R. H., *Phys. Rev. Lett.* **2001,** 8713.

(18) Talapin, D. V.; Murray, C. B., *Science* **2005,** 310, 86.

(19) Cho, K. S.; Talapin, D. V.; Gaschler, W.; Murray, C. B., *J. Am. Chem. Soc.* **2005,** 127, 7140.

(20) Korgel, B. A.; Fitzmaurice, D., *Adv. Mater.* **1998,** 10, 661.

(21) Tang, Z. Y.; Zhang, Z. L.; Wang, Y.; Glotzer, S. C.; Kotov, N. A., *Science* **2006,** 314, 274.

(22) Yu, J. H.; Joo, J.; Park, H. M.; Baik, S. I.; Kim, Y. W.; Kim, S. C.; Hyeon, T., *J. Am. Chem. Soc.* **2005,** 127, 5662.

(23) Penn, R. L., *J. Phys. Chem. B* **2004,** 108, 12707.

(24) Sun, S. H.; Fullerton, E. E.; Weller, D.; Murray, C. B., *IEEE Trans. Mag.* **2001,** 37, 1239.

(25) Wierman, K. W.; Hilfiker, J. N.; Sabiryanov, R. F.; Jaswal, S. S.; Kirby, R. D.; Woollam, J. A., *Phys. Rev. B* **1997,** 55, 3093.

(26) Wierman, K. W.; Kirby, R. D., *J. Magn. Magn. Mater.* **1996,** 154, 12.

(27) Hyun, C.; Lee, D. C.; Israel, C.; Korgel, B. A.; de Lozanne, A., *IEEE Trans. Mag.* **2006,** 42, 3799.

(28)   Ding, Y.; Majetich, S. A.; Kim, J.; Barmak, K.; Rollins, H.; Sides, P., *J. Magn. Magn. Mater.* **2004,** 284, 336.

(29)   Ono, K.; Okuda, R.; Ishii, Y.; Kamimura, S.; Oshima, M., *J. Phys. Chem. B* **2003,** 107, 1941.

Chapter 6: Synthesis and Magnetic Properties of Silica-Encapsulated FePt Nanocrystals[†]

6.1 INTRODUCTION

$L1_0$ FePt has high magnetocrystalline anisotropy (K_u), saturation magnetization and maximum energy product $[BH]_{max}$ (6.6×10^7 erg/cm^3 (~60 meV/nm^3), 1140 emu/cm^3 and 13 MGOe, respectively), making it a good candidate material for high density non-volatile magnetic memory. $L1_0$ FePt domains as small as 3 nm in diameter could be used as memory bits—their magnetic anisotropy energy ($K_u V$) would exceed kT (at room temperature) by about a factor of 25, and 1 Tb/in^2 storage density using 3 nm diameter FePt domains as individual bits in a monolayer would require an edge-to-edge separation of about 25 nm. Pioneering work by Sun and Murray has led to a well-developed colloidal synthesis of FePt nanocrystals in this size range and particles with narrow size distributions and good dispersion stability can be obtained. These colloidal nanocrystals, however, are compositionally disordered with very low magnetocrystalline anisotropy. To obtain the $L1_0$ phase with high magnetocrystalline anisotropy, the nanocrystals must be cast into films and annealed at relatively high temperature (>550 °C). During annealing, the organic capping ligands decompose and the particles sinter. Sintering is a major problem that destroys the size distribution and leads to polycrystalline films.

Several approaches have been studied to alleviate the problem of sintering, including the addition of impurities such as Sb or Cu that lower the fcc→$L1_0$ phase transition temperature, direct synthesis of the $L1_0$ phase using microwave radiation or biomolecule-aided particle growth, chemical tethering to substrates, and deposition of

thermally-resistant inorganic coatings. Although very interesting, the direct synthetic approaches to $L1_0$ FePt nanocrystals have thus far been relatively unsuccessful, with very low yields and poor magnetic properties. Substrate-tethering is limited to nanocrystal monolayers—most likely not suitable for magnetic memory applications, as multilayers will be needed for sufficient detection signal. FePt nanocrystals have been embedded in a host matrix of carbon or hafnium oxide by gas-phase sputtering over a nanocrystal monolayer or in salts such as NaCl by ball milling. These host matrices prevented sintering during annealing to the $L1_0$ phase. However, there is little control over the interparticle separation in the nanocrystal film or the coating thickness using these methods. Colloidal coating deposition methods can provide better control over the shell thickness of the protective layer. Iron oxide has been deposited as a shell material with good controlled coverage, with thicknesses of 2 to 5 nm. Iron oxide is interesting because it will deposit as a shell during the nanocrystal synthesis simply by using a higher Fe concentration in the reaction mixture. These iron oxide coatings have been shown to prevent FePt sintering up to ~700 °C, which is high enough for the fcc→$L1_0$ phase transition. However, this approach adds a soft magnetic impurity to the FePt film, which Liu *et al.* showed to lead to very low coercivities relative to the sintered $L1_0$ FePt films obtained from the bare FePt particles. A non-magnetic thermally-resistant coating that can be deposited with larger thicknesses is desired for many applications. Using colloidal methods, silica shells have been deposited on ferrite, iron oxide, and recently FePt nanocrystals. Yamamoto *et al*. annealed their silica-coated FePt nanocrystals and found that FePt did not sinter at temperatures below 900 °C; however, an ability to tune silica shell thickness was not reported.

Here the encapsulation of 6 nm diameter FePt nanocrystals in silica (SiO_2) shells (FePt@SiO_2) with tunable thickness from 10 nm to 25 nm is demonstrated. SiO_2

deposition was performed in water-in-oil microemulsions and the SiO_2 layer thickness could be controlled simply by varying the ratio of FePt nanocrystals to silica precursor. The as-made FePt@SiO_2 nanocrystals disperse in polar solvents such as ethanol/water mixtures.   Surface modification with octadecytrimethoxysliane (OTMOS) yielded FePt@SiO_2 particles that were dispersible in non-polar organic solvents.   The silica shell prevents FePt sintering at annealing temperatures up to ~850 °C.   Interestingly, annealing under nitrogen or air did not induce the fcc→$L1_0$ phase transition, even at temperatures as high as ~850 °C.   A hydrogen annealing environment was needed to induce the fcc-to-$L1_0$ phase transition at about 650 °C, which is higher in temperature compared to the organic monolayer coated nanocrystals (~550 °C).   Field-cooled (FC) and zero field cooled (ZFC) temperature dependent magnetization measurements showed that the 6 nm diameter $L1_0$ nanocrystals exhibited a blocking temperature above room temperature.   The coercivity depended on the silica shell thickness, increasing with increasing thickness, perhaps due to decreased magnetic dipole coupling between FePt domains.

6.2 EXPERIMENTAL SECTION

6.2.1 FePt nanocrystals

6 nm FePt nanocrystals were prepared by arrested precipitation using standard airless techniques on a Schlenk line according to methods reported by Chen *et al.*   0.5 mmol of platinum acetylacetonate (Pt(acac)$_2$, 97%, Aldrich) was mixed with 10 mL octyl ether (>97%, Fluka) in a 100 mL 3-neck flask.   The mixture was degassed for 1 hour and then heated to 100 °C under N_2.   1 mmol of iron pentacarbonyl (Fe(CO)$_5$, Aldrich), 8 mmol of oleic acid (Aldrich) and 8 mmol of oleylamine (Fluka) were then injected

while the mixture was stirred vigorously. The reaction mixture was heated at a rate of ~15 °C/min to 240 °C. The reaction mixture was then kept at 240 °C and stirred for 1 hr. The reaction flask was then heated to reflux (295 °C) for 2 hrs. The reaction solution was cooled to room temperature by removing the heating source. The nanocrystals were then precipitated with excess ethanol and collected by centrifugation. The nanocrystals were redispersed in toluene and precipitated again with excess ethanol and collected by centrifugation.

The synthesis of FePt nanocrystals was carried out by employing high temperature reduction of platinum precursor and thermal decomposition of iron source in the presence of capping ligands. At room temperature, platinum acetylacetonate (0.5 mmol) was mixed with 1,2-hexadecanediol (1.5 mmol) in dioctylether (20mL) in a three-neck flask. The mixture was agitated at room temperature while flushing with nitrogen for ~20 min. The mixture was heated to 100 °C, at which oleic acid (0.5 mmol), oleylamine (0.5 mmol), and iron pentacarbonyl (1 mmol) were injected, and the resulting mixture continued to be heated to the refluxing temperature of dioctylether. The reaction mixture was held at the refluxing temperature for 30 min, and was allowed to cool to room temperature by removing the heating element. The solution was then collected and centrifuged at 8000 rpm for 10 min, and a small amount of the poorly capped particles was precipitated out and discarded. The supernatant was mixed with 20 mL of ethanol and the FePt nanocrystals capped with organic stabilizer were flocculated and easily collected after another centrifugation at 8000 rpm for 10 min. The precipitate was carefully collected after an additional rinse with ethanol. The nanocrystals could be redispersed readily in organic solvents such as hexane.

6.2.2 Silica Coating Procedure

The FePt nanocrystals were coated with SiO_2 by base catalyzed silica formation from tetraethylorthosilane (TEOS) in a water-in-oil microemulsion. 8 mL of Igepal[®] CO-520 (($C_2H_4O)_n \cdot C_{15}H_{24}O$, n~5, Aldrich) was mixed with 170 mL cyclohexane (Aldrich) in a 250 mL Erlenmeyer flask and stirred. FePt nanocrystals were dispersed in cyclohexane at a concentration of 1 mg/mL and then injected into the cyclohexane/Igepal solution. The amount of FePt nanocrystals added ranged from 8 mg to 40 mg (*i.e.*, 8 mL to 40 mL), depending on the desired silica shell thickness. 1.3 mL of 30 % NH_4OH aqueous solution (EM Science) was then added dropwise and stirred for 2~3 minutes, followed by the addition of 1.5 mL of tetraethyl orthosilicate (TEOS, 98%, Aldrich). Depending on the desired silica shell thickness, the amount of TEOS added was varied from 0.5 mL to 12 mL. 16 mL of FePt/cyclohexane dispersion with 1.5 mL of TEOS gave ~16 nm thick SiO_2 shells. The mixture was stirred for 72 hours before adding methanol to collect particles. The particles were precipitated with excess hexane and collected by centrifugation. The particles were redispersed in ethanol. The FePt@SiO_2 nanocrystals were "washed" using this procedure at least 3 times to remove excess surfactant. The final product was stored as an ethanol dispersion.

6.2.3 FePt@SiO_2 Annealing and OTMOS coating

The FePt@SiO_2 particles were annealed in a tube furnace (TF55035A, Lindberg/Blue M). The particles were drop-cast onto a Si wafer, positioned into a 1-inch diameter quartz tube, and then placed in the tube furnace. Annealing was performed by purging the tube and the sample for 30 minutes with N_2 or 7% H_2/93% N_2 (purchased from Matheson Trigas) flow while heating at a rate of 60~70 °C/min. Samples annealed in air were not purged. The samples were annealed at the reported temperatures for 1 hr.

Surface functionalization of the silica-coated nanoparticles was carried out using the method reported by Wang *et al.* 10mL of ethanol dispersion of FePt@SiO$_2$ particles at a concentration of 1 mg/mL were mixed with 0.1 mL of 30 % NH$_4$OH aqueous solution. 0.5 mL of 10 vol% octadecyltrimethoxysilane (OTMOS, Aldrich) in CHCl$_3$ was added dropwise to the dispersion, followed by stirring for 24 hrs.

6.2.4 Materials Characterization

6.2.4.1 Transmission electron microscopy (TEM)

TEM images were obtained using either a JEOL 2010F operated at an accelerating voltage of 200 kV or a Phillips EM208 TEM at 80 kV. For TEM imaging, as-synthesized FePt nanocrystals were dispersed in chloroform and drop-cast on a carbon-coated 200-mesh Cu grid (Ladd Research). FePt@SiO$_2$ particles were imaged by TEM by dispersing the particles in ethanol and drop-casting onto a carbon-coated Cu TEM grid.

6.2.4.2 Scanning electron microscopy (SEM)

SEM images were obtained on a LEO 1530 HRSEM operating between 1.5 kV to 3 kV with working distance between 2 mm to 6 mm. For SEM imaging, samples were prepared by dispersing in ethanol and then drop-casting onto a 2 cm × 2 cm Si substrate (cut from 6 in. p-type (100) Si wafer, Nova Electronic Materials). The samples were not coated with metal.

6.2.4.3 X-ray diffraction (XRD)

XRD patterns were obtained on a quartz slide using a Bruker-Nonius D8 Advance diffractometer. Samples were typically scanned for ~12 hrs at a scan rate of 12 deg/min with 0.02 degree increments.

6.2.4.4 Superconducting quantum interference device (SQUID)

Magnetic properties were measured using a superconducting quantum interference device (SQUID, Quantum Design). The particles, either as-made or annealed, were collected in a gelatin capsule (Eli Lilly and Company) and inserted into the magnetometer. The temperature-sweeps were collected under a constant field of 1 kOe from 5 K to 300 K. The magnetization was also measured as a function of applied field at 5 K and 300 K. The magnetization data presented in this paper are not background subtracted for the diamagnetic signal from SiO_2 shell or the diamagnetic gelatin capsules because the contribution to the magnetic signal was negligible. At 50 kOe of applied field, the magnetization of $FePt@SiO_2$ particles ranges 1~10 emu/g while that of pure SiO_2 particles ranges 0.01~0.02 emu/g.

6.2.4.5 Magnetic force microscopy (MFM)

Ethanol dispersions of silica-coated particles were drop-cast onto MICA substrates for MFM measurements. Atomic force microscopy (AFM) and MFM images were simultaneously obtained using a Digital Instruments Multimode microscope operated in Tapping/Lift^{TM} mode under ambient conditions. This phase range is a measure of the strength of the magnetism of the sample (and the MFM tip), ranging from zero for nonmagnetic material up to 5 degrees for a computer hard drive. The MFM tips have a Co-Cr coating with a medium moment (~10^{-13} emu) and coercivity (~400 Oe).

6.3 RESULTS AND DISCUSSION

6.3.1 SiO$_2$ Coating of FePt Nanocrystals

Figure 6.1 shows TEM images of the oleic acid/oleylamine capped FePt nanocrystals that were used in the silica coating experiments. The nanocrystals were

relatively size-monodisperse with average diameter of (A) ~3 nm and (B) ~6 nm. The particles do not appear to have spherical morphology, but rather a cuboidal shape. These FePt nanocrystals were coated with SiO_2 using non-ionic surfactant-stabilized water-in-oil microemulsions as reaction media. NH_4OH was used to catalyze the decomposition of TEOS to silica over the course of about 3 days. Figure 6.2 shows TEM images of a representative sample of SiO_2-coated FePt nanocrystals. These particles have 16.12 ± 1.81 nm thick SiO_2 shells that were formed by mixing ~940 μL of TEOS with 10 mg FePt nanocrytals. Each silica sphere encapsulates one FePt nanocrystal, although a small fraction of silica particles have either two or zero FePt particles.
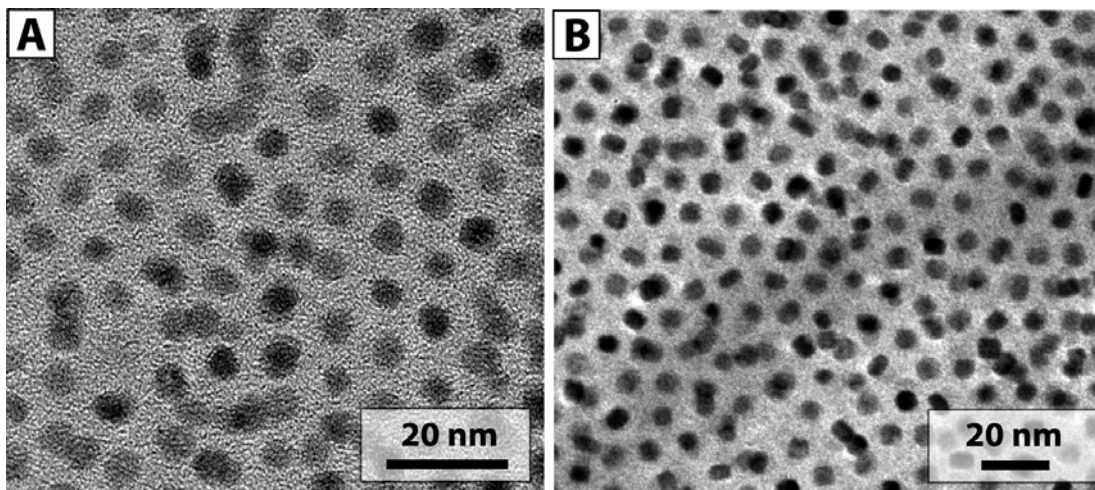
Figure 6.1. TEM images of FePt nanocrystals prior to coating with SiO_2. The average diameter of the particles was (A) ~3 nm and (B) ~6 nm.

The SiO_2 shell thickness could be controlled from 7 nm to 23 nm by adjusting the TEOS concentration and the ratio of TEOS to FePt nanocrystals used during the coating step. Figure 6.3 shows TEM images of FePt@SiO_2 obtained with varying silica shell thickness. At low TEOS concentrations, increasing TEOS/FePt increased the shell

thickness.   Above TEOS/FePt ratios of ~15 mL TEOS/80 mg FePt, the shell thickness levelled off and decreased slightly with higher TEOS concentrations.   In the range of higher [TEOS], the silica sphere diameter plateaus and more TEOS simply nucleates more FePt-free SiO_2 particles.   As a result, the average shell thickness remains nearly constant at high TEOs concentrations, even when 3 times as much TEOS was used as the case of Figure 6.2.   Figure 6.3F plots the SiO_2 shell thickness obtained as a function of TEOS/FePt ratio.
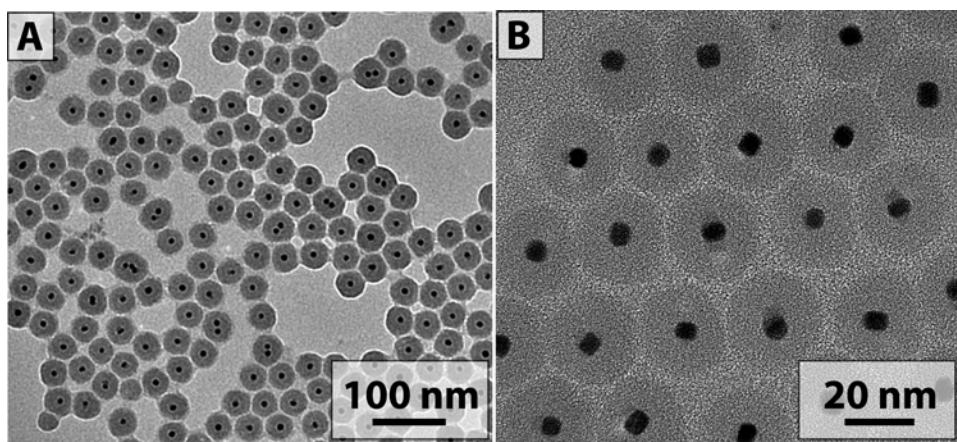
Figure 6.2. TEM images of FePt nanocrystals coated with SiO_2. 6 nm FePt nanocrystals are coated with ~16 nm thick SiO_2 shells.
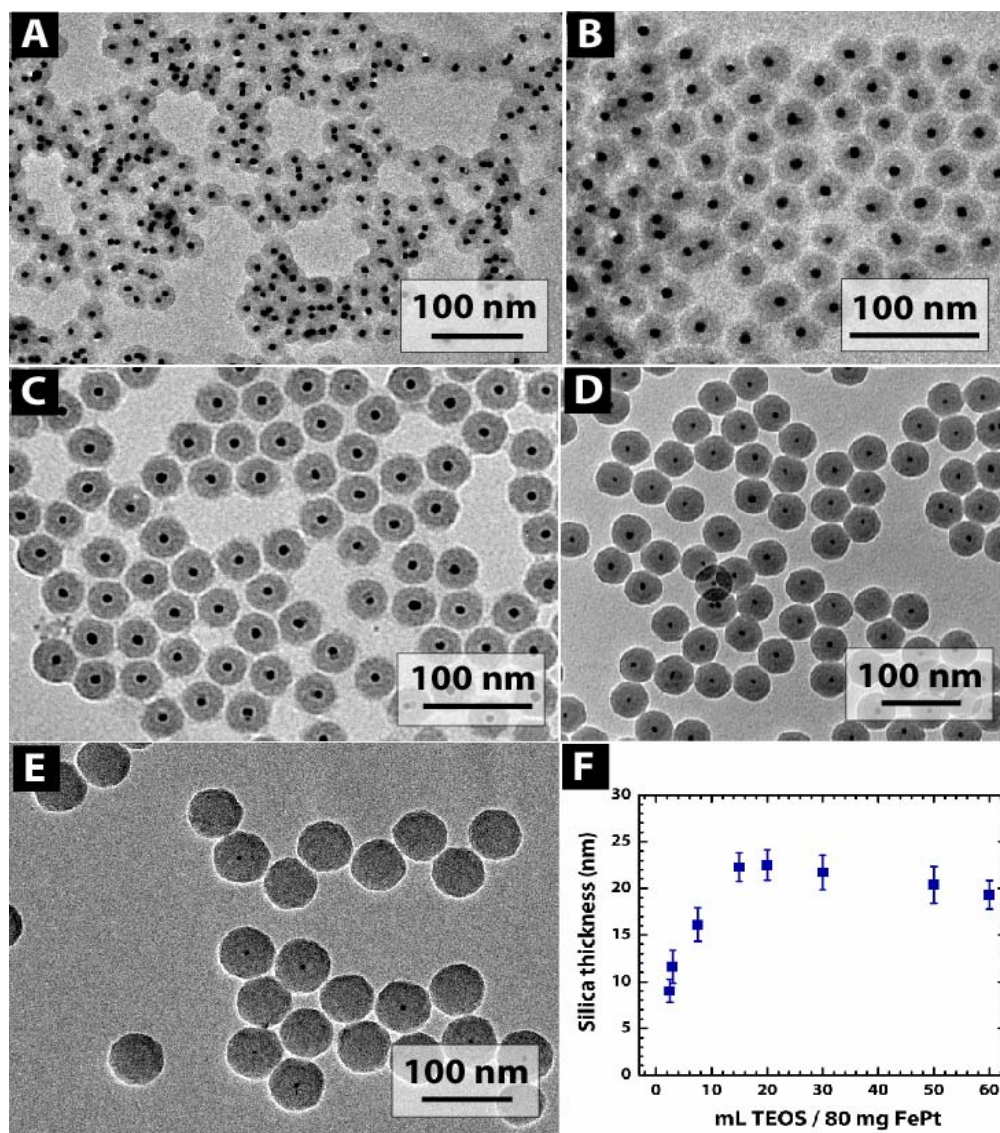
Figure 6.3. TEM images of FePt@SiO$_2$ particles with different SiO$_2$ thickness. Samples were prepared by dispersing (A) 16 mg, (B) 40 mg, (C) 16 mg, (D) 2.7 mg, or (E) 2.7 mg of FePt nanocrystals in 170 mL cyclohexane and 8 mL Igepal. 1.3 mL of 30% aqueous NH$_4$OH solution was added, followed by the addition of (a) 0.5 mL, (b) 1.5 mL, (c) 1.5 mL, (d) 0.65 mL, or (e) 1.6 mL of TEOS. In (e), some of the silica particles do not have FePt nanocrystals at their core, which occurred more frequently at higher TEOS/FePt ratios. The SiO$_2$ thicknesses are (a) 9.02 ± 1.26 nm, (b) 11.59 ± 1.76 nm, (c) 16.12 ± 1.81 nm, (d) 23.28 ± 1.56 nm, and (e) 23.96 ± 0.94 nm. Figure 8.3F plots the measured silica shell thickness for several TEOS/FePt ratios.

When smaller 2.7 nm diameter FePt nanocrystals were coated with silica, reaction conditions could not be identified to encapsulate individual nanocrystals. Regardless of the FePt concentration and the FePt/TEOS ratio, multiple FePt nanocrystals were encapsulated into the silica shells. Figure 6.4 shows TEM images of typical results.
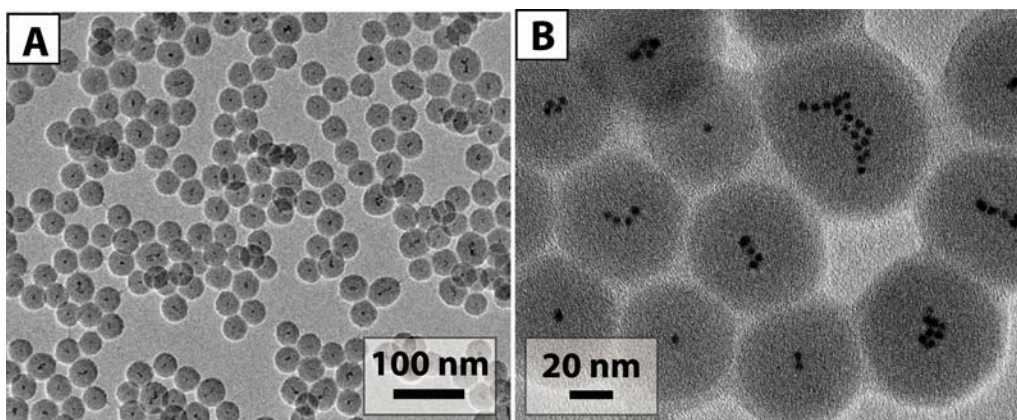
Figure 6.4. TEM images of FePt@SiO$_2$ particles with multiple 2.7 nm diameter FePt nanocrystals. A wide range of FePt concentrations and FePt/TEOS ratios were explored, yet reaction conditions could not be identified to encapsulate individually these smaller FePt nanocrystals in silica spheres.

6.3.2 SiO$_2$ Coating of Co and MnPt$_3$ Nanocrystals

The silica coating chemistry is quite oxidizing—NH$_4$OH is a strong oxidizing agent—and in fact, attempts to coat other metal nanocrystals such as Co and MnPt$_3$ have been failed: they are partially destroyed in the silica formation process. The Co nanocrystal solution became light green when NH$_4$OH was added, indicating the nanocrystals decomposed and Co^{2+} ions were generated. Figure 6.5 shows the TEM images of Co nanocrystals before and after a SiO$_2$-coating experiment. MnPt$_3$ nanocrystals also partially dissolve during the same silica coating procedure. FePt is more robust than Co or MnPt$_3$, but could still be susceptible to surface oxidation.

Annealing under a reducing environment like hydrogen appears to reverse or prevent any oxidation that may occur as a result of the coating step.
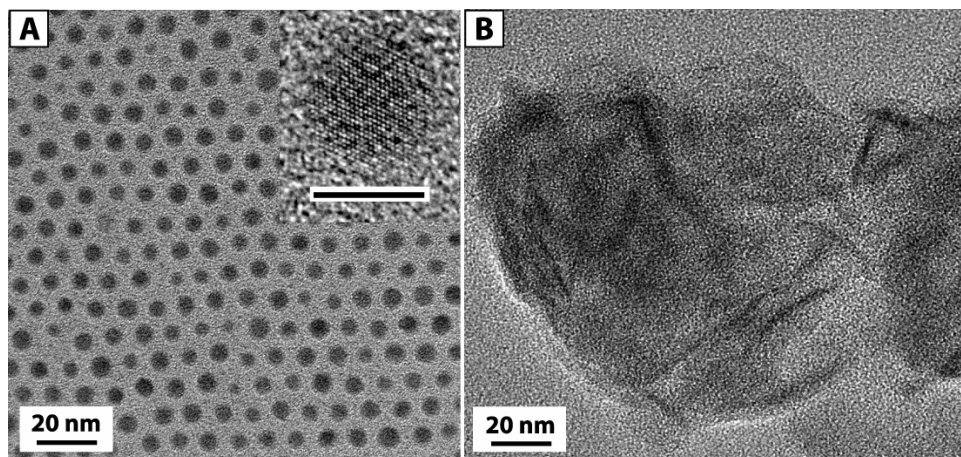
Figure 6.5. TEM images of Co nanocrystals (A) before and (B) after silica coating experiment.   EDS confirmed that the materials in (B) were Co-rich.

6.3.3 Annealing of FePt@SiO$_2$ nanoparticles

6.3.3.1 Annealing under forming gas

To obtain the hard magnetic L1$_0$ FePt phase, the FePt@SiO$_2$ nanocrystals were drop cast onto a silicon wafer and annealed in a tube furnace under 7%/93% H$_2$/N$_2$. Figure 6.6 shows XRD patterns of the FePt@SiO$_2$ nanocrystals annealed at increasing temperature.   First of all, the XRD peak widths do not narrow after annealing—until reaching temperatures of ~1000 °C—indicating that the primary particle size does not change and there is no sintering.   TEM images (Figure 6.7) of FePt@SiO$_2$ nanocrystals annealed at 700 °C confirm that the FePt cores do not sinter.   The silica-coated FePt nanocrystals transform to the L1$_0$ phase at about 650 °C~700 °C.   The unit cell transforms from cubic to tetragonal and the (110) scattering peak that does not appear

from the fcc material, appears at $2\Theta \sim 34°$.   The (111) diffraction peak also shifts to a slightly higher angle, confirming the fcc→$L1_0$ phase transition.
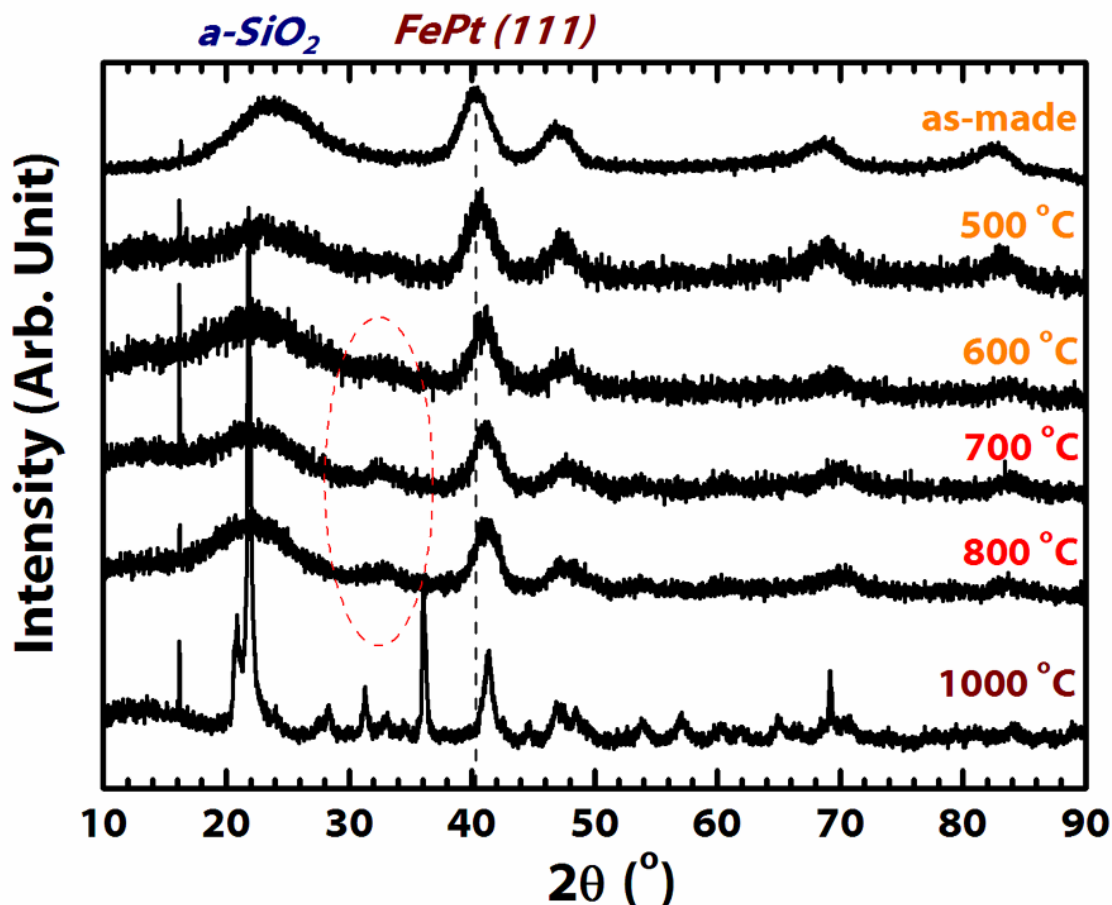
Figure 6.6. XRD patterns of the annealed FePt@SiO$_2$ particles annealed under 7% H$_2$/93% N$_2$ at different temperatures: a phase transition from the random alloy fcc phase to the fct $L1_0$ phase occurs when annealed at 600~700 °C; annealing at 1000 °C led to very sharp diffraction peaks as a result of structural collapse of the silica shell and FePt sintering as confirmed by TEM in Figure 6.7.   The labeled peaks indicate the evolution of the fct FePt phase.   The (111) peak shift supports the occurrence of the phase transition at annealing temperatures between 600 °C and 700 °C.

The silica shell decomposes at ~1000 °C as shown in the TEM image in Figure 6.7E and revealed by the sharp intense diffraction peaks in Figure 6.6.   Additional peaks

in the XRD pattern after annealing at 1000 °C correspond to cristobalite.   At 1000 °C, the SiO$_2$ shell crystallizes and no longer protects the FePt cores from coalescence.
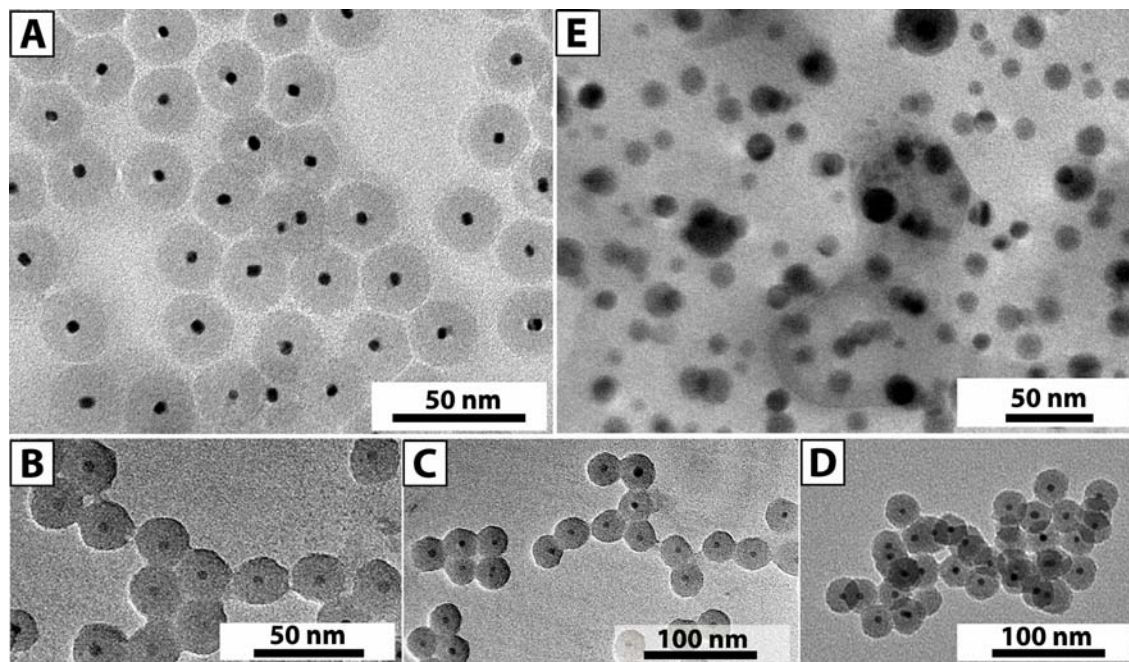
Figure 6.7. FePt@SiO$_2$ nanocrystals annealed under 7%/93% H$_2$/N$_2$ at different temperature. TEM images of (A) as-made FePt@SiO$_2$ particles; (B-D) after annealing at 700 °C; (E) after annealing at 1000 °C.   The FePt cores do not coalesce during 700 °C annealing, but 1000 °C annealing leads to significant FePt particle aggregation and colescence.

6.3.3.2 Annealing under N$_2$ and under air

The SiO$_2$ shell also affects the fcc→L1$_0$ phase transition.   Unlike films of organic monolayer-coated fcc FePt nanocrystals that transform to the L1$_0$ phase when annealed at ~550 °C under nitrogen, the silica-coated FePt nanocrystals did not transform to the L1$_0$ phase when annealed under nitrogen or air—until reaching 1000 °C when the SiO$_2$ shell disintegrated.   The SEM image in Figure 8.8B shows fusion of SiO$_2$ shell near the rim of the film, but most of the particles remain intact after annealing at 700 °C. Figures 6.9 and 6.10 show XRD patterns for FePt@SiO$_2$ nanocrystals annealed under

nitrogen and air, respectively.   The XRD pattern does not change until reaching $1000\,°C$ in either case.   There is a clear difference between the XRD patterns of the FePt@SiO$_2$ nanocrystals annealed under hydrogen compared to nitrogen or air at $700\,°C$ (Figure 6.11).   Annealing under hydrogen was *required* for the fcc→L1$_0$ phase transition of FePt particles coated with silica.

An arguably possible explanation is that hydrogen itself facilitates the fcc→L1$_0$ phase transition, as others have found for FePt films.   Hydrogen atoms have been proposed to enter the FePt lattice and induce local strain to enhance Fe and Pt mobility and structural reordering; however, others studying similar FePt films have proposed that hydrogen simply reduces the presence of oxidized species.   H$_2$ can easily penetrate the SiO$_2$ shell to reach the FePt core during annealing, as the diffusivity of H$_2$ in SiO$_2$ at $700\,°C$ is $3.14×10^{-7}$ cm^2/s and it can access the FePt core in microseconds.
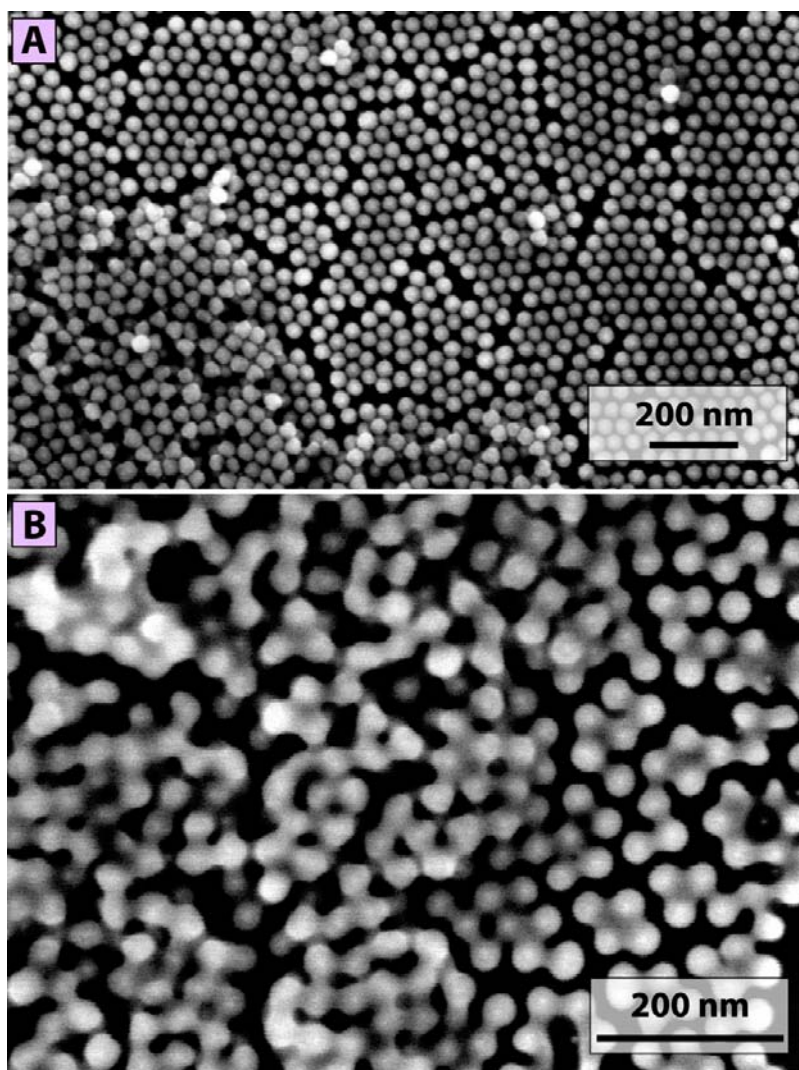
Figure 6.8. SEM images of FePt@SiO₂ particles (A) prior to annealing and (B) after annealing at 700 °C in stagnant air.
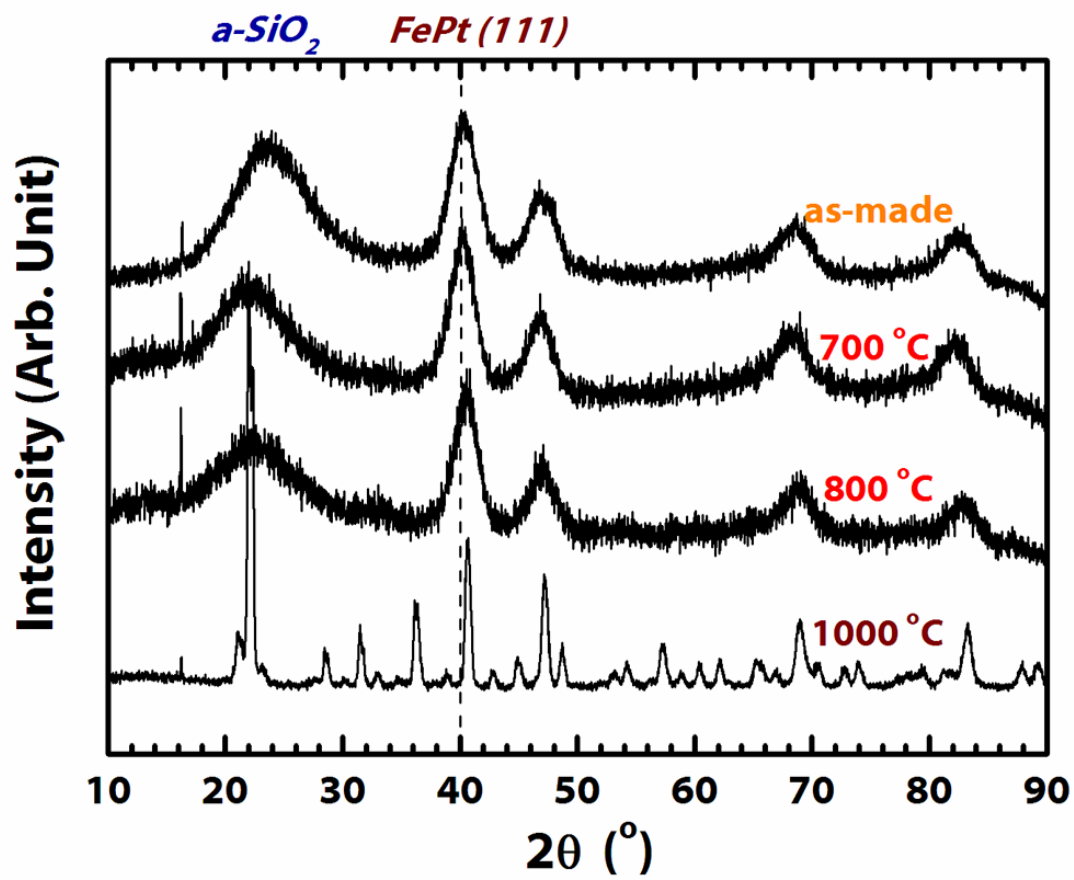
Figure 6.9. XRD patterns of FePt@SiO$_2$ particles annealed under N$_2$.
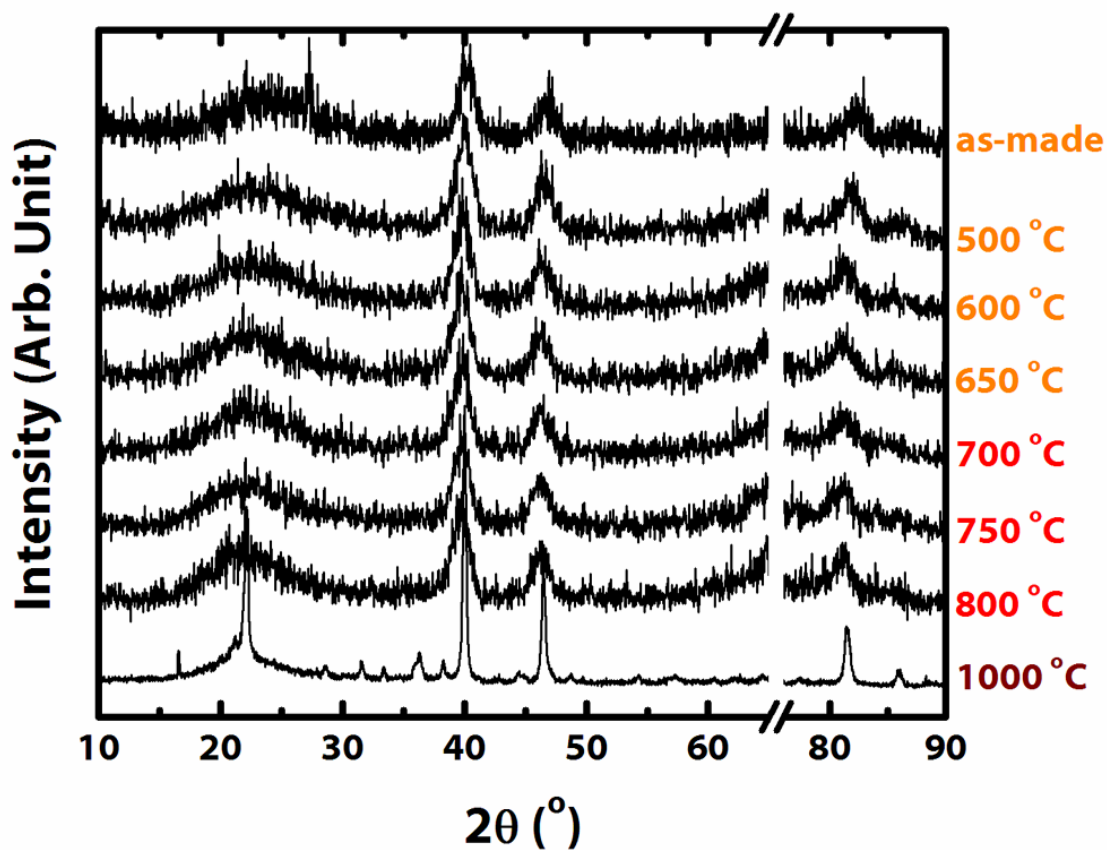
Figure 6.10. XRD patterns of FePt@SiO$_2$ particles annealed under stagnant air.   The particles were deposited onto Si substrate, and the sharp peak from the substrate was removed in a plotting program by putting a break (65°~76°) in the region.
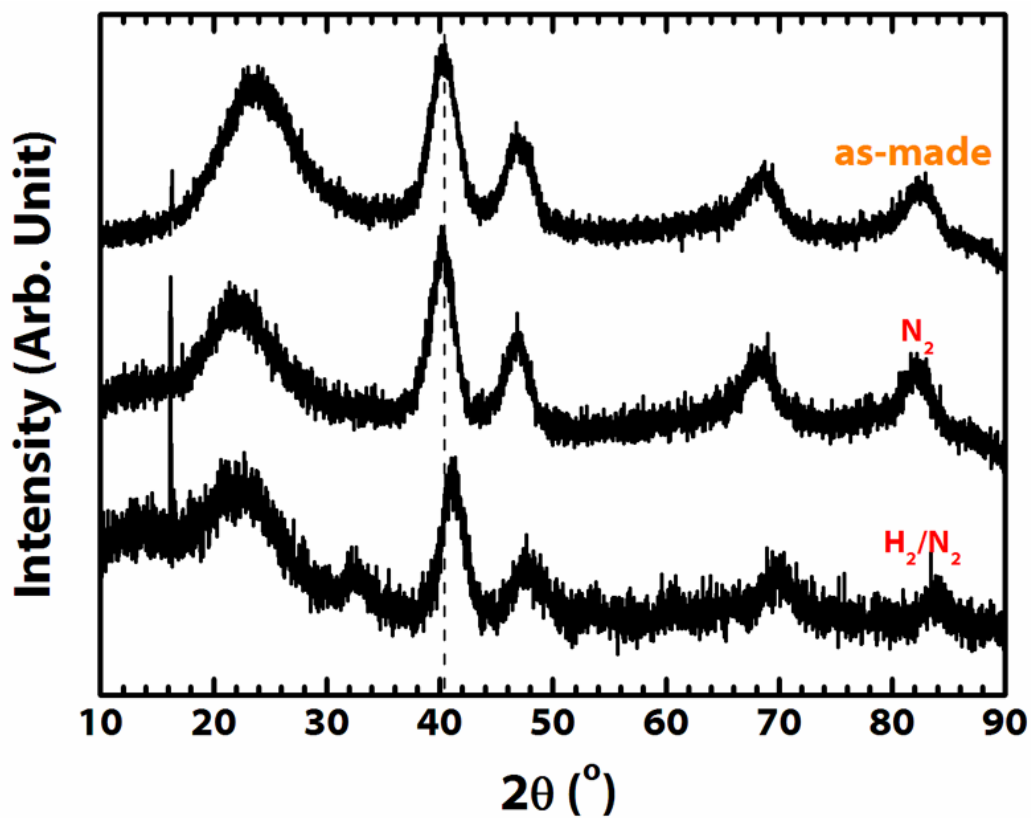
Figure 6.11. XRD patterns of as-made particles, particles annealed at 700 °C under N_2, and particles annealed at 700 °C under hydrogen.   Notice the shift of the FePt (111) peak when the particles were annealed at 700 °C.

6.3.4 Magnetic Properties of FePt@SiO₂ Nanoparticles

6.3.4.1 Field-cooled (FC) and zero field-cooled (ZFC) scans

Figure 6.12 shows field-cooled (FC) and zero field-cooled (ZFC) temperature sweeps of the magnetization under constant applied fields of 1000 Oe.   The as-made FePt@SiO₂ nanocrystals are superparamagnetic at room temperature (Figure 6.12A). The peak in the ZFC scan indicates that the as-made FePt@SiO₂ nanocrystals are superparamagnetic with a blocking temperature of ~30 K.   This agrees with reported magnetic measurements on organic-coated as-made FePt nanocrystals.   Since the FePt

diameter is 6 nm, the magnetocrystalline anisotropy is $\sim 2.3 \times 10^{-3}$ meV/nm^3, which is about four orders of magnitude lower than the bulk value for L1$_0$ FePt (~ 60 meV/ nm^3). At 5 K, which is below the blocking temperature, a field sweep shows hysteresis with a coercivity of ~ 2500 Oe (Figure 6.13A).

Magnetic measurements confirmed that FePt@SiO$_2$ nanocrystals annealed under air or nitrogen at 700 °C did not undergo the fcc→L1$_0$ phase transformation; whereas those annealed under hydrogen were transformed. In fact, annealing under N$_2$ or air *decreased* the blocking temperature and the coercivity significantly (at 5K: H$_c$=1000 Oe (N$_2$) and 200 Oe (air)) relative to the as-prepared sample (Figures 6.12B and 6.12C). Why hydrogen induces the fcc→L1$_0$ phase transition of the silica-coated nanocrystals, whereas nitrogen annealing does not, is not fully understood. Perhaps the oxidative silica coating environment is the reason: the silica treatment in combination with high temperature annealing appears to oxidize some of the FePt core to a softer magnetic material like iron oxide. However, XRD does not show evidence of oxidized species like iron oxide in the FePt@SiO$_2$ nanocrystals annealed under air or nitrogen. It is certainly possible, although unlikely, that small amounts of residual FePt oxidation, undetectable by XRD or TEM, could be responsible for preventing the phase transition under air or nitrogen annealing.

Figure 6.12D shows FC and ZFC scans and field sweeps (at 5 K) on FePt@SiO$_2$ nanocrystals annealed under hydrogen at 700 °C. The coercivity at 5 K has increased relative to the as-made nanocrystals by a factor of three to 8 kOe. The saturation magnetization is large and saturation is not reached, even at applied fields up to 5 T (50 kOe). The FC and ZFC scans indicate that the nanocrystals are superparamagnetic but that the blocking temperature exceeds room temperature, which is confirmed by the

observation of room temperature hysteresis in the field sweeps with relatively high coercivity ($H_c = $ ~2300 Oe).
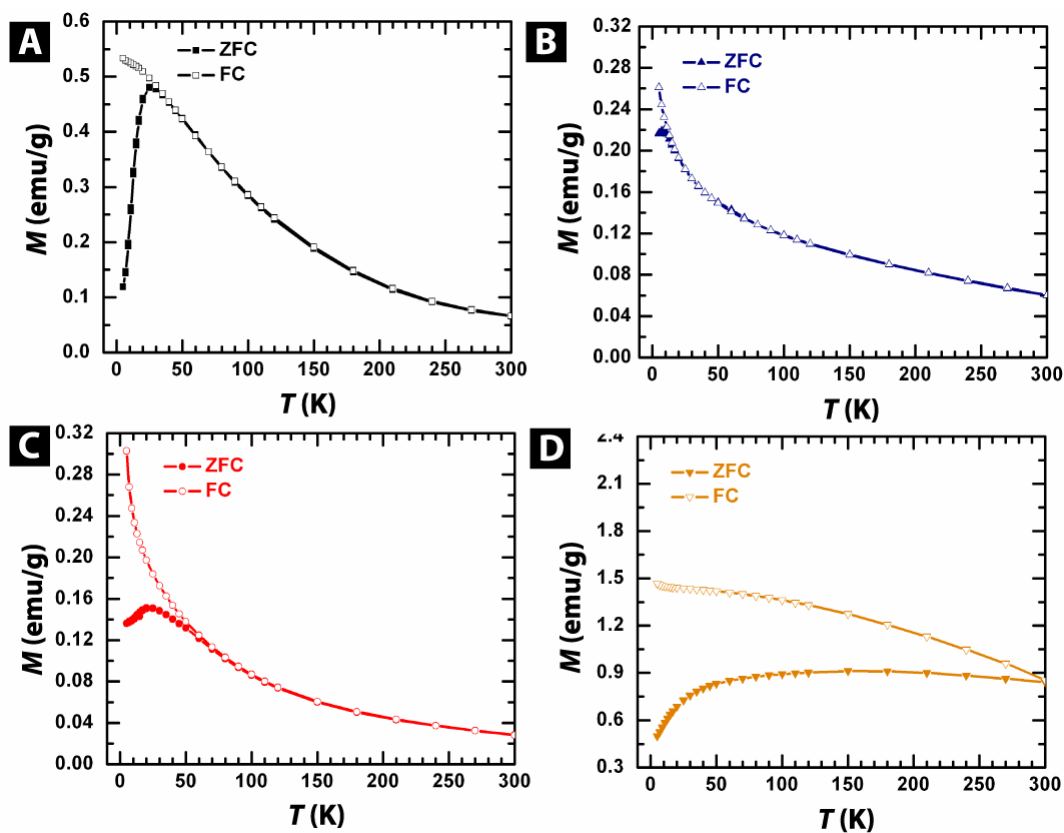
Figure 6.12. Zero-field-cooled (ZFC, filled symbols) and field-cooled (FC, empty symbols) magnetization scans of of FePt@SiO$_2$ particles: (a) as-made and annealed for 1 hr at 700°C in (b) air, (c) N$_2$, and (d) 7%/93% H$_2$/N$_2$. The particles annealed under H$_2$ exhibit a high blocking temperature, magnetic moment and coercivity (~8000 Oe).
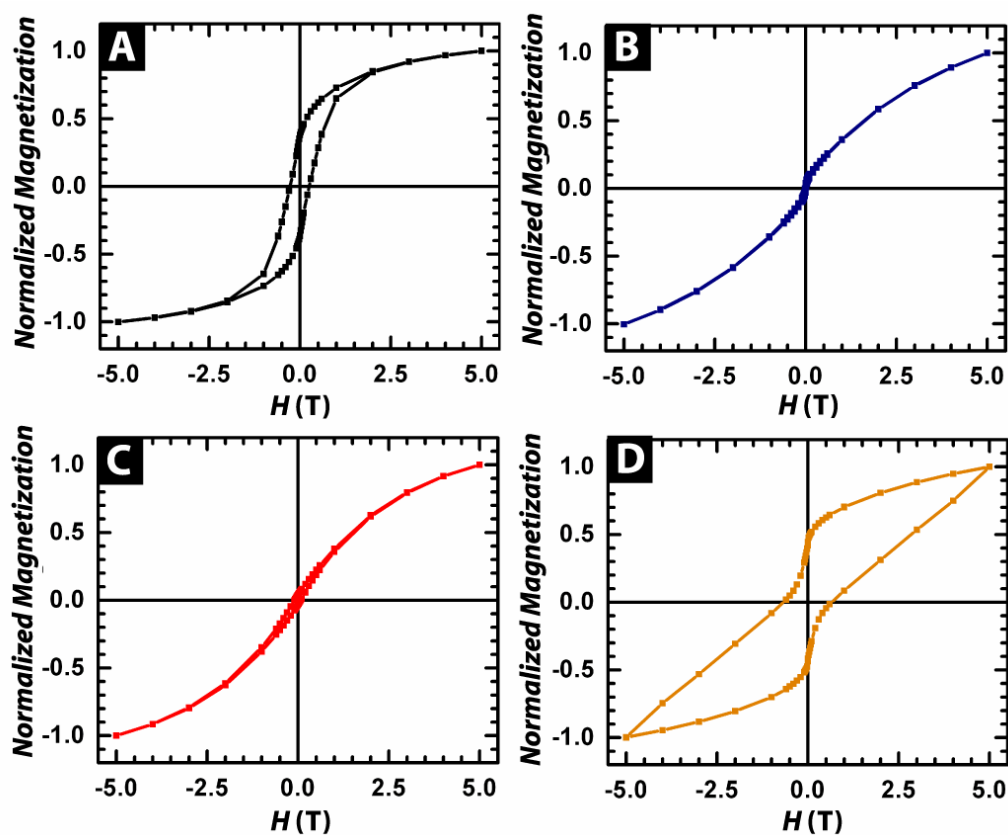
Figure 6.13. Field-sweep magnetization scans acquired at 5K: FePt@SiO$_2$ particles, (A) as-made and annealed for 1hr at 700 °C in (B) air, (C) N$_2$, and (D) 7%/93% H$_2$/N$_2$. The coercivity of the particles decreased when annealed under N$_2$ or air, although the saturation magnetization was higher after N$_2$-annealing than the as-made particles.

6.3.4.2 Constriction in hysteresis scan

The magnetization curves from the L1$_0$ FePt@SiO$_2$ nanocrystals exhibited "constricted" hysteresis loops near zero applied field. The magnetization relaxes more abruptly than expected for a typical ferromagnet when the applied field direction is switched. A similar relaxation of the magnetization was observed recently from 4 nm diameter L1$_0$ FePt nanocrystals obtained from a high temperature synthesis in the gas-phase, which was attributed to a distribution in size or composition in the sample. A

magnetic sample that is a mixture of hard and soft magnetic material (*i.e.*, large and small susceptibility, coercivity, and saturation magnetization) could give rise to these kinds of magnetization curves. For example, the hard magnetic $L1_0$ FePt cores could contain some soft magnetic Fe or iron oxide associated with them, as the remanent field dropped to less than ½ of the saturation magnetization M_{sat} when the field was removed and the coercivity was very low, only ~0.05 T (500 Oe) at 4.3 K. The coercivity of the $L1_0$ FePt@SiO$_2$ nanocrystals on the other hand was typically between 0.5~1 T (5~10 kOe) at 5 K and the remanence was always between 0.4 M_{sat} and 0.5 M_{sat}. For a collection of nanocrystals with random crystallographic orientations, the applied field rotates the magnetic moments into the direction of the field at saturation, which may be away from the magnetic easy axis of the particle—this spin rotation away from the magnetic easy axis could be the reason for the relatively slow rise in magnetization at higher applied fields. When the field is removed, the magnetic moments in each particle relax to their magnetic easy axis, which is the [001] direction in $L1_0$ FePt. For a random (uniform) distribution of magnetocrystalline orientations, one expects a remanence of $\dfrac{2}{\pi} M_{sat}$ (assuming no thermal broadening of the spin orientation distribution), which is close to what is experimentally observed. Furthermore, impurities such as iron oxide and Fe did not show up in the XRD data.

The dipole interaction between the nanoparticles could be responsible for the constricted hysteresis loop. Figure 6.14 shows a schematic of how the magnetic dipole coupling can influence the coercive field (the field strength required to reverse the magnetic spins). Magnetic dipole coupling between neighboring FePt nanocrystals can provide an additional demagnetization field, as dipole coupling favors antiparallel alignment of neighboring spins.
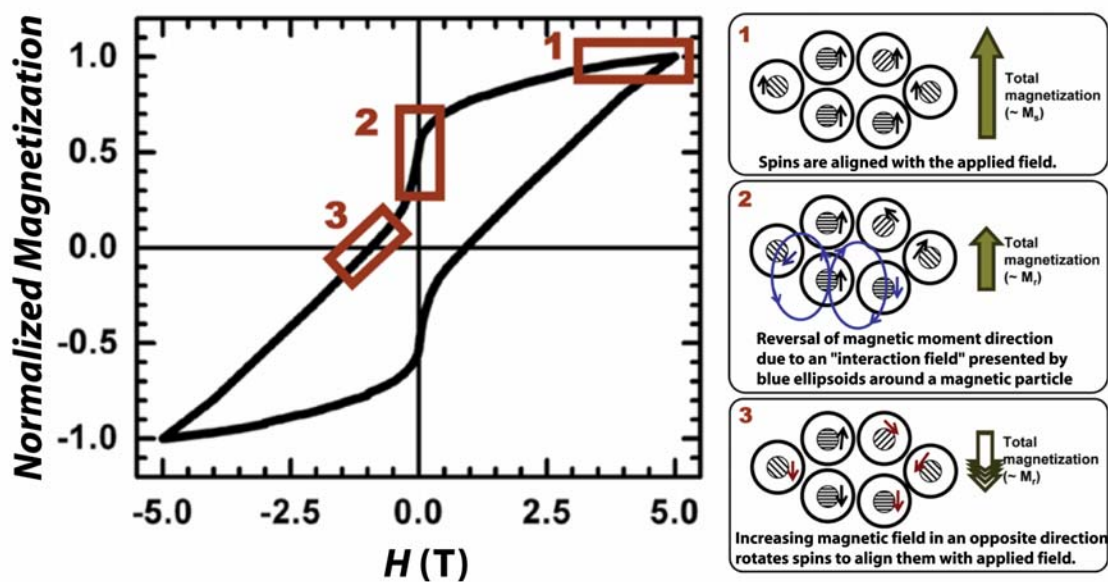
Figure 6.14. Schematic illustration of magnetic dipole interactions in the FePt@SiO$_2$ particle film and their relationship to the M-H curves.

6.3.4.3 Hysteresis scans of L1$_0$ FePt@SiO$_2$ with various shell thickness

The coercivity was observed to be a relatively strong function of silica shell thickness. Figure 6.15 shows the hysteresis scans (measured at 5 K) of FePt@SiO$_2$ particles with thickness ranging from ~4 nm to 25 nm. Certainly, the silica shell thickness determines the magnetic dipole coupling between nanocrystals, which for a bulk magnetic material determines the magnetic domain size and is responsible for ferromagnetic hysteresis. In these nanocrystals, the interparticle separation of several nanometers makes the dipole coupling *between* FePt domains relatively weak compared to the applied field energy and the magnetocrystalline anisotropy energy, yet the dipole coupling is relatively long range and varies as the inverse of the interparticle distance to the third power. Therefore, the dipole coupling between particles with 4 nm silica shells is about 2 orders of magnitude larger than the dipole coupling between particles with 25 nm thick shells. Recall that the FePt core diameter of all the samples shown in Figure

6.15 is the same, at 6 nm. It is very likely that magnetic dipole coupling between neighboring nanocrystals is reducing the coercivity and also leads to the constricted hysteresis loops.The remanence is approximately 0.45 times the saturation magnetization for all the samples, regardless of the shell thickness. As plotted in Figure 8.16, the coercivity measured at 5 K varies from less than 0.1 T for shells less than 5 nm thick up to 1.1 T for 25 nm thick shells. These measurements seem to indicate that the shell thickness significantly affects the coercivity, and most likely the constriction in the hysteresis curves is related to it.
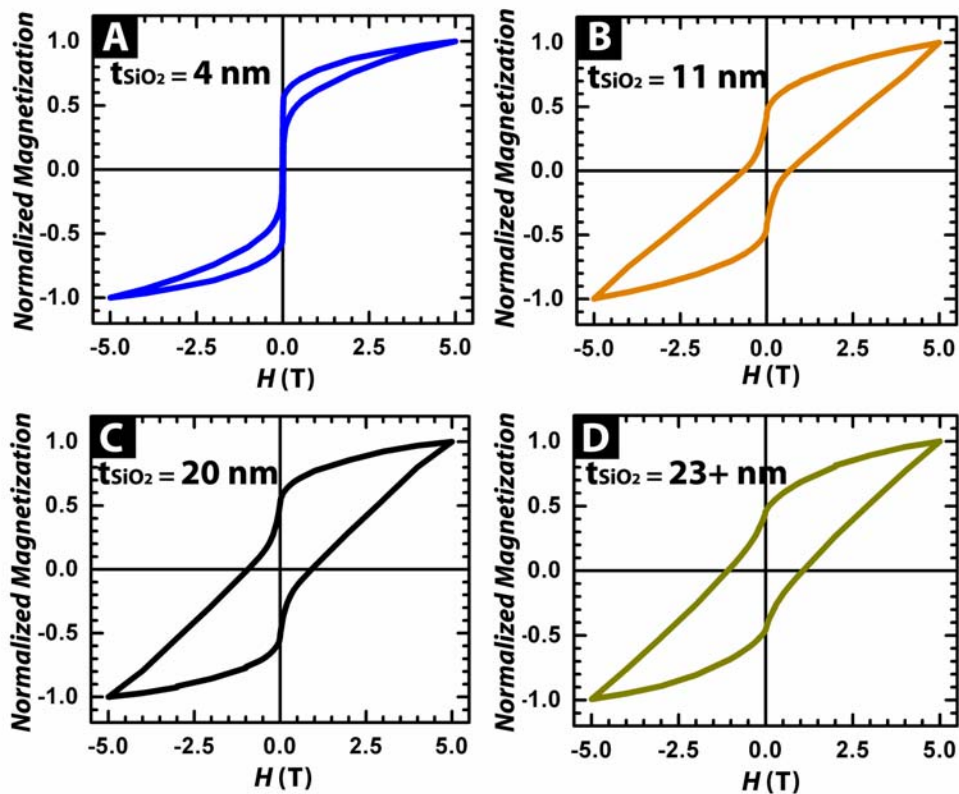
Figure 6.15. M-H curves (5 K) of FePt@SiO$_2$ nanocrystals (6 nm diameter FePt core) with varying silica shell thickness measured after annealing at 700 °C in forming gas for 1 hr.
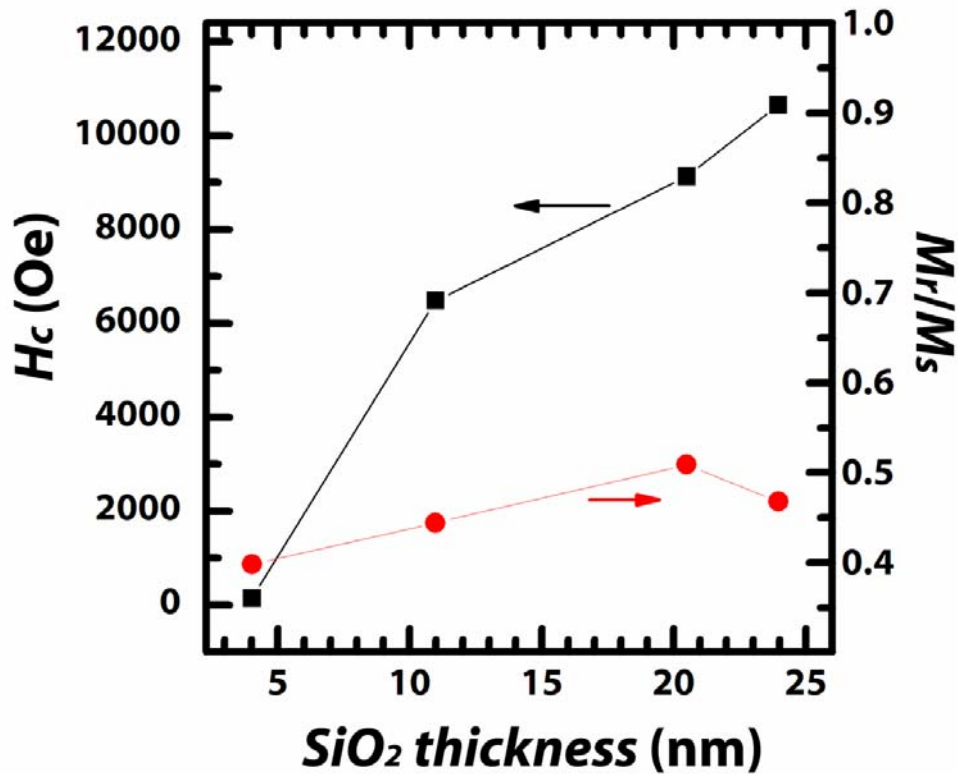
Figure 6.16. The coercivity and normalized remanence measured as a function of SiO_2 thickness.

6.3.5 Magnetic Properties of FePt@SiO$_2$ Particle Films

The magnetic storage media community has witnessed miniaturization of devices. The scaling runs have lately relied on the scaling of components, such as read/write heads. Scaling of magnetic grain size has appeared to be limited by superparmagnetism. The high K_u value of $L1_0$ FePt (7×10^6 J/m^3) allows FePt nanocrystals of 2.8 nm diameter to remain ferromagnetic at room temperature with a storage time of ~10 yrs. This single-domain feature is difficult to study with organic-passivated colloidal FePt nanocrystals because of the sintering at high-temperature annealing. FePt@SiO$_2$ thus provides a good testbed for the high areal-density applications. It is very important to study the magnetic properties of the films of FePt@SiO$_2$ particles. Magnetic force

microscopy (MFM) offers the capability of monitoring magnetization of small features. MFM has been used in the study of thin-film magnets.

A Digital Instruments microscope was used for the MFM measurements under ambient conditions. A monolayer of the particles, however, does not produce enough signal for the instrument to detect. Therefore, multi-layered particles were prepared by drop-casting on an insulating MICA substrate. Figure 6.17A shows AFM image of parts of an island (15 μm × 3.75 μm × 2.5 μm). An 8 T external field was applied along the film plane or normal to the plane prior to measurements. The field was then removed to allow the particles to reach remanence magnetization. An MFM tip (CoCr-coated, Veeco) was magnetized downward and phase shift of oscillating cantilever and the corresponding section analysis were recorded as the tip scans across the film as shown in Figure 6.17C, D, E, and F after the field was applied to the left, right, up, and down, respectively. In the "floating mode," in which the MFM tip was rastered at a fixed distance from the average sample surface and the tip did not trace the topography of the sample, the tip traced a flat rectangle at a distance 450~600 nm from the film surface. The line profile in the section analysis is an average of the scans contained between the two white lines in the MFM image. The dark and bright contrast along the edges of the film represents a phase shift due to the interaction between the MFM tip and the FePt nanocrystals.

The spatial resolution of the MFM tip was about ~30 nm and therefore only the average effect of many FePt nanocrystals was seen. Since the easy axes of the nanocrystals are randomly oriented, the film behaves as a composite with no average magnetocrystalline anisotropy. Consequently, the average remanent moment remains pointed in the direction of the external field that was last applied to saturate the individual moments. Magnetizing the film to opposite directions along the film results in inverted

phase shift patterns (Figures 6.17C and D). When the film was magnetized perpendicular to the surface, either upward or downward, the phase shift patterns also changed according to the magnetization direction as shown in Figures 6.17E and F. When the magnetization direction of the MFM tip was reversed to the upward direction, all the phase shift patterns were also inverted, as expected. Although the data suggest a strong dipole interaction at the rim of the island, there is no evidence of any domain-wall structure, which is usually seen on continuous ferromagnetic materials. To realize the measurement of the individual nanoparticles, the high-resolution MFM measurements or a cryogenic device system would be indispensable.
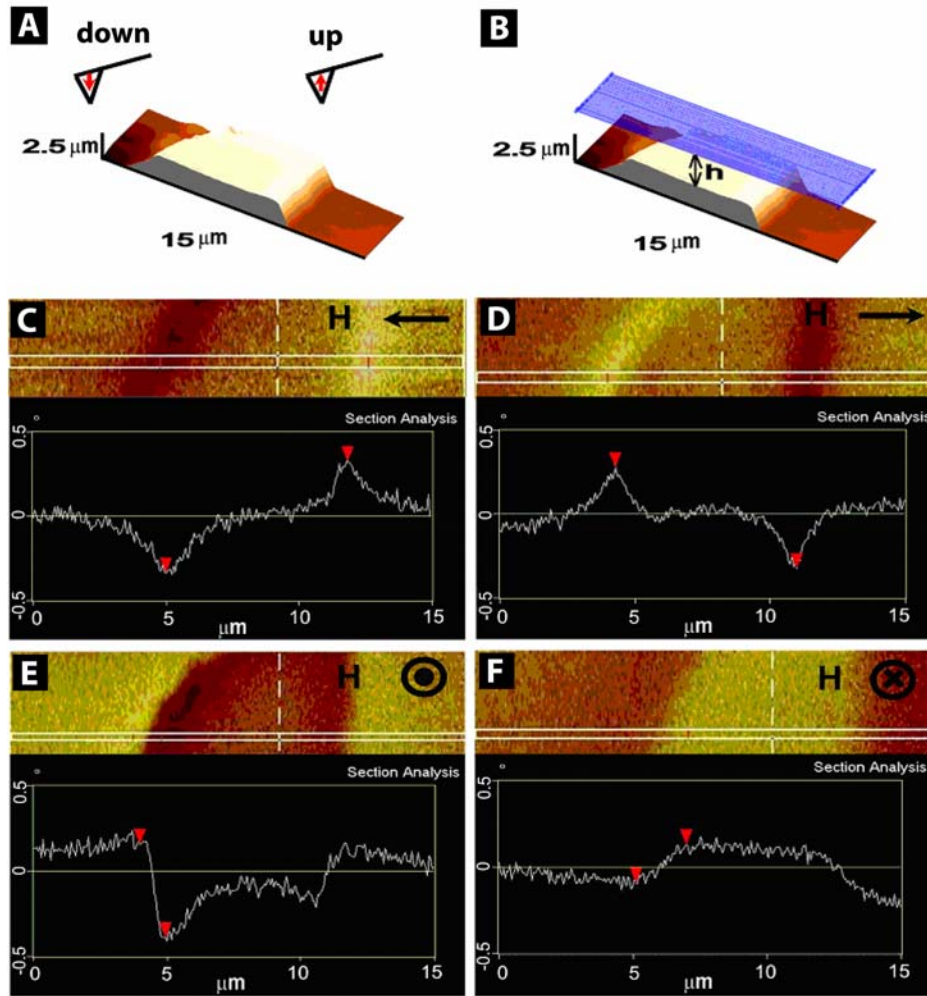
Figure 6.17. (A) Topography of a part of an island in a 2.5 μm-thick film.   The tip can be magnetized upward or downward.   (B) Schematic of the floating mode used to obtain the data, where h is the distance above the film surface.   (C), (D), (E), and (F) show the phase shift of the oscillating cantilever in the floating mode, and the corresponding section analysis, obtained at zero field after applying 8 Tesla to the left and to the right along the film plane, and up and down in the direction perpendicular to the film plane, respectively.   The line profile in the section analysis is the average between two horizontal white lines in the MFM image.   MFM images courtesy of C. Hyun.

6.3.6 Film Morphology

6.3.6.1 Spin casting of FePt@SiO$_2$ particle dispersion in ethanol

The as-made FePt@SiO$_2$ particles disperse in ethanol/water solutions, but exhibit a high degree of aggregation and sticking.   Since drop-casting of the particle dispersion generally results in poor films, other film deposition techniques have been attempted. Spin coating, for example, yielded a slightly better assembly (Figure 6.18).   However, the ordering was relatively in a very small range, and it was hard to find working parameters for getting any useful coverage.   At a low spin speed, e.g. 200 rpm, the particles were aggregated, while at a high speed, e.g. 1000 rpm, the coverage was not good and the area density was too low.

6.3.6.2 Evaporation of FePt@SiO$_2$ particle dispersion in ethanol

Alternatively, particle suspensions in concentrations ranging from 0.5 mg/mL to 4.0 mg/mL were allowed to evaporate while a Si substrate was immersed in a vertical direction, so as to minimize the sedimentation of aggregated particles.   SEM images of the resulting films are shown in Figure 6.19.   At a concentration of 4.0 mg/mL, a very thick layer of the particles formed on the substrate.   Some of the thick layers were relatively well-arrayed (Figure 6.19B), while in other areas layers had rough morphology. As the concentration of the dispersion decreased, the thickness of the deposition correspondingly decreased.   At 1.0 mg/mL, pretty uniform mololayer was formed, and in some areas the particles were relatively close-packed (Figures 6.19C and D).   At an even lower concentration, 0.5 mg/mL, the film demonstrated sub-monolayer coverage on the most of the substrate, leaving islands of monolayered particles (Figure 6.19E)
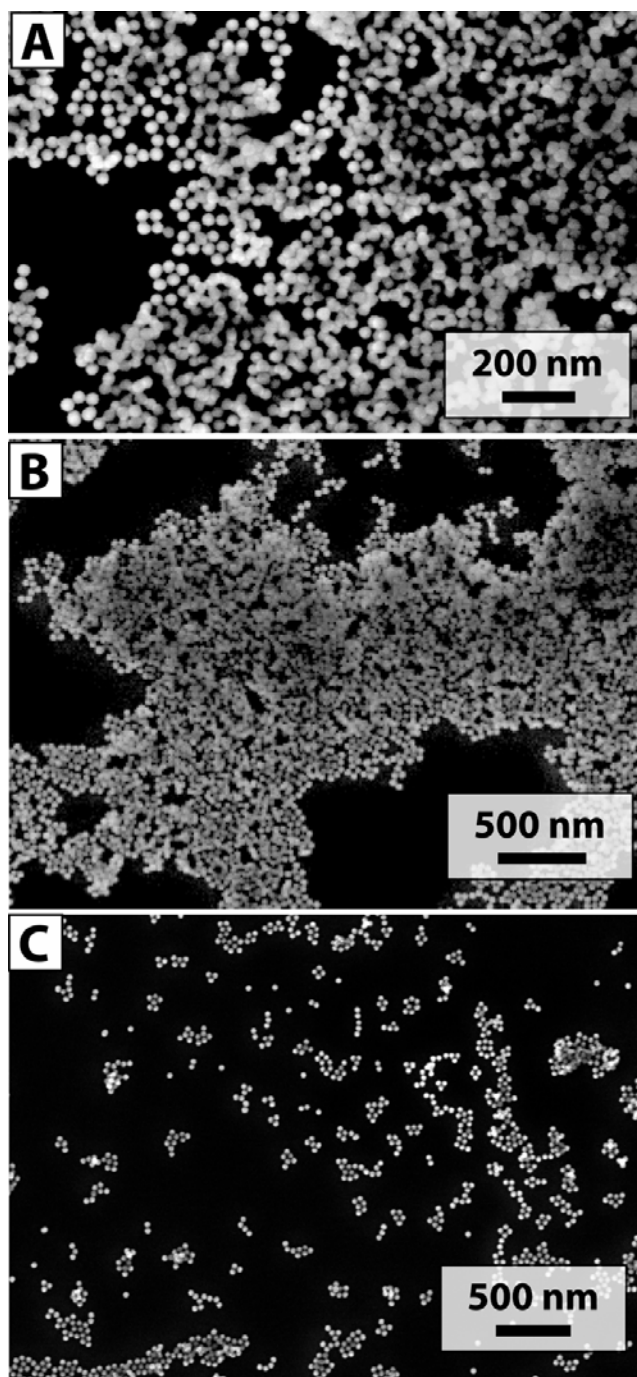
Figure 6.18. SEM images of 1 mg/mL ethanol suspension of FePt@SiO$_2$ particles spin-cast on Si substrates at a spin speed of (A) 200 rpm, (B) 500 rpm, and (C) 1000 rpm.

161
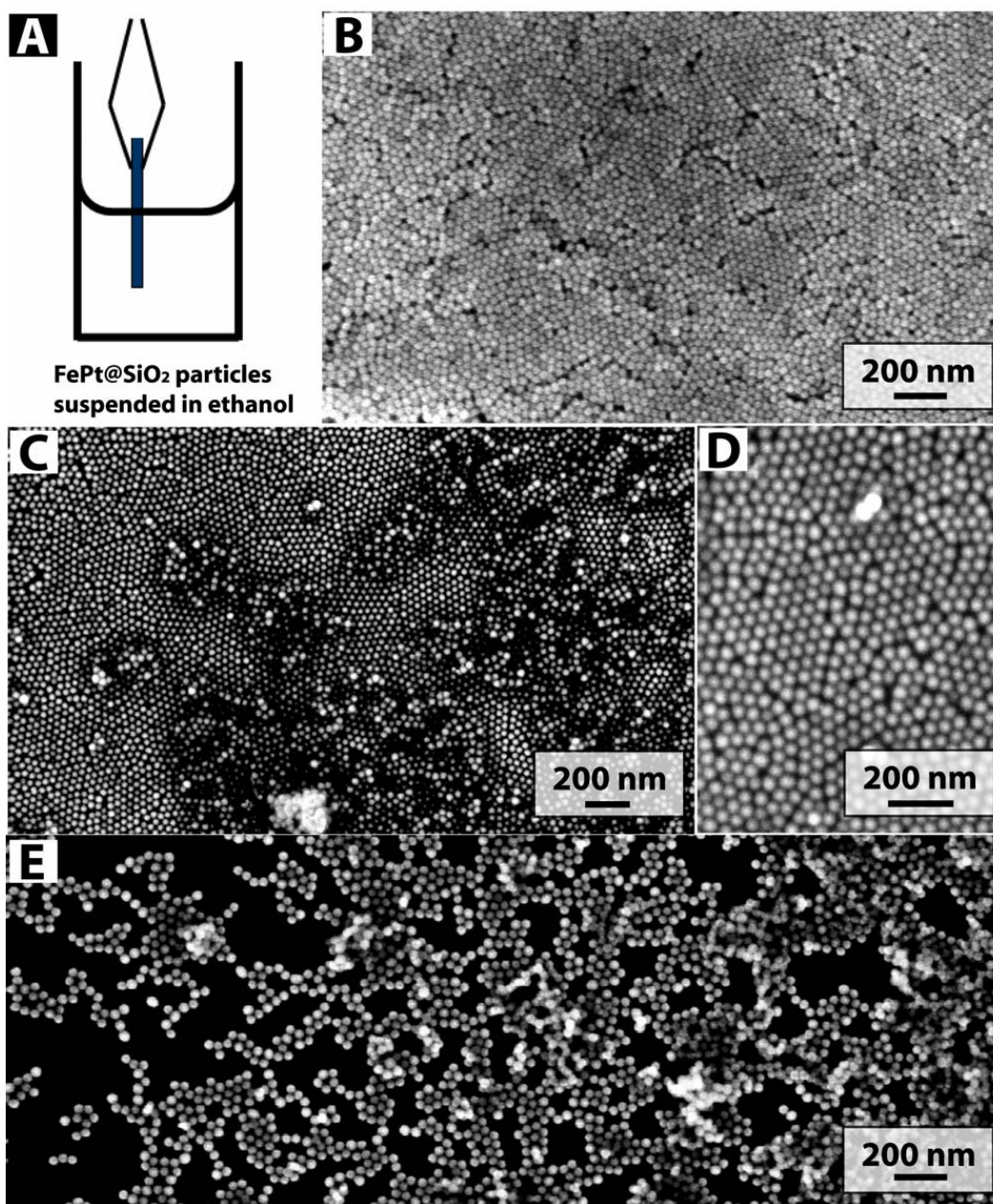
Figure 6.19. (A) Schematic of FePt@SiO$_2$ particle film deposition process.   A Si
substrate was immersed vertically into an ethanol suspension of the particles at
the concentration of (B) 4.0 mg/mL, (C-D) 1.0 mg/mL, and (E) 0.5 mg/mL.
The concentration of 1.0 mg/mL offered relatively good packing of the
particles.   4.0 mg/mL and 1.0 mg/mL concentrations resulted in thicker layers
and low coverage, respectively.

6.3.6.3 Surface treatment of FePt@SiO₂ particles

Despite the progress in developing techniques to deposit a relatively better layer of the silica-coated particles, the need of free-standing FePt@SiO$_2$ particles with better dispersion still remains.   Wang *et al.* have developed a procedure for chemically treating silica colloids using octadecyltrimethoxysilane (OTMOS).   The siloxane functional groups of OTMOS react with the silica surface when the particles are dispersed in chloroform for 24 hrs.   The hydrophobic tails are then exposed at the surface to make the FePt@SiO$_2$ particles hydrophobic with good dispersibility in chloroform or hexane. Figure 6.20 shows dispersions of as-made FePt@SiO$_2$ particles in an alcohol solution and OTMOS surface-functionalized particles in organic solvents.   Dispersions of the OTMOS treated particles remained optically clear for months, while particles without surface treatment sedimented in one day.   The SEM images in Figures 6.20D and E also show that the surface-treated particles form monolayers with better organization upon drop-casting than the particles with untreated surfaces.
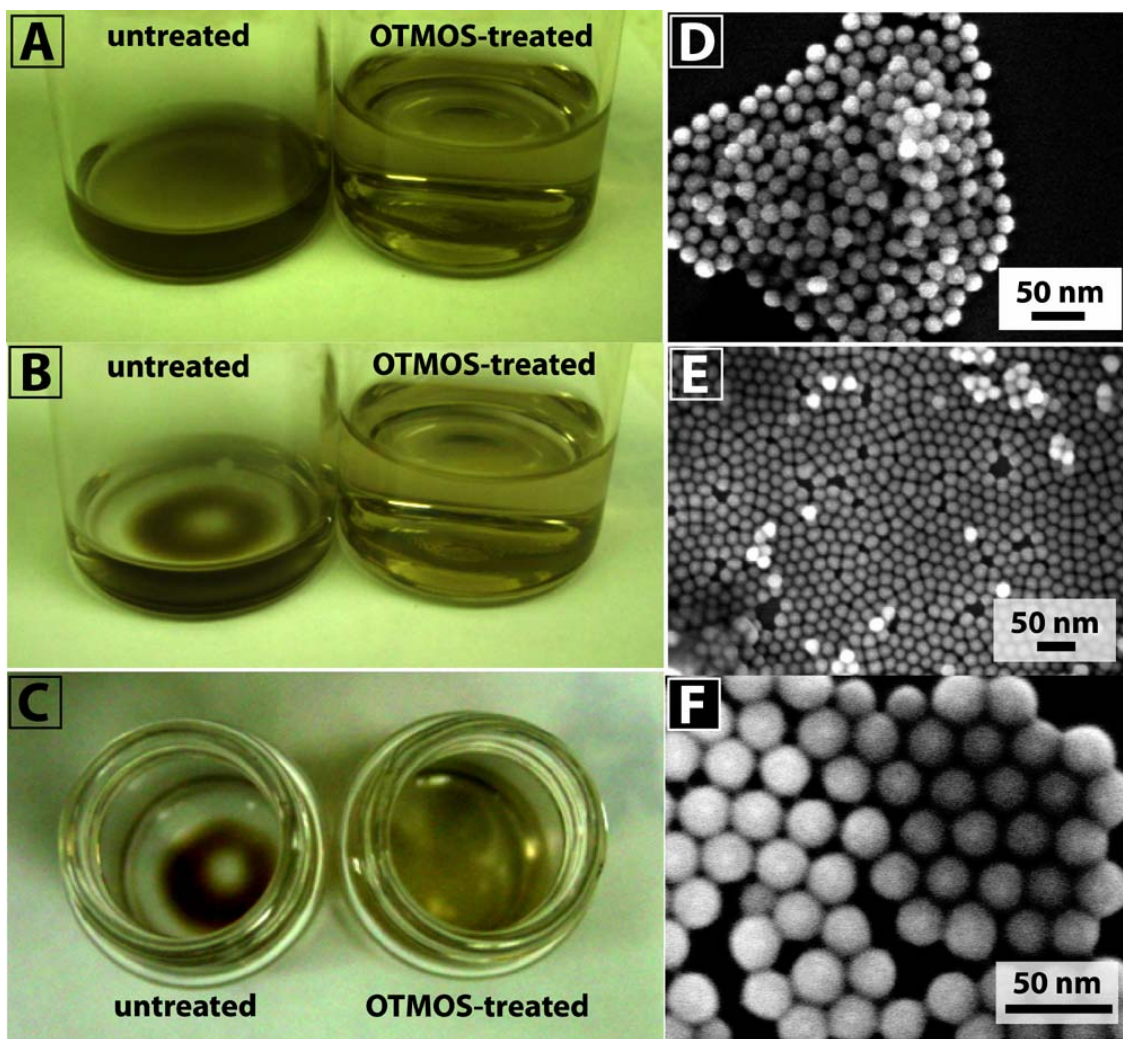
Figure 6.20. (A-C) Photographs of as-made and OTMOS-treated FePt@SiO$_2$ particles. Untreated particles were in ethanol, and OTMOS-treated ones in CHCl$_3$. (B) and (C) show the particle dispersions after 24 hrs. Surface treatment makes the particles hydrophobic and prevents the flocculation that occurs with untreated particles. SEM images of drop-cast particles (E) with and (E-F) without OTMOS treatment. The particles without surface functionalization tend to aggregate and do not crystallize into ordered structures.

164

6.4 CONCLUSIONS

Silica coatings were applied to colloidally-grown oleic acid/oleylamine capped FePt nanocrystals to prevent sintering during the high temperature annealing required to convert the FePt core from the compositionally disordered, soft magnetic, fcc phase to the compositionally layered, tetragonal, hard magnetic $L1_0$ phase. The silica coating prevents sintering at temperatures up to >850 °C. Interactions within films of the FePt@SiO$_2$ particles have also been studied using magnetic force microscopy (MFM). The signal from clusters of the particles was detectable, but the signal from an individual particle was below the detection limit of the MFM instrument. However, the MFM data suggests the existence of dipole interaction in the clusters. The silica shell could be modified with hydrophobic ligands (*i.e.*, OTMOS) for good dispersibility in organic solvents. The magnetic measurements indicate that the coercivity is strongly dependent on the FePt separation set by the silica layer thickness, most likely due to differences in magnetic dipole coupling between FePt domains. The approach outlined here for silica shell growth could offer a general platform for obtaining better thermal stability of many different nanocrystals in thin films for high-temperature processing. However, the oxidizing environment in the silica shell growth process may be a limitation of the effectiveness of this particular shell growth chemistry. Other less basic catalysts other than NH_4OH might be useful for other materials systems.

6.5 REFERENCES

(1)   Zeng, H.; Sun, S. H.; Li, J.; Wang, Z. L.; Liu, J. P., *Appl. Phys. Lett.* **2004,** 85, 792.

(2)   Lambeth, D. N.; Velu, E. M. T.; Bellesis, G. H.; Lee, L. L.; Laughlin, D. E., *J. Appl. Phys.* **1996,** 79, 4496.

(3)   Sun, S. H.; Murray, C. B.; Weller, D.; Folks, L.; Moser, A., *Science* **2000,** 287, 1989.

(4)   Sun, S., *Adv. Mater.* **2006,** 18, 393.

(5)   Perez-Dieste, V.; Castellini, O. M.; Crain, J. N.; Eriksson, M. A.; Kirakosian, A.; Lin, J. L.; McChesney, J. L.; Himpsel, F. J.; Black, C. T.; Murray, C. B., *Appl. Phys. Lett.* **2003,** 83, 5053.

(6)   Konno, T. J.; Sinclair, R., *Acta Metallur. Mater.* **1995,** 43, 471.

(7)   Yan, Q.; Kim, T.; Purkayastha, A.; Ganesan, P. G.; Shima, M.; Ramananth, G., *Adv. Mater.* **2005,** 17, 2233.

(8)   Takahashi, Y. K.; Ohnuma, M.; Hono, K., *J. Magn. Magn. Mater.* **2002,** 246, 259.

(9)   Nguyen, H. L.; Howard, L. E. M.; Giblin, S. R.; Tanner, B. K.; Terry, I.; Hughes, A. K.; Ross, I. M.; Serres, A.; Burckstummer, H.; Evans, J. S. O., *J. Mater. Chem.* **2005,** 15, 5136.

(10)   Reiss, B. D.; Mao, C.; Solis, D. J.; Ryan, K. S.; Thomson, T.; Belcher, A. M., *Nano Lett.* **2004,** 4, 1127.

(11)   Mizuno, M.; Sasaki, Y.; Yu, A. C. C.; Inoue, M., *Langmuir* **2004,** 20, 11305.

(12)   Chen, M.-P.; Kuroishi, K.; Kitamoto, Y., *IEEE Trans. Mag.* **2005,** 41, 3376.

(13)   Elkins, K.; Li, D.; Poudyal, N.; Nandwana, V.; Jin, Z. Q.; Chen, K. H.; Liu, J. P., *J. Phys. D* **2005,** 38, 2306.

(14)   Liu, C.; Wu, X. W.; Klemmer, T. J.; Shukla, N.; Weller, D.; Roy, A. G.; Tanase, M.; Laughlin, D., *Chem. Mater.* **2005,** 17, 620.

(15)   Zeng, H.; Li, J.; Wang, Z. L.; Liu, J. P.; Sun, S., *Nano Lett.* **2004,** 4, 187.

(16)   Chen, M.; Liu, J. P.; Sun, S. H., *J. Am. Chem. Soc.* **2004,** 126, 8394.

(17)   Tago, T.; Hatsuta, T.; Miyajima, K.; Kishida, M.; Tashiro, S.; Wakabayashi, K., *J. Am. Chem. Soc.* **2002,** 85, 2188.

(18)   Yi, D. K.; Selvan, S. T.; Lee, S. S.; Papaefthymiou, G. C.; Kundaliya, D.; Ying, J. Y., *J. Am. Chem. Soc.* **2005,** 127, 4990.

(19)   Yi, D. K.; Lee, S. S.; Papaefthymiou, G. C.; Ying, J. Y., *Chem. Mater.* **2006,** 18, 614.

(20)   Aslam, M.; Fu, L.; Li, S.; Dravid, V. P., *J. Colloid. Int. Sci.* **2005,** 290, 444.

(21)   Yamamoto, S.; Morimoto, Y.; Ono, T.; Takano, M., *Appl. Phys. Lett.* **2005,** 87.

(22)   Wang, W.; Gu, B. H.; Liang, L. Y.; Hamilton, W., *J. Phys. Chem. B* **2003,** 107, 3400.

(23)   Osseo-Asare, K.; Arriagada, F. J., *J. Colloid. Int. Sci.* **1999,** 218, 68.

(24)   Arriagada, F. J.; Osseo-Asare, K., *J. Colloid. Int. Sci.* **1999,** 211, 210.

(25)   Leistner, K.; Thomas, J.; Schlorb, H.; Weisheit, M.; Schultz, L.; Fahler, S., *Appl. Phys. Lett.* **2004,** 85, 3498.

(26)   Lai, C. H.; Wu, Y. C.; Chiang, C. C., *J. Appl.   Phys.* **2005,** 97.

(27)   Vedantam, T. S.; Liu, J. P.; Zeng, H.; Sun, S., *J. Appl.   Phys.* **2003,** 93, 7184.

(28)   Doremus, R. H., *Diffusion of Reactive Molecules in Solids and Melts*. John Wiley & Sons, Inc.: New York, 2002.

(29)   Stappert, S.; Rellinghaus, B.; Acet, M.; Wassermann, E. F., *J. Cryst. Growth* **2003,** 252, 440.

(30)   Nalwa, H. S., *Magnetic Nanostructures*. American Scientific Publishers: New York, 2002.

(31)   Shima, T.; Takanashi, K.; Takahashi, Y. K.; Hono, K.; Li, G. Q.; Ishio, S., *J. Magn. Magn. Mater.* **2003,** 266, 171.

(32)   de Lozanne, A., *Microscopy Research and Technique* **2006,** 69, 550.

(33)   Wiesendanger, R., *MRS Bull.* **1997,** 22, 31.

Chapter 7: Conclusions and Future Research Directions

7.1 CONCLUSIONS

Nanoscale materials exhibit interesting size- and shape-dependent properties, such as energy level quantization. Because of their unique electrical, optical and mechanical properties, they have been regarded as novel materials for several new technologies in widely diverse application areas. The applications require effective and tunable synthesis methods that enable control over composition, size, and properties. Availability of cost-effective synthesis also provides technological advantages.

Solution-based approaches are thought to be a testbed for large-scale, low-cost manufacturing of nanomaterials, and synthesis of a few classes of nanomaterials has been demonstrated in a technologically meaningful scale. The solution-based synthesis methods are capable of producing large quantities of materials with controlled surface chemistry because the precursor dispersibility significantly exceeds that in gas-phase approaches.

The research presented in this dissertation aimed to demonstrate the controlled synthesis of silicon and carbon nanomaterials in solution phase, and discussed the possibility of scale-up of the explored synthetic approaches. With magnetic colloidal nanocrystals, the collective properties of nanomaterials were examined and the control over the properties was demonstrated.

7.1.1 Silicon Nanowires

Silicon nanowires have attracted a great deal of attention since the refreshed synthetic methods were developed by the Lieber group. They studied the growth of silicon nanowires in gas phase with a good control over the nanowire diameter and

surface roughness. In 2000, Holmes et al. translated the reaction parameters into a supercritical fluid system, in which free-standing Au nanocrystals were reacted with diphenylsilane in supercritical cyclohexane. Their experimental results were very interesting because there had rarely been a successful synthesis of crystalline silicon nanomaterials in solution. However, both the quantity and quality of the product remained to be improved. Therefore, it was critical to identify a good reaction parameter window for the SFLS synthesis. This work addressed the optimum temperature and flow rate for Si nanowire synthesis, as described in Chapter 2. Several different silicon precursors were alternatively reacted to understand the effect of precursor decomposition. It turned out that the precursor decomposition was pivotal in determining the morphology of final product. Alkylated silanes have too strong C-Si bond that is impossible to thermally cleave under the reaction conditions; therefore, there is little reaction product and few silicon nanowires. On the other hand, trisilane is very reactive and at the reaction temperatures (350 ~ 500 °C), the molecule forms amorphous silicon particles. Although reactive, trisilane does not break into silicon atoms because Si-Si bond is still thermodynamically stable. Arylated silanes demonstrated significant improvement in the nanowire production over other precursor classes. Phenylsilane and diphenylsilane both have Si-C bonds, which are still relatively strong to thermolyze at the reaction temperatures. However, the arylsilanes have been known to undergo disproportionation reaction, where a phenyl group transfers to other arylsilanes to reduce to silanes.

The synthesis capabilities of the supercritical fluid reactor were extended to prepare the silicon nanowires in continuous flow through reactions. This versatility offers a possibility to grow the nanowires in large quantities. In fact, the growth has been scaled up in the case of germanium nanowires where the growth conditions are

169

relatively more forgiving than the case of silicon. Growth of silicon nanowires with various metal nanoparticles as seeds was also presented. Most of the transition metal nanoparticles have a eutectic temperature far above the reaction temperature used in the study. It is believed that the solution-phase diffusion of silicon atoms was responsible for the growth of silicon nanowires in some metals.

7.1.2 Carbon Nanotubes

Due to their interesting electronic, mechanical, and structural properties, carbon nanotubes have been extensively studied by many research groups. The growth reaction has relied on the gas-phase degradation of carbon sources at relatively high temperatures (700 ~ 2000 °C). Recently, CVD approaches demonstrated successful reactions at a relatively low reaction temperature (650 ~ 700 °C), and opened a possibility of synthesizing these materials in the pressurized solution. In supercritical fluid, multiwall carbon nanotubes and amorphous carbon nanofilaments were both produced (Chapter 4). Toluene was used both as a reaction medium and carbon source for the nanotube growth. At temperatures equal to or above 600 °C, multiwall carbon nanotubes were formed under a ferrocene concentration of ~2.5 mM in toluene. The production yield and selectivity of nanotubes in the total product both increased when the reaction was carried out in a continuous flow-through reactor.

7.1.3 Magnetic Nanocrystals

Magnetic nanocrystals constitute an interesting class of materials, since magnetic storage media are developed in such a way that magnetic domain size decreases to an amazingly small size. Colloidal synthesis of magnetic nanoparticles enables the fabrication of the crystal grains in a 1-nm precision. In the past decade or so, colloidal synthesis has proven to be an excellent route to synthesize crystals in a uniformity

otherwise hard to achieve. Although 3~4 nm nanocrystals are sufficiently small enough for the high areal density applications, processing of nanocrystals poses a problem: as nanocrystal size becomes small, magnetic energy gets correspondingly small and starts competing against thermal energy. This so-called superparamagnetism renders the magnetization weak and nanocrystals far less attractive for the desired storage applications. In order to overcome the superparamagnetism, high magnetocrystalline anisotropy (K_u) materials should be introduced. FePt and MnPt$_3$ fall into those high K_u materials, and the nanocrystals of the platinide alloys were successfully synthesized via a previously reported recipe or a modified version. However, as-synthesized colloidal nanocrystals exhibited low magnetization because they had compositionally disordered crystal structures. To transform the crystal structures into chemically ordered ones, the nanocrystals were annealed at elevated temperatures of ~580 °C. The crystal structure transformed from chemically disordered cubic to compositionally ordered structures, which were verified by X-ray diffraction studies; however, the nanocrystals sintered at the high-temperature annealing. As discussed in Chapter 5, the sintering led to loss of control over the nanocrystal size.

Chapter 6 reports the encapsulation of the colloidal FePt nanocrystals in amorphous silica. Water-in-oil microemulsions were exploited to grow the amorphous silica shell around the colloidal nanocrystals. The shell thickness could be controlled by changing silicon precursor (tetraethylorthosilicate, TEOS) and FePt nanocrystals: the more TEOS used relative to FePt nanocrystals, the thicker the silica shell that was grown. Annealing experiments revealed that the silica-coated particles did not sinter when annealed at as high as 800 °C, while the crystals underwent phase transformation to compositionally layered structures, which in turn exhibited the desired hard magnetic properties.

Silica-coated nanocrystals exhibited interesting magnetic properties. The magnetic field sweep scan showed constriction at a near-zero applied field. The significant drop in total magnetization was attributed to a few hypothetical reasons: 1) as magnetic nanocrystals are separated by a diamagnetic silica shell, the dipole interactions between the nanocrystals come into play and flip the neighboring magnetic moment to decrease the overall magnetic moments; 2) as-synthesized FePt nanocrystals have composition distribution, where portions of the nanocrystals favor $FePt_3$ crystal structures and since $FePt_3$ is antiferromagnetic, the antiferromagnetic and ferromagnetic particles show combinatory hysteresis scan that looks constricted; 3) the surfaces of the FePt nanocrystals could be slightly oxidized and the surface spins are relatively even at zero-magnetic field. More scrutiny is required to disclose the most responsible reason.

7.2 FUTURE RESEARCH DIRECTIONS

7.2.1 Silicon Nanowires

Silicon nanowire synthesis has reached the point where ~40 mg of nanowires are obtained in one reaction inside a flow-through reactor. This is a profound progress considering an initial semi-batch reaction yielded <1 mg of nanowires with relatively poor purity. Scale-up of the synthesis into the <100 mg scale would offer an exciting opportunity to further increase the synthesis quantity. It has been observed that as the reactor size increases, the fluid dynamics signature changes so greatly that the resulting product is influenced. Reaction parameters that work for the small scale synthesis do not necessarily produce desired nanowire materials. Meanwhile, Ge nanowires have been synthesized in ~g scale reactions using a Parr reactor. Since Si precursor decomposition is less forgiving and requires a narrow reaction parameter window to

172

fabricate silicon nanowires in such a scale, understanding of the fluid dynamics in supercritical fluid reactor is a prerequisite.

7.2.2 Carbon Nanotubes

Carbon MWNTs and filaments are produced by Fe nanocrystal-seeded growth in supercritical toluene. This marks a promising first step towards the development of a high throughput solution-phase synthesis of carbon nanotubes. The primary challenge to the process appears to be the stabilization of Fe seed nanocrystals at $600^{\circ}C$ in the desired size range to produce MWNTs. Possibly, pre-formed sterically stabilized nanocrystals could be fed into the reactor as seeds and preliminary research in our laboratory in this direction has shown that MWNTs can be produced but at lower yield, perhaps due to a "blocking effect" of adsorbed hydrocarbon ligands. At any rate, the catalyst particle size appears to determine the morphology of the carbonaceous product and is a critical parameter that must be controlled for success. Another factor that determines the quality of the carbonaceous product—*i.e.*, ratio of MWNTs to filaments, or the production of *single* wall nanotubes—is the reaction temperature. SWNTs were not found in the supercritical toluene synthesis, presumably because the reaction temperature was too low. The problem is that at temperatures much higher than $625\ ^{\circ}C$, toluene homogeneously decomposes very rapidly, competing with heterogeneous nanotube and filament growth to produce large quantities of graphitic byproducts. The byproducts actually appear to poison the metal catalyst particles and prevent nanotube formation under these conditions. Ideally, a supercritical solvent that is thermally stable at higher temperatures, such as CO_2 or water, could provide a promising alternative in which toluene would be fed into the reactor as a reactant with the expectation that it would decompose with a high yield. Our research group has contributed in establishing

173

the chemistry and physics of nanometer-scale materials in supercritical CO_2 and H_2O, and believes that such a reaction scenario is possible.

7.2.3 Magnetic Nanocrystals

Size dependent properties of magnetic nanocrystals and quantum dots have been intensively studied for the past few years. The 'arrested precipitation' technique has provided a unique solution to precise control over nanocrystal size and shape in colloidal phase. Control of shape and size of each nanocrystal has enabled the manipulation of magnetic properties. Versatility of the colloidal synthesis has also generated the interest in nanoscale heterostructures. Understanding the interactions between the different functional components within a nanostructure will serve as a bridge between the fundamental study and practical applications of these materials. To understand the interactions between magnetic components and luminescent parts in heterostructures, several synthetic avenues could be explored. For example, core-shell nanostructures with ferromagnetic core and antiferromagnetic shell could be a good test-bed to study exchange coupling in the nanometer regime. There have been a few research results that have reported similar structures, but the synthetic precision remains yet to be addressed. Heterostructures of magnetic and optical components could also be a very exciting topic. The understanding of the interactions between magnetic and optical materials interfaced with each other in the controlled colloidal nanostructures should allow the manipulation of the spins. The controlled growth of heterostructures of magnetic metal cores with luminescent semiconductor encapsulation will offer the bifunctionality. The magnetic component could be utilized as either magnetic resonance image contrast agent or magnetic handle in bioassays, and the optical part of the heterostructures could offer the luminescence that would be useful for complementary imaging agent.

174

Bibliography

Lange's Handbook of Chemistry, Mc-Graw Hill, Inc., New York, 1999.

Andrews, R.; Jacques, D.; Qian, D. L. and Rantell, T., "Multiwall carbon nanotubes: Synthesis and application," *Acc. Chem. Res.* (2002), 35, 1008-1017.

Arriagada, F. J. and Osseo-Asare, K., "Synthesis of nanosize silica in a nonionic water-in-oil microemulsion: Effects of the water/surfactant molar ratio and ammonia concentration," *J. Colloid. Int. Sci.* (1999), 211, 210-220.

Aslam, M.; Fu, L.; Li, S. and Dravid, V. P., "Silica encapsulation and magnetic properties of FePt nanoparticles," *J. Colloid. Int. Sci.* (2005), 290, 444-449.

Barns, R. L.; Freeland, P. E.; Kolb, E. D.; Laudise, R. A. and Patel, J. R., "Dislocation-Free and Low-Dislocation Quartz Prepared by Hydrothermal Crystallization," *J. Cryst. Growth* (1978), 43, 676-686.

Barrelet, C. J.; Greytak, A. B. and Lieber, C. M., "Nanowire photonic circuit elements," *Nano Lett.* (2004), 4, 1981-1985.

Batson, P. E., "Atomic resolution analytical microscopy," *IBM J. Res. & Dev.* (2000), 44, 477-487.

Bean, C. P. and Livingston, J. D., "Superparamagnetism," *J. Appl. Phys.* (1959), 30, S120-S129.

Bloch, F., *Z. Phys.* (1932), 74, 295.

Bower, C.; Zhou, O.; Zhu, W.; Werder, D. J. and Jin, S., "Nucleation and growth of carbon nanotubes by microwave plasma chemical vapor deposition," *Appl. Phys. Lett.* (2000), 77, 2767.

Bronikowski, M. J.; Willis, P. A.; Colbert, D. T.; Smith, K. A. and Smalley, R. E., "Gas-phase production of carbon single-walled nanotubes from carbon monoxide via the HiPco process: A parametric study," *J. Vac. Sci. Technol. A* (2001), 19, 1800-1805.

Brown, W. F., "Virtues and Weaknesses of the Domain Concept," *Rev. Mod. Phys.* (1945), 17, 15.

Brust, M.; Walker, M.; Bethell, D.; Schiffrin, D. J. and Whyman, R., "Synthesis of Thiol-Derivatized Gold Nanoparticles in a 2-Phase Liquid-Liquid System," *J. Chem. Soc., Chem. Commun.* (1994), 801-802.

Burian, A.; Dore, J. C.; Fischer, H. E. and Sloan, J., "Structural studies of mutliwall carbon nanotubes by neutron diffraction," *Phys. Rev. B* (1999), 59, 1665-1668.

Chen, C. C.; Yeh, C. C.; Chen, C. H.; Yu, M. Y.; Liu, H. L.; Wu, J. J.; Chen, K. H.; Chen, L. C.; Peng, J. Y. and Chen, Y. F., "Catalytic growth and characterization of gallium nitride nanowires," *J. Am. Chem. Soc.* (2001), 123, 2791-2798.

Chen, M.; Liu, J. P. and Sun, S. H., "One-step synthesis of FePt nanoparticles with tunable size," *J. Am. Chem. Soc.* (2004), 126, 8394-8395.

Chen, M.-P.; Kuroishi, K. and Kitamoto, Y., "Magnetic Properties and Microstructure of Isolated Fe-Pt Nanoparticle-Monolayer Assembly by

Protective Coating," *IEEE Trans. Mag.* (2005), 41, 3376-3378.

Cho, K. S.; Talapin, D. V.; Gaschler, W. and Murray, C. B., "Designing PbSe nanowires and nanorings through oriented attachment of nanoparticles," *J. Am. Chem. Soc.* (2005), 127, 7140-7147.

Coutant, R. W. and Levy, A., "Kinetic study of the thermal decomposition of selected cyclohexyl and phenylsilanes.," *U.S. Clearinghouse Fed. Sci. Tech. Inform.* (1969),

Dai, H.; Rinzler, A. G.; Nikolaev, P.; Thess, A.; Colbert, D. T. and Smalley, R. E., "Single-wall nanotubes produced by metal-catalyzed disproportionation of carbon monoxide," *Chem. Phys. Lett* (1996), 260, 471-475.

Dai, H. J.; Kong, J.; Zhou, C. W.; Franklin, N.; Tombler, T.; Cassell, A.; Fan, S. S. and Chapline, M., "Controlled chemical routes to nanotube architectures, physics, and devices," *J. Phys. Chem. B* (1999), 103, 11246-11255.

Davidson, F. M.; Lee, D. C.; Fanfair, D. D. and Korgel, B. A., "Lamellar twinning in semiconductor nanowires," *J. Phys. Chem. C* (2007), 111, 2929-2935.

Davidson, F. M.; Schricker, A. D.; Wiacek, R. and Korgel, B. A., "Supercritical fluid-liquid-solid synthesis of Gallium Arsenide nanowires seeded by alkanethiol-stabilized gold nanocrystals," *Adv. Mater.* (2004), 16, 646-649.

de Lozanne, A., "Application of magnetic force microscopy in nanomaterials characterization," *Microscopy Research and Technique* (2006), 69, 550-562.

Delzeit, L.; Nguyen, C. V.; Chen, B.; Stevens, R.; Cassell, A.; Han, J. and Meyyappan, M., "Multiwalled carbon nanotubes by chemical vapor deposition using multilayered metal catalysts," *J. Phys. Chem. B* (2002), 106, 5629-5635.

Dinega, D. P. and Bawendi, M. G., "A solution phase chemical approach to a new crystal structure of cobalt," *Angew. Chem. Int. Ed.* (1999), 38, 1788-1791.

Ding, Y.; Majetich, S. A.; Kim, J.; Barmak, K.; Rollins, H. and Sides, P., "Sintering prevention and phase transformation of FePt nanoparticles," *J. Magn. Magn. Mater.* (2004), 284, 336-341.

Dingman, S. D.; Rath, N. P.; Markowitz, P. D.; Gibbons, P. C. and Buhro, W. E., "Low-temperature, catalyzed growth of indium nitride fibers from azido-indium precursors," *Angew. Chem. Int. Ed.* (2000), 39, 1470-+.

Doremus, R. H., Diffusion of Reactive Molecules in Solids and Melts, John Wiley & Sons, Inc., New York, 2002.

Dresselhaus, M. S.; Dresselhaus, G. and Avouris, P., Carbon Nanotubes : Synthesis, Structure, Properties, and Applications, Springer, New York, 2002.

Duan, X. F.; Huang, Y. and Lieber, C. M., "Nonvolatile memory and programmable logic from molecule-gated nanowires," *Nano Lett.* (2002), 2, 487-490.

Duan, X. F. and Lieber, C. M., "General synthesis of compound semiconductor nanowires," *Adv. Mater.* (2000), 12, 298-302.

Ebbesen, T. W. and Ajayan, P. M., "Large-scale synthesis of carbon nanotubes," *Nature* (1992), 358, 220-222.

Elkins, K.; Li, D.; Poudyal, N.; Nandwana, V.; Jin, Z. Q.; Chen, K. H. and Liu, J. P., "Monodisperse face-centred tetragonal FePt nanoparticles with giant coercivity," *J. Phys. D* (2005), 38, 2306-2309.

Evans, E. L.; Thomas, J. M.; Thrower, P. A. and Walker, P. L., "Growth of filamentary carbon on metallic surfaces during the pyrolysis of methane and acetone," *Carbon* (1973), 11, 441-445.

Frenkel, J. and Dorfman, J., *Nature* (1930), 126, 274.

Gilman, H.; Tomasi, R. A. and Wittenberg, D., "Thermal stability of triphenylsilane, di- and tri(aralkyl)silanes, dibenzylmethane, and tribenzilmethane," *J. Org. Chem.* (1959), 24, 821-824.

Gogotsi, Y.; Libera, J. A. and Yoshimura, M., "Hydrothermal synthesis of multiwall carbon nanotubes," *J. Mater. Res.* (2000), 15, 2591-2594.

Gogotsi, Y. G. and Yoshimura, M., "Formation of carbon-films on carbides under hydrothermal conditions," *Nature* (1994), 367, 628-630.

Grebinski, J. W.; Richter, K. L.; Zhang, J.; Kosel, T. H. and Kuno, M., "Synthesis and Characterization of Au/Bi Core/Shell Nanocrystals: A Precursor toward II-VI Nanowires," *J. Phys. Chem. B* (2004), 108, 9745-9751.

Gudiksen, M. S.; Lauhon, L. J.; Wang, J.; Smith, D. C. and Lieber, C. M., "Growth of nanowire superlattice structures for nanoscale photonics and electronics," *Nature* (2002), 415, 617-620.

Hahm, J. and Lieber, C. M., "Direct ultrasensitive electrical detection of DNA and DNA sequence variations using nanowire nanosensors," *Nano Lett.* (2004), 4, 51-54.

Hanrath, T. and Korgel, B. A., "Crystallography and surface faceting of germanium nanowires," *Small* (2005), 1, 717-721.

Hanrath, T. and Korgel, B. A., "Nucleation and growth of germanium nanowires seeded by organic monolayer-coated gold nanocrystals," *J. Am. Chem. Soc.* (2002), 124, 1424-1429.

Hanrath, T. and Korgel, B. A., "Supercritical fluid-liquid-solid (SFLS) synthesis of Si and Ge nanowires seeded by colloidal metal nanocrystals," *Adv. Mater.* (2003), 15, 437-440.

Hofer, L. J. E.; Sterling, E. and McCarthy, J. T., "Structure of the carbon deposited from carbon monoxide on iron, cobalt and nickel," *J. Phys. Chem.* (1955), 59, 1153-1155.

Hofmann, S.; Ducati, C.; Robertson, J. and Kleinsorge, B., "Low-temperature growth of carbon nanotubes by plasma-enhanced chemical vapor deposition," *Appl. Phys. Lett.* (2003), 83, 135-137.

Holmes, J. D.; Johnston, K. P.; Doty, R. C. and Korgel, B. A., "Control of thickness and orientation of solution-grown silicon nanowires," *Science* (2000), 287, 1471-1473.

Holmes, J. D.; Ziegler, K. J.; Doty, R. C.; Pell, L. E.; Johnston, K. P. and Korgel, B. A., "Highly luminescent silicon nanocrystals with discrete optical transitions," *J. Am. Chem. Soc.* (2001), 123, 3743-3748.

Hu, J. T.; Odom, T. W. and Lieber, C. M., "Chemistry and physics in one dimension: Synthesis and properties of nanowires and nanotubes," *Acc. Chem. Res.* (1999), 32, 435-445.

Huang, M. H.; Wu, Y. Y.; Feick, H.; Tran, N.; Weber, E. and Yang, P. D., "Catalytic growth of zinc oxide nanowires by vapor transport," *Adv. Mater.* (2001), 13, 113-116.

Huang, Y.; Duan, X. F.; Cui, Y.; Lauhon, L. J.; Kim, K. H. and Lieber, C. M., "Logic gates and computation from assembled nanowire building blocks," *Science* (2001), 294, 1313-1317.

Hubert, H.; Garvie, L. A. J.; Devouard, B.; Buseck, P. R.; Petuskey, W. T. and McMillan, P. F., "High-pressure, high-temperature synthesis and characterization of boron suboxide (B_6O)," *Chem. Mater.* (1998), 10, 1530-1537.

Hyeon, T., "Chemical synthesis of magnetic nanoparticles," *Chem. Comm.* (2003), 927-934.

Hyeon, T.; Chung, Y.; Park, J.; Lee, S. S.; Kim, Y. W. and Park, B. H., "Synthesis of highly crystalline and monodisperse cobalt ferrite nanocrystals," *J. Phys. Chem. B* (2002), 106, 6831-6833.

Hyeon, T.; Lee, S. S.; Park, J.; Chung, Y. and Bin Na, H., "Synthesis of highly crystalline and monodisperse maghemite nanocrystallites without a size-selection process," *J. Am. Chem. Soc.* (2001), 123, 12798-12801.

Hyun, C.; Lee, D. C.; Israel, C.; Korgel, B. A. and de Lozanne, A., "Sintering effect of annealed FePt nanocrystal films observed by MFM," *IEEE Trans. Mag.* (2006), 42, 3799-3702.

Kamins, T. I.; Li, X. and Williams, R. S., "Growth and structure of chemically vapor deposited Ge nanowires on Si substrates," *Nano Lett.* (2004), 4, 503-506.

Kamins, T. I.; Williams, R. S.; Basile, D. P.; Hesjedal, T. and Harris, J. S., "Ti-catalyzed Si nanowires by chemical vapor deposition: Microscopy and growth mechanisms," *J. Appl. Phys.* (2001), 89, 1008-1016.

Kang, E.; Park, J.; Hwang, Y.; Kang, M.; Park, J. G. and Hyeon, T., "Direct synthesis of highly crystalline and monodisperse manganese ferrite nanocrystals," *J. Phys. Chem. B* (2004), 108, 13932-13935.

Kim, N. S.; Lee, Y. T.; Park, J.; Han, J. B.; Choi, Y. S.; Choi, S. Y.; Choo, J. B. and Lee, G. H., "Vertically aligned carbon nanotubes grown by pyrolysis of iron, cobalt, and nickel phthalocyanines," *J. Phys. Chem. B* (2003), 107, 9249-9255.

Kittel, C., "Theory of the Structure of Ferromagnetic Domains in Films and Small Particles," *Phys. Rev.* (1946), 70, 965-971.

Kong, J.; Cassell, A. M. and Dai, H., "Chemical vapor deposition of methane for single-walled carbon nanotubes," *Chem. Phys. Lett* (1998), 292, 567-574.

Kong, J.; Soh, H. T.; Cassell, A. M.; Quate, C. F. and Dai, H., "Synthesis of individual single-walled carbon nanotubes on patterned silicon wafers," *Nature* (1998), 395, 878-881.

Konno, T. J. and Sinclair, R., "Crystallization of Amorphous-Carbon in Carbon-Cobalt Layered Thin-Films," *Acta Metallur. Mater.* (1995), 43, 471-484.

Korgel, B. A. and Fitzmaurice, D., "Self-assembly of silver nanocrystals into two-dimensional nanowire arrays," *Adv. Mater.* (1998), 10, 661-665.

Korgel, B. A.; Fullam, S.; Connolly, S. and Fitzmaurice, D., "Assembly and self-organization of silver nanocrystal superlattices: Ordered "soft spheres"," *J. Phys. Chem. B* (1998), 102, 8379-8388.

Kuznetsov, V. L.; Usoltseva, A. N.; Chuvilin, A. L.; Obraztsova, E. D. and Bonard, J. M., "Thermodynamic analysis of nucleation of carbon deposits on metal particles and its implications for the growth of carbon nanotubes," *Phys. Rev. B* (2001), 64, 235401.

Lai, C. H.; Wu, Y. C. and Chiang, C. C., "Effects of forming gas annealing on low-temperature ordering of FePt films," *J. Appl. Phys.* (2005), 97, 10H305.

Lambeth, D. N.; Velu, E. M. T.; Bellesis, G. H.; Lee, L. L. and Laughlin, D. E., "Media for 10 Gb/in(2) hard disk storage: Issues and status," *J. Appl. Phys.* (1996), 79, 4496-4501.

Lee, D. C.; Ghezelbash, A.; Stowell, C. A. and Korgel, B. A., "Synthesis and Magnetic Properties of Colloidal MnPt3 Nanocrystals," *J. Phys. Chem. B* (2006), 110, 20906-20911.

Lee, D. C.; Hanrath, T. and Korgel, B. A., "The role of precursor-decomposition kinetics in silicon-nanowire synthesis in organic solvents," *Angew. Chem. Int. Ed.* (2005), 44, 3573-3577.

Lee, D. C. and Korgel, B. A., "Metal nanocrystal-seeded synthesis of carbon nanotubes and nanofibers in a supercritical fluid," *Mol. Simul.* (2005), 31, 637.

Lee, D. C.; Mikulec, F. V. and Korgel, B. A., "Carbon nanotube synthesis in supercritical toluene," *Journal of the American Chemical Society* (2004), 126, 4951-4957.

Leistner, K.; Thomas, J.; Schlorb, H.; Weisheit, M.; Schultz, L. and Fahler, S., "Highly coercive electrodeposited FePt films by postannealing in hydrogen," *Appl. Phys. Lett.* (2004), 85, 3498-3500.

Levitt, A. P., Whisker Technology, John Wiley & Sons, Inc., New York, 1970.

Libera, J. and Gogotsi, Y., "Hydrothermal synthesis of graphite tubes using Ni catalyst," *Carbon* (2001), 39, 1307-1318.

Lieber, C. M., "The incredible shrinking circuit - Researchers have built nanotransistors and nanowires. Now they just need to find a way to put them all together," *Sci. Am.* (2001), 285, 58-64.

Liu, C.; Wu, X. W.; Klemmer, T. J.; Shukla, N.; Weller, D.; Roy, A. G.; Tanase, M. and Laughlin, D., "Reduction of Sintering during Annealing of FePt Nanoparticles Coated with Iron Oxide," *Chem. Mater.* (2005), 17, 620-625.

Louchev, O. A. and Hester, J. R., "Kinetic pathways of carbon nanotube nucleation from graphitic nanofragments," *J. Appl. Phys.* (2003), 94, 2002-2010.

Lu, X. M.; Hanrath, T.; Johnston, K. P. and Korgel, B. A., "Growth of single crystal nanowires in supercritical silicon solution from tethered gold particles on a silicon substrate," *Nano Letters* (2003), 3, 93-99.

Mizuno, M.; Sasaki, Y.; Yu, A. C. C. and Inoue, M., "Prevention of Nanoparticle Coalescence under High-Temperature Annealing," *Langmuir* (2004), 20, 11305-11307.

Morales, A. M. and Lieber, C. M., "A laser ablation method for the synthesis of crystalline semiconductor nanowires," *Science* (1998), 279, 208-211.

Murray, C. B.; Norris, D. J. and Bawendi, M. G., "Synthesis and Characterization of Nearly Monodisperse CdE(E=S, Se, Te) Semiconductor Nanocrystallites," *J. Am. Chem. Soc.* (1993), 115, 8706-8715.

Murray, C. B.; Sun, S. H.; Doyle, H. and Betley, T., "Monodisperse 3d transition-metal (Co, Ni, Fe) nanoparticles and their assembly into nanoparticle superlattices," *MRS Bull.* (2001), 26, 985-991.

Nalwa, H. S., Magnetic Nanostructures, American Scientific Publishers, New York, 2002.

Neel, L., "Thermoremanent magnetization of the fine powders," *Rev. Mod. Phys.* (1953), 25, 293.

Nelson, L. E.; Angelotti, N. C. and Weyenberg, D. R., "The free radical-catalyzed disproportionation of arylsilanes. A new homolytic aromatic displacement reaction," *J. Am. Chem. Soc.* (1963), 85, 2662-2663.

Nguyen, H. L.; Howard, L. E. M.; Giblin, S. R.; Tanner, B. K.; Terry, I.; Hughes, A. K.; Ross, I. M.; Serres, A.; Burckstummer, H. and Evans, J. S. O., "Synthesis of monodispersed fcc and fct FePt/FePd nanoparticles by microwave irradiation," *J. Mater. Chem.* (2005), 15, 5136-5143.

Nikolaev, P.; Bronikowski, M. J.; Bradley, R. K.; Rohmund, F.; Colbert, D. T.; Smith, K. A. and Smalley, R. E., "Gas-phase catalytic growth of single-walled carbon nanotubes from carbon monoxide," *Chem. Phys. Lett* (1999), 313, 91-97.

Nosaka, Y.; Yamaguchi, K.; Miyama, H. and Hayashi, H., "Preparation of Size-Controlled Cds Colloids in Water and Their Optical-Properties," *Chem. Lett.* (1988), 605-608.

Ono, K.; Okuda, R.; Ishii, Y.; Kamimura, S. and Oshima, M., "Synthesis of ferromagnetic Mn-Pt nanoparticles from organometallic precursors," *J. Phys. Chem. B* (2003), 107, 1941-1942.

Osseo-Asare, K. and Arriagada, F. J., "Growth kinetics of nanosize silica in a nonionic water-in-oil microemulsion: A reverse micellar pseudophase reaction model," *J. Colloid. Int. Sci.* (1999), 218, 68-76.

Park, J.; An, K. J.; Hwang, Y. S.; Park, J. G.; Noh, H. J.; Kim, J. Y.; Park, J. H.; Hwang, N. M. and Hyeon, T., "Ultra-large-scale syntheses of monodisperse nanocrystals," *Nat. Mater.* (2004), 3, 891-895.

Park, J.; Koo, B.; Yoon, K. Y.; Hwang, Y.; Kang, M.; Park, J.-G. and Hyeon, T., "Generalized synthesis of metal phosphide nanorods via thermal decomposition of continuously delivered metal-phosphine complexes using a syringe pump," *J. Am. Chem. Soc.* (2005), 127, 8433-8440.

Park, J.; Lee, E.; Hwang, N. M.; Kang, M. S.; Kim, S. C.; Hwang, Y.; Park, J. G.; Noh, H. J.; Kini, J. Y.; Park, J. H. and Hyeon, T., "One-nanometer-scale size-controlled synthesis of monodisperse magnetic iron oxide nanoparticles," *Angew. Chem. Int. Ed.* (2005), 44, 2872-2877.

Park, S. J.; Kim, S.; Lee, S.; Khim, Z. G.; Char, K. and Hyeon, T., "Synthesis and magnetic studies of uniform iron nanorods and nanospheres," *J. Am. Chem. Soc.* (2000), 122, 8581-8582.

Pell, L. E.; Schricker, A. D.; Mikulec, F. V. and Korgel, B. A., "Synthesis of amorphous silicon colloids by trisilane thermolysis in high temperature supercritical solvents," *Langmuir* (2004), 20, 6546-6548.

Peng, S.; Wang, C.; Xie, J. and Sun, S., "Synthesis and stabilization of monodisperse Fe nanoparticles," *J. Am. Chem. Soc.* (2006), 128, 10676-10677.

Peng, X.; Manna, L.; Yang, W. D.; Wickham, J.; Scher, E.; Kadavanich, A. and Alivisatos, A. P., "Shape control of CdSe nanocrystals," *Nature* (2000), 404, 59-61.

Penn, R. L., "Kinetics of oriented aggregation," *J. Phys. Chem. B* (2004), 108, 12707-12712.

Perez-Dieste, V.; Castellini, O. M.; Crain, J. N.; Eriksson, M. A.; Kirakosian, A.; Lin, J. L.; McChesney, J. L.; Himpsel, F. J.; Black, C. T. and Murray, C. B., "Thermal decomposition of surfactant coatings on Co and Ni nanocrystals," *Appl. Phys. Lett.* (2003), 83, 5053-5055.

Petit, C.; Taleb, A. and Pileni, M.-P., "Self-organization of magnetic nanosized cobalt particles," *Adv. Mater.* (1998), 10, 259-261.

Pileni, M.-P., "Self-assemblies of nanocrystals: fabrication and collective properties," *Appl. Surf. Sci.* (2001), 171, 1-14.

Puntes, V. F.; Krishnan, K. M. and Alivisatos, A. P., "Colloidal nanocrystal shape and size control: the case of cobalt," *Science* (2001), 291, 2115-2117.

Puntes, V. F.; Zanchet, D.; Erdonmez, C. K. and Alivisatos, A. P., "Synthesis of hcp-Co nanodisks," *J. Am. Chem. Soc.* (2002), 124, 12874-12880.

Qian, F.; Li, Y.; Gradecak, S.; Wang, D. L.; Barrelet, C. J. and Lieber, C. M., "Gallium nitride-based nanowire radial heterostructures for nanophotonics," *Nano Lett.* (2004), 4, 1975-1979.

Reed, B. W.; Chen, J. M.; MacDonald, N. C.; Silcox, J. and Bertsch, G. F., "Fabrication and STEM/EELS measurements of nanometer-scale silicon tips and filaments," *Phys. Rev. B* (1999), 60, 5641-5652.

Reiss, B. D.; Mao, C.; Solis, D. J.; Ryan, K. S.; Thomson, T. and Belcher, A. M., "Biological Routes to Metal Alloy Ferromagnetic Nanostructures," *Nano Lett.* (2004), 4, 1127-1132.

Ren, Z. F.; Huang, Z. P.; Xu, J. W.; Wang, J. H.; Bush, P.; Siegal, M. P. and Provencio, P. N., "Synthesis of large arrays of well-aligned carbon nanotubes on glass," *Science* (1998), 282, 1105-1107.

Saunders, A. E.; Sigman, M. B. and Korgel, B. A., "Growth kinetics and metastability of monodisperse tetraoctylammonium bromide capped gold nanocrystals," *J. Phys. Chem. B* (2004), 108, 193-199.

Shah, P. S.; Holmes, J. D.; Doty, R. C.; Johnston, K. P. and Korgel, B. A., "Steric stabilization of nanocrystals in supercritical CO2 using fluorinated ligands," *J. Am. Chem. Soc.* (2000), 122, 4245-4246.

Shah, P. S.; Holmes, J. D.; Johnston, K. P. and Korgel, B. A., "Size-selective dispersion of dodecanethiol-coated nanocrystals in liquid and supercritical ethane by density tuning," *J. Phys. Chem. B* (2002), 106, 2545-2551.

Shah, P. S.; Husain, S.; Johnston, K. P. and Korgel, B. A., "Nanocrystal arrested precipitation in supercritical carbon dioxide," *J. Phys. Chem. B* (2001), 105, 9433-9440.

Shao, M.; Li, Q.; Wu, J.; Xie, B.; Zhang, S. and Qian, Y., "Benzene-thermal route to carbon nanotubes at a moderate temperature," *Carbon* (2000), 40, 2961-2973.

Shevchenko, E. V.; Talapin, D. V.; Schnablegger, H.; Kornowski, A.; Festin, O.; Svedlindh, P.; Haase, M. and Weller, H., "Study of nucleation and growth in the organometallic synthesis of magnetic alloy nanocrystals: The role of nucleation rate in size control of CoPt3 nanocrystals," *J. Am. Chem. Soc.* (2003), 125, 9090-9101.

Shima, T.; Takanashi, K.; Takahashi, Y. K.; Hono, K.; Li, G. Q. and Ishio, S., "High coercivity and magnetic domain observation in epitaxially grown particulate FePt thin films," *J. Magn. Magn. Mater.* (2003), 266, 171-177.

Sigman, M. B.; Ghezelbash, A.; Hanrath, T.; Saunders, A. E.; Lee, F. and Korgel, B. A., "Solventless Synthesis of Monodisperse Cu2S Nanorods, Nanodisks, and Nanoplatelets," *J. Am. Chem. Soc.* (2003), 125, 16050-16057.

Stach, E. A.; Pauzauskie, P. J.; Kuykendall, T.; Goldberger, J.; He, R. R. and Yang, P. D., "Watching GaN nanowires grow," *Nano Lett.* (2003), 3, 867-869.

Stappert, S.; Rellinghaus, B.; Acet, M. and Wassermann, E. F., "Gas-phase preparation of L1(0) ordered FePt nanoparticles," *J. Cryst. Growth* (2003), 252, 440-450.

Steigerwald, M. L.; Alivisatos, A. P.; Gibson, J. M.; Harris, T. D.; Kortan, R.; Muller, A. J.; Thayer, A. M.; Duncan, T. M.; Douglass, D. C. and Brus, L. E., "Surface Derivatization and Isolation of Semiconductor Cluster Molecules," *J. Am. Chem. Soc.* (1988), 110, 3046-3050.

Stowell, C. A. and Korgel, B. A., "Iridium nanocrystal synthesis and surface coating-dependent catalytic activity," *Nano Lett.* (2005), 5, 1203-1207.

Stowell, C. A.; Wiacek, R. J.; Saunders, A. E. and Korgel, B. A., "Synthesis and characterization of dilute magnetic semiconductor manganese-doped indium arsenide nanocrystals," *Nano Lett.* (2003), 3, 1441-1447.

Sun, S., "Recent Advances in Chemical Synthesis,

Self-Assembly, and Applications of FePt

Nanoparticles," *Adv. Mater.* (2006), 18, 393-403.

Sun, S. H.; Fullerton, E. E.; Weller, D. and Murray, C. B., "Compositionally controlled FePt nanoparticle materials," *IEEE Trans. Mag.* (2001), 37, 1239-1243.

Sun, S. H. and Murray, C. B., "Synthesis of monodisperse cobalt nanocrystals and their assembly into magnetic superlattices (invited)," *J. Appl. Phys.* (1999), 85, 4325-4330.

Sun, S. H.; Murray, C. B.; Weller, D.; Folks, L. and Moser, A., "Monodisperse FePt nanoparticles and ferromagnetic FePt nanocrystal superlattices," *Science* (2000), 287, 1989-1992.

Swihart, M. T. and Girshick, S. L., "Thermochemistry and kinetics of silicon hydride cluster formation during thermal decomposition of silane," *J. Phys. Chem. B* (1999), 103, 64-76.

Tago, T.; Hatsuta, T.; Miyajima, K.; Kishida, M.; Tashiro, S. and Wakabayashi, K., "Novel synthesis of silica-coated ferrite nanoparticles prepared using water-in-oil microemulsion," *J. Am. Chem. Soc.* (2002), 85, 2188-2194.

Takahashi, Y. K.; Ohnuma, M. and Hono, K., "Effect of Cu on the structure and magnetic properties of FePt sputtered film," *J. Magn. Magn. Mater.* (2002), 246, 259-265.

Talapin, D. V. and Murray, C. B., "PbSe nanocrystal solids for n- and p-channel thin film field-effect transistors," *Science* (2005), 310, 86-89.

Tang, Z. Y.; Zhang, Z. L.; Wang, Y.; Glotzer, S. C. and Kotov, N. A., "Self-assembly of CdTe nanocrystals into free-floating sheets," *Science* (2006), 314, 274-278.

Thess, A.; Lee, R.; Nikolaev, P.; Dai, H.; Petit, P.; Robert, J.; Xu, C. H.; Lee, Y. H.; Kim, S. G.; Rinzler, A. G.; Colbert, D. T.; Scuseria, G. E.; Tomanek, D.; Fischer, J. E. and Smalley, R. E., "Crystalline ropes of metallic carbon nanotubes," *Science* (1996), 273, 483-487.

Tuan, H.-Y.; Lee, D. C.; Hanrath, T. and Korgel, B. A., "Catalytic Solid-Phase Seeding of Silicon Nanowires by Nickel Nanocrystals in Organic Solvents," *Nano Lett.* (2004), 5, 681-684.

Tuan, H.-Y.; Lee, D. C. and Korgel, B. A., "Nanocrystal-Mediated Crystallization of Silicon and Germanium Nanowires in Organic Solvents: The Role of Catalysis and Solid-Phase Seeding," *Angew. Chem. Int. Ed.* (2006), 45, 5184-5187.

Vanderwielen, A. J.; Ring, M. A. and Oneal, H. E., "Kinetics of Thermal-Decomposition of Methyldisilane and Trisilane," *J. Am. Chem. Soc.* (1975), 97, 993-998.

Vedantam, T. S.; Liu, J. P.; Zeng, H. and Sun, S., "Thermal stability of self-assembled FePt nanoparticles," *J. Appl. Phys.* (2003), 93, 7184-7186.

Vossmeyer, T.; Katsikas, L.; Giersig, M.; Popovic, I. G.; Diesner, K.; Chemseddine, A.; Eychmuller, A. and Weller, H., "Cds Nanoclusters - Synthesis, Characterization, Size-Dependent Oscillator Strength, Temperature Shift of the Excitonic-Transition Energy, and Reversible Absorbency Shift," *J. Phys. Chem.* (1994), 98, 7665-7673.

Wagner, R. S. and Ellis, W. C., "Vapor-liquid-solid mechanism of single crystal growth," *Appl. Phys. Lett.* (1964), 4, 89-90.

Wang, D. and Dai, H., "Low-temperature synthesis of single-crystal germanium nanowires by chemical vapor deposition," *Angew. Chem. Int. Ed.* (2002), 41, 4783-4786.

Wang, W.; Gu, B. H.; Liang, L. Y. and Hamilton, W., "Fabrication of two- and three-dimensional silica nanocolloidal particle arrays," *J. Phys. Chem. B* (2003), 107, 3400-3404.

Watkins, J. J.; Blackburn, J. M. and McCarthy, T. J., "Chemical fluid deposition: Reactive deposition of platinum metal from carbon dioxide solution," *Chem. Mater.* (1999), 11, 213-215.

Weller, D. and Moser, A., "Thermal effect limits in ultrahigh-density magnetic recording," *IEEE Trans. Mag.* (1999), 35, 4423-4439.

Wernsdorfer, W.; Doudin, B.; Mailly, D.; Hasselbach, K.; Benoit, A.; Meier, J.; Ansermet, J.-P. and Barbara, B., "Nucleation of magnetization reversal in individual nanosized nickel wires," *Phys. Rev. Lett.* (1996), 77, 1873-1876.

Westwater, J.; Gosain, D. P.; Tomiya, S.; Usui, S. and Ruda, H., "Growth of silicon nanowires via gold/silane vapor-liquid-solid reaction," *J. Vac. Sci. Technol. B* (1997), 15, 554-557.

Wierman, K. W.; Hilfiker, J. N.; Sabiryanov, R. F.; Jaswal, S. S.; Kirby, R. D. and Woollam, J. A., "Optical and magneto-optical constants of MnPt3," *Phys. Rev. B* (1997), 55, 3093-3099.

Wierman, K. W. and Kirby, R. D., "Long-range order and magnetic properties of MnxPt1-x thin films," *J. Magn. Magn. Mater.* (1996), 154, 12-16.

Wiesendanger, R., "Correlation between nanoscale structural, electronic, and magnetic properties of thin films by scanning-probe microscopy and spectroscopy," *MRS Bull.* (1997), 22, 31-35.

Woods, S. I.; Kirtley, J. R.; Sun, S. H. and Koch, R. H., "Direct investigation of superparamagnetism in Co nanoparticle films," *Phys. Rev. Lett.* (2001), 8713,

Wu, Y.; Cui, Y.; Huynh, L.; Barrelet, C. J.; Bell, D. C. and Lieber, C. M., "Controlled growth and structures of molecular-scale silicon nanowires," *Nano Lett.* (2004), 4, 433-436.

Wu, Y.; Fan, R. and Yang, P., "Block-by-block growth of single-crystalline Si/SiGe superlattice nanowires," *Nano Lett.* (2002), 2, 83-86.

Wu, Y. Y. and Yang, P., "Direct observation of vapor-liquid-solid nanowire growth," *J. Am. Chem. Soc.* (2001), 123, 3165-3166.

Xia, Y.; Yang, P.; Sun, Y.; Wu, Y.; Mayers, B.; Gates, B.; Yin, Y.; Kim, F. and Yan, H., "One-dimensional nanostructures: synthesis, characterization, and applications," *Adv. Mater.* (2003), 15, 353-389.

Yamamoto, S.; Morimoto, Y.; Ono, T. and Takano, M., "Magnetically superior and easy to handle L1(0)-FePt nanocrystals," *Appl. Phys. Lett.* (2005), 87,

Yan, Q.; Kim, T.; Purkayastha, A.; Ganesan, P. G.; Shima, M. and Ramananth, G., "Enhanced Chemical Ordering and Coercivity in FePt Alloy Nanoparticles by Sb-Doping," *Adv. Mater.* (2005), 17, 2233-2237.

Yaws, C. L., Handbook of Thermodynamic Diagrams, Gulf Publishing Company, Houston, Texas, 1996.

Yi, D. K.; Lee, S. S.; Papaefthymiou, G. C. and Ying, J. Y., "Nanoparticle Architectures Templated by SiO2/Fe2O3 Nanocomposites," *Chem. Mater.* (2006), 18, 614-619.

Yi, D. K.; Selvan, S. T.; Lee, S. S.; Papaefthymiou, G. C.; Kundaliya, D. and Ying, J. Y., "Silica-coated nanocomposites of magnetic nanoparticles and quantum dots," *J. Am. Chem. Soc.* (2005), 127, 4990-4991.

Yu, J. H.; Joo, J.; Park, H. M.; Baik, S. I.; Kim, Y. W.; Kim, S. C. and Hyeon, T., "Synthesis of quantum-sized cubic ZnS nanorods by the oriented attachment mechanism," *J. Am. Chem. Soc.* (2005), 127, 5662-5670.

Zeng, H.; Li, J.; Wang, Z. L.; Liu, J. P. and Sun, S., "Bimagnetic Core/Shell FePt/Fe3O4 Nanoparticles," *Nano Lett.* (2004), 4, 187-190.

Zeng, H.; Sun, S. H.; Li, J.; Wang, Z. L. and Liu, J. P., "Tailoring magnetic properties of core/shell nanoparticles," *Appl. Phys. Lett.* (2004), 85, 792-794.

Zeppenfeld, K., "Anisotropy of plasma oscillations in graphite," *Z. Phys.* (1968), 211, 391-399.

Ziegler, K. J.; Doty, R. C.; Johnston, K. P. and Korgel, B. A., "Synthesis of organic monolayer-stabilized copper nanocrystals in supercritical water," *J. Am. Chem. Soc.* (2001), 123, 7797-7803.

Vita

Doh Chang Lee, the first child of Jung Key Lee and Jung In Lyu, was born on February 26, 1978 in Seoul, Korea. After graduating from the Seoul Science High School in 1996, he entered the Seoul National University in pursuit of undergraduate education. In 2000, he graduated with a B.S. degree in Chemical Engineering. Then, he carried out his research on selective hydrogenation under the supervision of Professor Sang Heup Moon and received a M.S. degree in the Seoul National University in 2002. He entered graduate school at The University of Texas at Austin in the Department of Chemical Engineering. He joined Professor Brian A. Korgel's research group and has pursued his Ph.D research on silicon nanostructures, carbon nanotubes, and magnetic nanocrystals.

Permanent address: Seocho4-dong, Acrovista Apt. 1602, Seocho-gu, Seoul, Korea
This dissertation was typed by the author.

187